U.PORTO

FEUP FACULDADE DE ENGENHARIA
UNIVERSIDADE DO PORTO

Alternative materials infiltration in 3D ceramic models printed by Binder Jetting: a feasibility assessment

Edwin Marcelo Ocaña Garzón

2019

Alternative materials infiltration in 3D ceramic models printed by Binder Jetting: a feasibility assessment

Edwin Marcelo Ocaña Garzón

Thesis submitted to the Faculty of Engineering of the University of Porto - FEUP
in partial fulfilment of the requirements for the degree of
Doctor in Mechanical Engineering

Advisor: Jorge Lino Alves, PhD
Associate Professor at FEUP

Department of Mechanical Engineering (DEMec)

Doctoral Program in Mechanical Engineering (PRODEM)

Faculty of Engineering of the University of Porto (FEUP)

Porto, July 2019

To God,

and my family.

Acknowledgements

This thesis would not have been possible without the support of many to whom I am very and sincerely grateful.

First of all, I am deeply grateful to my Father God, who has always remained at my side, putting angels on my path to get me up every time I fell, and has given me opportunities and privileges in life.

To my parents, Mauro and Rosa, to whom I dedicate all I have obtained, because they gave me everything with so much sacrifice. From them I received the best teachings of life from my first days, leaving me their legacy, honesty, the value of the simple things of life and supporting me at all times also making me know that I always count on them.

To my children, Belén, Sofia and José Daniel, for their motivation and joy that they give me every day with a simple smile, a word and their sweetness encouraging me to take on new challenges and overcome even the most difficult ones.

To my wife, Margoth, who patiently endured and supported me in the good and hard times.

To my brothers Hernán and Nancy who have always sought my personal advancement with their advice and support.

To all my family, of whom I am proud, who are wonderful, namely my grandparents who have been exemplary. All of them have given me their support when it has been necessary.

To my advisor, Professor Jorge Lino, who has trusted me and gave me the opportunity to successfully complete my PhD.

To Carlos Naranjo, and other colleague professors from Universidad de las Fuerzas Armadas-ESPE, who trusted and supported me to obtain the funding to study this doctorate.

To Leonardo Santana, a real friend in and out of the University, who with his sincerity and advice gained my trust and friendship, being also a key support to successfully complete this work.

To Beatriz Graça, Carla Monteiro and Susana Sousa, staff from FEUP, at one time or another, supported me academically with great collaboration.

To Aurelio Netto, Professor of the Instituto Federal de Educação, Ciência e Tecnologia de Santa Catarina- IFSC, who disinterestedly contributed with his time to structure this work.

To my colleagues in the Laboratory of Product Development and Services of FEUP, who gave me their time and support in the day-to-day work.

Finally, to all of those who directly or indirectly contributed to this thesis, and have not been mentioned for a lapse of memory.

"Trust in the Lord with all your heart, and lean not on your own understanding" (Proverbs 3:5-NIV)

July, 2019
Edwin Ocaña Garzón

Financial Support

This research is supported by the: Universidad de las Fuerzas Armadas ESPE, Ecuador under grant – Orden de rectorado Nº 2014-299-ESPE-a-3, and Project NORTE-01-0145-FEDER-000022 - SciTech - Science and Technology for Competitive and Sustainable Industries, cofinanced by Programa Operacional Regional do Norte (NORTE2020), through Fundo Europeu de Desenvolvimento Regional (FEDER).

Abstract

One of the major limitations associated with Binder Jetting (BJ) technology, with plaster powder-base materials, is the low mechanical strength of green three-dimensional printed (3DP) components. In order to overcome this disadvantage, post-processing (PP) operations are required, being the infiltration with polymeric materials the mostly used technique. The scarcely available literature, plus the limited infiltrating materials accessible to all types of users, make this stage an arduous task and strongly dependent on solutions offered by BJ technology providers, which are generally higher cost. Based on these limitations, the opportunity to develop a doctoral research was presented with the aim of providing tools to better understand the steps of printing and infiltration, as well as the selection and adequate application of alternative infiltrating materials (not necessarily dedicated to infiltration of 3DP parts), aiming to improve the flexural properties of 3DP models, with simple and fast procedures. For this purpose, the study was divided into five stages: i) characterization of the printing powder, ii) evaluation of 3DP parts in their green condition, iii) thermal and mechanical analysis of 3DP models infiltrated with methods and materials suggested by the supplier of the technology BJ, iv) selection (based on technical, economic and accessibility criteria), characterization and infiltration of 3DP samples with alternative infiltrants, and v) cure improvement (time and flexural properties) of the material with grater challenges to infiltration process, identified in the previous study. Among the main characterizations used, the chemical composition, morphology, particle size distribution, permeability measurement, hydraulic conductivity, pore size distribution, thermal analysis, and mechanical (static and dynamic) tests are highlighted. The obtained results demonstrate the possibility of using alternative infiltrating materials, different of those suggested by the supplier of the technology, thus offering a viable set of solutions to reduce post-processing times and costs, while also improving the mechanical properties of infiltrated 3DP models. More generally, this research contributes to re-stimulate and disseminate scientific studies in the field of BJ technology.

Keywords: 3D Printing, Binder Jetting, plaster powder, infiltration, alternative infiltrants, epoxy resin, flexural properties.

Resumo

Uma das maiores limitações associadas à tecnologia *Binder Jetting* (BJ), com materiais à base de pó de gesso, é a baixa resistência mecânica em verde dos componentes impressos tridimensionalmente (3DP). Para superar esta desvantagem, são necessárias operações de pós-processamento (PP), sendo a técnica de infiltração com materiais poliméricos a mais utilizada. A pouca difusão literária, e a restrita quantidade de materiais infiltrantes disponíveis e ao alcance de todo o tipo de utilizadores, tornam esta etapa uma tarefa árdua e fortemente dependente de soluções oferecidas pelos fornecedores da tecnologia BJ, que são geralmente de maior custo. Baseado nestas limitações, verificou-se a oportunidade de se desenvolver uma investigação de doutoramento com o objetivo de fornecer ferramentas para aumentar a compreensão das etapas de impressão e infiltração, além da seleção e aplicação adequada de materiais infiltrantes alternativos (não necessariamente dedicados à infiltração de peças 3DP) visando melhorar as propriedades mecânicas à flexão de modelos 3DP, com procedimentos simples e rápidos. Para tal, o estudo foi dividido em cinco etapas: i) caracterização do pó de impressão, ii) avaliação das peças 3DP na sua condição em verde, iii) análise térmica e mecânica de modelos 3DP infiltrados com métodos e materiais sugeridos pelo fornecedor da tecnologia BJ, iv) seleção (com base em critérios técnicos, económicos, e de acessibilidade), caracterização, e infiltração de amostras 3DP com infiltrantes alternativos, e v) melhoramento da cura (tempo e propriedades à flexão) do material com maiores desafios ao processo de infiltração, identificado no estudo anterior. Entre as principais caracterizações utilizadas ao longo das etapas mencionadas, destacam-se: composição química, morfologia, distribuição de tamanho de partícula, medição da permeabilidade, condutividade hidráulica, distribuição do tamanho de poro, análises térmicas, e ensaios mecânicos (estáticos e dinâmicos). Os resultados obtidos demostram a possibilidade de se utilizar materiais infiltrantes alternativos aos sugeridos pelo fornecedor da tecnologia, oferecendo assim um conjunto de soluções viáveis para reduzir os tempos e custos de pós-procesamento, e melhorar as propriedades mecânicas à flexão dos modelos 3DP infiltrados. De um modo mais geral, esta investigação contribui para reimpulsionar e difundir estudos científicos no âmbito da tecnologia BJ.

Palavras-chave: 3D Printing, Binder Jetting, pó de gesso, infiltração, infiltrantes alternativos, resina epóxi, resistencia à flexão.

Table of Contents

List of Figures

List of Tables

Nomenclature (List of Symbols)

Permeability

k	permeability
K	hydraulic conductivity
Ks	saturated hydraulic conductivity
ϕ_o	apparent porosity measured by saturated liquid technique
Lv	low viscosity
Hv	high viscosity
Do	default print orientation
Vo	vertical print orientation
Ds	default saturation level of binder/volume ratio
Hs	high saturation level of binder/volume ratio
Cl	colour binder
nCl	colourless binder
h_0	initial fluid level
h_1	final fluid level
L	length of porous sample
A	cross-sectional area of porous specimen
t	time
μ	fluid dynamic viscosity (or absolute)
ρ	fluid density
g	gravity acceleration
m_d	weight in dry state
m_{sub}	weight measured in an immersion liquid
m_s	weight of porous specimen saturated with liquid
ϕ_{Hg}	apparent porosity measured by MIP technique

Thermal and mechanical analysis

Tg_0	glass transition temperature of uncured resin
${}_{gel}Tg$	glass transition temperature where gelation and vitrification can simultaneously occur
Tg_∞	glass transition temperature of a fully reacted material
α	degree of cure of thermosetting material
CY	cyanoacrylate infiltrant (ColorBond™)
MS	magnesium sulphate infiltrant (Epsom Salt)
W	distilled water as infiltrant
$E1$	epoxy resin as infiltrant (StrengthMax™)
$E2$	epoxy resin as infiltrant (Biresin CR83-6™)
$E3$	epoxy resin as infiltrant (Elantas EC131LV / W342™)
U	urethane resin as infiltrant (Crystal Clear® 200)
σ_{fM}	maximum flexural stress
E_B	flexural E-modulus

E'	storage module (stiffness)
E''	loss modulus- (damping)
$tan\ \delta$	loss factor (phase angle)
Δh_{total}	total reaction heat or total enthalpy of reaction
$h(t)$	specific (residual) reaction heat at time “t” (specific enthalpy of cure)
ν	dynamic viscosity of the infiltrant resins (or absolute)
RP	reduction porous rate
CT	conditioning time before bending test
R_m, R_f	moderate and, rapid heating cure ramps

Acronyms

3D	Three Dimensional
3DP	Three-Dimensional Printing
AM	Additive Manufacturing
ANOVA	Analysis of Variance
BJ	Binder Jetting
CAD	Computer-Aided Design
CPJ	Colour Jet Printing
DGEBA	Diglycidyl Ether of Bisphenol-A
DMA	Dynamic Mechanical Analysis
DOE	Design Of Experiments
DSC	Differential Scanning Calorimetry
EDS	Energy Dispersive Spectroscopy
FEUP	Faculty of Engineering of the University of Porto
FTIR	Furier Transform Infrared Spectroscopy
LD	Laser diffraction
LDPS	Laboratory of Development of Products and Services
MIP	Mercury Intrusion Porosimetry
MJ	Material Jetting
PCL	Poly(ε-caprolactone)
PEEK	Polyether Ether Ketone
PF	Phenol Formaldehyde
PMMA	Polymethyl Methacrylate
PP	Post-Processing
PSD	Particle Size Distribution / Pore Size Distribution
RC	Rapid Casting
RIC	Rapid Investment Casting
RP	Porous Reduction rate
RP&T	Rapid Prototyping and Tooling
RSD	Relative Standard Deviation
RT	Room Temperature
RTM	Resin Transfer Moulding
SED	Secondary Electron Detector
SEM	Scanning Electron Microscopy
SGM	Spiral Growth Manufacturing
SLA	Stereolithography
SLM	Selective Laser Melting
TGA	Thermogravimetric Analysis
TTT	Time-Temperature-Transformation
UFA-ESPE	Universidad de las Fuerzas Armadas - ESPE
UVL	Ultraviolet Light

Publications related to this work

- Ocaña Garzón Edwin, Alves J. L. Mechanical properties of bending 3DP models of different thickness infiltrated with alternative materials Int J Adv Eng Technol. 2019; 3(2):27-37.
- Ocaña-Garzón Edwin, Leonardo Santana, Alves J. L. Study of permeability and hydraulic conductivity of 3D Printed plaster parts by Binder Jetting. 1st International Conference on Advances in Mechanical and Mechatronics Engineering; 8 -9 nov 2018; Ankara, Turkey 2018. p. 119-24.
- Ocaña Garzón Edwin J. L. A. Infiltration for improvement of the mechanical and thermal properties of 3D printed parts with plaster powder material. 2nd Doctoral Congress in Engineering; jun 2017; Porto, Portugal.
- Ocaña G. E., Alves J. L., Neto R. Study of the viability of manufacturing ceramic moulds by additive manufacturing for rapid casting. Ciência & Tecnologia dos Materiais. 2017; 29(1): e275-e80.
- Ocaña G. E., Alves J. L., Neto R. Influence of Infiltration Post-Processing in Binder Jetting Technology In: Advanced Structured Materials. Lucas F.M. da Silva, editor. 65. Porto, Portugal: Springer; 2016. p. 416.

Submitted Publications.

- Ocaña Garzón Edwin., Leonardo Santana, Lino J. Permeability and hydraulic conductivity of 3D printed plaster parts. Engineering Science and Technology, an International Journal, 2019.

Publications to submit

- Ocaña Garzón Edwin., Leonardo Santana, Lino J. Alternative infiltrants for 3D parts printed with plaster powder-based material by Binder Jetting; journal of the brazilian society of mechanical sciences and engineering, 2019.
-

Chapter 1. Introduction

1.1 Problem presentation and thesis motivation

The fast-paced evolution of the industrial sector in basically all its areas, make its manufacturing processes increasingly competitive and flexible, which has forced the incorporation of new technologies that allow its rapid adaptation and evolution. Such is the case of additive manufacturing (AM), also known as three-dimensional printing (3DP) (1).

AM is the process of fabricating objects from a three-dimensional Computer-Aided Design (CAD) data in which materials are laid layer-by-layer (2), to produce the final shape of the part by addition of materials, in contrast to conventional machining methods such as milling, drilling or grinding, which are subtractive in nature. Due to its very nature, AM has an enormous potential manufacture complex geometries (3).

Today, AM technology, more than being a support for existing processes, it is also capable of producing parts that go into final products (direct manufacturing) and completely independent functional parts (1, 4).

Binder Jetting (BJ) technology was one of the first AM developed technologies, known as 3D printing in its origins, and remaining as one of the seven categories of AM processes approved by the ISO/ASTM 52900 standard in 2012 (5). Applications of BJ processes are extremely dependent upon the material being processed. The most common material used for this process is plaster-based powder to build parts.

Low-cost BJ machines commonly use plaster-based powders and water-based binders, in some cases colourful, to print models (6). Due to its a relatively low cost raw material, it has instigated an interest in applications of conceptual models, prototypes for different applications, illustration models for architecture or sculptures.

One of the major limitations of this process and such materials is the low mechanical resistance offered by the green parts printed that necessarily require post-processing (7, 8). One of the most used post-processing methods is infiltration, usually with polymeric materials.

Some of the disadvantages about the infiltration process on plaster-based powder 3DP parts is associated with the lack of deep literature that does not allow its clear understanding, restricting the identification of infiltrating materials that satisfactorily fulfil their task with competitive properties. This comprises a restriction on the amount of infiltrants available, thus increasing costs and dependence on the current solutions offered by this technology´s manufacturers. Additionally, this dependence leads to a set of infiltration guidelines that occupy consumer times and reduce the efficiency and competitiveness of this AM technology when compared to others.

Based on the present scenario, it was verified the opportunity to develop a research that provides a better understanding about the infiltration process of plaster-based 3DP models build by BJ technology, focusing on a proposal of alternative infiltrant materials. Always seeking to improve the mechanical properties with respect to the traditionally proposed, with simple and rapid infiltration processes that are available to all types of users. To achieve this, the need to evaluate the characteristics of the medium to be infiltrated such as porosity and permeability was also verified.

1.2 General aim

To identify the influence factors in the infiltration process by immersion of plaster-based 3DP models, and to propose the use of alternative infiltrants with simple and efficient processes when compared to the suggestions of the Binder Jetting technology provider, aiming to improve the final mechanical properties of the infiltrated 3DP models.

1.3 Specific aims

- Characterize the printing powder by identification of its particle size distribution, chemical composition, and morphology;
- Characterize the 3DP model in green state (prior to infiltration) by an analysis of its chemical composition, morphology, mechanical properties (tensile and bending), permeability, and porosity;
- Analyse the mechanical (tensile and bending), and thermal properties of 3DP parts infiltrated with infiltrants suggested by the supplier of the BJ technology;
- Selection and characterization of alternative infiltrants through mechanical (statics and dynamics) thermal and viscosity tests;
- Evaluate the influence on flexural mechanical properties of printed parts with different thickness when infiltrated with alternative materials of various viscosities;
- Optimize the flexural mechanical properties of the alternative infiltrants, seeking a decrease in the infiltration process time, operating the variables of their curing process.

1.4 General Methodology

In order to fulfil the research goals, the methodological structure presented in Figure 1 was used.

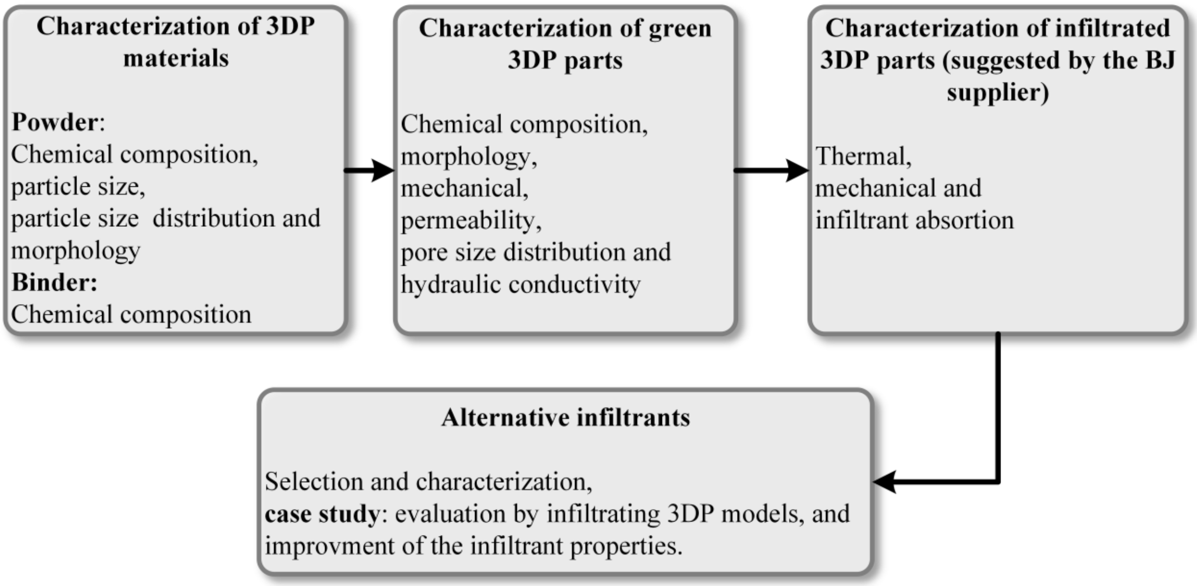

Figure 1. Methodological Structure of the thesis

The study began with the identification of the printing raw materials and its characterization. The chemical composition, particle size distribution (PSD), and morphology of the printing powder were analysed by Energy Dispersive Spectroscopy (EDS), laser diffraction (LD) and Scanning Electron Microscope (SEM), respectively. No individual characterizations of the binder were made, but it was considered the chemical analysis of a green 3DP model and the literary review.

The chemical composition, morphology and mechanical behaviour of 3DP parts in bending and tension in green state were analysed by EDS, SEM and mechanical tests. In all the studies of this thesis, both materials and printing parameters were fixed, in order to allow a better analysis of the processes of infiltration (elimination of noises).

However, the actual influence of the main printing parameters on the permeability of 3DP models as well as the hydraulic conductivity (when it is crossed by a fluid) were subsequently verified and measured experimentally, in a permeameter specifically developed for this purpose. The hydraulic conductivity was measured with viscosity fluids similar to the commonly used infiltrants, thus simulating the infiltration process. These studies were reinforced with the evaluation of the porosity and pore size distribution (PSD) of the 3DP models.

3DP specimens infiltrated with materials and methodologies according to the suggestions of this technology supplier (traditional), were evaluated at thermal and mechanical level (tensile and bending). The best results obtained were the reference base for later comparisons.

The alternative materials selection was based on criteria adjusted to physical and mechanical properties that allow surpassing final properties in 3DP models with infiltration processes and lower costs than the referential ones. These materials were previously characterized, both mechanically and thermally, and later contrasted in a wide range of possibilities. The proposed infiltrants were analysed by being infiltrated in 3DP models of different thickness to verify their real influence on the mechanical properties of bending.

Finally, an improvement of the cure process of the most suitable alternative infiltrant to optimize its flexural mechanical properties with shorter process times was proposed.

1.5 Outline of the thesis

Each chapter is comprised by an introduction and literature review focusing on the respective theme under analysis.

In chapter 2, the plaster-based powder printing material is characterized by its particle size distribution, chemical composition and morphology, and additionally, the chemical composition and morphology of a green 3DP model are evaluated.

In Chapter 3, the influence of the main printing parameters on the permeability and hydraulic conductivity of plaster-based 3DP porous models, with fluids of different viscosity, is experimentally evaluated.

In Chapter 4, the tensile and bending mechanical properties of 3DP parts in green state and infiltrated are analysed. The materials and methods of infiltration were based on the BJ technology manufacturers´ suggestions. Later, the morphology and thermal behaviour of the infiltrated parts are investigated.

Chapter 5 deals with the application of alternative infiltrants on 3DP parts, with improved mechanical properties and processing times. This was divided into three parts:

i. In part I, alternative infiltrating materials to those suggested by the BJ technology manufacturer are discussed and selected, besides mechanically and thermally characterized to compare them with infiltrating potentials, where their costs were also observed.

ii. Part II deals with a case study about the influence on the bending properties of 3DP samples of different thickness infiltrated with alternative materials.
iii. In part III, it is proposed to improve the flexural properties and penetration capacity of the infiltrant by optimizing its cure process and reducing its viscosity.

In Chapter 6, a discussion about the conducted research is summarized, presenting the conclusions of the work and suggesting topics for the continuation of this line of research.

Additionally, in Appendix 1, an initial exploratory study was presented evaluating the viability of printing moulds for aluminium direct casting, with the use of infiltrants commonly used in investment casting.

Chapter 2. Characterization of powder material and three-dimensional printing models in the green state

2.1 Introduction

Binder Jetting (BJ) technology was originally called 3DP, and although the term was never registered (1), it has undergone innumerable development and adaptations to fit different applications. BJ is a process in which a liquid bonding agent is selectively deposited through inkjet print nozzles, in droplets of approximately 80 μm in diameter to join powder materials in a powder bed creating a layer, and provide bonding to the previously printed layer. After printing a layer, the powder bed is lowered and a new layer of powder is spread onto it (usually through a rolling mechanism). These processes (printing binder into bed; recoating bed with new layer of powder) are repeated until the part, or array of parts, is completed (1, 6, 9). A schematic of the BJ process is shown in Figure 2.

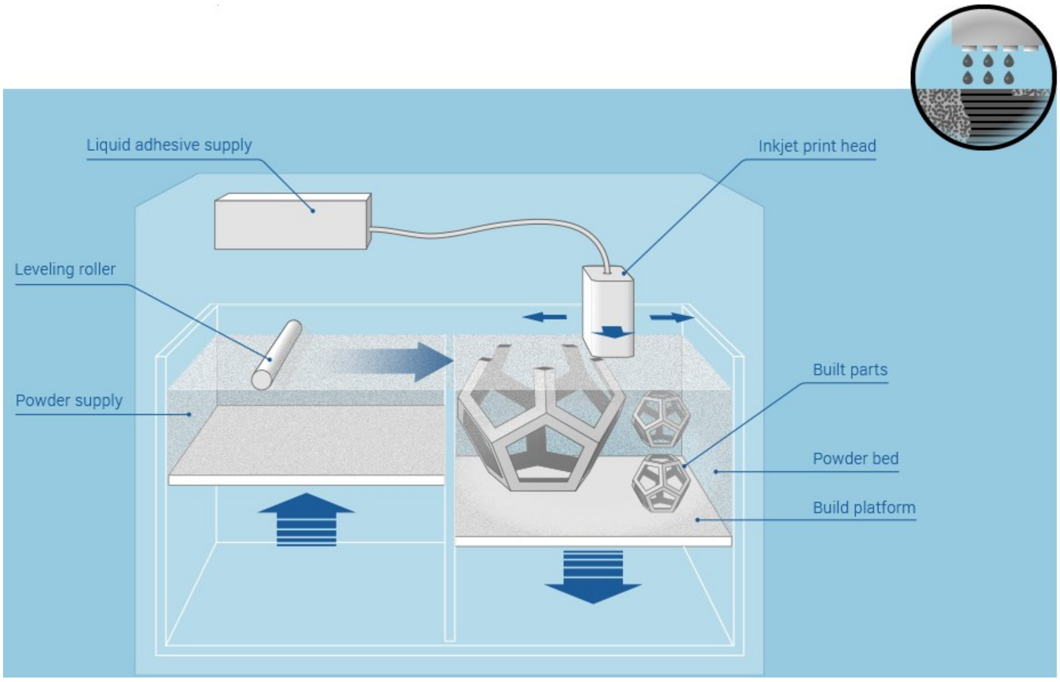

Figure 2. Schematic of Binder Jetting (10)

Colour Jet Printing technology (CJP) use inkjet print heads from commercial printers to print the binder with or without colour. Most CJP equipment build layer thicknesses of around 100 μm. Considering this thickness, one voxel (volumetric pixel) represents a 100 μm cubic volumetric space. This process could be particularly interesting to build structures with controlled porosity, depending on the grain size and post-processing. This process is planning by the software, discretizing it in filling patterns established by the manufacturer in two regions: a perimeter region receives a greater quantity of binder (shell with a greater density and mechanical resistance) while the internal region is bounded with less density, to avoid the saturation of the powder by the fluid (3).

An overview of the main features as well as the capabilities of BJ technology with dry powder-based materials are summarized in Table 1.

Table 1. Overview of the main features and capabilities of BJ technology (3, 7, 11)

Features	
+	Broad material range
+	No support structure needed
+	Cost efficient, unused print material is recycled and high speed printing
+	Printing in full colour quality
-	Small green strength
-	High porosity and poor stability
-	Depowdering difficult due to weak bonding between particles in green state
-	Powder can be trapped inside the body
-	Post-processing are usually required to get dense parts with final properties, increasing the processing time.
Capabilities	
Smallest layer thickness for dry powder method 50 μm, with Lab Platform (ExOne, USA) (6)	
Smallest feature for dry powder method: 350- 500 μm (12)	

The models built by 3DP, especially in ceramic powders, are not strong enough to be used as functional parts such as those made by other prototyping technologies, so they require post-processing (PP) to improve the desired strength or final characteristics. The mechanical strength is a factor in the design of the vast majority of printed pieces and even more in brittle materials such as plaster. For functional components, PP is a critically important aspect of 3DP, but it is often overlooked in literature and by the media.

Complete 3DP process involves 3DP plus PP, to which is a considered a challenge (7, 13). PP encompasses all activities that occur from the time a build is complete (green body) to the moment a 3DP part is ready for its intended use (final part). Green strength refers to the initial strength after printing and before any post-processing. After printing, a typical green body can be composed by 30% – 75% vol. powder, 10% vol. binder, and the rest is void space (14).

Successful realization of a specific 3DP process involves not only the printing process itself, but also powder and binder material system (15) understanding, along with printing process details, such as printing parameters and PP, all of them playing a major role in determining the final mechanical properties of the parts produced.

The lack of understanding in the interplay between the powder properties and the final mechanical properties of 3DP models raised the need for a systematic investigation of printing powder for 3DP (11) and PP.

Good quality of a printed piece with a specific 3DP process involves not only the printing process itself, but also a combination of a powder and binder material system along with process details for printing and PP, both of which playing a major role in determining the mechanical properties of the printed parts (16). Figure 3, summarizes the main parameters of both BJ printing and infiltration, which combined will affect the final characteristics of the functional model.

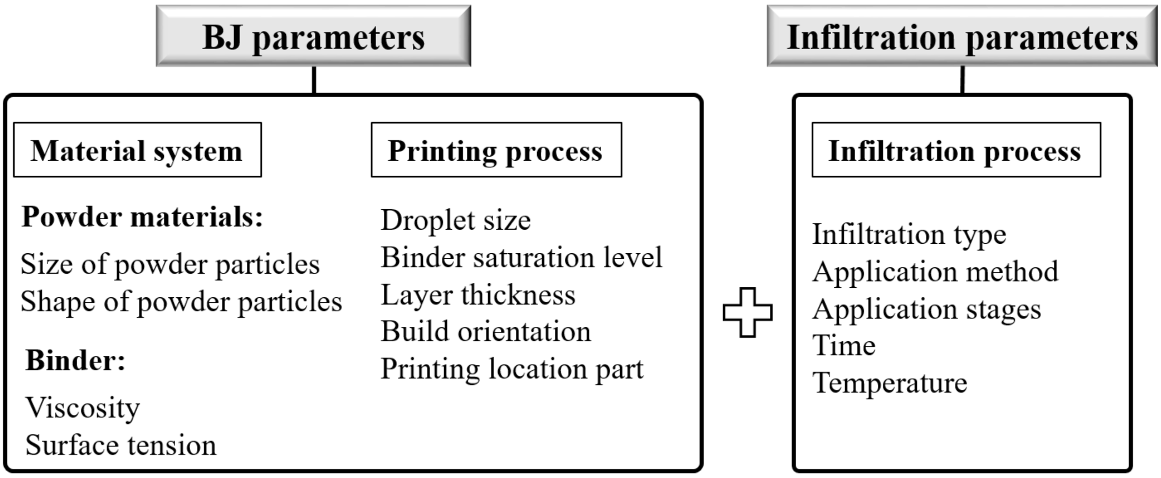

Figure 3. Key parameters on Binder Jetting and infiltration process

2.1.1 Powder and binder materials

The main property of the powder is the depositability, which depends on the size and shape of the particles. For dry state, preferred particles are less than 20 microns, while particles smaller than 5 microns can be deposited both dry and wet (17). Fine powders (~ $1 \mu m$) tend to agglomerate due to the Van der Waal's forces and moisture effect (18).

To exploit the advantages of powders with small and large particles, multimodal powders are used. Larger particles allow the powder mixture to be easily spread in dry state, while the smaller particles fill the interstices among the large particles, to increase the density of the printed part (19).

In both dry and wet deposition methods, the particle shape is less important than the size, but spherical powders are preferred for dry deposition because they tend to have a better flow

(20) and low internal friction (16). Table 2 shows the powder characteristics and the influence on printing.

Table 2. Powder characteristics and the influence on printing (adapted from (15))

Size	**Advantages**	**Disadvantages**
Large particles >20 μm	Can be spread dry, large pores facilitate fluid migration in bed	Largest particle establishes minimum layer thickness
Small particles <5 μm	Increased sinterability, lower surface roughness, thinner layers, smaller minimum features	Difficult to spread, agglomerate, may require slurry deposition
Shape		
Spherical	Tend to flow well, low internal friction	
Faceted/Anisotropic (20)	Potentially increased packing ratio	Inhibits spreading

One of the most common materials used for 3D printing by BJ is calcium sulphate-based powder. Among various transformations presented by calcium sulphate, it is found two different hydrates and anhydrous form. Its di-hydrate is known as gypsum ($CaSO_4.2H_2O$), and the chemical transformation is promoted by heat and/or pressure above 120 °C, where the gypsum loses three quarters of its water to become plaster of Paris, and the rest at 163 °C to become calcium sulphate (21-23). This process is summarized in dehydration and calcination as shown in Figure 4.

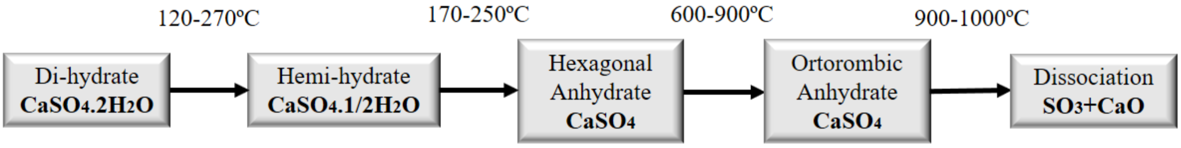

Figure 4. Dehydration and calcination of calcium sulphate (adapted from (23))

Calcium sulphate hemi-hydrate α or hemi-hydrate β are produced depending on the calcination method, if performed in an autoclave or open atmosphere, respectively (23). However, the chemical reaction of curing or hardening is the same for both products and is reversible at atmospheric temperatures and pressures (21, 24).

There are different ways for binding the powder particles. Some of the common selection criteria are (i) binder location (in-liquid vs. in-bed), (ii) binder residue in the final part, and (iii) binder material limitations. It is also important to review the binding methods, some of the most common are: organic liquids, in-bed adhesives, hydration systems, acid/base systems, inorganics, metal salts, solvents, phase-changing materials, and sintering aids/inhibitors (15, 25).

The most relevant parameters of the liquid binder material are: the viscosity and surface tension (15). The spread characteristics are important because a liquid that wicks out considerably from the impact area results in a rougher surface texture. Higher liquid binder viscosity delays the spreadability (20), while a viscosity reduction is achieved by lowering the solids loading or adding dispersants (26).

Within the line of plaster-based materials for 3D printing, commercially available in the market, are those provided by 3D Systems (ex-Z Corporation). They suggest the combination of core powder/binder (called as high performance composites): zp®150/zb®60, zp®151/zb® 60, and zp®150/zb63, depending on the adaptability of the 3D printer (27). Some of these materials have been characterized in previous studies in terms of grain size, chemical composition and thermoanalysis (11, 28-31). Currently 3D Systems has replaced this high performance composites range with the powder/binder combination: VisiJetPXL Core®/VisiJet PXL®.

The VisiJet PXL® clear binder solution is an aqueous commercial clear solution with a viscosity similar to pure water, which is a colourless liquid that is miscible with water and most common organic solvents. The viscosity of the binder was almost similar to water.

2.1.2 Printing Parameters

The parameters inherent to the printing process are: droplet size (32), binder saturation level (33), printing layer thickness, orientation and location of the printed part (see Figure 5), which influence the strength and surface quality of the 3D printing process.

The saturation level is the ratio of ink to bed pore volume and depends on the droplet size, droplet spacing, layer thickness, and bed packing density (25). The saturation level needs to be high enough to allow the ink to penetrates into the previous layer to bind the part in the vertical direction (16), but not so high that excess ink wicks away from the impact zones and roughens the surface finish by binding extra powder (34).

Part orientation relative to the print-head travel path affects printing. Test parts should either be designed to examine this behaviour, or the same test part should be printed at various orientations (15).

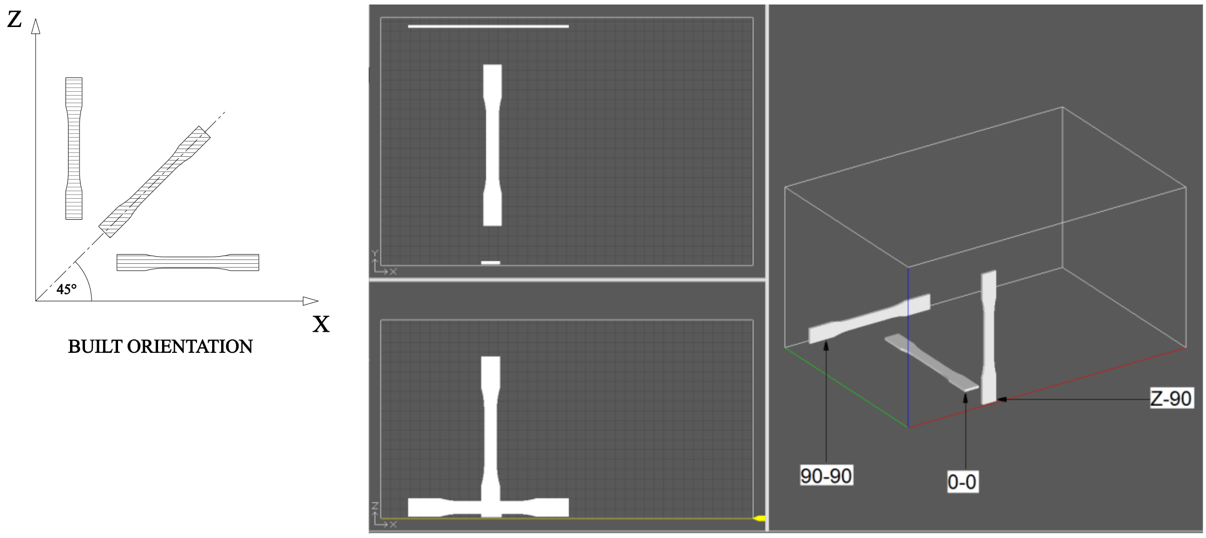

a) b)

Figure 5. a) Built orientation relative to Z axis (adapted from (35)), and b) view of three built orientations in 3D Edit Pro 2.0 software (adapted from (36))

Several studies have been conducted to characterize the plaster-based printing materials as well as to optimize their parameters aiming to achieve best characteristics of the green 3DP models. The main characteristics analysed are: mechanical strength, surface quality and accuracy of green specimens. These studies are summarized in Table 3.

Table 3. Previous studies on the influence of different parameters in BJ green parts in plaster based materials

	Materials				Printing Parameters				Green body Study	Final properties of 3DP sample				
	Powder	Binder	Characterization		Binder Saturation	Layer thickness	Built Orientation	Built Position		Tensile	Bending	Compression	Surface Quality	Fracture
			Chemical Comp.	Particle Size										
Vaezi, et al. (37)	zp 102	zb56			x	x			x	x	x			
Zañartu, et al. (38)	zp 131	zb60	x	x	x	x			x					
Butscher A. (11)	zp 130	zb58	x	x					x			x		
Asadi, et al. (39)	zp150	zb63	x			x	x		x			x	x	
Feng et al. (40)	zp150	zb60						x	x		x	x	x	
Gao-Feng et al. (41)	VisiJet PXLCore	VisiJet PXL							x		x	x		x
Lizardo et al. (42)	zp150	zb61							x	x	x	x		
Farzadi et. al (43)	zp150	zb63	x	x					x			x		

The significant effects of printing parameters such as layer thickness and binder saturation level on flexural and tensile strengths properties, integrity, and dimensional accuracy of the 3DP were studied by Vaezi, et al.(37). Mechanical tests and microscopic examinations were carried out to find that layer thickness and binder saturation level, combined together, have a significant effect on strength, integrity, and dimensional accuracy of green body part.

Zañartu et al. (38), studied the effect of different parameters: layer thickness, jetted binder volume per layer, type of binder and temperature on mechanical properties of green body parts, made with an experimental 3DP equipment based on a spiral growth manufacturing (SGM) device. Two types of binder fluids (zb®60 and demineralized water) and one plaster-based material (zp®131) were used and characterized. They found that the layer thickness has the highest effect on apparent density, hardness and fracture strength on the green 3D printed parts. The binder saturation is significant on fracture strength when considered together with the layer thickness.

Relevant calcium phosphate-based powder properties such as powder particle size, flowability, wettability and compaction rate were analysed and discussed in order to optimize these properties and achieve successful results. These characterizations formed the basis for obtaining geometric and dimensional accuracy in structures for scaffold engineering built by 3D printing (11).

The major printing parameters examined by Asadi et al. (39), were layer thickness, delay time of spreading the next layer, and build orientation of the specimens, to optimize them in the manufacture of a prototype scaffold with calcium sulphate-based material, and commercial 3DP material (zp®150 and zb®63). They identified that layer thickness is the most influential parameter on the quality of scaffolds built by 3D printing. In addition, when coupled build orientation and new layer spreading delay time, they constitute the most important factors influencing the dimensional accuracy, compressive strength, and porosity of the samples.

Feng et al. (40), conducted tests with printed samples using commercial 3DP materials (zp®150 and zb®60). The surface structure of cubic 3DP samples, such as layered microstructure, striped structure and orthotropy was analysed. In addition, compression and bending tests were performed to determine the mechanical behaviour. They verified that the materials are orthotropic, and that both mechanical properties and failure depends on inter-layer and inter-strip (when the print nozzle applies the binder solution at predetermined locations, strip by strip until one layer is constructed), suggesting that the behaviour of 3D printed structures depends strongly on the printing direction.

The dynamic coalescence of cracks and the mechanical behaviour on bending and compression were studied in 3DP cubes with commercial plaster-based powder (Visijet PXLcore®). The behaviour of these 3DP models was compared with natural rocks. The crack paths and their development were captured by a high-speed camera revealing that the wing crack may or may not occur at the tip of the present cracks. No characterizations were made to the 3D printing materials (41).

Pristine and infiltrated 3DP samples built with plaster-based material (ZP^{TM} 150, and their Zb^{TM} 61 binder) were tested in tensile, bending and compression. In this case, the 3DP models in green state were used as a reference to compare its mechanical behaviour when they were subsequently infiltrated. Likewise, no characterizations of the printing materials were made (42).

The effects of layer printing delay parameters on the physical (morphology) and mechanical properties (compressive strength, toughness and tangent modulus) of printed scaffolds were investigated. All mechanical properties of samples printed with a delay of 300 ms. were observed to be higher than other samples built with lower printing delays. This study carried out a brief chemical characterization and distribution of particle size analysis of the printing powder Zp 150® (43).

Most studies about binder jetting technology using plaster-based materials mainly analyse the printing parameters, and the final properties of some pristine structures (basically scaffolds), leaving a gap in characterization of printing materials.

The particle size and chemical composition of printing powder, along with other parameters, play an important role during 3D printing, also impacting the intermediate and final quality (morphology) of the product, while also having a direct influence on the infiltration process. Therefore, an appropriate knowledge of this material is required (44).

For particle size analysis, optical instruments based on the measurement of laser light scattered by the particles such as laser diffraction (LD) have now become a popular and standard laboratory technique. Compared with other particle sizing techniques, LD has the advantage of high speed, good reliability and high reproducibility. It is increasingly being applied for process and quality control of powder processes, both in solid–liquid suspensions and gas–solid systems (45, 46).

To analyse the chemical composition and morphological properties of powder materials an elemental analysis technique Energy Dispersive Spectroscopy (EDS) was used, where samples are stimulated by electrons or high-energy photons, and detect the spectrum of outgoing photons. It is usually combined with scanning electron microscopy, which makes it a versatile tool for acquiring a composition map of the sample (47). The EDS technique, when integrated with dedicated software package for element identification (EID), measures strength of association between particle spectra and reference library spectra (software). Correlation scores range (or certainty) from 0 to 1, where 0 means that there is no correlation and 1 means strong correlation.

The present chapter proposes to characterize the printing powder by size distribution and chemical composition, and analyse the morphology and chemical composition of a green 3D printed model. These results will provide a clear view of the base material and the constitution of the green 3DP model. This could create an important opportunity to improve the infiltration process.

2.2 Materials and 3D Printer

2.2.1 3D Printing materials

All 3D printing components and test samples were built with plaster-based powder, commercially known as VisiJet PXL® Core (48), and water based binder solution VisiJet PXL® (3D Systems, USA) (39, 49). This material system offers numerous capabilities to build high-definition full colour concept models for a variety of commercial applications, assemblies and prototypes.

The main constituent of the printing powder (VisiJet PXL® Core) is 80 - 90% calcium sulphate hemihydrate ($CaSO_4.0.5H_2O$), with a melting point of 1450 ºC and density of 2.6 – 2.7 g.cm^{-3} and a water solubility of 0.83% (20 ºC in gl^{-1}) (48).

The binder used throughout this work is VisiJet PXL® clear. The colourless version was always used, except where indicated otherwise. The VisiJet PXL® binder solution is not classified as a hazardous substance (50), and it has 98% water content, commercially formulated with a 2-pyrrolidone (0-1%). The pH of the binder at 20ºC is 9.8, and its boiling point is 100ºC, with a melting point of 0 ºC. It has a density of 1.0 gcm^{-3}, and it is water soluble, with the viscosity similar to pure water (49).

2.2.2 3D Printer and parameters

All 3DP specimens and models were designed in Solidworks® software and saved in “stl” files when no colour was required while wrml, ply or zrp files were used for colour models. These files were imported to the 3D printer Projet 660 Pro (3D Systems, USA) (51), available at the Laboratory of Development of Products and Services (LDPS) of the Faculty of Engineering of the University of Porto-FEUP (see Figure 6) . This 3D printer is equipped with a 3DPrint™ 1.0 System Software© and an automated power loading recycling and removal.

The 3D printer, with a build chamber of 254x381x203 mm has also a cabin for cleaning printed parts with a compressed air gun and drying system at 70ºC. The printer has a resolution of 600 x 540 dpi, layer thickness of 0.1 mm, and its 1520 inkjets allows a vertical build speed up to 28 mm/hour. These main characteristics of the 3D printer are showed in Figure 6.

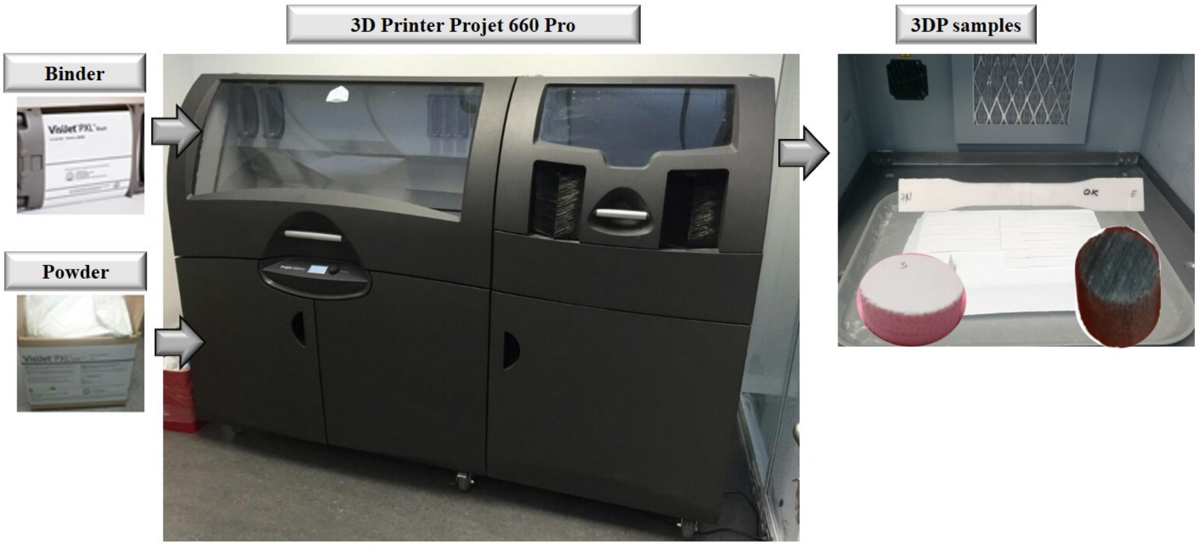

Figure 6. 3D printer and printing materials with some printed specimens in the cleaning chamber

In order to avoid influence (noise) of the 3D printing process in the subsequent post-processing, when required (in the next chapters), the 3D printing process and respective parameters were adjusted and kept constant in this thesis (except where indicated otherwise). The printing process methodology is indicated in Figure 7 and the selected parameters are depicted in Table 4.

As it can be seen in Figure 7, once the design of the 3D model is generated, it is imported to the printer on a corresponding file format, where it can be edited. Printing details are adjusted and the model is positioned with the printer software.

The printer and material levels are checked, the printing parameters selected and the model printed. After printing, the parts are allowed to dry at 55ºC for 2 hours in the same 3D Printer's build chamber.

The loose powder is then cleaned by the automatic vacuum system, removing the coarse loose powder, leaving only the fine loose powder to be manually sucked with nozzles of different diameter. The final cleaning is concluded by removing the remaining loose powder with compressed air gun and brushes of different sizes.

Finally, samples are removed from the cleaning chamber and dried in forced air convection oven SLW53 STD (PolEko, Poland) at 60 °C for 24 hours, and oven cooling. The samples are then stored in airtight containers until their use.

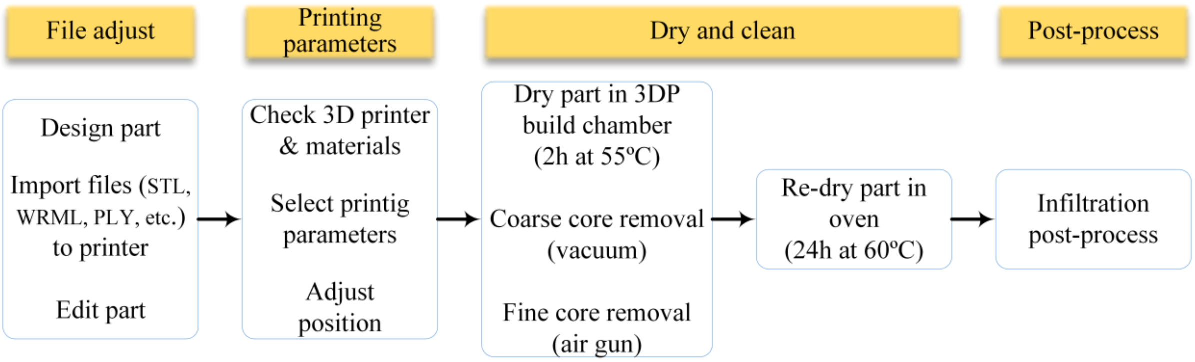

Figure 7. 3D printing process methodology

The printing parameters were selected based on two criteria; first, the flexibility of varying parameters within the printer range, and second, discarding those parameters that produce the best and the worst mechanical strength, opting for the ones that reflect the average mechanical resistance. This usually occurs using the "quick place" command (3D Print ® V1.0 software), (52). The default printing parameters used are shown in Table 4.

Table 4. Default printing parameters selected

3D printing parameters	**Values or condition**
Build position	Right rear corner of the build 3DP chamber
Build orientation (degrees regarding the X axis of the machine)	0
Saturation level at 100% binder/volume ratios (shell and core)	0.24; 0.12
Bleeding correction factors (X; Y; Z)	0.091; 0.071; 0.076
Layer thickness (mm)	0.01
Vertical building speed (mm/h)	28
Post-impression drying of specimens in the printing chamber	2 hours at 55 ºC
Re-dry in oven	24 hours at 60 ºC

To print a batch of 3D specimens, it was preferred to select the build orientation of 0 degrees regarding the X axis, while the build position was the right rear corner of the build 3DP chamber (except where otherwise specified) where the powder is best spread. Unlike other AM processes, these parameters do not turn out to be as influential. While it is true that the position for each sample has varied, this variation has been small, considering that the build position does not have a significant impact on the mechanical strength (53). In a general way, the strength of a non-infiltrated part will be somewhat affected by build orientation, but once a part is infiltrated, it uniformly takes the strength characteristics of the infiltrant product (52).

The binder saturation level is the ratio between the binder volume spread by the printing jets and the volume occupied by the 3D printed model. It is not recommended to activate the bleeding compensation function to build parts with features under 1.27mm, but using instead the default values of the machine (52).

2.3 Characterization of powder and green 3DP model

The methodology established in this chapter consists of: (i) characterization of the printing powder material by particle size distribution (PSD) and chemical composition analysis, and (ii) analysis of the morphology and chemical composition of the green 3D printed model.

2.3.1 Chemical composition and morphological analysis of powder and green 3DP model

The elemental chemical composition and morphological analysis, of both powder and green 3DP parts were carried out on a scanning electron microscope (SEM) (Phenom ProXL, USA), equipped with two detector systems, a fully integrated Energy X Ray Dispersive Spectroscopy (EDS), and Secondary Electron Detector (SED).

Detailed chemical powder composition, obtained from a micro volume via a spot analysis, was performed using an EDS analytical technique. Therefore, dry particles were charged and scattering them into the microscope chamber through a proprietary venting/loading mechanism. The elements were mapped with a beam acceleration voltage of 15 kV, and an acquisition real time of 265 seconds, supported by the dedicated software package Element Identification (EID). Due to the database included in the software, it was not necessary to change the use of external software packages or references to obtain a result of the elemental chemical composition.

The morphological analysis and chemical composition of a green 3DP model was carried out on the larger side (outer surface) of the sample designed and printed as shown in Figure 8. This 3DP model was used in a previous study (see Appendix 1), whose internal CAD dimensions are: AxBxH = 35x25x20 mm, axb = 30x20 mm, and 4.0 mm thick wall (54).

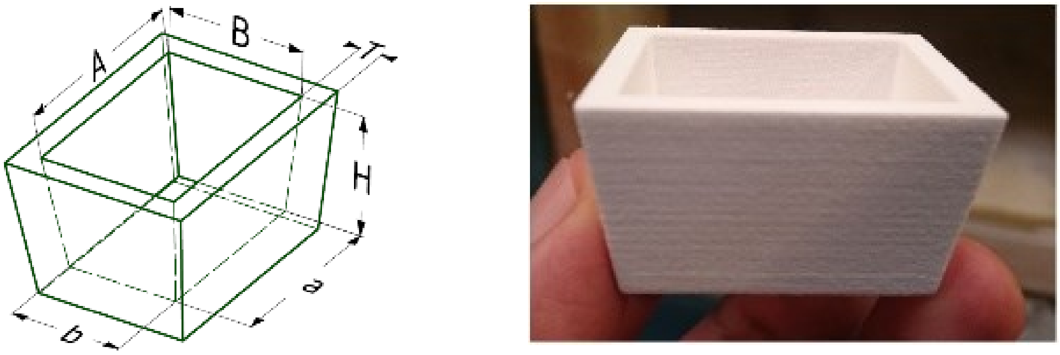

a) b)

Figure 8. 3D model for microscopic analysis a) CAD design, and b) green 3DP model

This specimen was designed as a solid, and saved in stl format, later printed in the 3D printer Projet 660 Pro printer (3D Systems, USA), following the process and the parameters indicated above in 2.2.2.

2.3.2 Powder particle size distribution

The particle size distribution of powder was performed in a Mastersizer 3000 equipment (Marlvern Instruments, UK) which uses the laser diffraction technology (LD), which is one of the most popular techniques to characterize particles due to its speed, easy use, and flexibility. It was performed in a wet and dry condition. For dry analysis, pressures of 0, 1, 2, 3 and 4 bar were used, while for the wet analysis, 2 bar of pressure and ethanol dispersant were used.

In laser diffraction measurements, the angular scattering intensity data was analysed to calculate the size of the particles that created the scattering pattern using the Lorenz-Mie theory (in ProSuite® software) of light scattering. Results of particle size distribution are therefore, reported as equivalent spherical diameters in volume distribution curves. The most common approach for expressing (LD) results is to report the D10, D50 and D90 values, based on a volume distribution. An additional approach to describe distribution width is normalizing the standard deviation by dividing it by its mean. This is approach is known as the Relative Standard Deviation or RSD (55). Table 5 summarizes the parameters used for both, wet and dry tests.

Table 5. Parameters for particle size analysis of powder by Laser Diffraction (wet and dry conditions)

Parameter specifications	
Particle Name	Gypsum (RI 1.525)
Dispersant Name	Ethanol (for wet)
Particle Absorption Index	0.100
Weighted Residual	0.35 %
Particle Refractive Index	1.525
Dispersant Refractive Index	1.360 (for wet)
Laser Obscuration	2.02% for dry and 6.09 % for wet

2.4 Results and Discussion

2.4.1 Powder Characterization

The results of the plaster-powder VisiJet PXL core® particle size distribution (PSD) are depicted in Figure 9, according to dry and wet dispersion conditions. These results are presented as equivalent spherical diameters in a volume distribution. The values corresponding to 10, 50 and 90% (D10, D50, and D90) of the PSD are highlighted in the same Figure 9.

This powder is characterized by a non-symmetric particle size distribution, with an equivalent diameter concentrated on 36.1 μm. The greater relative standard deviation (RSD) was RSD-Dx10 = 17.2, while the smallest was RSD-Dx90 = 3.33. There is a high number of fine particles of up to 7.12 μm in diameter, but their volume is only 10% (Dx10), while 50% reach diameters of up to 36.1 μm (Dx50), and 90% reach a diameter of up to 77.3 μm. This characterization denotes that the powder is a material with a low degree of agglomeration.

The particle size distribution curve of VisiJet PXL core® powder, when contrasted with its predecessor, Zp 150® powder, maintain a similar trend. Its main difference is that the Zp150® powder consists of finer particles in all its representative statistical values. Thus, Zp 150® has Dx10 = 0.64 μm, Dx50 = 27 μm, and even its larger particles Dx90 = 69 μm (43). The Zp131® powder shows an average particle size of approximately 40 μm (38).

These results suggest that VisiJet PXL core® has an average grain size similar to Zp131®, but with respect to Zp 150®, it has improved tendency to packaging; however, the porosity generated in a 3DP model will be similar, so its behaviour in the infiltration post-processes will be identical in these two powders.

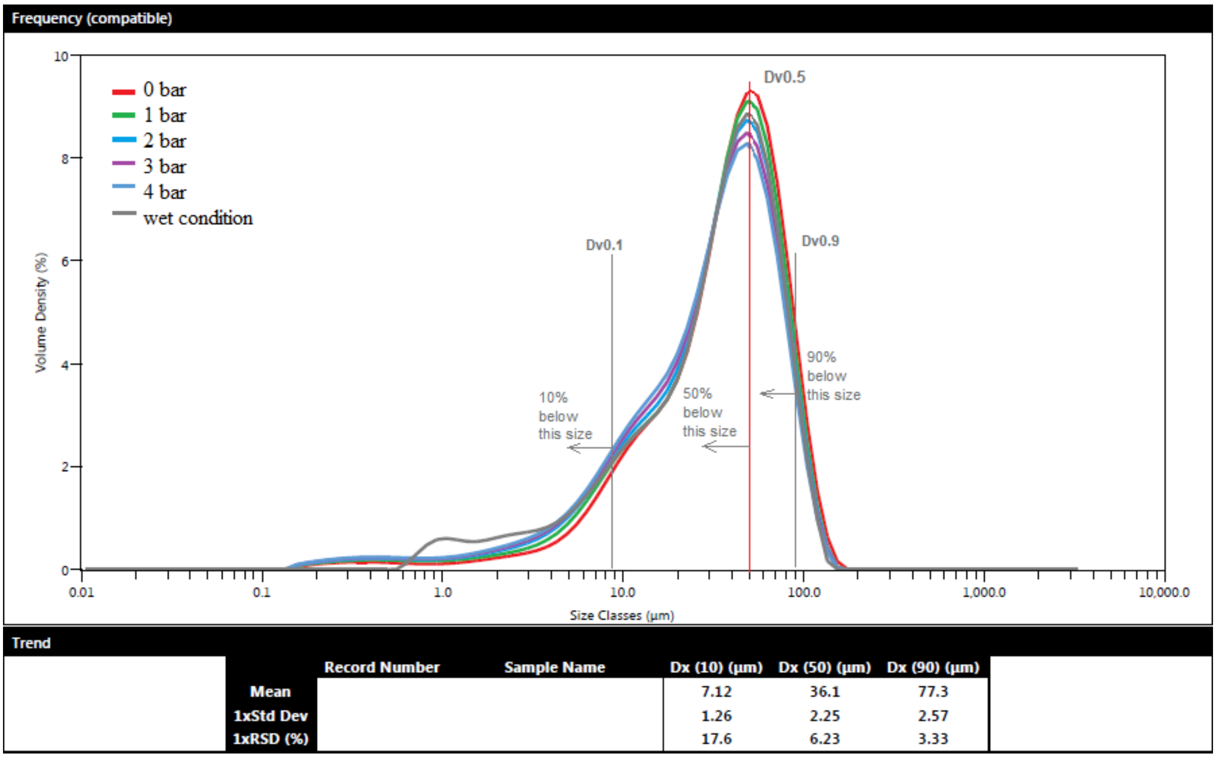

Trend

	Record Number	Sample Name	Dx (10) (μm)	Dx (50) (μm)	Dx (90) (μm)
Mean			7.12	36.1	77.3
1xStd Dev			1.26	2.25	2.57
1xRSD (%)			17.6	6.23	3.33

Figure 9. Overlay particle size distribution of 3D printing VisiJet PXL core® powder, in volume density (%)

The dry dispersed particles were analysed by SEM, showing a noticeable differentiation both in size and appearance (colour contrast), as shown in Figure 10.

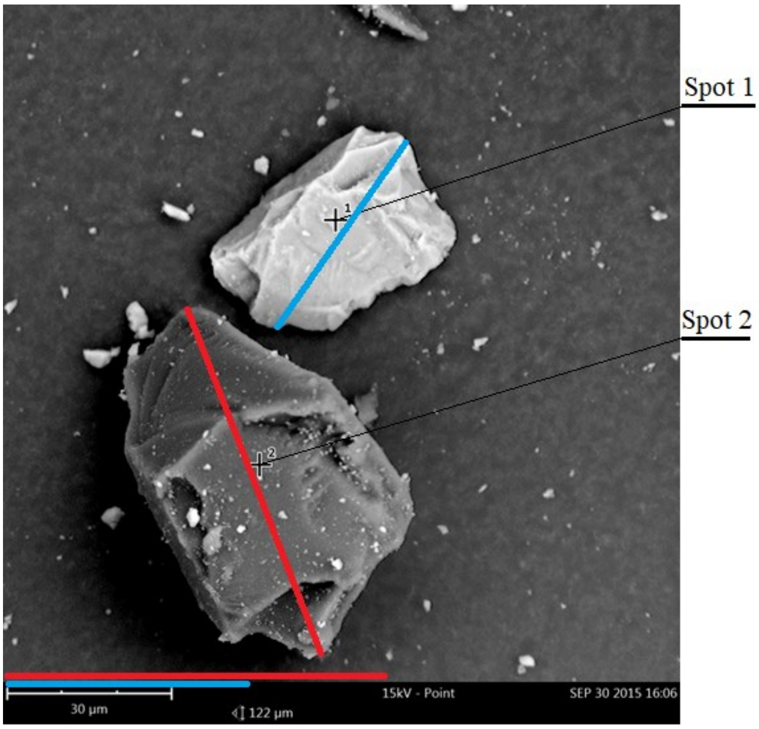

Figure 10. SEM analysis of large representative particles of VisiJet PXL core® powder

After a detailed scan, two of these large particles with different contrast, denoted as spot 1 and spot 2 in Figure 10, were selected and showed approximately a maximum dimension of 45 and 75 μm respectively. These estimations were made with the scale tool integrated into the microscope software.

Regarding the shape of the particles, polygonal rounded geometries can be generally observed in several SEM images, although an analysis dedicated to this purpose was not carried out. In the same way, larges particles with different colour contrast were considered as representative to analyse the chemical powder composition. Figure 11 shows the image of these particles, their chemical spectrum, weight percentage and respective certainty.

Particle 1 has a similar composition to calcium sulphate hemihydrate particles ($CaSO_4.0.5\ H_2O$), (Figure 11, b) (56), known as plaster of Paris or gypsum plaster (57). Particle 2, in turn, contains calcium sulphate, with additives commonly used for plasters (58).

In a general way it can be observed that the VisiJet PXL core® powder has a high concentration of calcium sulphate hemihydrate as its predecessor Zp 150® (30, 43).

Zp131®, an older version with similar characteristics but with less performance in its green strength, currently not commercialized, whose main constituent is $CaSO4.0.67H_2O$ showed a chemical composition (wt %) of carbon 14.4, oxygen 46.0, aluminium 0.1, sulphur 16.2 and calcium 23.3 (38). The presence of a considerable carbon percentage, may also be due to the fact that this element was used as a conductive coating during the SEM test.

This chemical analysis shows that the VisiJet PXL core® material maintains a base composition similar to its predecessors with some modifications for slight improvements, especially regarding its green strength, which has been a weak point of this type of 3D printing process.

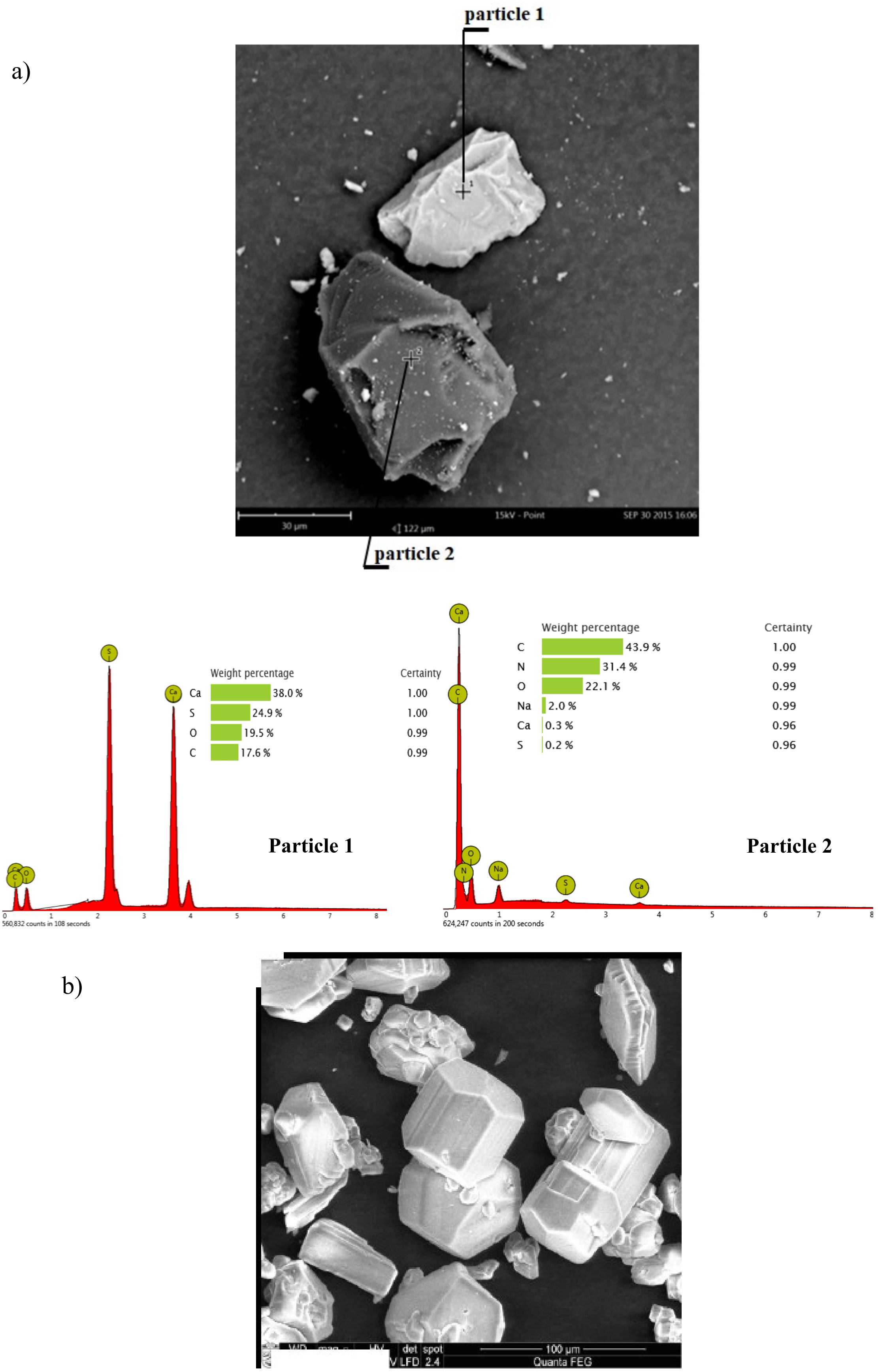

Figure 11. a) Chemical analyses (wt %) of powder particles 1 and 2, and comparison with b) crystals of α-$CaSO_4 \cdot 0.5H_2O$ SEM microphotographs (adapted from (56)

2.4.2 Green body printing part characterization

The elementary mapping carried out on the surface of the green 3DP model, shows the morphology of the powders agglutinated with the binder (Figure 12), where the predominant geometry of the grains with sharp edges was observed. It is also possible to observe that small particles tend to fill the gaps among the larger particles, which makes sense considering that using a multimodal powder makes larger particles spread easily and avoid packaging, while smaller particles fill the gaps among the larger particles, causing an improvement in the surface finish (19).

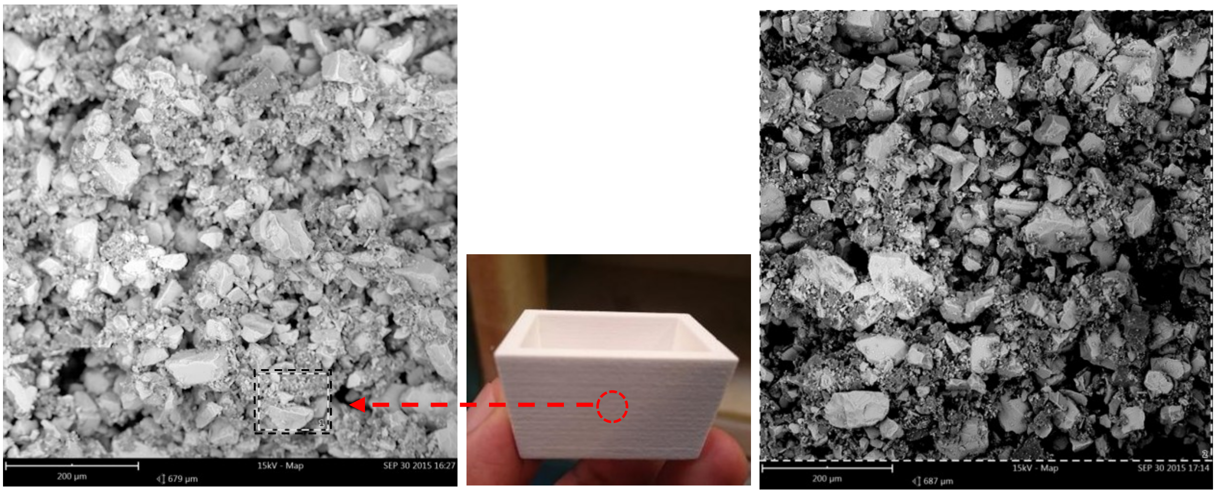

Figure 12. 3D printed green body (centre) and SEM images of mapping 1 (left) and mapping 2 (right)

The distribution of the elemental chemical composition was made in the area framed in a red circle on the surface of the 3DP model (centre of Figure 12). The left side of Figure 12 shows the mapping 1 area, while the right side shows the mapping 2.

The chemical composition on mapping 1 is depicted in Figure 13 a) with its respective spectrum, where a structure with a small concentration of sulphur was observed, characteristic of calcium sulphate, as already mentioned. There is also a high carbon content with 26.6%, which could correspond to plaster additives for 3DP (15, 25, 59). In mapping 2, and their respective spectrum (Figure 13 b)), it is possible to perceive a structure with high concentrations of oxygen and carbon with 47.8% and 33.5%, respectively.

As seen in Figure 13 a), and Table 6, the nitrogen content verified in the 3DP model comes from areas with higher concentration of binder, which is constituted, among other elements, by 2-Pyrrolidone (C_4H_7NO) (50).

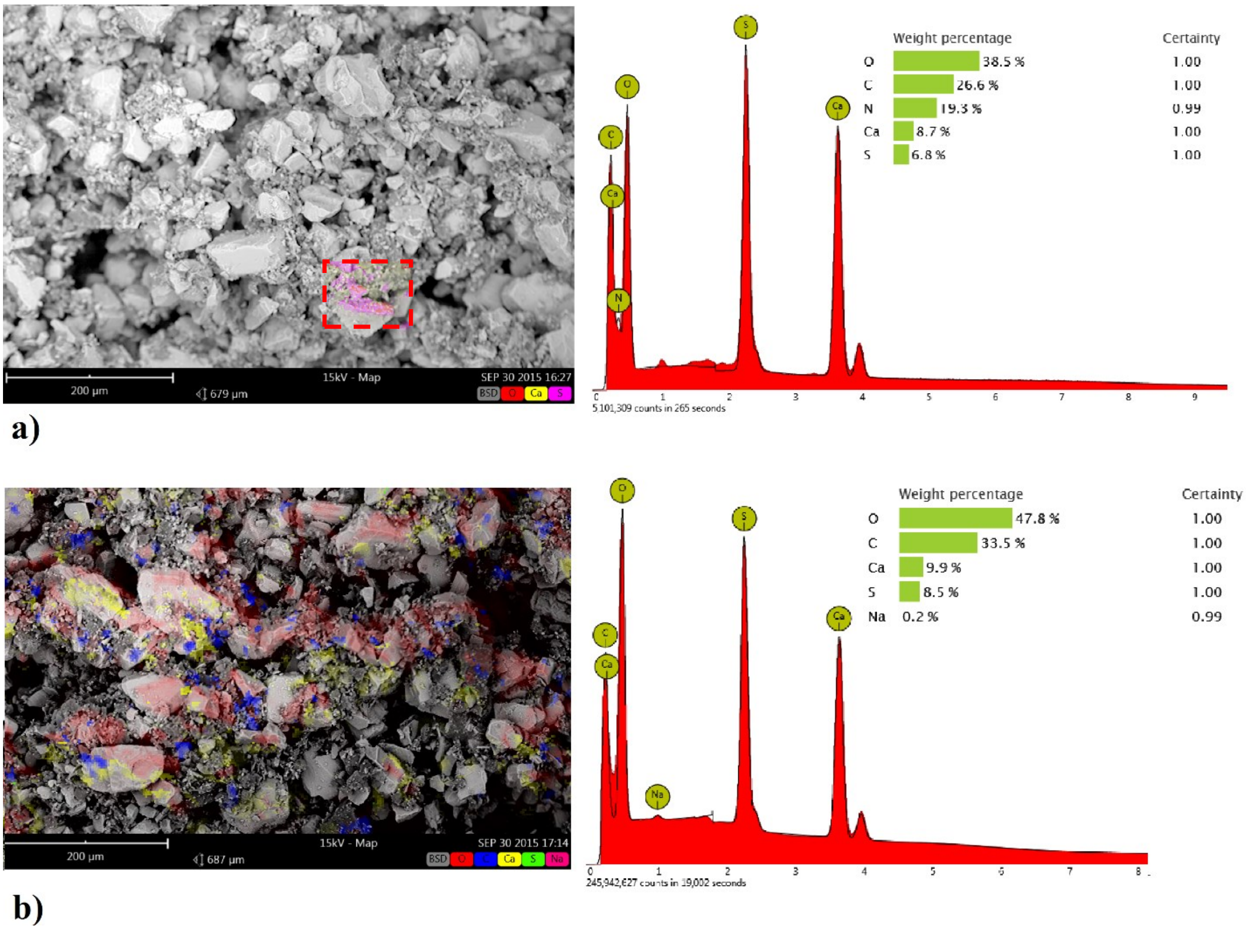

Figure 13. SEM images of elemental chemical analysis of a green body specimen and respective spectrum according to a) mapping 1, b) mapping 2

In Table 6, mappings 1 and 2 of the 3DP model as well as spot 1 and 2 of the powder particles are compared. For mapping 1 and 2, the wt% of the chemical element has been kept in decreasing order, being these: oxygen, carbon, calcium and sulphur (shaded part), except for the nitrogen that appeared with representative quantity only in mapping 1 and spot 2. Sodium only appeared in minimum quantity in mapping 2 and spot 2.

Table 6. Chemical composition (wt%) of the 3DP model and plaster powder particles (all certainties are 0.96-1.00)

Element		**3DP**		**Powder**	
symbol	**name**	**map 1**	**map 2**	**Spot 1**	**Spot 2**
O	Oxygen	38.5	47.8	19.5	22.1
C	Carbon	26.6	33.5	17.6	43.9
Ca	Calcium	8.7	9.9	38	0.3
S	Sulphur	6.8	8.5	24.9	0.2
N	Nitrogen	19.3	-	-	31.4
Na	Sodium	-	0.2	-	2

These slight differences in the chemical analysis of the green model with respect to powder indicates, in an indirect way, the binder composition. Thus, it would confirm that VisiJet PXL clear® binder is basically constituted by water with minimal quantities (0-1wt%) of 2-Pyrrolidone (49). This makes the binder a non-influential material in the subsequent infiltration processes of 3DP models.

2.5 Conclusions

Before selecting infiltrants and infiltration processes to apply to plaster-based 3DP models, it is compulsory to characterize the base material as well as its printing parameters.

Plaster-based powder commercially known as VisiJetPXL core®, used to print 3D models was analysed at its chemical level, particle size, and particle size distribution. Laser diffraction analysis revealed it is a multimodal powder, due to its large particles content of $D_x90=77.3\ \mu m$, and its small particles content $D_x10=7.12\ \mu m$, and even some particles with diameters smaller than 0.5 μm. Therefore, it can take advantage of powders' properties with small and large particles. That is, a finer particle size may improve bulk characteristics, such as porosity or hardenability, but larger particles will tend to flow better, a crucial property during infiltration process.

VisiJetPXL core® grain size was slightly increased to improve packaging problems of its predecessors Zp150® and Zp131®, as well as its green strength performance.

Regarding the chemical composition, VisiJetPXL core® basically reveals to be constituted by hemihydrate calcium sulphate of type α (α-$CaSO_4.0.5H_2O$), while the binder apparently maintains the basic constitution of its predecessors (aqueous).

Because Visijet PXL ® material system has similar characteristics to their predecessors, it can be anticipated that the results obtained in stages of infiltration in future studies, can be contrasted with those printed with predecessor materials.

Chapter 3. Infiltration tests to assess the permeability and hydraulic conductivity of 3D printed plaster parts under different conditions

3.1 Introduction

Extensive studies of permeability have been conducted mainly in the fields of geology, petroleum and bioengineering, leaving only some researches in the field of three-dimensional printing (3DP) (60-62). In this area, binder jetting technology requires post-processes as infiltration, being the permeability (k) and the hydraulic conductivity (K) influencing factors in the penetration of the infiltrant into the 3DP model, thus improving its mechanical strength (63, 64).

Permeability is the most important physical property of a porous medium, which describes its conductivity with respect to fluid flow and depending on the combination of porosity, pores size, orientation, tortuosity and interconnectivity (60). The hydraulic conductivity is a combined property of the medium and the fluid, expressing the ease with which a fluid is transported through a porous matrix (65). The SI unit for permeability is the square meter (m^2), although the darcy units is also widely used. For hydraulic conductivity, the SI units are the meters per second (m/s).

For many permeable media, the constant-head permeameter is a suitable method to determine the saturated hydraulic conductivity (K_s), while, for low permeable media, the falling-head permeameter test is a proposed laboratory method (66).

The mathematical modelling of the flow in porous materials is a complex procedure that requires the support of approximation methods. In recent years, no analytical fluid mechanics method has been proposed to investigate the flow characteristics through porous materials. Hence, to evaluate this phenomena, methodologies have been proposed, generally with a continuum approach. Within the equations with continuum approach, Darcy’s law, the equations of Blake-Kozeny-Carman or Ergun are highlighted. The Darcy’s law in its early form is a linear Newtonian model that links the local pressure variation in the flow direction with the fluid velocity (67). Darcy's law has been applied with many approaches from its early form. Darcy's law is accepted to be representative of laminar flow when the Reynolds number is less than one (67)).

The porosity is another important geometrical property, it is a measure of the fluid storage capacity of a porous material (67, 68). The effective or apparent porosity (ϕ_o) considers the interconnected pores, so it is related to permeability, but not the absolute porosity that considers both connected and not connected pores. Apparent porosity is open pore volume as a percentage of bulk volume, and total porosity is a total pore volume as a percentage of bulk volume (69).

There are many methods to measure the porosity, the selection criteria should extend beyond the expected pore-size range and take into account the suitability of sample preparation and material property (70). Two of the commonly used methods to measure the apparent porosity in calcium sulphate porous materials are the total free water porosity measurements and Mercury Intrusion Porosimetry (MIP) (71). The MIP technique does not give representative values of total porosity, so this method is generally limited to pore accesses from around 375 to 0.003 (μm). Total mercury porosities for 3DP samples will be thus provided only for information (72).

Given the importance of the infiltration phenomena, the present study proposes to experimentally assess the influence of the selected process parameters on the permeability and hydraulic conductivity of plaster-based 3DP models, simulating the infiltration process with infiltrants of different viscosities.

3.2 Materials and methods

To experimentally evaluate the influence on permeability-k and the hydraulic conductivity-K of an infiltrated 3DP model, a L_{16} orthogonal Taguchi experimental design (DoE) was performed where five factors that varied in two levels (low and high) were selected. These factors are: sample thickness (*A*), infiltrant type (*B*), build orientation (*C*), binder saturation (*D*) and colour sample (*E*), as shown in Figure 14 and Table 7.

Table 7. DoE with factors and levels for 3DP permeability test samples.

Levels	**Sample thickness (*A*) (mm)**	**Infiltrant type (*B*)**	**Build orientation (*C*)**	**Binder saturation (*D*)**	**Colour (*E*)**
Low	3.2	Lv	Do	Ds	Cl
High	9	Hv	Vo	Hs	nCl

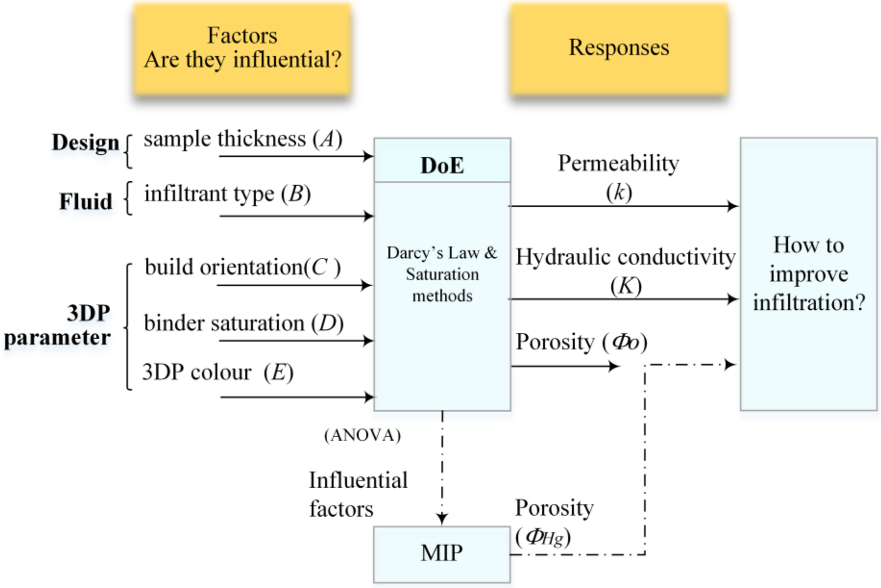

Figure 14. Research methodology to determine the permeability, hydraulic conductivity and porosity of 3DP parts.

The sample thicknesses were 3.2 and 9.0 mm. To simulate a real infiltrant, two mineral oils were selected, with low "*Lv*" and high viscosity "*Hv*". Two build print orientations were selected, the default orientation "*Do*", where the software places the model inside the 3D printer chamber to print in a shorter time, and a vertical orientation "*Vo*", with the model aligned its largest dimension along the Z-axis of the printing chamber (see Figure 16).

The saturation level for the binder/volume ratio of 3D printing was established at two levels: Default saturation "*Ds*" (0.24 for the shell and 0.12 for the core), and high saturation "*Hs*" (0.24 for all volume of the printed solid). These two binder saturation levels can be seen in Figure 15, for example, for a cubic geometry of 10 mm side, the configuration and dimensions of default saturation *"Ds"* (lighter area, powder with less binder) and high saturation *"Hs"* binder (areas with more binder, in the shell and on the struts) can be observed.

Finally, the influence of printing models with colour binder "*Cl*" and colourless "*nCl*" was analysed (using a clear binder).

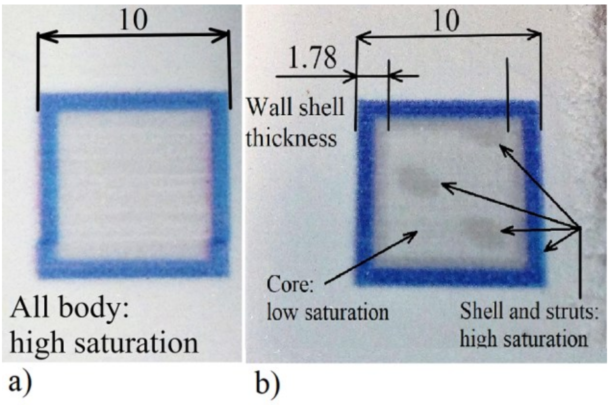

Figure 15.Configuration and dimensions of saturation binder, a) high saturation "*Hs*" and b) default saturation "*Ds*" for a cubic geometric

Two batches of sixteen cylindrical samples of 30 mm diameter were printed with plaster-based powder (VisiJet PXL Core®, 3D Systems) and water based binder solution (VisiJet PXL®, 3D Systems) in a Projet 660 Pro 3D printer, (see Figure 16). A layer thickness of 0.01 mm was set for all samples. After printing, the models were dried in the 3D printer's build chamber for 2 hours at 55ºC, after which the specimens were first depowered. Finally, samples were dried in a forced air convection oven SLW53 STD (PolEko, Poland) at 60 °C for 24 hours. With the same construction procedure, two batches of cylindrical samples of 8 mm diameter and 20 mm high were printed, for the porosimetry test.

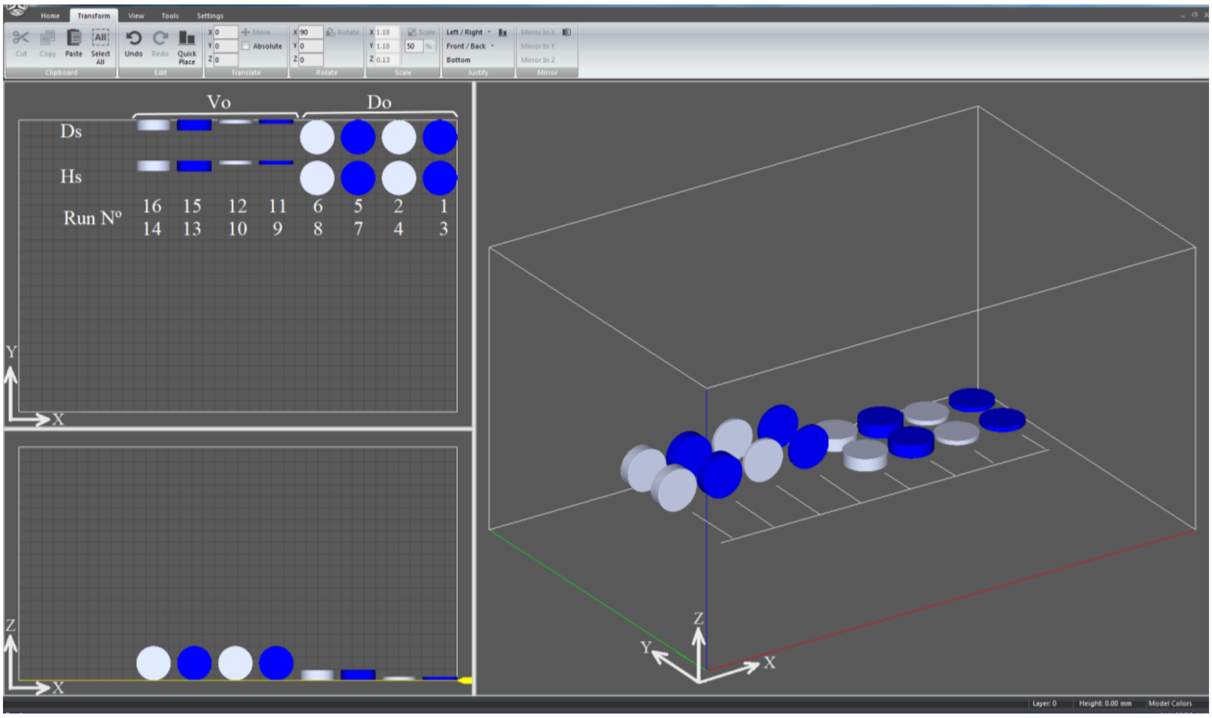

Figure 16. Layout of the 3DP samples in the 3D printer build chamber

3.2.1 Permeameter development and permeability measurement

There is no information on permeability and hydraulic conductivity measurements of 3D printed models with plaster-based materials, so in this study, a custom made device was designed to allow work as a constant head or falling head permeameter, according to the permeability that presents the 3DP models.

Preliminary results determined the convenience of using the device as a falling head permeameter. For this reason, the permeability and hydraulic conductivity were determined using the falling head permeameter presented in Figure 17. Low and high viscosity mineral oils (Motul 7100 4t and Renolit EP2) were used as fluid to simulate the infiltrant fluids. The apparatus is equipped with an external level meter to check the height of the column and two rubber O-rings mounted on upper and bottom grids, sealing the lateral passage of the fluid to allow a unidirectional flow of the fluid trough the porous sample.

Before starting the permeability test, each sample was placed in the permeameter cylinder in the right position (Figure 17). All the couplings that compose the permeameter were spliced, the reservoir was filled with the respective test fluid, all valves were opened and it was verified that there were no leakages.

With all valves open, the fluid passed through the porous medium, allowing the sample to saturate it for around two hours, to expel any air voids that may be present in the sample. Then, the reservoir valve (top) was closed to allow disconnecting the standpipe-reservoir fitting, allowing the fluid contained in the standpipe to pass freely. When the fluid column in the standpipe dropped from 1.72 m (h_0) to 1.62 m (h_1), their time was recorded. For each condition, three time measurements were made at room temperature (~23 ± 2 ºC), and their average was obtained.

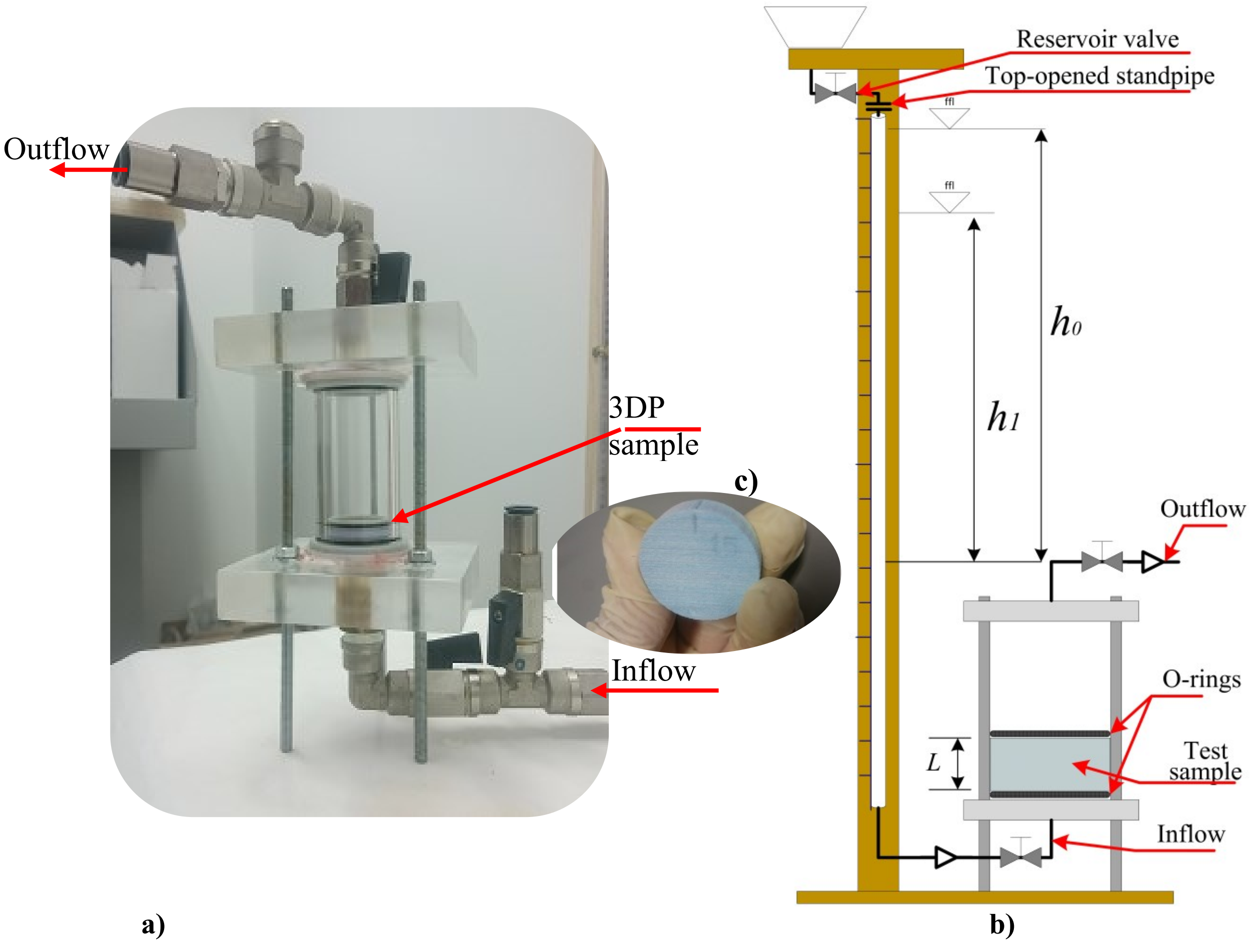

Figure 17. a) Custom-made rigid wall falling head permeameter, b) its scheme and c) 3DP sample

The hydraulic conductivity and permeability constants were established according to ASTM 5856 (73) and based on Darcy's law equation (1) and (2), respectively (74), where, a (m^2) is the cross-section area of the standpipe, L (m) is the length of sample, A (m^2) is the cross-section area of specimen, t (s) is the time for fluid drop from h_0 to h_1 (cm) (initial and final fluid level), μ (Pa·s) is the fluid dynamic viscosity (or absolute), ρ (kg/m^3) is the fluid density and g (m/s^2) is the gravity acceleration:

$$K = \frac{aL}{At} \ln\left(\frac{h_0}{h_1}\right) \tag{1}$$

$$k = K\left(\frac{\mu}{\rho g}\right) \tag{2}$$

The apparent porosity (ϕ_o) of the samples was estimated by liquid saturation and immersion technique, by saturating a sample (75), according to the standard ASTM C20. Samples were weighed in dry state (m_d), using a scale (Mettler Toledo H31AR, d=0.1mg, Switzerland), and then immersed in a 150 ml bath of oil under 4 bar of vacuum for 3 to 5 minutes, to ensure the filling of the voids with the fluid. Then, the samples were weight, and suspended in an immersion liquid (m_{sub}). Samples were then removed and dabbed with paper towels to clean any excess liquid and weighted to determine their saturated weight (m_s). The apparent porosity (ϕ_o) was calculated from Eq. (3) (69, 72, 76):

$$\phi_o = \frac{m_s - m_d}{m_s - m_{sub}} \tag{3}$$

Additionally, porosity (ϕ_{Hg}.) and pore size distribution (PSD) of macropores were estimated for the most representative samples of the permeability test by the mercury intrusion porosimetry method (MIP), in a Micromeritics AutoPore IV 9500 Mercury porosimeter (Micromeritics Instrument, USA), with pressure range of 0.34 to 228 MPa (0.50 to 33000 psi).

3.3 Results and discussions

The tests carried out on the falling head permeameter allowed to measure the hydraulic conductivity (*K*) and the permeability (*k*), while the apparent porosity (ϕ_o) was measured by the saturation method. According to DoE, three repetitions for each combination of factors (same condition) were performed for all tests. The average results of each condition was collected in Table 8.

An analysis of variance (ANOVA) was carried out with a 95% confidence interval to validate the real significance of each factor on the responses *K* and *k*. Figure 18 shows the means and standard errors of hydraulic conductivity and permeability for all analysed factors and levels, organized from right to left, according to their highest contribution. The ones with a statistically significant contribution ($P_{value} < 0.10$) are highlighted in the yellow box. The horizontal line plotted represents the mean of means for all factors.

The significant factors, in decreasing order, for hydraulic conductivity are:

- Infiltrant type (*B*), build orientation (*C*), and their interactions *B*x*C*, all of these with P=0.000, and

The significant factors, in decreasing order for permeability are:

- Build orientation (*C*), P=0.002, binder saturation (*D*), P=0.089, and their interactions *A*x*C*, P=0.007 and *A*x*D*, P=0.094.

Table 8. Experimental results of hydraulic conductivity-*K*, permeability-*k*, and apparent porosity-ϕ_o for L_{16} orthogonal array sample, measured by falling head permeameter and saturation methods.

Combination	**sample thickness (*A*)**	**Infiltrant type (*B*)**	**Build orientation (*C*)**	**Binder saturation (*D*)**	**Colour (*E*)**	***K* (µm/s)**	***k* (µm2)**	***ϕo (%)***
1	3.2	Lv	Do	Ds	C	0.08	1.04	47.68
2	3.2	Lv	Do	Ds	nC	0.08	0.97	35.85
3	3.2	Lv	Vo	Hs	C	0.23	2.93	40.41
4	3.2	Lv	Vo	Hs	nC	0.28	3.61	34.47
5	9	Hv	Do	Ds	C	0.04	1.99	45.09
6	9	Hv	Do	Ds	nC	0.03	1.93	38.08
7	9	Hv	Vo	Hs	C	0.03	1.51	38.71
8	9	Hv	Vo	Hs	nC	0.02	0.99	36.27
9	3.2	Hv	Do	Hs	C	0.03	1.77	40.17
10	3.2	Hv	Do	Hs	nC	0.01	0.56	39.09
11	3.2	Hv	Vo	Ds	C	0.05	2.86	41.79
12	3.2	Hv	Vo	Ds	nC	0.07	4.03	41.22
13	9	Lv	Do	Hs	C	0.10	1.24	40.48
14	9	Lv	Do	Hs	nC	0.12	1.56	34.70
15	9	Lv	Vo	Ds	C	0.22	2.87	43.05
16	9	Lv	Vo	Ds	nC	0.20	2.58	43.92

For hydraulic conductivity, Figure 18 a), the infiltrant type (factor *B*) has a substantial difference between the two levels *Lv* and *Hv,* denoting the greatest contribution of factor B regarding other factors. The infiltrant type, despite not being dependent on the porous medium, is the most important factor for the infiltration process.

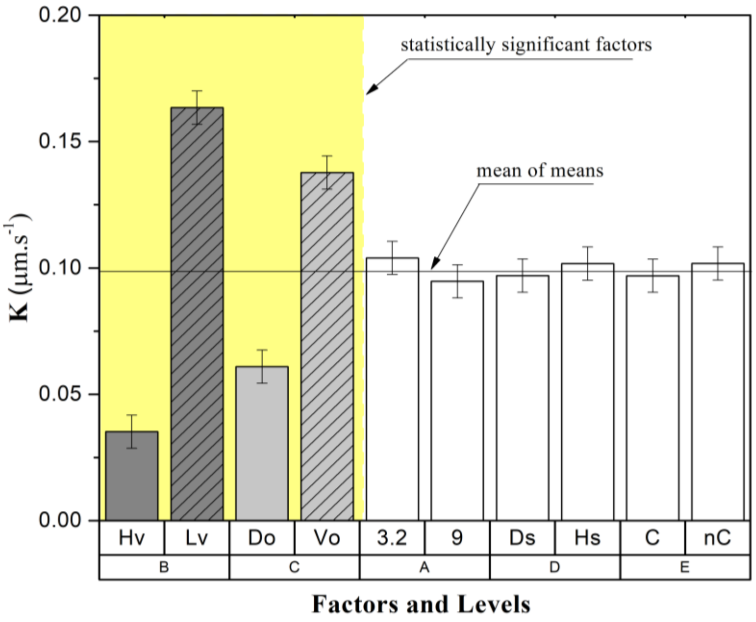

a)

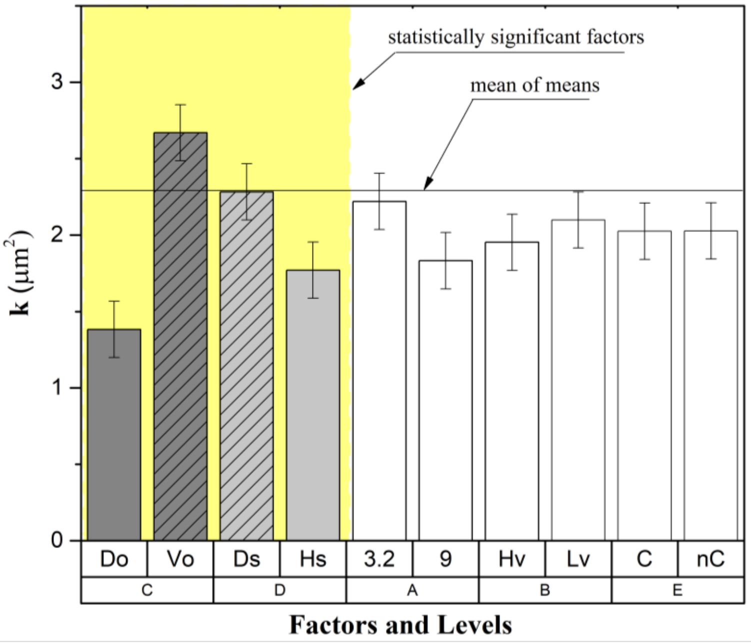

b)

Figure 18. Pareto ANOVA diagram to identify the fitted mean and its standard error of a) hydraulic conductivity (*K*), and b) permeability (*k*) of 3DP samples. The significant factors are highlighted in the yellow square

The build orientation (factor *C*), showed the second and first significance for the *K* and *k* responses, respectively. The vertical orientation (*Vo*) showed higher values for *K* and *k* when compared to default orientation (*Do*). This may basically be due to the parallel layers orientation to the flow, not creating barriers that hinder the passage of the fluid, as happened with the layers perpendicular to the flow, as outlined in Figure 19 a).

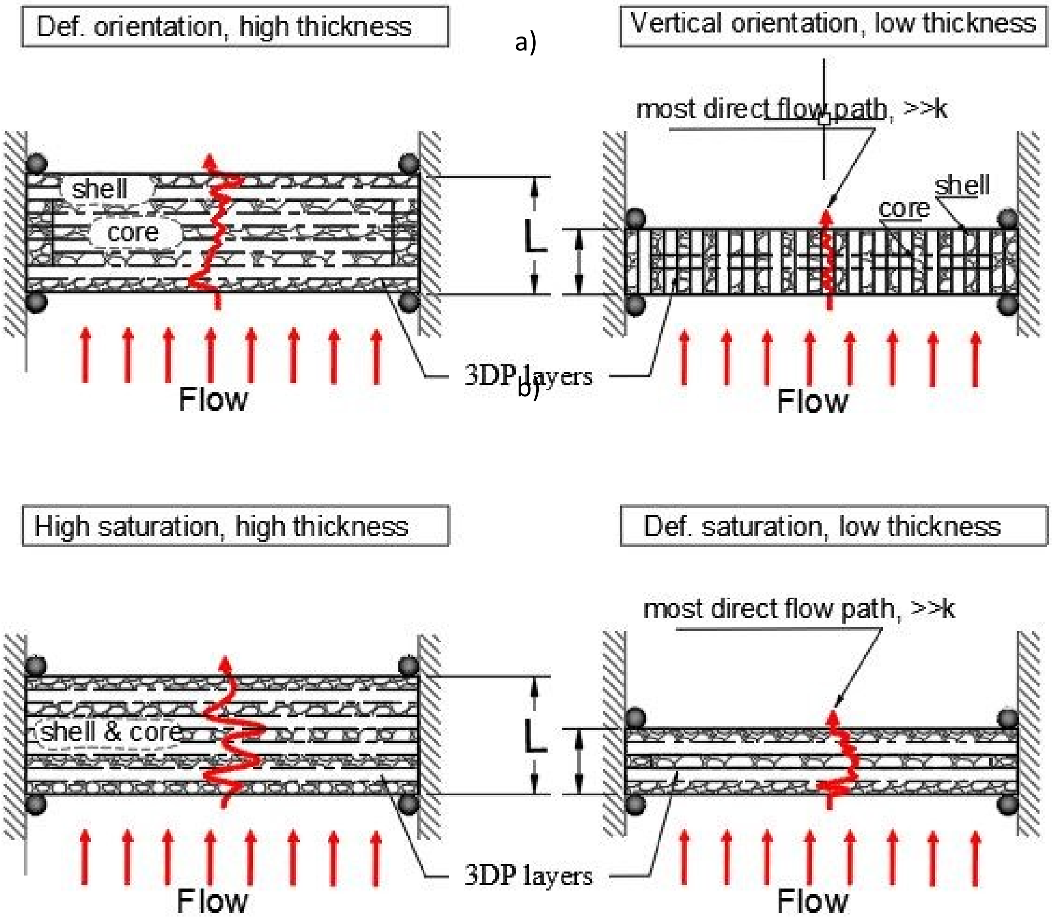

Figure 19. Cross section of the 3DP samples mounted on the porosimeter. The fluid passes through the sample thickness "L" printed with different a) build orientation, and b) binder saturation. The length of the flow path was outlined (in red line) according to the significance found for these factors.

The "binder saturation" factor (D) was only significant for the permeability of the 3DP sample. The default saturation level (*Ds*) showed better permeability compared to high saturation level (*Hs*). This could be because when printing a body in default saturation mode, the infiltrant will flow more easily in the zone with less concentration of binder (core), since here the powder grains keep a light linkage.

3D printed samples with the most significant parameters (runs 1,3, 13 and 15) were tested by the MIP technique, whose permeability (k_{Hg}) and apparent porosity (ϕ_{Hg}) results are shown in Table 9, which are in contrast with the techniques described above.

Table 9. Samples permeability (k_{Hg}) and apparent porosity (ϕ_{Hg}), measured by Mercury Intrusion Porosimetry method, and apparent porosity (ϕ_o)

Run	**Factors**			***k*** (μm²)	***ϕo*** *(%)*	***k** Hg* (μm²)	***ϕHg*** *(%)*
	A	***C***	***D***				
1	3.2	Do	Ds	1.04	47.68	0.40	46.99
3	3.2	Vo	Hs	2.93	40.41	0.31	45.93
13	9	Do	Hs	1.24	40.48	0.18	49.37
15	9	Vo	Ds	2.58	43.05	0.21	45.17

The cumulative volume of intruded/extruded mercury, and the pore size distribution curve (dV/dlog(D)) were obtained from mercury intrusion technique by applying the Washburn equation with assumed contact angles of 130º as depicted in Figure 20. The cumulative volume of intruded/extruded mercury of two consecutive intrusion/extrusion cycles, and the pore size distribution (considered in the first cycle) curves are showed as a function of pore diameter. The cumulative volume of intruded/extruded mercury curve clearly reveals the monomodal nature of the pore size for this 3DP sample, i.e. it consists of macropores between 10 and 30 μm diameter.

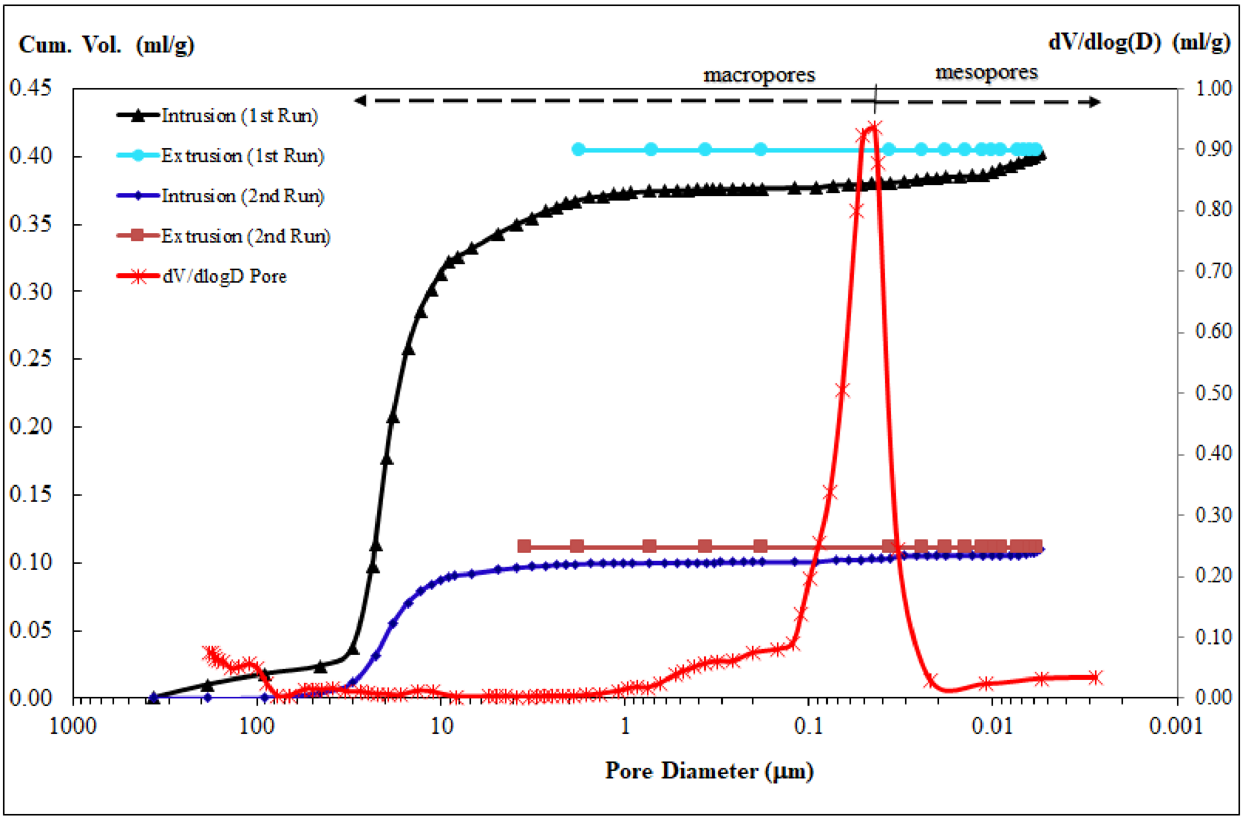

Figure 20. Intrusion/extrusion cycles into a 3DP sample and pore size analysis (dV/dlog(D) in red line) from MIP technique, displayed as a function of pore diameter

Upon depressurization, especially in the first cycle, the extrusion curve does not follow the same path, if compared to intrusion, thus indicating that some mercury is permanently retained in to the pores (Figure 20, horizontal cyan line, extrusion 1st run). Commonly, mercury intrusion/extrusion always occurs along with entrapment. Entrapment is a signal that the mass transfer rate inside and outside of the macropores would not be rapid enough to avoid disintegration of liquid mercury during extrusion (71). The cause of intrusion/extrusion hysteresis and entrapment are not the same, whereas since hysteresis is produced by inherent and structural effects. The entrapment phenomenon seems to be related with kinetic effects at the time of mercury extrusion, in addition to the tortuosity and chemistry surface of the pores.

The cause of entrapment is the deceleration factor of the dynamics associated with the disintegration of the mercury in the voids that makes steam transport a key issue of the extrusion process (77). As a result, specimens with small pores, low porosity and highly tortuous network show great number of entrapment comparatively to samples with large pores and high porosity (71, 77). Therefore, it is considered feasible to correlate the entrapment behaviour with typical transport properties of a 3D printed specimen.

The MIP test showed a pore size distribution with a mean diameter of 11 μm and a mode of 0.018 μm. The minimum pore diameter detected was 0.005 μm, which agrees with the mesopore range detected by this technique (71). More than 90% of the pores detected were macropores (diameter > 0.05 μm), which makes these samples a permeable material.

3.4 Conclusions

The present study evaluated experimentally the influence of the build orientation, binder saturation, printing colour and thickness parameters on the permeability and hydraulic conductivity of plaster-based 3D printing samples by simulating the infiltration process with two infiltrants of similar viscosities to the common resins for post-processing.

The significant factors, in decreasing order, for hydraulic conductivity, were the infiltrant type and build orientation, while for the permeability were the build orientation and binder saturation. Since the infiltrant type is a significant variable in the conductivity of the fluid through the porous medium, it deserves a deeper study of this variable in future infiltration processes.

The entrapment shown as a result of mercury intrusion/extrusion in the 3D model, suggests that these may have small pores, low porosity and high tortuosity, despite being a porous material (more than 90% of the pores are macropores, D > 0.05μm).

A more efficient infiltration process of 3DP models (reaching greater depth or less time) will be achieved with a low viscosity infiltrant, if its predominant flow is perpendicular to a model printed in vertical orientation (highest hydraulic conductivities would be achieved). A thin thickness of the model, although not fundamental by itself, together with these aforementioned factors, can also improve its hydraulic conductivity.

Chapter 4. Mechanical and thermal characterization of 3DP parts in green state and infiltrated with conventional infiltrants

4.1 Introduction

Post-processing (PP) is not only the typical removing of support material, there are considerable additional stages involved in additive manufacturing (AM) technologies. In binder jetting (BJ), the immediately result after printing, is a bound green part embedded in loose powder (15), therefore, the first PP is a minimum post-printing bed manipulation or depowering to handle the print part. Next, some optional PP steps may include sintering, infiltration, coating (25), machining, or polishing; depending on the desired improvement of final characteristics, which can be; surface finish, reduction of stress concentrations, increase of strength, or highlight bright colours. The two most common PP steps are sintering and infiltration (15).

Infiltration is a way to achieve high density parts without the large shrinkage associated with sintering to full density (78). Infiltration occurs when the selected liquid is drawn into the open pores of the printed part through capillary action and solidifies. Both low and high temperature infiltration are possible, depending on the part material and binding mechanism (25). The first occurs at or slightly above room temperature, and the second at temperatures between -6 to 10 °C of the infiltrants melting point (14).

4.2 Materials commonly used as infiltrants

Examples of infiltrates include molten wax, varnish, lacquer, cyanoacrylate, polyurethane, and epoxy resins (79). Two infiltrants commonly used are cyanoacrylates and epoxy resins (80). This variety of materials and PP methods suggests that a deeper analysis at this stage is worthwhile. Moreover, there are no significant contributions in the literature concerning this issue.

4.2.1 Cyanoacrylates

In general, cyanoacrylate is an acrylic resin that has excellent pore penetration capacity, thanks to its low viscosity. Cyanoacrylates polymerize rapidly (cure) at room temperature (81) or in the presence of water without the need of any curing agent and form a strong bond between two adherents. There is a wide variety of cyanoacrylates, among these, α-cyanoacrylates are an important class of adhesives that are widely used by industry and homeowners in various applications. Among all α -cyanoacrylates, the most common ones are alkyl α-cyanoacrylates such as methyl, ethyl, butyl, and isobutyl α–cyanoacrylates (82). Methyl is indicated for metal and ethyl for everything else.

To achieve an improved penetration in plaster-based 3DP models, cyanoacrylate requires a low viscosity and its polymerization time should be sufficient to penetrate into the model, so that the infiltrant dedicated to this purpose is usually diluted, offering a weakened final mechanical resistance. 2-Octyl cyanoacrylate is a cyanoacrylate ester typically used as industrial and domestic adhesives and for wound closure. It is closely related to octyl-cyanoacrylate (83).

Advantages of cyanoacrylates include lack of solvents, rapid curing, and the availability with multiple viscosities. Disadvantages include bond brittleness, limited gap curing, poor peel strength, low durability of bonds with glass, poor solvent and temperature resistance, and rapid bonding to skin (83), and beyond that some types have toxicity problems (84). Several works (42, 53, 80, 81, 85-95) and a previous study of ours (96) have been conducted to analyse different properties provide by the cyanoacrylates when infiltrating plaster-based 3DP models.

4.2.2 Epoxy resins

Epoxy resins are another of the most widely used infiltrants. These materials systems are some of the most important thermosetting polymeric materials commonly used as polymer matrices for composite materials, coatings, adhesives, electronic encapsulants (97) and infiltrants of wood or any materials, in order to increase and seal its porous structure.

Most high strength epoxy resins have relatively high viscosities (greater than 1000 mPa.s) which together with their coloration, time and specific cure conditions may not achieve optimal infiltration of 3DP models. Therefore, it is preferable to characterize them and identify the degree of cure, to finally be optimized (98). Suppliers of equipment and printing materials also provide infiltrants adapted to each core material, so it is necessary to know the compatibility between them as shown in the ZPrinter consumables catalogue (27).

Important thermal factors in epoxy systems involve the glass transition temperature and the degree of cure. During the gel time and the vitrification time, there are three characteristic glass transition temperatures (T_g): T_{g0}, ${}_{gel}T_g$ and $T_{g\infty}$. T_{g0} is the temperature below which no significant reaction of the epoxy — hardener mixture occurs (storage temperature). ${}_{gel}T_g$ is the temperature at which gelation and vitrification can simultaneously occur in an ideal system. $T_{g\infty}$ is the glass transition temperature of a fully reacted material at which the conversion degree (α)

reaches its maximum value (theoretically, $\alpha = 1$ for full cure) (99). Gelation is an abrupt and irreversible transformation of the system from a viscous liquid to an elastic gel, while, vitrification includes a physical transformation from a liquid or rubbery state to a glassy state, as a result of a growth in the crosslinking density of the thermosetting polymer (100).

T_{g0} and $_{gel}T_g$ are obtained in Differential Scanning Calorimetry (DSC) experiments, and T_g is taken as the midpoint between the onset and end of the inflectional tangents on the heat flow curve (101) in the second heating run (102). T_g of the cured epoxy is increased accompanying the curing process. When it exceeds the curing temperature T_c, the mobility of the reactants is hindered, and the reaction rate is decreased (102)

Polymeric materials such as cyanoacrylate or epoxy resins have a significant variation in their performance at different temperatures, so, it is worthy to understand such behaviour. Two of the most used techniques for thermal characterization of polymers are the thermogravimetric analysis (TGA) and the differential scanning calorimetry (DSC).

TGA is a widely used technique to evaluate the mass variation of a sample (including degradation), as a function of temperature or in an isothermal or non-isothermal regime. DSC is one of the most widespread analytical method to measures the temperatures and heat flows associated with transitions in materials as a function of temperature or time in a controlled atmosphere. Therefore, it is used to characterize the degree of cure of thermosetting materials (103).

DSC analysers capture the exothermic heat flow which is released during the cross-linking process of a reactive polymer in respect of curing time under isothermal or non-isothermal conditions (98). The technique allows to measure the variation of the enthalpy of cure, in the case of thermosets. The density of crosslinks is inversely proportional to the area located below the exothermic peak (104), and the heat capacity of a polymer is sensitive to temperature and shows significant change during glass transition, thus allowing the corresponding glass transition temperature (T_g) to be measured (98).

4.2.3 Waxes

Waxes are commonly used as infiltrants in the post-processing stage of plaster-based 3DP parts to give a surface treatment that enhances the colour and gives it a slight shine. Mechanically they do not provide greater resistance to the 3DP model, so they are usually applied as a second infiltrant after a pre-infiltration with other material (usually cyanoacrylate or epoxy resins). Applied directly as an infiltrant it is estimated that a 3DP model could reach a tensile and bending resistance of 9.2 MPa and 11.7 MPa, respectively (1, 51).

Currently there are suppliers of devoted wax materials for 3D printing marketed under the brands of 3D Systems (commercially named Paraplast X-TRA Wax), DWS, Long Yuan, Solidscape, among others (1). However, there are many other brands not dedicated to 3D printing that could be an option. This is the case of the Alba common wax (made in Croatia), that shows a tensile strength of 2.83 MPa when infiltrating plaster-based 3DP models, compared to models infiltrated with genuine Paraplast X-TRA Wax, whose tensile strength is 3.03 MPa (however, much lower than that stipulated by the manufacturer 9.2 MPa) (81).

3DP models built with commercial plaster material (ZP100, 3D Systems) were infiltrated with a common type of wax (Saengtienchai, Thailand). This wax was heated at 60ºC and 3DP specimens were immersed in the molten wax for 10 minutes. These models reached a 9 MPa resistance to bending, whenever the models remained exposed to a dry environment. But, when the models were exposed to 168 hours room storage condition (23 ºC and 55 % relative humidity-RH), their resistance dropped to 5 MPa (86).

Successful realization of a specific 3DP process involves not only the printing process itself, but also the powder and binder material system (15) together with the details (parameters) of printing process and infiltration, which play a major role in determining the final properties of the parts produced (16). Therefore, after understanding the characteristics of a green 3DP model, it is now crucial to know how to infiltrate it.

4.2.4 Parameters of the post-process infiltration

There are several parameters in the infiltration post-process that influence the final properties of the 3DP parts, Figure 21 shows its main parameters. On the left side of the fishbone scheme, the time and temperature for the application and infiltrant's cure are presented, whereas the right side shows the parameters related to the application methods and the type of infiltrant material.

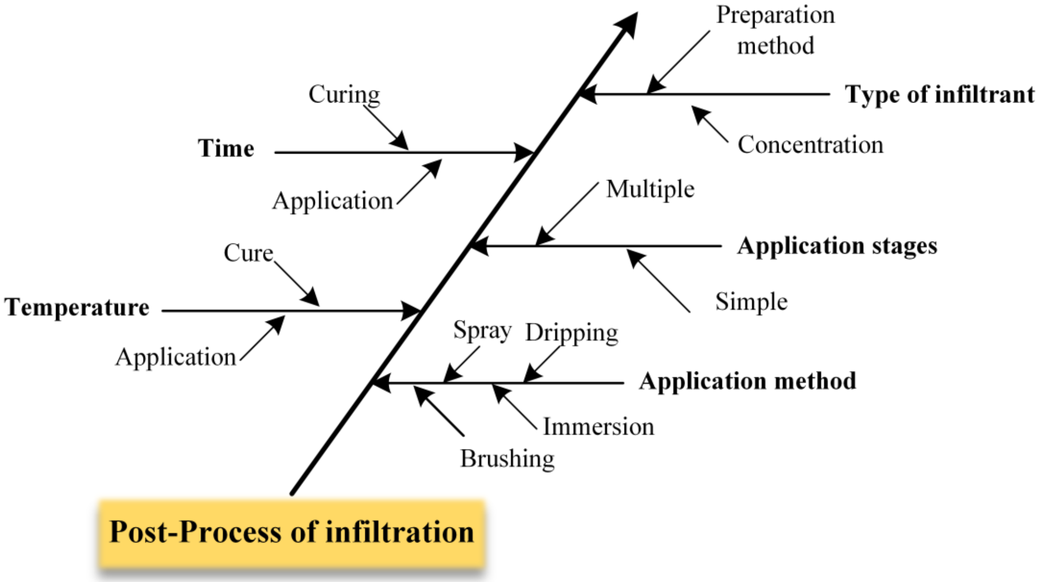

Figure 21. Fishbone diagram with parameters of post-process infiltration (adapted from (94))

Several studies that reviewed the print parameters that interact with the mechanical properties of infiltrated specimens in 3DP plaster materials, are summarized on Table 10. In general, they do not perform the characterization of base materials.

Table 10. Previous studies of influential parameters in infiltrated plaster-based 3DP parts

	Materials		Printing Parameters				Post-process				Final properties of 3DP sample				
							Infiltration								
	Powder	Binder	Binder Saturation	Layer thickness	Build Orientation	Built Position	Type	Time	Method	Absorption	Tensile	Flexion	Compression	Surface Quality	Roughness
Impens, et al. (105, 106)	zp150	zb59			x		x	x		x	x		x		
Galeta, et al. (81)	zp 130	zb56		x	x		x				x				
Gharaie, et al. (35)	zp 150	zb63		x	x		x				x				
Frascati (53)	zp 130	zb58			x	x	x			x	x	x			
Suwanprateeb, et al. (87)	biomat.mix							x	x	x		x			
Pilipović et al. (95)	zp102	zb56					x				x	x		x	x

Impens et al. (105, 106), studied 3D printing parts infiltrated with polyurethane resin, cyanoacrylate, epsom salt and epoxy resin. They previously analysed the time and depth of infiltration by immersion, and reviewed the effects of the type of infiltrant and print part orientation on the compressive, tensile and flexural strength. They found that for most brittle materials, the ultimate compressive strength is much larger than the ultimate tensile strength.

The compressive strength trends are more consistent in behaviour compared to the tensile and flexural results. They also showed that infiltrates can significantly improve the mechanical characteristics, but can also occur a performance degradation with Epsom salts infiltrants.

Galeta et al. (81), compared the application of infiltrants suggested by the provider of 3DP materials (genuine) with other affordable alternative infiltrants used instead of the genuine ones. The results of the tensile test revealed that the strength of 3D printed samples comes mainly from the infiltrants, but it may be further increased by selecting the best combination of the layer thickness and the build orientation. The strength of the samples infiltrated with alternative infiltrants was equivalent to that obtained with genuine infiltrants, thus confirming that the use of alternative infiltrants could be an adequate option. They also observed that thinner build layers produced stronger parts.

Gharaie et al. (35), investigated how tensile properties of parts fabricated by 3D printing are affected by build orientation, and by post-processing methods of infiltration and drying of parts. Results obtained for various parameters were compared to investigate the optimum procedure to achieve the highest tensile strength.

Although there are some studies carried out on the mechanical characterization of infiltrated 3DP models with the materials indicated in Table 10, both the printing materials and the infiltrants in question are the predecessors to those used in this study, so it justifies a thermo-mechanical study of infiltrated 3DP specimens.

The 3D models built from ceramic materials such as calcium sulphate hemihydrate ($CaSO_4.0.5H_2O$), in its green state (without infiltrate), also experience transformations especially dehydration and phase transitions (107). These changes can be observed through thermal analysis, such as differential scanning calorimetry (DSC) and thermogravimetric analysis (TGA). During an increase in temperature, the first transformations have been observed due to H_2O associated with successive dehydration processes occurring for free water content around 80 ºC to 179 ºC. These alterations also produce phase changes, to finally transform over 500 ºC in CaSO.

The structure of this chapter focuses on analysing the mechanical resistance to tensile and bending of green 3D printed samples (without infiltrating), and infiltrated using materials, methods, parameters and equipment suggested by 3D Systems suppliers. The absorption of the infiltrant in the samples will be analysed through their weight as well as their morphology by SEM analyses. In addition, a thermal investigation was carried out to measure the degree of polymerization of the infiltrants.

4.3 Materials and methods

For this study four types of infiltrants were used to infiltrate flexural and tensile 3DP samples, three of these infiltrants are recommended by the supplier of the BJ technology (3D Systems, USA). These are epoxy resin, cyanoacrylate and magnesium sulphate, and the fourth was distilled water, hereafter called as *E1, CY*, *MS* and *W*, respectively. The last group of specimens were not infiltrated, which will constitute the green bodies referential.

The "*E1"* infiltrant (StrengthMax, USA) is an organic low viscosity epoxy resin composed of two parts. Its chemical components are basically 3-aminomethyl-3,5,5trimethylcyclohexylamine and benzyl alcohol (108). This epoxy resin Strength Max (*E1* stands out) and will be used in later studies as a reference.

The "*CY"* infiltrant (ColorBond™, USA) is an ultra-fast-curing organic infiltrant, mainly constituted by Ethyl-2-cyanoacrylate and hydroquinone (109). Like many cyanoacrylates, this polymerizes in contact with water.

The magnesium sulphate "*MS"* heptahydrate at 100%, commercially know as Epsom Salt (Blue Cross Lab, USA), is a colourless component in the form of crystals that needs to be dissolved in water, preferably lukewarm (110).

4.3.1 Sample preparation

Five samples were printed for each type of infiltrant (including non-infiltrated ones) for both tensile and bending tests. Currently there is no specific standard for tensile and bending tests for samples manufactured by additive manufacturing (AM) processes. Additionally, considering that the infiltrated 3D printed components are built of ceramic and polymer, being this last one responsible for the greatest final mechanical resistance of the parts, it has been a common practice to apply for bending test, the ASTM D790-10 standard (111), which is not technically equivalent to ISO 178, and for tensile tests ASTM D638-10 (112) (technically equivalent to ISO 527-1).

All specimens were printed in a Projet 660 Pro 3D printer (3D Systems, USA) with the 3D printing materials and default parameters as indicated in Chapter 2. The build orientation of the samples were 0º, relatively to the machine X axis, as it is shown in Figure 22.

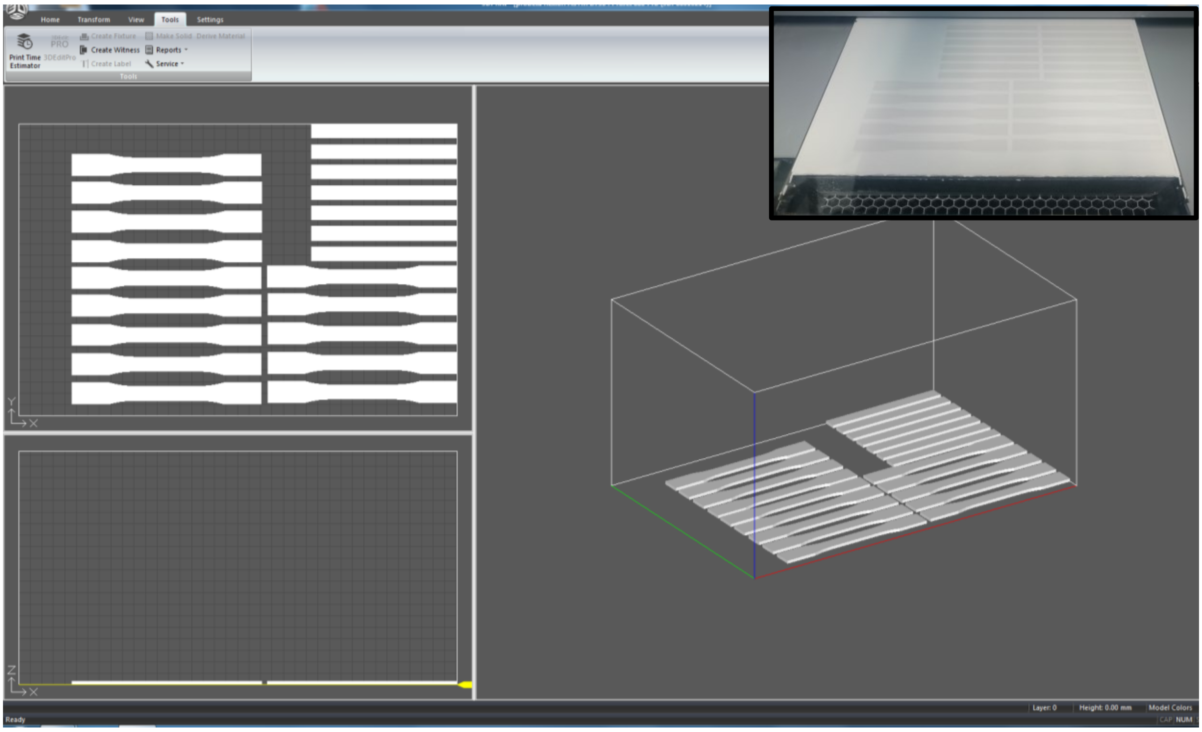

Figure 22. Print orientation and position of the printed test specimens for tensile and flexural tests

After printing, and before infiltration, the drying, cleaning and depowering processes are made in the same 3D Printer's build chamber (see Figure 23), where parts are allowed to dry at 55ºC for 2 hours. Then the loose powder is cleaned by the automatic vacuum system to remove coarse loose powder (Figure 23 a)), leaving only the fine loose powder to be manually sucked with different diameter nozzles (Figure 23 b)). The final cleaning is concluded by removing the remaining loose powder with compressed air gun and brushes of different sizes (Figure 23 c)), leaving them ready for the next stage of drying in an oven.

Finally, samples are removed from the cleaning chamber and dried in forced air convection oven SLW53 STD (PolEko, Poland) at 60 °C for 24 hours, and oven cooling. The samples are then stored in airtight containers until their use.

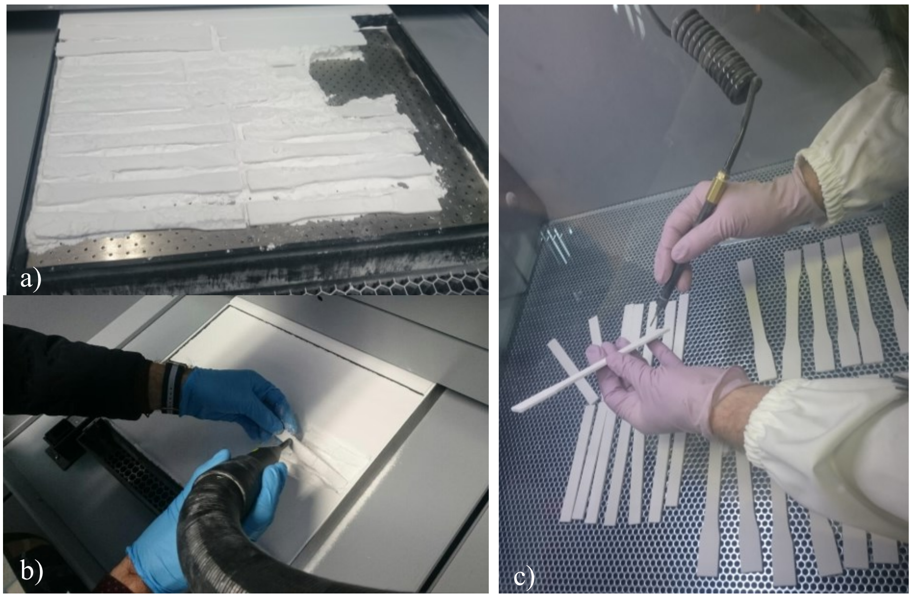

Figure 23. Cleaning stages: depowdering in the 3D printing chamber with vacuum system for a) coarse core removal, b) fine core removal and c) depowdering with compressed air gun

4.3.2 Infiltration process

For each type of infiltrant the manufacturer suggests its own application process, which include mixing ratios, and application time. These methods and parameters are summarized in both Table 11 and Figure 24. Before each infiltration, the respective mixtures were prepared. Epoxy resin (*E1*) mixture was prepared in the ratio of 5 parts in resin and 2 of hardener, and manual mixture for 5 minutes. *MS* mixture was prepared with 200 ml of magnesium sulphate, to which was added 250 ml of hot water at 60 ºC to enable its dissolution, and manually shaken for 5 minutes. In the case of cyanoacrylate and water, no premix is required.

Table 11. Methods and main infiltration parameters

Infiltration parameters	**Cyanoacrylate (*CY*)**	**Magnesium sulphate (*MS*)**	**Distilled water (*W*)**	**Epoxy Resins (*E1*)**
Infiltration method	dripping	spraying	spraying	immersion
Mixing time of the components (min.)	-	1	-	2
Immersion time (min.)	-	-	-	5
Cure, time–temperature (h, ºC)	24 at RT*			
Post cure, time–temperature (h, ºC)	2.5 at 70			

**RT: 23 ± 2ºC*

To infiltrate the samples with *E1*resin, the simple full immersion method was used, submerging the samples for 5 minutes to allow their full saturation (see Figure 25 a)). For *CY*, a dropper bottle was used, because of its almost instantaneous drying. Several thin layers where then applied to permit the absorption of the liquid until its saturation (see Figure 25 b)). To infiltrate with magnesium sulphate (*MS*) and water (*W*), a spray was used to lightly spray the surface of the specimens until a slight superficial reaction of the plaster was observed.

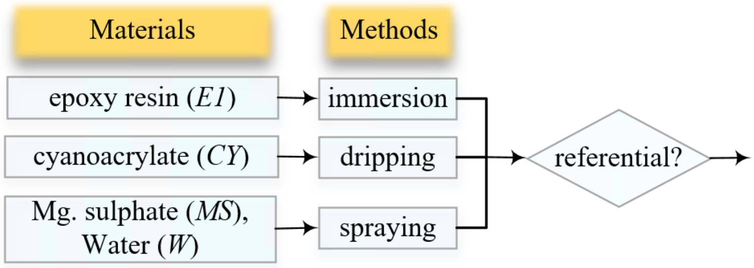

Figure 24. Materials and infiltration methods suggested by technology provider BJ

The cure conditions were the same for all infiltrated 3DP samples. Therefore, subsequent to the infiltration, and prior to the mechanical tests, all the samples were allowed to dry for 24 hours at room temperature. To obtain the final strength, the post-cure condition was adopted according to the suggestions of epoxy resin infiltrant manufacturer, seen Table 11. The details of infiltration and curing procedures are given in the corresponding infiltrants user guides (113, 114). In the case of water, and epsom salt infiltrants, their cure conditions were the same as those of the epoxy resin infiltrant.

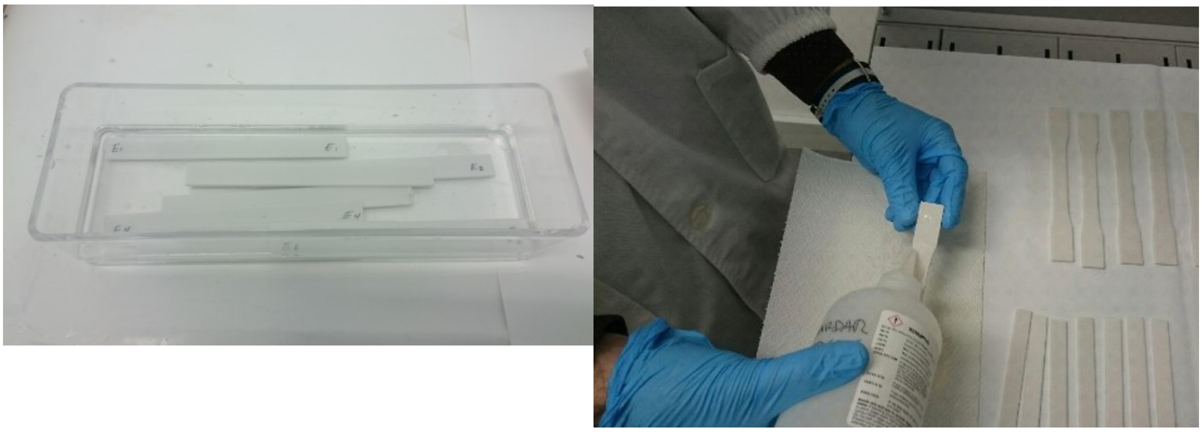

a) **b)**

Figure 25. Samples infiltrated with a) Epoxy resin (*E1*) for bending test, and b) Cyanoacrylate (*CY*) for tensile test

4.3.3 Experimental Techniques

4.3.3.1 Infiltrant absorption

All samples were weighed in a micro-scale JS-100XV (Jennings, Phoenix USA) with 100 g capacity. and accuracy of 0.01 g and measured at room temperature (RT~23 ± 2 ºC, and 50% HR) with a digital calliper with accuracy of 0.01mm (Mitutoyo, Japan), after drying and before infiltration (green state). This method of weighing and measuring was repeated after infiltration curing time. The percentage of absorbed infiltrate was only calculated for flexural samples, due to the simple geometry. Equation (4) was used to determine the percentage of the absorbed infiltrate, and is based on weight change (86):

$$Infiltrant\ absorption, after\ cure\ (\%) = \frac{weight\ after\ curing\ \ (g) - Green\ sample\ weigth\ (g)}{Green\ sample\ weight\ (g)}\ x\ 100 \qquad (4)$$

For each specimen, the dimensional control of its cross section (width and thickness) was made in three different points as suggested by several authors (111, 112), measured in the middle and ends of the samples, to obtain its mean value.

4.3.3.2 Tensile and bending test

Three-point bending test was conducted according to ASTM D790-10 standard in a Universal testing machine (TIRAtest 2705, Germany) with a load cell of 5 kN (Figure 26 a)). The samples were supported by two roods of 5mm radius with a span of 64 mm, and upper load rood press on the middle. The crosshead load speed was 2 mm/s.

Tensile Tests were conducted according to the ASTM D638-10 standard in a Universal test machine (INSTRON 4507, England), using a 200 kN load cell and a 5 mm/min speed, with a 50 mm gage length extensometer as seen in Figure 26 b).

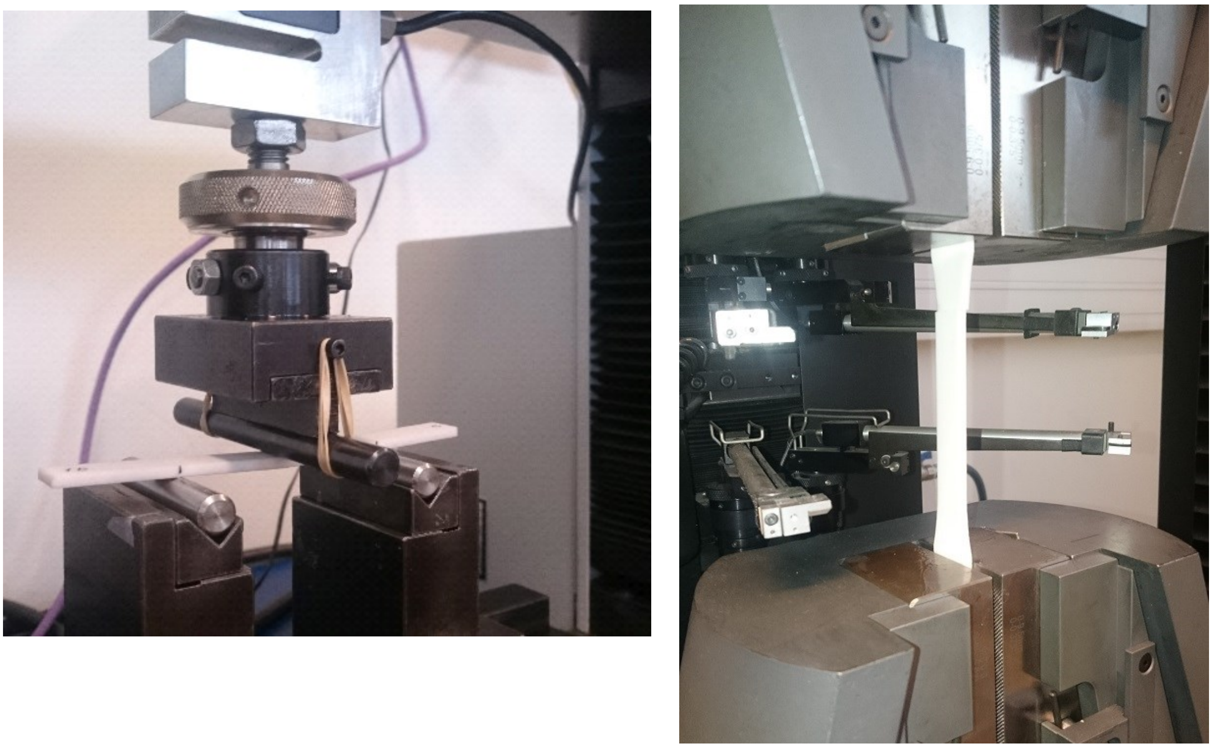

a) **b)**

Figure 26. a) Bending and b) tensile tests of 3DP samples

Both tests were carried out at room temperature (~23 ºC), with at least five specimens (with and without infiltration) to get their mean and standard deviation. The machine software provides the force (*F*) applied at different time intervals (*t*) with their respective strains. To get the stress, in bending test (support span = 64 mm > 51.2 mm), the following equation (5) was applied, as suggested by ASTM D790-10 standard:

$$\sigma_f = \left(\frac{3PL}{2bd^2}\right)\left[1 + 6\left(\frac{D}{L}\right)^2 - 4\left(\frac{d}{L}\right)\left(\frac{D}{L}\right)\right] \tag{5}$$

where:

σ_f is the stress in the outer fibres at midpoint (MPa);

P, load at given point on the load-deflection curve (N);

L, support span (mm);

b, width (mm);

d, depth (mm), and

D, maximum deflection at the centre of the beam (mm).

The flexural strength (σ_f) or maximum flexural stress (σ_{fM}) sustained by the test specimen during a bending test, was calculated according to Eq. (5), when *P* is the load at break point.

For tensile analysis, the maximum tensile strength (MPa) of samples infiltrated with *E1* and *CY* was calculated by dividing the maximum load (*N*), applied by the machine at break point, by the average original cross-sectional area in the gage length segment of the specimen in (mm^2).

4.3.3.3 Thermogravimetric analysis and differential scanning calorimetry

In order to identify the degradation temperature of the infiltrants and thermal stability of the 3D infiltrated samples, a thermogravimetric analysis (TGA) was performed, in a TA-SDT Q600 (TA Instrument, USA) equipment. 3DP samples infiltrated with epoxy resin, cyanoacrylate and water and cured with approximate weights of 10 mg were selected. The tests were conducted with a heat ramp of 20.00 °C.min^{-1} up to 800 °C equilibrated from 30ºC, with purge flow in the sample of 50 ml.min^{-1} with air, to simulate the real cure environment of the samples.

In order to identify the enthalpy of cure, as well as the exothermic peaks and the glass transition temperatures of infiltrants, differential scanning calorimetry analysis (DSC) of infiltrated 3DP samples were carried out from 0 to 250 °C, with a heating rate of 10 °C.min^{-1}, in a DSC Q20 equipment (TA instruments, USA), calibrated with indium and with a nitrogen purge flow of 50 ml.min^{-1}.

4.4 Results and discussions

4.4.1 Tensile and bending test

Due to low mechanical strength for tensile test of samples with some types of infiltrants, only 3DP samples infiltrated with *E1* and *CY* were tested. In the other cases, samples were broken outside the area, invalidating the test.

The results obtained for both experimental tests are presented in Figure 27 and Figure 28, and compared with the suppliers data. It can be seen that they are lower than the ones indicated by the supplier as found in other studies for samples infiltrated with the same materials *E1* and *CY* (115).

For flexural strength, it can be concluded that even for samples infiltrated with *E1* (16.45 ± 1.15 MPa) and *CY* (14.68 ± 1.15 MPa), their standard deviation does not intersect each other Figure 27 a) and its zoom in b), i.e., there is a statistical significance between them and the other infiltrates. In the case of 3DP parts infiltrated with *MS*, the values obtained were too low, 0.66 MPa, suggesting a possible failure in the application method (see Figure 27). In this case the suggested infiltration method is mild spray, with a minimum amount of infiltrant, which is difficult to estimate an exact amount of infiltrant to place on the 3DP model.

Compared to the green body part (not infiltrated), the flexural strength of the samples infiltrated with *E1* increased by 447%, *CY* by 388%, *W* by 150%, and only with *MS* decreased by 78%.

Water as infiltrant allowed a considerable increase in the flexural strength of the samples, but during the infiltration they lost consistency and while drying. They were deformed according to the quantity of absorbed water.

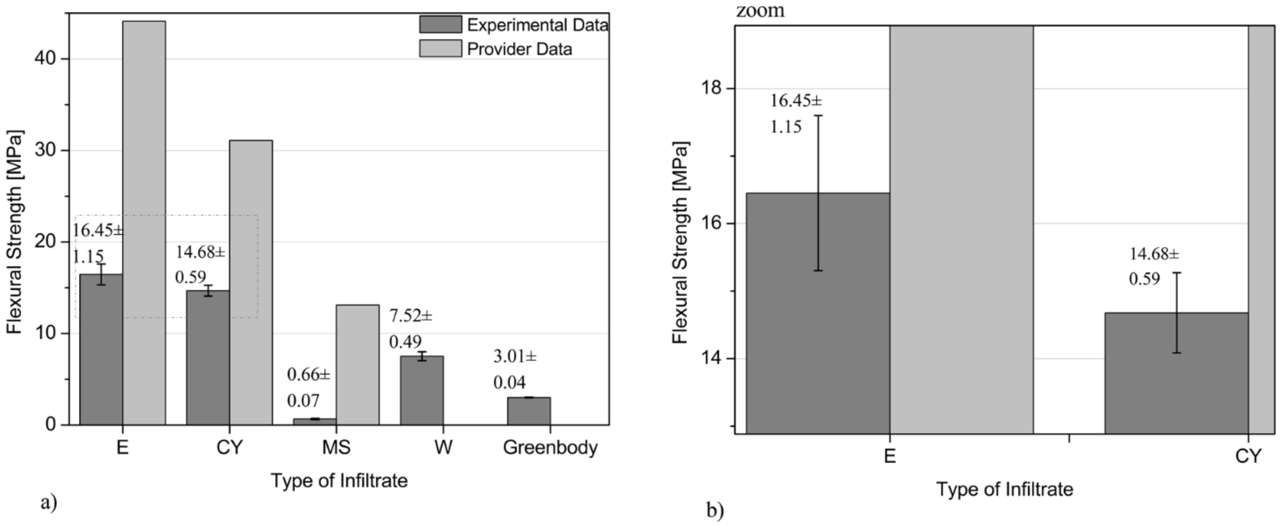

Figure 27. a) Maximum flexural strength of infiltrated and not infiltrated 3DP samples vs. manufacturing data, and b) zoom of part a)

Analysing the tensile strength, as shows Figure 28, samples infiltrated with *E1* showed a slightly lower average strength value of 9.16 ± 2.17 MPa, regarding 9.67 ± 0.45 MPa for *CY*. Such broad standard deviation in *E1*, statistically, means that no relevant influence of these two types of infiltrants on the effect of tensile strength can be observed.

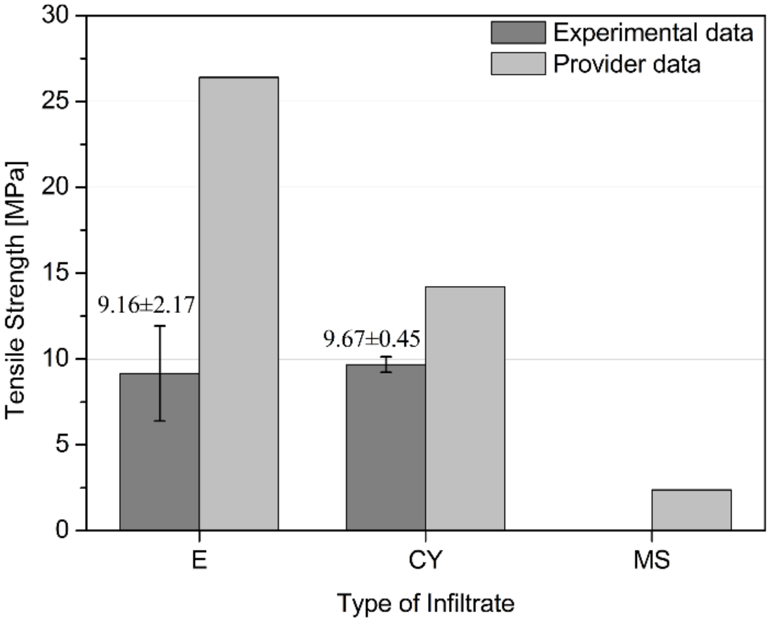

Figure 28. Maximum tensile strength of infiltrated specimens compared with manufacturer data

Tensile tests demonstrated that the 3DP models infiltrated with epoxy resin have practically the same tensile strength as the ones infiltrated with Cyanoacrylate; this is contrary to the results presented by some authors (53, 81, 106), who claimed that with epoxy better strength was achieved, compared to some Cyanoacrylates. On the other hand, in bending analysis, this study agrees with Frascati's results (53), i.e., epoxy resin, enhances the flexural strength.

It is known that the mechanical strength of an infiltrated 3DP model is extremely dependent on the amount of infiltrant absorbed by the model. So, to achieve greater infiltrant absorption, the infiltrant must basically be of low viscosity, whereas the models, in the same printing conditions, will depend on their thickness.

4.4.2 Infiltrant absorption

Equation (4) was applied in order to calculate the infiltration absorption of several samples. Figure 29, shows this absorption tendency, through linear regressions with equations of type $y=a+bx$, where a is the Y axis interception, and b is the slope of the line.

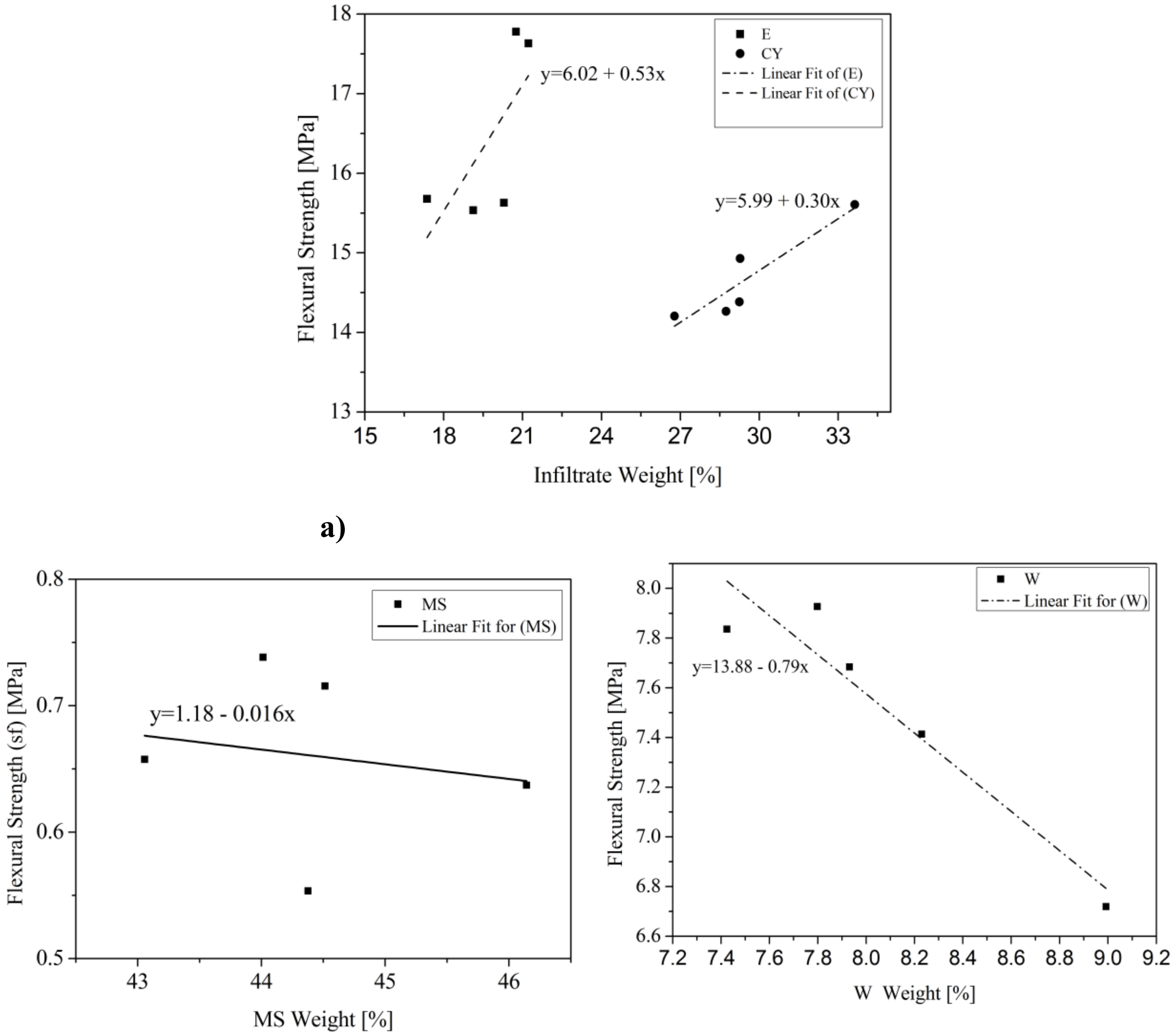

a)

b) **c)**

Figure 29. Weight of dry infiltrant absorbed by specimens (%) vs. Flexural strength: a) (*E1*) and (*CY*), b) (*MS*), and c) for (*W*)

Figure 29 a), indicates a directly proportional relationship between the absorption of infiltrants *E1* and *CY* and their flexural strength, i.e., the greater the absorption of infiltrants, the stronger their resistance becomes. In particular, for *E1*, with slight increases in infiltrant absorption, its increases in resistance is greater, as confirmed by the linear fit equation with a greater slope.

Figure 29 b) and c), show an inverse proportional relationship, i.e., the more infiltrate absorbed with *MS* and *W*, the weaker their flexural strength becomes, especially with *W,* where the equation of the linear fit, shows a greater slope. In other words, an excessive amount of infiltrate *MS* and *W* may reduce flexural strength, suggesting that the use of a better dosage can avoid saturation.

4.4.3 Thermogravimetric analysis and differential scanning calorimetry

Thermogravimetry of 3DP models infiltrated with water, cyanoacrylate and epoxy resin conducted in air atmosphere is shown in Figure 30. The mass loss does not occur regularly, which can be due to two reasons: the test was conducted in a non-inert atmosphere (air), and the samples are made up of materials with different thermal properties (ceramic powder and polymeric infiltrants). This loss begins to be significant from 135, 148 and 175ºC for epoxy resin (*E1*), water and cyanoacrylate respectively. This indicates that the cyanoacrylate initiates its degradation at a slightly higher temperature, even than the epoxy resin.

Three stages of degradation and/or phase changes taking place in the endothermic peaks are denoted, as shown in the Table 12. The constituent base of the samples is plaster, so it is worth observing the existence of two-step release of H_2O (107) from $CaSO_4.2H_2O$ (dihydrate) into $CaSO_4.1/2H_2O$ (hemihydrate) and finally into $CaSO_4$ (anhydrite) (116, 117). These stages are evident in the specimen only infiltrated with water (i.e., powder/binder: VisiJet PXL Core®/VisiJet PXL®) which phases takes place at 175 ºC, 320 ºC and 465 ºC (see Table 12). These values are slightly different from those found in the predecessor material ZP131 powder, whose degradation phases took place at temperatures of 165 °C, 182 °C, 307 °C and 450 °C (31).

Table 12. Endothermic peaks found in thermogravimetric analysis (TGA) of infiltrated 3DP samples

Sample Condition	**Endothermic Peaks (ºC)**		
3DP-CY	215	320	490
3DP-E1	150	320	530
3DP-W	175	320	465

When reaching the final temperature of the test (800 ºC), two percentages of mass were left over, 75% for those infiltrated with water, and about 63% for those infiltrated with cyanoacrylate and epoxy resin. This is basically due to the difference in densities of the specimens, since those infiltrated with polymers leave solid residues even after their degradation.

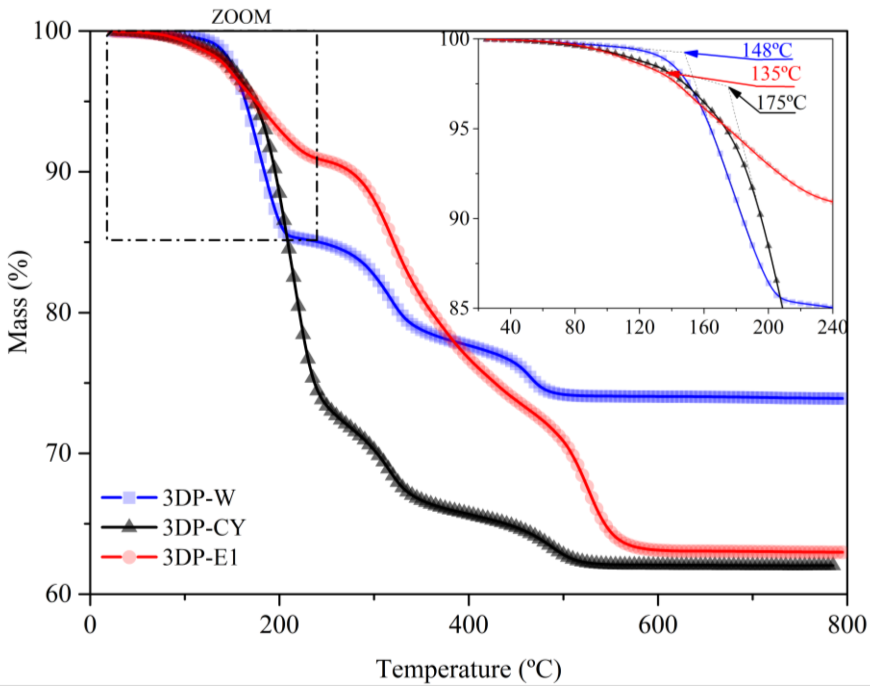

Figure 30. Thermogravimetry of 3DP models infiltrated with water, cyanoacrylate and epoxy resin in air atmosphere

These degradation tendencies agrees with other authors results for the epoxy-amine system resins (99, 118) and for the poly ethyl cyanoacrylate (119, 120). It has been suggested that the stability of the epoxy resins depends on its constituent components and its thermal oxidative degradation process (commonly in two stages) (121). The stability of the cyanoacrylate basically depends on the nature of the initiator, polymerization method, and the length of alkyl side chains (119, 120).

Based on these results, a maximum cure temperature of 135°C could be established for the epoxy resin ($E1$), thus optimizing the curing process.

Preliminary DSC tests were conducted in order to evaluate the degree of cure and thermal reactions within the 3DP samples infiltrated with water (W) cyanoacrylate (CY), and epoxy resin ($E1$). The infiltration and cure processes were carried out according to the supplier's recommendations mentioned above.

The results obtained in the single scann are shown in Figure 31 and Table 13, whose 3DP samples infiltrated with cyanoacrylate and epoxy resin denotes a similar behaviour (so, they maintain the same scale on the Y-axis). Peak temperatures for cyanoacrylate are slightly higher than for epoxy resin, where their higher endothermic peaks were registered at 186 ºC and 178 ºC respectively, suggesting degradation from these temperatures (119-121), with heat flows into the samples (endothermic), as presented in Table 13.

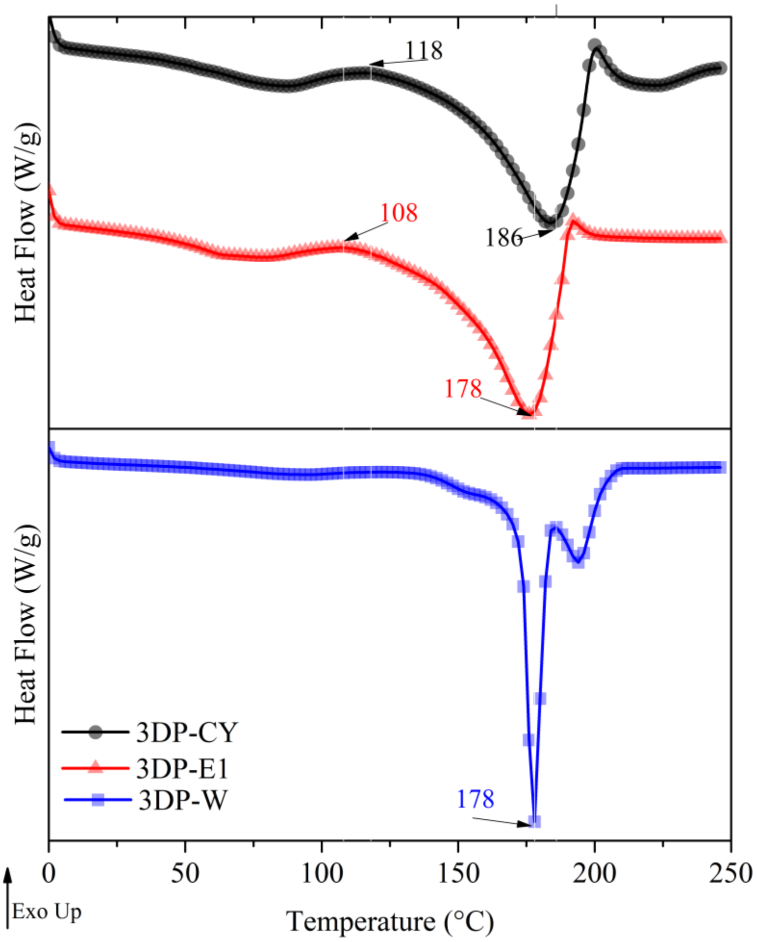

Figure 31. DSC curves of 3DP specimens infiltrated with water (*W*), cyanoacrylate (*CY*), and epoxy resin (*E1*).

The 3DP specimen infiltrated with water (3DP-W) clearly shows two consecutive endothermic peaks at 178 ºC and 195 ºC, suggesting a bimodal evaporation of free water content and/or phase changes The first peak is visibly greater, where heat flows into the sample as a result of endothermic process (For polymeric materials, it sometimes shows the melting stage) and has a representative value of 253.8 J/g. For a type of plaster used in the construccion sector, Mansour et al.(122) showed that the evaporation temperature of the free water content was around 77 °C and 175 °C, being the latter, the greatest peak, agreeing with what was found in this study.

Table 13. Exothermic temperature, and endothermic phases for 3DP samples infiltrated with *W*, *CY* and *E1*

Sample Condition	**Exothermic Peak**	**Endothermic phase**	
	(ºC)	(ºC)	(J/g)
3DP-CY	118.0	184.8	212.9
3DP-E1	108.0	176.9	222.0
3DP-W	-	177.1	253.8

An exothermic peak after an endothermic glass transition, this usually comes from crystallization phenomenon. For the case of the *CY* and *E1* samples, this occurs at 118 ºC and 108 ºC respectively.

4.5 Conclusions

The mechanical and thermal behaviour of 3DP models before and after the infiltration processes is a relevant analysis to understand the influence of infiltrants and their processes. This will allow to have an appropriate criterion in selecting infiltrants that meet the desired final characteristics in a product.

The almost zero standard deviation observed in the bending test of the green samples show an excellent repeatability that the 3DP printer maintains. As such, the printing process would not be a significant noise when analysing the infiltration processes.

Large increases in flexural strength were obtained: 447%, 338% and 150% for epoxy resin, cyanoacrylate and water, respectively, which suggest a strong influence of PP in this technology. Particularly the epoxy resin *E1* shows the best performance, even with less weight of infiltrant absorbed. These results highlight the importance of further researching, about infiltrants types.

The infiltration with water, in spite of improving considerably the bending strength, deforms the samples, denoting that water does not totally react with the base material, changing its composition completely. So, it did not meet the conditions of an infiltrant must meet, that is to fill the interstices between the powder grains bonded with binder during printing (green body porosity), and while not modifying the dimensional accuracy of the test samples in the post-processing stage.

On both experimental bending and tensile tests, the strength obtained when compared to those displayed by the material supplier were significant lower (less than 50%). However, they are consistent with other studies mentioned in this chapter.

Large standard deviations in the mechanical strength of the infiltrated specimens were found. This is a characteristic of manual processes (especially for brushing and dripping). For this reason, we suggest to establish simple infiltration methodologies that provide a homogeneous penetration as a future work.

Small standard deviations in the bending test of green 3DP samples were found. This suggests good repeatability in the printing process as well as handling and cleaning post-processes, allowing the infiltration processes to be more clearly analysed, since the noise produced by the printing factors was practically zero.

Since the results of strength to both bending and tensile are quite low compared to those indicated by the supplier, even for common applications (conceptual models, prototypes, etc.), it is proposed, as future work, to make use of infiltrants dedicated to different applications, as well as to infiltration of 3DP models of different thicknesses.

Thermal studies suggested degradation temperatures of the components of 3DP samples infiltrated with cyanoacrylate (*CY*) and epoxy (*E1*), which will be referential for future curing processes (for *E1*). Phase changes such as water evaporation and/or crystallization were also found.

Chapter 5. Selection of infiltrants for plaster-based 3DP models, case study and infiltrant cure improvement

5.1 Introduction

Additive Manufacturing (AM) revolutionized the way of thinking about manufacturing processes. In the last decade, AM processes were characterized by an exponential growth coupled not only with different manufacturing mechanisms´ capacities of adding successive layers in different materials but also with the expiration of the first patents. Nowadays, there is no doubt that this family of manufacturing processes is capable of producing freeform parts with topological optimization in almost any type of material (7, 13, 123).

The Binder Jetting (BJ) process, referred in the beginning as three dimensional printing (3DP) (13), has the advantage of printing models (sometimes in full colour) for different industrial sectors, which is extremely important in the development of new products and easily materialization of ideas. Regarding the strength of these 3DP models, especially in plaster-based materials, the resulting products may be porous (124), brittle and easily damaged (84). So, a post-processing (PP) is usually demanded to produce parts with enough mechanical strength, shiny appearance and other technological characteristics (125).

Two of the most commonly used PP for BJ are sintering and infiltration (15), with the latter being the most popular due to its simplicity (126). Infiltration is a way to achieve higher density (78), and improve, among others, the mechanical properties of the 3DP green parts, where its quality basically depends on the type of infiltrant (53) and its process. There is a wide universe of infiltrant materials as well different infiltration techniques, either by simple immersion, with or without vacuum, drip, brush, or spray (15, 127).

The selection of these processes depends on the infiltrant type and the specific objective of the 3DP model. However, each infiltrant requires its own process and conditions of application to the 3DP model (as shown in Figure 21). Thus, there is a challenging task of selecting an infiltrant that meets the expected characteristics and applying them in similar conditions (post-processes) allowing compare them and discerning their advantages and disadvantages.

For the purpose of this chapter, our line of investigation was divided in three main parts:

I. *Selection of alternative infiltrants:* It starts by emphasizing the requirements of potential infiltrants. Then, the most relevant properties obtained by recent studies with infiltrants not devoted to infiltrate 3DP parts are reviewed. Finally, the main mechanical and thermal properties are compared, as well as the costs of possible infiltrants versus pre-selected infiltrants. The properties of the pre-selected infiltrants were obtained in tests according to the post-process conditions to be used in subsequent works.

II. *Case study:* The influence on the bending mechanical properties of 3DP samples infiltrated with the selected alternative materials of different viscosity, and the thickness of the printed models is analysed.

III. *Infiltrant characteristics improvement:* It is proposed to improve the bending properties and penetration capacity of the infiltrant by optimizing its cure and reducing its viscosity.

I. Selection of alternative infiltrants

5.2 Requirements of potential infiltrants and their selection

Within the main characteristics that would be expected from an infiltrant to fulfil its expected purpose, the capacity to fill the pores spaces and exhibit good flow and wetting of the pore structure are certainly among the most important ones. For 3DP parts in plaster-based materials, the infiltrant must be in a liquid state (but not aqueous) as it would react with the plaster (126). Based on literature review and experience with plaster infiltration, several requirements for suitable infiltrants were identified:

- It should be liquid at room temperature but able to solidify under suitable conditions; this transformation must be irreversible;
- The change in volume during the liquid to solid transformation should be as small as possible;
- Insoluble in water, thus the infiltrant should not react with plaster-base material;
- The infiltrant should have a low viscosity and a high wettability for the plaster powder so as to enable the infiltrant to soak into the 3D part and fill the pores;
- On solid state, the infiltrant must have reasonable strength, hardness and chemical resistance so as to be used for practical applications;
- Enough pot life to allow the infiltration process;
- As the infiltration is usually a manual process, infiltrants must avoid release toxic gases;
- The infiltrant should preferably be colourless, so as not to modify the original colour of the 3DP part, as well as a reasonable resistance to degradation by humidity, UV radiation, etc.;
- Curing time and temperature: a short cure time (without being extreme) is convenient, to shorten the post-processing time. A total cure at room temperature will be preferred, to avoid additional infrastructures such as ovens;
- Not being a technical requirement its availability, is important, as well as a reasonable cost per kilogram;

5.3 Alternative infiltrants materials

A quick overview of the above suggestions, discourage the selection of some materials, such as materials filled with fibers (depending on the size of these), or aqueous solutions. Some organic polymers have generally low strength and hardness and they cannot withstand higher temperatures. Polyester resins, despite being economical and presenting excellent mechanical resistance, are difficult to handle because they release potential toxic gases. However, certain thermosetting resins, and engineering polymers justify further investigation.

5.3.1 Epoxy resins and cyanoacrylates

As stated above, some materials have been typically used as infiltrants. However, due to the current universe of available materials, including epoxy resins and cyanoacrylates, there is a wide range of products that could be an alternative when compared to those offered by manufacturers of equipment and materials for 3D printing. Although most studies on infiltration of plaster-based 3DP models, have been made with infiltrants devoted for this purpose, there are some proposals for alternative materials. Infiltration processes in other fields such as dental medicine, oil and soil infiltrations, can also contribute to the present study, so they will be reviewed.

Within the commonly used infiltrants, epoxy resins have been described as a material that provides an excellent combination of mechanical and chemical properties, turning them into one of the most important thermosetting polymers, used in a wide range of applications (128). Another group of materials widely used as infiltrants of plaster-based 3DP models is the cyanoacrylates. More details about these materials were also described in 4.1.

Knowing that epoxy resins provide good mechanical strength, and considering high temperature resistance of the printing model, it could make the decision to use high-temperature resistance epoxies. In this case, the problem usually originates due to its high viscosity, as demonstrated by infiltrating plaster-based 3DP models with “resin services HTR-212” and “Ad-Tech Epoxy EEL-335” high-temperature epoxies, whose viscosities are around 800 to 1000 mPa.s. Therefore, the infiltrants failed to penetrate sufficiently into the printed model, providing a resistance of just 7 and 12 MPa, for tensile and flexural respectively (53).

Epoxy resins intended for resin transfer moulding (RTM) applications, with low viscosities of around 600 mPa.s, have been used as infiltrants of 3DP models, such as the epoxy systems " System Three Clear Coat " and " Ad-Tech Epoxy CER-112 ". These present a better penetration into the printed model, reaching a moderate strength of 16 and 20 MPa, for tensile and bending respectively (53).

Epoxy systems dedicated to adhesive applications, commercially known as LOCTITE® EA 9483 (Henkel, Europe), despite its high viscosity, around 1000 mPa.s, were applied as infiltrants of 3DP samples. The final tensile strength obtained is 7.42 MPa. This value is slightly lower than the 9.27 MPa obtained when a genuine epoxy infiltrant (Z-Max, 3D Systems, USA) was used in this same study. This lower resistance is due to the high viscosity of the non-genuine infiltrant (81).

Cylindrical samples of 12.7 mm diameter printed with plaster-based material Zp150, infiltrated with the epoxy resin Z-Max (3D Systems, USA), with a viscosity of 120 mPa.s (27), during several immersion times (up to 120 seconds), were mechanically tested. The best results obtained with different printing parameters reached 17.99 and 7.63 MPa bending and tensile strength, respectively (90, 106).

Cyanoacrylates dedicated to infiltration of 3DP models, marketed by BJ technology manufacturers such as ColorBond™ (113) (3DSystems, USA), adapted to the requirements of an infiltrant as it low viscosity and transparency. Its cost which can reach 213 € / Kg (129), limits its use for a common user, promoting a search for alternative infiltrants.

In the case of alternative infiltrants belonging to the family of cyanoacrylates, the CA Plus N5, a super-glue for home use, with ultra-low viscosity of 2 mPa.s, was selected. This infiltrant achieves a slight penetration of just 0.254 mm, giving a tensile strength of 5 MPa. Considering its high price of 285 €/kg, and the fact that it does not penetrates models of great thickness, it is not an alternative (53).

Another type of commercial cyanoacrylate (LOCTITE® 406™, Henkel, Europe), with viscosity of 12-22 mPa.s, achieved a tensile strength of 4.02 MPa, somewhat higher than that obtained in the same study (2.10 MPa) with a cyanoacrylate (Z-Bond, 3D System, USA) dedicated to infiltration of plaster 3DP models (81).

In the case of cyanoacrylates, the adhesive commercially available as SG-2 (Alteco Chemical PTE Ltd) was tested as an infiltrant of 3DP models built with plaster-based material (ZP100, 3D Systems). The selected infiltration method was simple drip. These infiltrated models offered resistance to bending of 15 MPa when the models remained exposed to a dry environment, but when the models are exposed to moisture, their resistance dropped to only 1 MPa (86). This denotes a poor moisture resistance of the cyanoacrylates.

Due to the wide variety of cyanoacrylates currently available, for the infiltrant materials selection stage, the technical data of one of the most common type of cyanoacrylates will be referred. This is the 2-cyanoacrylate, whose main application is bone-bone adhesive (130). Its technical data is collected in Table 14.

As stated in 4.1, the problem of cyanoacrylates basically lies in its low penetration and brittleness due to its almost instantaneous polymerization, in addition to its poor moisture resistance (90).

Table 14. Physical, mechanical and thermal data of 2-cyanoacrylate (130)

Characteristic	
Density (g/cm^3.)	1.25
Melting point (°C)	205
Glass transition temperature by DMA (°C)	96
Tensile strength at break (MPa)	31- 43
Young modulus (GPa)	3.1-3.6
Flexural strength at break (MPa)	104-122
Flexural modulus (GPa)	3.40 - 3.84

5.3.2 Other infiltrant materials

Phenol formaldehyde resins (PF) or phenolic resins are synthetic polymers obtained by the reaction of phenol or substituted phenol with formaldehyde. They are used as the basis for Bakelite. PFs were the first commercial synthetic resins (plastics), and at one time the primary material used for the production of circuit boards. Yet they have been largely replaced by epoxy resins and fiberglass cloth (131). PFs are made by two main production methods. One reacts phenol and formaldehyde directly to produce a thermosetting network polymer, while the other restricts the formaldehyde to produce a pre-polymer, known as ”novolac”, which can be moulded and then cured with the addition of more formaldehyde and heat (132).

Within the group of thermoplastics, acrylic resins are found, highlighting polymethyl methacrylate (PMMA) that stands out because it is a highly transparent and colourless fluid substance. It is also highly resistant to UV damage. PMMA presents a good hardness, stiffness and abrasion resistance and reasonably high tensile strength and modulus. It has low smoke emission. As far as limitations are concerned, PMMA shows poor solvent resistance, being susceptible to stress cracking, crazing and is brittle when compared to engineering thermoplastics. Besides, it is not resistant to contact with mineral acids, and being subject to water absorption, although it is reasonably low, it has a considerable effect on its dimensions (133, 134).

Poly(ε-caprolactone) (PCL) belongs to the family of plastics (thermoplastic, semi-crystalline), is characterized by being a biodegradable and non-toxic material, with low melt viscosity and low melting point. It has reasonable resistance to polar solvents and water, with good UV resistance and reasonable tensile strength for common applications. As limitations, it cannot be steam sterilized and shows poor resistance to non-polar solvents (133, 134).

Polymeric infiltration with PCL was performed in porous hydroxyapatite samples manufactured by 3DP. Three routes of infiltration were conducted including melt infiltration of low, high molecular weight PCL, and combination of both. The combination of low and high molecular weight infiltration yielded the greatest increase in the flexural properties (around 6.5 to 10 MPa) and could better maintain than other routers a high level of flexural properties during 28 days immersion in simulated body fluid (135, 136).

Printing models by BJ, based on a commercial PMMA polymer blend, were characterized and evaluated in terms of their strength and surface finish. The two component of medical grade epoxy resin (EPO-Tek 301) with low viscosity (around 100 and 200 mPa.s) were used to improve the mechanical strength, while wax was used to improve surface finishing. Flexural strength values of 2.91 MPa and 26.6 MPa were obtained for the green and infiltrated parts, respectively (137).

Acrylic resins are commonly used as adhesives, with cures usually fast and at room temperature. They have an excellent shear resistance, peel and shock resistance. Commonly they are expensive, but they compete with epoxy adhesives due to their fast set times at room temperature, flexibility and easy adherence to even oily surfaces (133, 134).

An acrylate infiltrant obtained by mixing triethylene glycol dimethacrylate (Esschem Inc.), 2,2-bis[4(2-hydroxy-3methacryloyloxypropyloxy)-phenyl]propane (Esschem Inc.), and urethane dimethacrylate (Esschem, Inc.), with Benzoyl peroxide (Merck, Inc.) as initiator, was used as an infiltrator of plaster-based 3DP models. These models presented a resistance to bending of 18 MPa when remained exposed to a dry environment, but, when immersed in water at 23 ºC for 168 hours, their resistance dropped to 2 MPa (86).

An ultra-low viscosity and light curing resin infiltrant was used in dental areas, where the infiltration is done through capillarity. In this case, it was used an infiltrant not dedicated for 3DP models, but for permanent teeth of bovine animals (138, 139). But due to its high cost and the cure of only part affected by light, these type of materials are no longer a viable alternative for applications on this study.

Most polyester thermosets are used in fiberglass-polyester composite materials, liquid casting, furniture products, boats, trucks cabs, etc. They are less rigid and stronger than epoxies, and considerably cheaper than epoxy and vinyl ester (134). Unsaturated polyester resins generally have higher toughness than other low-cost thermosets, with good UV and colour resistance. Defect free laminates and mouldings can be achieved under lower pressures and with low cost equipment in contrast to high pressures.

Compared with epoxies and vinyl esters, polyesters are less tough, less water resistant and present inferior heat resistant to epoxy. Their curing is exothermic, resulting in cracks, especially in thick sections. Catalysts used for curing can oxidize metals, and electrical properties could be affected by high humidity (134).

The toxic nature of its fumes, especially of the catalyst, (methyl ethyl ketone peroxide – MEKP), produces a strong styrene odour, which carries a safety risk if proper protection is not used. This becomes a great disadvantage when handling this type of resins, especially for non-specialized users.

By infiltrating plaster-based 3DP parts with the polyurethane glue (Armor Coat), mechanical resistances, depending on the printing orientation of the model, of 3 to 4 MPa for tensile, 10 to 16 MPa for compression and 10 to 11 MPa for bending were obtained (90).

5.4 Selection and characterization of alternative infiltrant materials

Based on the reviewed literature and the availability of materials in the market, the following stages of material selection study will be carried out:

i) Pre-selection of possible infiltrants;

ii) Definition of process conditions, for manufacturing samples of infiltrant materials with the same conditions (to compare them in future infiltration process of 3DP models);

iii) Mechanical and thermal characterization of specimens manufactured under the conditions previously selected;

iv) The previously obtained data will be analysed and compared to the universe of potential families of infiltrant materials. This task will be supported by the CES Edupak 2018 software.

As previously mentioned in this and previous chapters, there is a wide universe of possible infiltrant materials. For this reason, it is advisable to pre-select some ones that meet the aforementioned infiltrant characteristics, then characterize their properties of interest and compare them with their material families. Since the majority of possible infiltrants are thermosetting polymers, their behaviour is both thermally and mechanically affected.

Considering the thermosetting resins for structural applications, the dependence of the elastic modulus with the temperature deserves to be evaluated quickly and efficiently, since the cured resin provides the final resistance to the infiltrated 3DP parts.

Components based on some thermosetting resins are viscoelastic in nature, exhibiting a combination of both elastic and viscous behaviour (140). Two techniques commonly used to characterized them are Differential Scanning Calorimetry (DCS, described in Chapter 4), and the Dynamic Mechanical Analysis (DMA).

DMA is a test methodology that can evaluate the elastic modulus and viscous module of materials as a function of time, temperature and frequency (141). Among the main properties to be evaluated by the DMA are the viscoelastic parameters related to the performance of the material, such as the storage module-E' (stiffness), the loss modulus-E'', the loss factor-tan δ (damping), in addition, relaxation changes such as vitreous transition and its glass transition temperature (T_g), and other segmental movements (141, 142). Some of these definitions and material properties can be found in the respective ASTM D4092 standard (143).

These data are particularly valuable for evaluating the last stages of curing, the characteristics of the fully cured final product, as well as the modulus of fully cured thermosetting resins (144). From the curves obtained in the DMA test of thermosets, the T_g can be determined by the loss factor or damping factor, $\tan \delta$ curve peak. Also by recurring to DMA the curing of the resin can be verified (145).

According to the type of test to be performed, different accessories can be used to fix the sample in the DMA equipment for tensile, compression, torsion, shear, three-point bending, double cantilever and single-cantilever bending tests (146-148). For the most reliable result, it is recommended to compare with other methods of analysis, for example, the elastic modulus measured by mechanical tests (147, 148).

5.4.1 Selection of infiltrant materials

Considering both the literature reviewed and the requirements that potential infiltrants must meet and the availability in the market, three epoxy resins and one urethane resin were pre-selected. An epoxy resin dedicated to infiltration of plaster-based 3DP models was kept as a referential. This resin is commercially known as Strength Max (3D Systems Inc., USA), and it is basically constituted by 3-aminomethyl-3,5,5trimethylcyclohexylamine and benzyl alcohol (108), referred in the previous chapter as "*E1*".

The two other epoxy resins are basically composed by a bisphenol-A-(apichlorhydrin) and epoxy (149, 150); a Biresin CR83 and a catalyst CR83-6 (Sika, Germany), hereinafter called "*E2*", and a EC131LV and hardener W342 (Elantas, Germany), designated *"E3"*.

The rigid urethane casting resin belongs to the family of polyurethane elastomers. It is basically composed by Methylenedicyclohexyl disocyanate (35% - 85%), commercially known as Crystal Clear® 200 (Smooth-On, USA), hereinafter called "*U*" (151). It is water white clear and specifically made for applications that require clarity with low viscosity, and cures at room temperature with negligible shrinkage. Cured casting is UV resistant and is not brittle. It is commonly used in encapsulation, prototypes models, lenses or jewellery. Heat cured products offer advantages over the room temperature cure (151).

The typical physical data of these four selected resins are collected in Table 15 (more details are presented in Appendix 2 to Appendix 5). For the purpose of this study, these resins name designation and their main applications are included. Their colour, viscosities of the mixtures and cure time, as suggested by suppliers, as well as costs are highlighted: *E1, E2*, and *U* resins show a low viscosity, while *E3* shows a medium viscosity. Resins *E2* and *E3* are commonly used in resin transfer moulding (RTM), therefore, are readily available. *U* resin stands out as the most expensive, while *E2* and *E3* are the most economical.

Table 15. Main physical data of the infiltrants, adapted from (108, 149-151)

Characteristic	**Strength Max^{TM}**	**Biresin CR83-6**	**EC131LV / W342**	**Crystal Clear 200**
Code assigned	***E1***	***E2***	***E3***	***U***
Applications and characteristics	Infiltration of 3DP parts of plaster-base powder	Infusion and injection of complex and thin geometries	Good surface finish, very good resistance to UV	Encapsulation, prototypes, sculpture, jewellery, UV resistant
Colour	Clear	Colourless to yellowish	Violet to colourless	Colourless, clear
Mix ratio parts by weight	5:2	10:3	10:2.5	10:9
Viscosity, 25ºC (resin) (m.Pa)	-	510	1000-1600	
Viscosity, 25ºC (mixed) (m.Pa)	120	170	-	600
Density, 25ºC (mixed) (g.cm^{-3})	0.94	1.15	1.08 – 1.12	1.04
Pot life (min)	45 for 500 g*@23 ºC	180 for 100g@RT	22-32; 100 ml @25 ºC	20@RT
Cure time	2h@70 ºC / 24h@23 ºC	8h@70 ºC / 12h@55 ºC	24h@RT+15h@60 ºC	16h@RT + 6h@70 ºC
Cost, excluding VAT (€/kg)	33.44	12.12	19.00	67.50

5.4.2 Preparation of specimens and resin samples

To understand how to achieve some final characteristics of an infiltrated 3DP model, it is important to know the infiltrant behaviour independently. For this reason, the cure conditions of the selected resins were defined, focusing on obtaining a short cure time, and therefore less time of infiltration process.

These cure and post-cure conditions were based on the suggestions of the resin manufacturers (see Table 15), but adjusted to a single condition, with cure parameters close to those suggested for resin *E1* (referential). These process conditions are collected in Table 16, and will be kept for all studies in this chapter. All samples were cured at RT (23 ± 2 ºC) for 24 hours, and post-cured in a forced air convection oven SLW53 STD (PolEko, Poland) at 70 °C for 2.5 hours.

Table 16. Experimental conditions for cure and post-cure

Conditions	Time (h)	Temperature (ºC)
Cure	24	RT*
Post-cure	2.5	70

**RT= 23±2 ºC, ~50 % HR*

All resin samples were manufactured under the selected cure and post-cure conditions. These tests include tensile and bending, as well as differential scanning calorimetry (DSC) and dynamical mechanical analysis (DMA). The resins were mixed in the appropriate ratios (see Table 15), and cast in open silicone moulds, a technique widely used and accepted for resins without fillers and static cure (104).

5.4.3 Differential Scanning Calorimetry of resins

The differential scanning calorimetry analysis (DSC) was described in Chapter 4. It is used to study the thermal behaviour of *E1, E2, E3* and *U* resins, capturing the exothermic heat flow. It was performed according to ASTM E1356-14 (152) in a DSC Q20 equipment (TA instruments, USA), as shown in Figure 32 a). Samples of 16 to 24 mg of cured epoxy resins (*E1, E2* and *E3*) and the urethane resin (*U*) were heated from -60 ºC to 200 ºC with a heating rate of 10°C.min $^{-1}$, in an atmosphere of nitrogen, with a flow rate of 50 ml.min^{-1}. The curing and post-cure conditions of the resin samples occurred as indicated in Table 16.

5.4.4 Dynamic Mechanical Analysis of resins

The dynamic mechanical analysis (DMA) was performed on the four resin prototype systems *E1, E2, E3* and *U* to assess if their cure was completed, find their glass transition temperature (T_g) and to better understand the temperature dependent strength behaviours. A dual cantilever beam clamp was employed using a commercial instrument (TA Instruments DMA Q800), as shown in Figure 32 b). The storage modulus (E') was measured from 30 to 200 ºC. The samples were cast in open rectangular silicone moulds of 35 mm x 15mm x 3.8

mm. An amplitude of 100 μm was selected to avoid exceeding the maximum load capacity (18 N). Specimens were cyclically loaded at 1 Hz and heated at 5 ºC per minute.

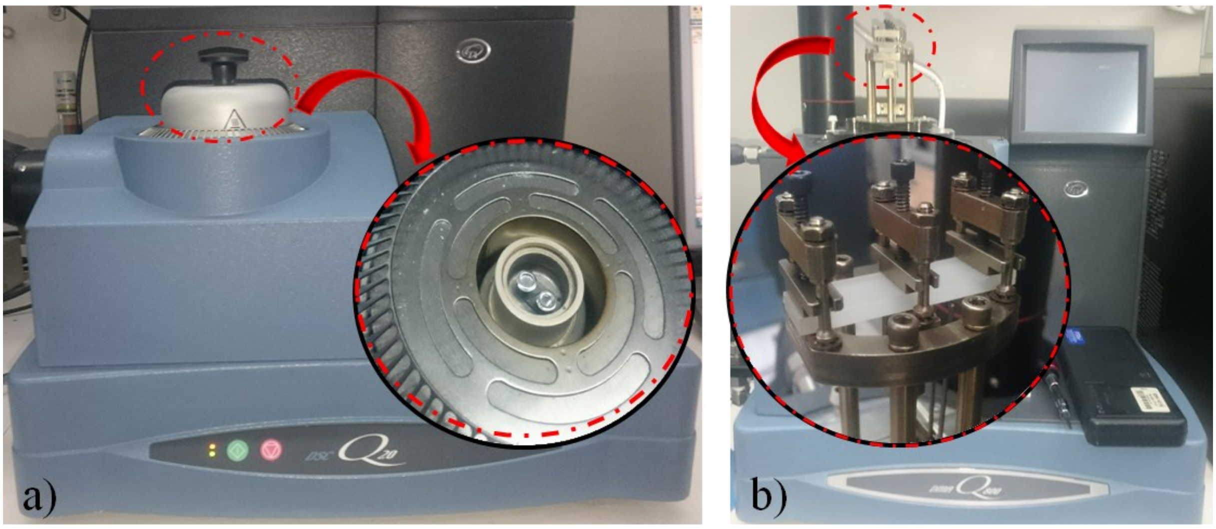

Figure 32. Test of a) DSC, and b) DMA of cured resin samples *E1*, *E2*, *E3* and *U*

The glass transition temperatures (T_g) of resin samples were also determined by DMA from peaks in the loss factor ($tan\,\delta$) curve, while the complete cure was determined in the storage modulus curve. The storage modulus, $tan\,\delta$ and other parameters were calculated according to ASTM D4092 (143).

5.4.5 Tensile and bending characterizations

Tensile tests were conducted according to the ASTM D638-10 standard in a Universal test machine (MTS 810, USA) at room temperature (RT), using a 10 kN load cell and a 5 mm/min speed, with a distance of 50 mm between extensometer legs (see Figure 33 a)). Five specimens were manufactured for each resin.

Three-point bending tests were carried out at RT, according to ASTM D790, in a universal testing machine with a 10 kN load cell (MTS 810, USA). Five samples of 127.5 x 12 x 3.2 mm of each resin were tested. The samples were supported by two rods of 5 mm radius with a span of 50 mm, and loaded by an upper rod of 4 mm radius (see Figure 33 b)). The crosshead load speed was set at 2 mm.min^{-1}.

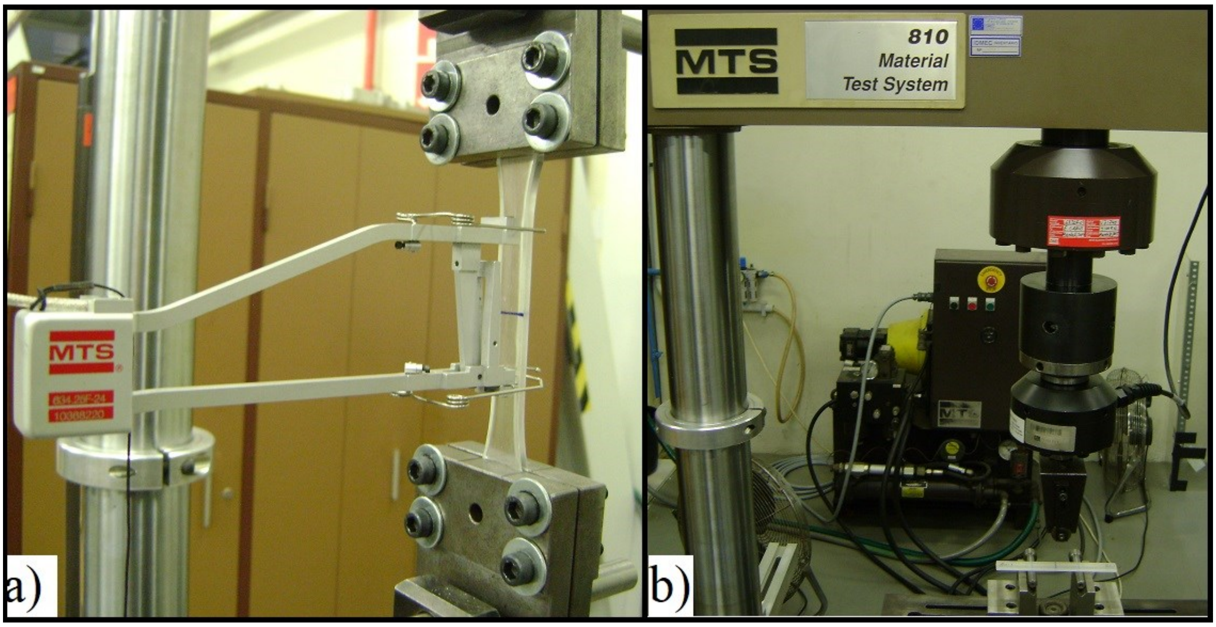

Figure 33. a) Tensile, and b) bending and tests of resin samples

5.5 Results and discussions

The objective of the study at this stage was to quickly assess important processing (curing) parameters such as glass transition temperature (T_g), and the completion of cure.

The thermograms obtained in the first scan of the DSC test using the cured samples of epoxy resins (*E1, E2* and *E3*) and the urethane resin (*U*) are depicted in Figure 34, while the enthalpy of curing (Δh) or residual heat of the reaction, and the temperature at the maximum exothermic peak ($T_{peak}\ or\ T_g$) is collected in Table 17.

The heat flow curves of the resins made by the DSC test (Figure 34) shows the *E2* resin at the highest exothermic peak, occurring in the range ~55-180 °C. The peak area generated 396 J/g of enthalpy, with a T_g value of 116.1ºC. With a very close difference between resin *E3* and *E1,* slightly smaller peaks are depicted, whose residual enthalpy values are 253.9 and 340.5 J/g at T_g of 104.5 and 105.9ºC respectively (153).

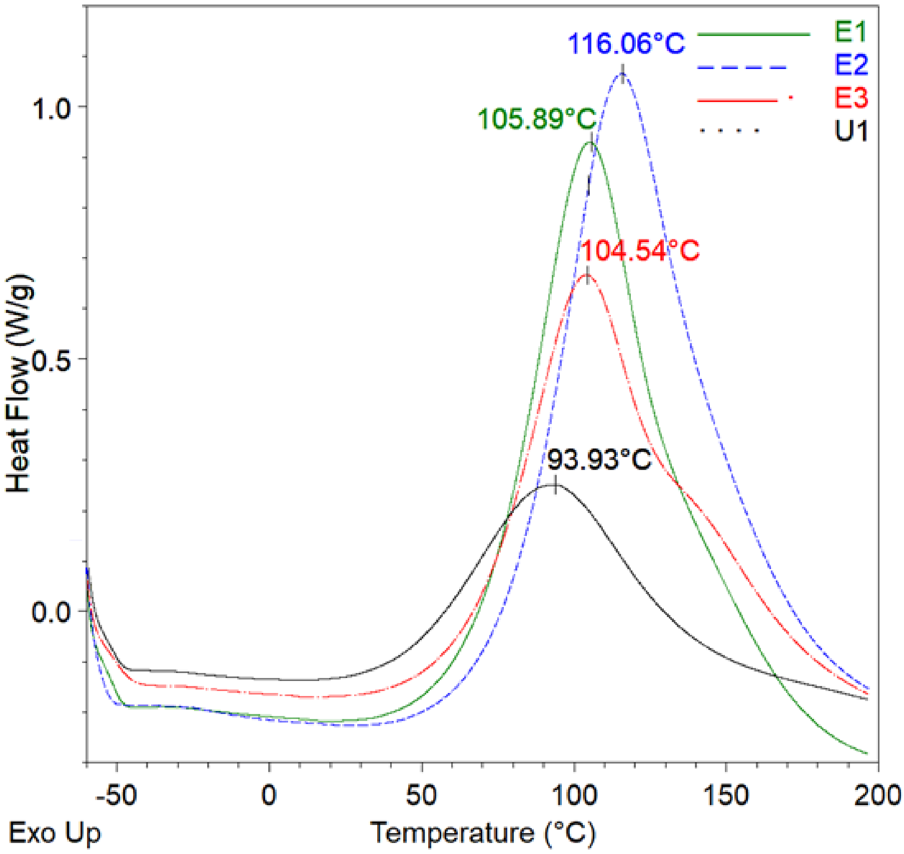

Figure 34. DSC thermograms of specimens of cured resin ($E1$, $E2$, $E3$ and U)

Finally, the resin U shows the lowest exothermic peak, between ~35 and 140 °C. This peak generated an area of 127.70 J/g of residual enthalpy with a T_g value of 93.9 ºC. These results would indicate that *E2* resin with the highest T_g = 116 ºC and heat flow of 396 J/g, would have a greater enthalpy of cure. Therefore, this resin could substantially increase its properties by optimizing its cure.

Table 17. Exothermic peak temperatures ($T_{g\ DSC}$) and energy released by the cured resin samples

	E1	***E2***	***E3***	***U***
Temperature, $T_{peak} = T_{g\ DSC}$ (ºC)	105.89	116.06	104.54	93.93
Heat flow or enthalpy of cure Δh (J/g)	340.50	396.00	253.90	127.70

From the DMA curves, it is possible to study the macroscopic characteristics of viscoelastic materials. However, as the results are directly related to the molecular structure, it is also possible to study microscopic properties related to molecular mass and cross-links, especially in polymers (141, 146).

The storage modulus (E') and the loss factor ($tan\ \delta$) for the four resins samples are shown in Figure 35. The respective T_g is indicated on peaks of the tan δ curves.

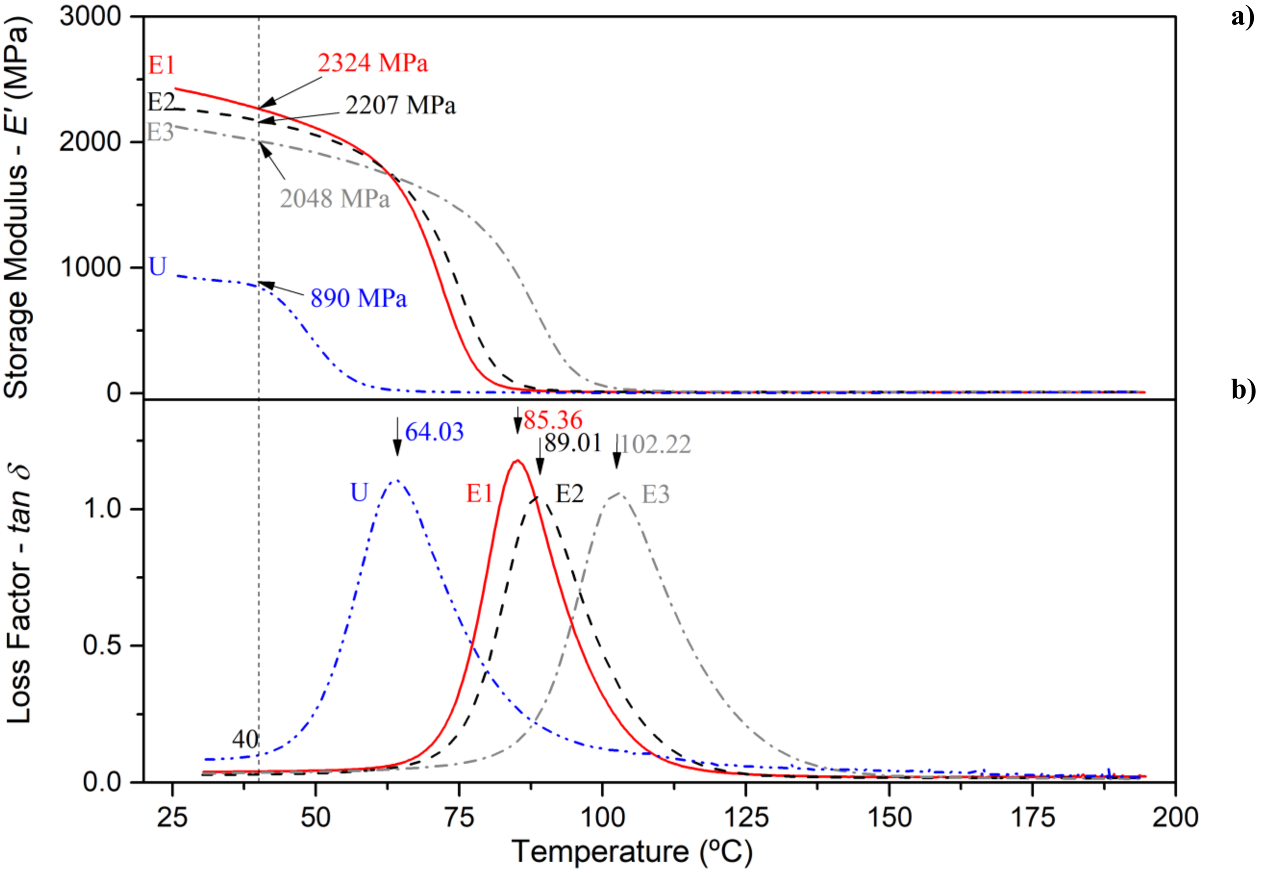

Figure 35. Dynamic-mechanical properties of epoxy ($E1$, $E2$, $E3$) and urethane (U) resins, a) storage modulus (E'), indicating the values at 40 ºC, and b) loss factor ($tan\ \delta$). Peaks show the T_g´s

The four resin samples show different viscoelastic behaviours, as observed in the curves of Figure 35 a). The storage module has been highlighted at a temperature somewhat higher than room temperature (40 °C), where slight differences were observed between epoxy resins, with values from 2048 to 2324 MPa. The resin U stands out, for showing the lowest storage module with 890 MPa, as seen in Table 18.

Under the cure conditions indicated above, and at 40ºC, the $E1$ resin is the most stiff resin, denoting a greater molecular organization in its molecular network (141, 145), that would directly affect the mobility of their links (141). It is possible to make these assumptions because the cure conditions are best suited to the $E1$ resin, according to the resin supplier suggestions.

Table 18. Glass transition temperatures ($T_{g\,DMA}$), useful operating temperature range and storage modulus E' of cured resin samples obtained in DMA test

	E1	***E2***	***E3***	***U***
Temperature, $T_{g\,DMA}$ (ºC)	85.36	89.01	102.22	64.03
Useful operating range temperature (ºC)	67.02	68.42	79.90	47.04
Storage modulus at 40ºC (E') (MPa)	2324	2207	2048	890

On the other hand, resin U is the less stiff resin (at least for these curing conditions). This response can be seen in the curve of E' 'and $tan\ \delta$, in the glass transition temperature range, as well as in the higher value of $tan\ \delta$ (141).

In decreasing order, the T_g were detected at 102.2, 89.0, 85.4 and 64.0 ºC for resins $E3$, $E2$, $E2$ and U respectively as shown in Figure 35 b) and Table 18. The glass transition temperature is depending on the samples' age. At early age, T_g values are usually lower than materials with greater aging factor (154).

For engineering purposes, the useful operating temperature range or working temperature of a thermoset epoxy is considered to be the range over which the storage modulus is nearly constant (145). Therefore, for samples $E1$ and $E2$, the working temperature is up to ~ 67-68ºC, where E' begins to decrease precipitously (see Figure 35, and Table 18). For sample $E3$, the useful operating range extends to approximately 80ºC. This higher temperature, together with the higher T_g (102.2ºC), confirms a higher useful operating range. On the contrary, the resin U presents the lowest operating range only ~47 ºC, which is confirmed through its lowest T_g (64.0 º C).

The results of the mechanical tensile and bending tests performed on the resins $E1$, $E2$, $E3$ and U are summarized in Table 19, which shows the average values obtained from the five specimens and the respective standard deviations. Specimens were cured according to the conditions established in Table 16.

These results are depicted in Figure 36, showing the maximum tensile strength (MPa) versus Young's modulus (GPa). The pre-selected materials are highlighted with red text and boxes. Representative materials of the plastics' families, thermo-plastics, natural materials, elastomers and composites were chosen for comparison purposes. These materials are commonly used in engineering applications and meet the characteristics for potential infiltrants.

The characteristics of these materials were extracted from the CES Edupack 2018 database (134), as well as from the literature.

Similarly, Figure 38 shows the flexural strength (MPa) obtained in the mechanical test versus the price (€/kg) of the resins and other potential materials. The prices of the pre-selected materials are in accordance to the Portuguese market in June 2017.

Table 19. Average values and standard deviation of tensile and bending tests of cured resins $E1$, $E2$, $E3$ and U

	E1	***E2***	***E3***	***U***
Tensile strength (rupture), σ_{tM} (MPa)	61.23±5.67	85.89±13.68	66.82±7.23	42.80±1.95
Young's Modulus, E_t (GPa)	3.05±0.03	3.68±0.82	2.92±0.06	1.85±0.09
Flexural strength (rupture), σ_{fM} (MPa)	112.4±2.34	105.4±5.26	61.82±18.01	70.72±1.19
Flexural E- Modulus, $E_{B.}$ (GPa)	3.01±0.09	3.11±0.07	3.42±0.12	2.06±0.11

In general, it is possible to seen in Figure 36 that the selected epoxy resins have greater tensile strength and Young's modulus than all natural and elastomers materials. Even within the family of plastics, the epoxy resins are those with higher tensile strengths and greater stiffness. The resin $E2$ and $E3$ exhibit such tensile strength, surpassing slightly the $E1$ resin (referential). All epoxy resins are considerably more resistant to tensile stresses and stiffer than U resin.

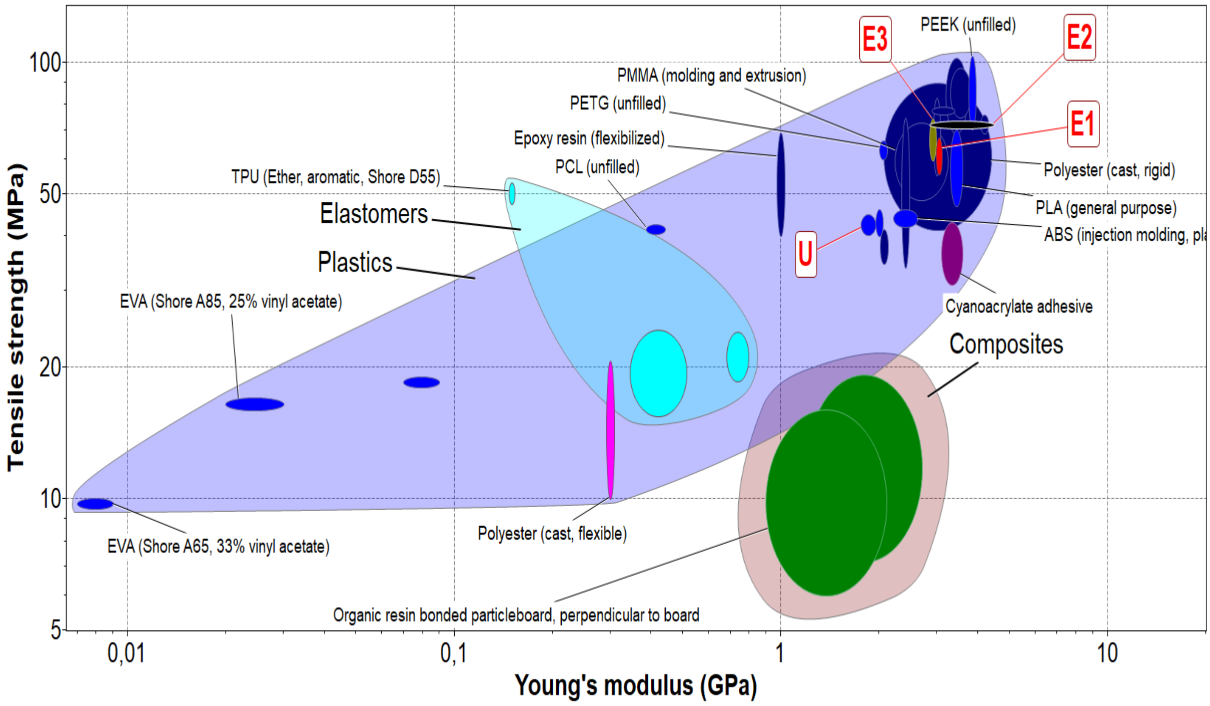

Figure 36. Tensile strength (MPa) vs. Young's modulus (GPa) of $E1$, $E2$, $E3$ and U resins compared with other potential infiltrants, supported by (134)

The resistance achieved on infiltrated 3DP models will depend not only on the strength of the infiltrant material but also on many factors related with the infiltration process (described in Figure 21), such as the viscosity of the infiltrant, the thickness of the 3DP model, among others. However, it is suitable to have a high mechanical resistance infiltrant, since the infiltrant is responsible for transferring considerably its final resistance to the infiltrated 3DP model. Thus, it is possible to predict that the pre-selected epoxy resins are a good option to withstand the tensile stresses.

As shown in Figure 36, pre-selected resins exceed, in terms of tensile strength, when compared to materials such as polyethylene terephthalate glycol (PETG), cyanoacrylate adhesives, polylactic acid (PLA), acrylonitrile butadiene styrene (ABS), and ethylene vinyl acetate (EVA). The same applies for all elastomers like thermoplastic polyurethanes (TPU) and organic resins such as pine resins. Materials of lower tensile strength and Young's modulus are corks (of natural origin). The mechanical characteristics of cyanoacrylate is based on adhesives cyanoacrylates (130), collected in Table 14.

Polyether ether ketone (PEEK) is one of the few polymers that overcome the resistance of pre-selected epoxy resins, however, this material requires high temperatures to keep it in liquid state.

Preliminary infiltration tests were performed on 3DP models of rectangular sections. These samples were infiltrated by full immersion in ABS diluted in acetone with 99.9% purity. In order to analyse the penetration behaviour in to the 3DP model, immersion times of 5, 10 and 150 min were employed.

Initial results showed adequate mechanical resistance for thin thicknesses (3.2mm). Figure 37 displays the cross section of the post-infiltrated samples, where partial penetration was obtained. Greater penetration was reached in the samples subjected to 5 minutes of immersion, achieving slightly more penetration than those submerged for 10 minutes. The lowest penetration samples were those of 150 minutes of immersion.

This phenomenon, was due to the 3DP model material (plaster-based) being highly hygroscopic, thus evaporating the acetone upon contact. This allowed just a superficial penetration of the polymer solution, sealing the superficial pores with solidified polymer and preventing inward penetration even for extended times.

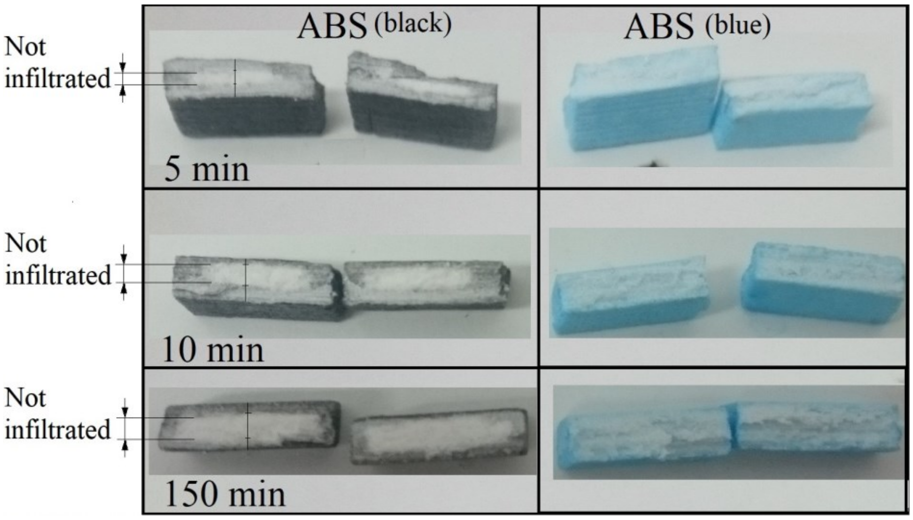

Figure 37. 3.2 mm thick cross sections of plaster-based 3DP samples infiltrated with black and blue diluted ABS solution. Full immersion for 5, 10 and 150 minutes The clear part shows the non-infiltrated area.

Figure 38 shows that resins $E2$ and $E1$ present a slightly higher flexural strength (105 MPa and 112 MPa, respectively) than $E3$ (62 MPa) and U (71 MPa) resins. The $E2$ resin is the most economical (12.1 €/kg), followed by $E3$ resin (19.0 €/kg). This makes resin $E2$ and $E3$ the best infiltrant options considering these two variables.

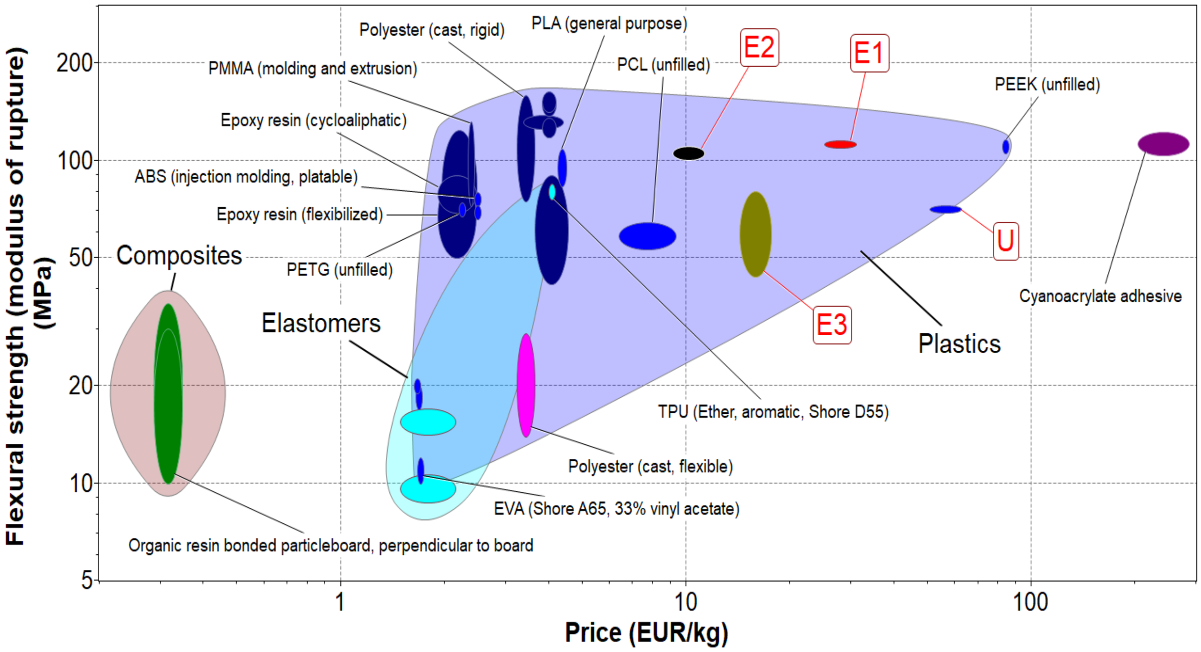

Figure 38. Flexural strength (MPa) vs. price (€/kg) of $E1$, $E2$, $E3$ and U resins compared with other potential infiltrants, supported by (134)

The cost of the U- resin (67.5 €/kg) exceeds by more than 200% the cost of $E1$ (33.4 €/kg). The urethane U-resin, with its excellent transparency, would virtually not distort the colour of the 3DP models, and would also provide considerable flexibility due to the low Young's and flexural modulus, as presented in Table 19. However, the relatively low resistance to both tensile and bending, in addition to a low T_g and the high cost per kilogram, make this resin an expensive infiltrant option.

The price and quality of cyanoacrylates, another widely used infiltrant, depends on its particular type, dilution, and brands. A cyanoacrylate dedicated to infiltration of 3DP models costs about 285 €/kg (Colorbond, 3D Systems, USA) (109, 113). This is more than 400% the cost of the U resin, which also makes it a very expensive option.

In Chapter 4, plaster-based 3DP samples were infiltrated with the $E1$ resin (referential) under the same cure conditions as those performed in this study. The tensile and flexural strengths found were 9.16 MPa and 16.45 MPa, respectively (as shown in Figure 27 and Figure 28). Both tensile and flexural strengths are consistent with the results found in other studies (53, 81) when infiltrating 3DP models with alternative epoxy resins. These tensile strengths are of 7 to 16 MPa, and 12 to 20 MPa for bending.

As shown in Figure 36 and Table 19, the tensile strength of resins $E2$ and $E3$ are slightly higher than $E1$. Additionally, the T_g of $E2$ and $E3$ are higher than T_g of $E1$ (Figure 35 and Table 18), which allows to predict that the resistances of resins $E2$ and $E3$ could be increased even more by adjusting their cure conditions.

5.6 Conclusions

The present study reviewed the requirements of potential infiltrants for plaster-based 3DP models. Different studies were analysed, and materials not typically used to the infiltration of 3DP models were used. Potential infiltrants were selected, and the thermomechanical properties characterized under the same cure condition. Then, these potential infiltrants were compared with a selected group of other materials and their families' materials.

The thermo-mechanical tests carried out revealed the possibility of improving mechanical properties, especially for resins $E2$ and $E3$ by adjusting the curing conditions.

The results showed that the resins $E2$ and $E3$ presented the best mechanical properties, both in tensile and bending tests, keeping costs per kilogram lower. The $E3$ resin was the one that showed the lowest rigidity, which could be suitable to infiltrate 3DP models, since they are stiffer.

For the next stage of this work, it is proposed to continue with the study of the infiltrants' viscosity as a function of temperature, as well as their behaviours when infiltrating models with different thicknesses.

II. Case study: Mechanical properties of 3DP models with different thicknesses infiltrated with alternative materials

5.7 Introduction

Infiltration is the most used post-process (PP) in Binder jetting (BJ) technology (15). The success of the final characteristics of the 3DP infiltrated models depends on the characteristics of the infiltrant material (53), the infiltration process, and the thickness of the 3DP model.

Once the infiltrant has been applied, it must penetrate into the model but, depending on its type and model thickness, different penetrations can be achieved (81), and consequently the mechanical strength that the model can withstand also changes (155). However, this (binomial) combination, infiltrant and model thickness, should be furtherly studied, to optimize the infiltration process.

The majority of the researches concerning BJ have explored the printing properties of this technology (15, 25, 28, 32, 39, 156-158), but only a few studies Table 20 are devoted to PP and, and within these, the penetration of the infiltrant into the model, leaving the relation with the final bending properties not discussed in depth.

The main achievements of some research studies concerning the effects of the infiltration process on the mechanical properties of 3DP parts in plaster-based materials are summarized in Table 20. The first publications that relate the effects on the mechanical properties of infiltrated 3DP parts with epoxy resins and waxes appeared in 2004 (124, 159) in an informative way.

3D printed parts with plaster and cellulose-based materials infiltrated with acrylic, cyanoacrylate, and wax were compared when in direct contact with water or exposed to moisture (86). The author concluded that in humid environments, plaster samples are not as resistant as cellulose ones, especially in direct contact with water, suggesting a careful selection of the materials system to produce models with good performance.

Frascati (53) used several infiltrants in his research and concluded that the best strength was reached with epoxy resins, and more specifically with the least viscous ones.

Pilipovic et al. (95) compared the final tensile and flexural strengths of 3DP parts obtained by polyjet vs. those obtained by BJ infiltrated with genuine (supplied by 3DP equipment manufacturer) and non-genuine infiltrants. The parts were analysed in terms of their printing parameters rather than their infiltration process, emphasizing that non-genuine infiltrants provide similar strengths to genuine ones.

Table 20. Studies of plaster-based 3DP parts infiltrated with not dedicated infiltrants

		Printing Parameters			Infiltration				Mechanical Effects			Infiltrants
		Layer thickness	Built Orientation	Built Position	Type	Time	Method	Absorption	Tensile	Flexural	Compression	
Impens et al	(105, 106)		x		x	x		x	x		x	PU, Epsom salt, epoxy, wax and glues (CY)
Galeta et al	(81)	x	x		x				x			Epoxy and CY (genuine), Loctite Hysol 9483 (epoxy resin)
Gharaie et al.	(35)	x	x		x				x			Z90 (superglue)
Pilipović et al.	(95)				x				x	x		Zmax, CY (genuine), Loctite Hysol 9483 A&B (epoxy resin)
Frascati	(53)		x	x	x			x	x	x		Zmax, and high temp.epoxy resin.
Suwanprateeb	(86)					x	x	x		x		Heat-cure acrylic, cyanoacrylate, wax
Steele et al.	(159)								x		x	Z-Max
Hackney et al.	(124)				x					x		Different viscosity waxes

The effects of printing build orientation, and post-processing methods on the tensile strength of 3DP parts were investigated by Gharaie et al. (89), finding that the highest strength was achieved by a combination of 45º direction, Z90, super glue infiltration, and baking in an oven at 75ºC for 2 hours. In addition, they verified that the drying process of 3DP green parts had minimal effect on the final strength. For the same purpose, Galeta et al. (81), reported that the strength of 3D printed samples is mainly related with the infiltrants, but it may be further increased by selecting the best combination of layer thickness and build orientation.

Impens et al. (90, 106) observed that after five minutes of complete immersion, the infiltrant no longer penetrates the printed models, regardless its viscosity, concluding that the specimens infiltrated with epoxy resins are stronger overall, and the specimens whose immersion time reached 120 seconds, were the strongest. They also concluded that 3D printer powder material does not react similarly with different materials used as infiltrants, and cannot be easily predicted from just one study.

It should be noted that, the strength of a non-infiltrated part will be rather affected by build orientation; models oriented along the X-axis and Y-axis are stronger than the ones oriented along Z-axis. Once a part is infiltrated, it uniformly takes the strength characteristics of the infiltrant product (52).

It is also worth considering the behaviour of a thermosetting material by itself and not necessarily when it is an infiltrant of a 3DP model.

In the case of a cold-curing structural epoxy resin for civil engineering applications, its curing reaction was analysed as a function of the curing time (from 7 to 62 days) and different sample thicknesses (from 0.8 to 40 mm). The influence of the sample thickness on the curing reaction of the resin was also investigated, finding a strong influence of the thickness on the curing degree of cross-linking reactions. In particular, the relaxation enthalpy and the residual heat of reaction decrease by increasing the sample thickness. This is possibly due to the fact that by increasing the sample thickness, the heat of reaction developed increases, thus obtaining greater degrees of cross-linking and higher glass transition temperatures (160).

These researches seem to indicate that a clear relation between samples thickness and type of infiltrant, aiming to reach the best mechanical properties, is still undefined. This research tries to fill this gap by studying the flexural properties of 3DP samples infiltrated with three different epoxy resins; two of them of general application in RTM (resin transfer moulding) and a third one recommended by 3DP manufacturers. The flexural study was selected because bending test shows the ability of the part to withstand the fracture in use; additionally, this is also a reasonable guide to tensile strength (161, 162).

An additional contribution of this research is to select and apply new infiltrant materials and not only those commonly used in the 3DP market or those proposed in previously reviewed studies, taking into consideration the relevant characteristics that infiltrants must meet.

This study is structured as follows: firstly, the infiltrants (pure resins) were characterized, later the plaster-based samples were infiltrated by full immersion, and the flexural properties determined. Finally, the results obtained were validated using statistical tools, and discussed.

5.8 Materials and Methods

To evaluate the relationship between the types of resins and the different thicknesses of the 3DP samples (input -factors) and the effect on the maximum flexural strength "σ_{fM}" and flexural E-modulus "E_B" (output -response), the study was divided in two stages (Figure 39): i) characterization of infiltrants, and ii) characterization of 3DP infiltrated parts.

For stage i), Figure 39 (left side), three epoxy resins were selected as infiltrants, two of them used in applications other than 3DP parts infiltration, and a third one dedicated to infiltration of 3DP plaster parts. The molecular structure, viscosity and flexural properties of each resin was determined.

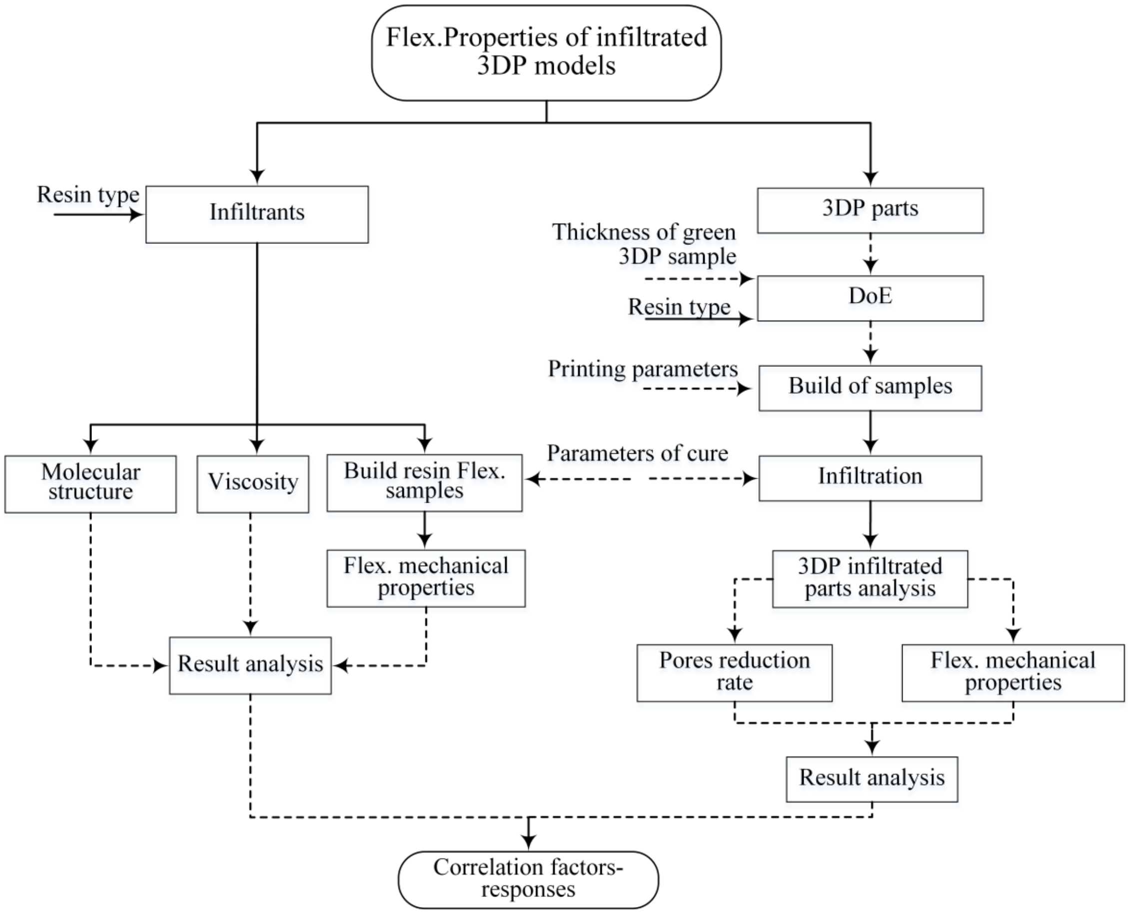

Figure 39. Diagram of the research stages

For stage ii), Figure 39 (right side), a full factorial Design of Experiments (DoE) was adopted. Flexural samples of different thickness were printed followed by infiltration. These samples were weighed before and after infiltration to evaluate their pores reduction, and then the infiltrated samples were tested in bending. Analysis of Variance (ANOVA) was used to validate the results by calculating the means of each level, for each factor.

5.8.1 Characterization of infiltrants

Three types of bi-component epoxy resins were selected as infiltrant. The urethane resin, was discarded as mentioned in 5.6 mainly due to its high cost and low mechanical strength (see

Table 15, in 5.4.1). One of these infiltrants is commercially known as Strength Max (3D Systems Inc., USA), (108), called in this study as *E1* (used as reference). The Biresin CR83 and a catalyst CR83-6 (Sika, Germany) (149, 150), called *E2*, and a EC131LV and hardener W342 (Elantas, Germany), designated *E3* were also selected.

Among the important characteristics that must be met by infiltrant materials, in order to improve the mechanical strength of the 3DP parts, a reasonable mechanical strength (at least equal to or greater than referential resin *E1*), and low viscosity must be mentioned. Therefore, when working with several resins as infiltrants, it was necessary to identify and compare them at the molecular level with the reference resin.

5.8.1.1 Fourier-transform infrared (FTIR) spectroscopy

Fourier-transform infrared (FTIR) spectroscopy analysis is a sensitive method with a wide field of application. In this case, it was used to identify and compare the chemical composition of resins at molecular level (128). The FTIR spectroscopy analysis was performed in a 630 FTIR spectrometer (Agilent Cary, USA) to analyse, in liquid state, the resin (component A) and the mixture with their respective curing agent (B), hereafter called mix-resin. This test was carried out using the path–length attenuated total reflectance (path–length ATR) technique, and the spectra was obtained at a frequency range of 4000 to 650 cm^{-1}, with 4 clean scans and 140 background scans, with a resolution of 4 cm^{-1}.

5.8.1.2 Measurement of the viscosity of the resins

The variation of infiltrant viscosity (ν) is an important factor, since a low viscosity facilitates its infiltration. Therefore, the variation of the viscosity as a function of time and temperature was measured starting from an initial temperature at room temperature. A tuning fork vibro-viscometer model SV-10 (A & D, Japan) was used to measure the viscosity (ν) and the pot life of the mix of resins.

Considering the proportions of the two components of the resins, they were manually pre-mixed and placed in a container where the two thin plate sensors in a fork configuration were immersed. These sensors drive with electromagnetic force to vibrate at the natural (resonant) frequency of 30 Hz within the sample fluid (Figure 40). The amount of resin was adequate to keep the two thin plate sensors fully submerged in them. Each resin was tested for at least 30 minutes, considering that this time should be lower than their pot life.

Viscosity is then calculated based on the proportional relation between the viscous resistance of the sample fluid and the amount of electric current required to drive and maintain the sensor plates at a constant vibration amplitude.

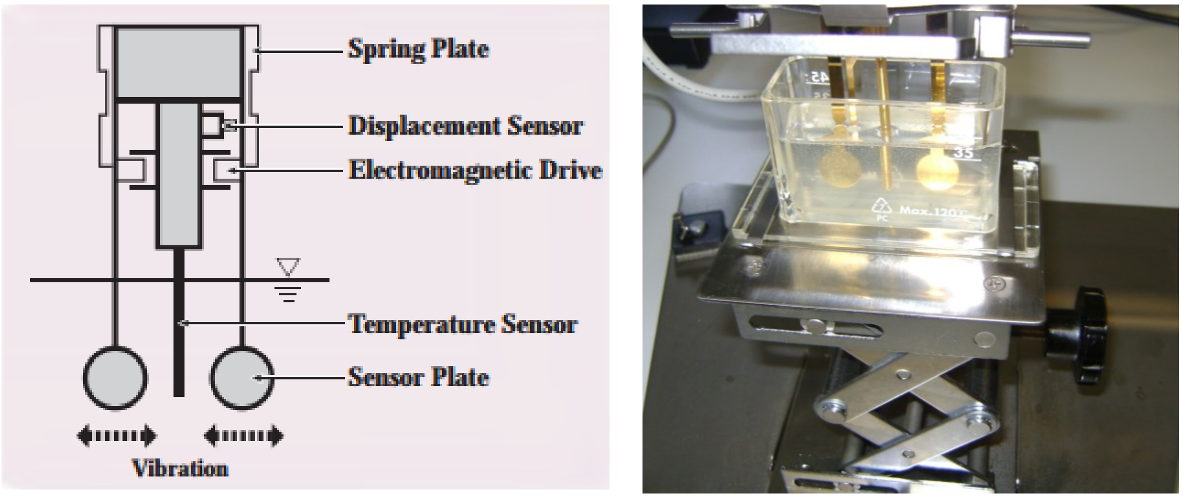

a) b)

Figure 40. a) Schematic diagram of the vibro-viscometer (adapted from (163)), b) experimental measurement of viscosity (resin $E2$)

The tensile and bending tests of the resins were carried out in the previous part I (Selection of alternative infiltrants). These results will be considered for comparison with the 3DP infiltrated specimens.

5.8.2 Characterization of infiltrated 3DP samples

A DoE was employed to identify the influence of the resin type and thickness of the infiltrated 3DP sample on the maximum flexural strength (σ_{fM}), and E-flexural modulus (E_B). For each of these two factors, three levels were analysed, as shown in Table 21. The geometry recommended by ASTM D790 was adopted to define the sample thickness of 3.2 mm (*C2*). Two other thicknesses were also selected: one slightly thinner, of 2.5 mm (*C1*), and a thicker one with 9.0 mm (*C3*) (see Table 21). Based on a full factorial design and the number of factors and levels, an arrangement of nine factors combinations was obtained, where *YE1*, *YE2* and *YE3* correspond to 3DP specimens infiltrated with resins *E1*, *E2* and *E3*, respectively (Table 22). The tests were performed with five samples for each combination, resulting in a total of forty-five specimens.

Table 21. Factors and assigned levels for DoE of 3DP samples

Factors	**Levels**		
	1	**2**	**3**
Infiltrated 3DP sample	*YE1*	*YE2*	*YE3*
Thickness of the 3DP sample (mm)	*C1*=2.5	*C2*=3.2	*C3*=9.0

Table 22. Tested factors with full factorial DoE and their corresponding assigned codes

Combination	**Factors**		**Code for infiltrated 3DP sample**
	Resin type	**Thickness of the 3DP sample (mm)**	
1	*E1*	*C1*=2.5	*YE1-C1*
2	*E2*	*C1*=2.5	*YE2-C1*
3	*E3*	*C1*=2.5	*YE3-C1*
4	*E1*	*C2*=3.2	*YE1-C2*
5	*E2*	*C2*=3.2	*YE2-C2*
6	*E3*	*C2*=3.2	*YE3-C2*
7	*E1*	*C3*=9.0	*YE1-C3*
8	*E2*	*C3*=9.0	*YE2-C3*
9	*E3*	*C3*=9.0	*YE3-C3*

To avoid the influence (noises) of other parameters that are not under study, both the printing and infiltration parameters were adjusted and kept constant. The printing parameters were selected according to the 3DPrint® software default values that are suitable for most part geometries (52): binder saturation level at 100%, binder/volume ratios of 0.24 for shell and 0.12 for core, printing layer thickness of 0.01 mm, and vertical building speed of 28mm/h.

The printing materials are plaster-based powder (VisiJet® PXL Core) (48), and water based binder solution VisiJet® PXL (39, 49). The 3DP samples were manufactured by batches according to their thickness on a 3D printer Projet 660 Pro (3D Systems, USA), in a build position and orientation as shown in **Figure 41**.The build position and orientation were selected for a maximum build speed by placing the samples with the smallest dimension along the Z-axis (this is automatically detected by the 3DPrint software V1.0). After printing, the samples were dried at 70ºC for 2 hours. in the same build chamber.

To determine the infiltrant absorbed by the 3DP samples, porous reduction rate (*RP*) was determined according to equation (6). For this, samples were weighed in a HDL-300 (Scale House, USA) precision scale, before ("m_b" - bulk mass before infiltration) and after infiltration and cure ("m_a"), respectively. The real mass "m_r", was estimated assuming a totally compact theoretical mass according to equation (7), where, δr is the real density of the printing powder (2.6 g/cm^3) (48), and V_r is the CAD dimensions of the samples, where width "*w*", thickness "*t*" and length "*L*" are shown in Table 23.

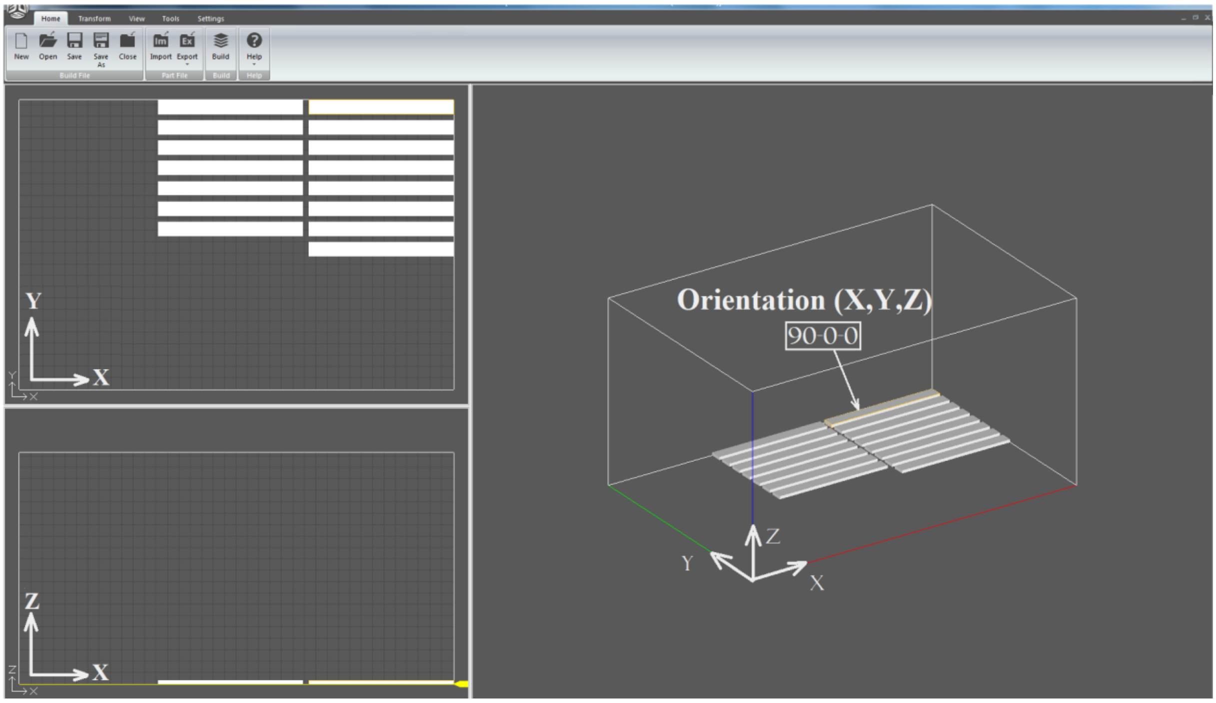

Figure 41. Build position and orientation of a batch of samples in the 3D printer chamber

Considering that the resins have similar densities (see Table 15 on page 72), it was assumed that $m_{aE1} = m_{aE2} = m_{aE3} = m_a$.

$$RP = \frac{m_r - m_b}{m_r - m_a} \tag{6}$$

$$m_r = V_r . \delta_r \tag{7}$$

Table 23. Real mass and volume calculated from theoretical samples dimensions

Density, δr (g/cm^3)	**CAD dimensions, *w*x*t*x*L* (mm)**	**Volume, *Vr* (cm^3)**	**Mass, *mr* (g)**
2.6	C1: 10.0x2.5x60.0	1.50	3.90
	C2: 12.7x3.2x127.0	5.16	13.42
	C3: 12.7x9.0x165.0	18.86	49.03

The infiltration of the 3DP samples was performed by the simple full immersion method, following the conditions indicated in Table 24, as seen in Figure 42. This method was selected due to its simplicity of application (it does not require equipment and operator skills), additionally, it presents a uniform and deeper absorption from the 3DP model when compared with the other manual methods. The selected immersion time was five minutes, because at atmospheric conditions, this type of infiltrants are not able to further penetrate into the samples (90, 106).

Table 24. Parameters for infiltration of samples by full immersion

Parameter (units)	**Values**
Mixing time of resin parts (min)	2
Immersion time (min)	5
Cure, time - temperature (h @ ºC)	24 @ RT*
Post cure, time – temperature (h @ ºC)	2.5 @ 70

**RT: ~23 ± 2º C ~50 % RH*

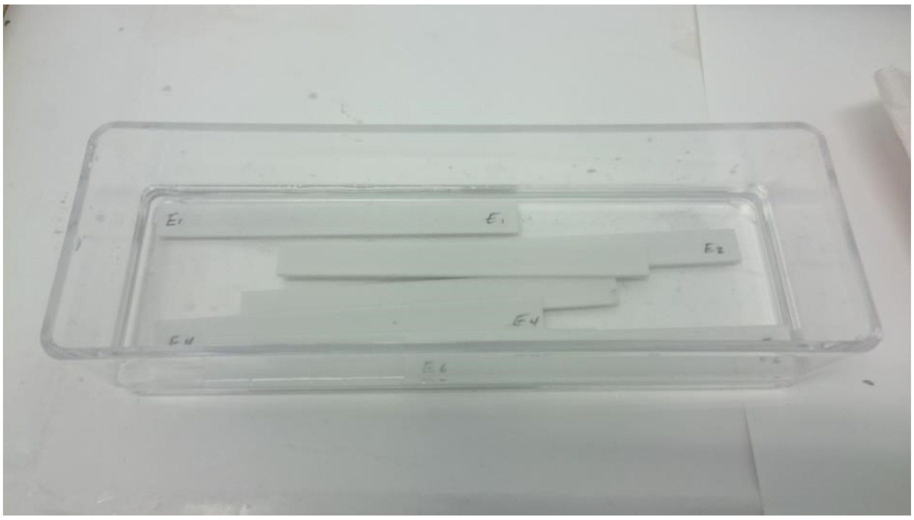

Figure 42. Simple full immersion method used to infiltrate 3DP samples for flexural test

For each resin, the two components were manually mixed according to the ratios indicated in Table 15 in batches of 300 ml to guarantee enough volume to fully immerse the 3DP specimens. The mixture was then poured into a container and the 3DP specimens were fully immersed for 5 minutes. Before being removed the excess resin is wiped from the surface with paper towels, and then they are allowed to cure on wax paper for 24 hours at RT. The infiltrated 3DP specimens were baked for 2.5 hours at 70 °C, and after cooling, the samples were stored in an airtight container until the mechanical tests. It is worth noting that both cure and post-cure conditions were the same as the ones used for resin samples, according to Table 16 defined in 5.4.

A three-point bending test was performed according to ASTM D790-10 in the same equipment previously described. The support span was set at 40, 50, and 135 mm for samples thicknesses of 2.5, 3.2 and 9.0 mm, respectively.

5.9 Results and discussions

5.9.1 Characterization of resins

The spectra of the resins (bases) Figure 43 a), and the mix-resins (resin with the catalyst), Figure 43 b), are cut between the amplitudes of 2750 and 1700 cm^{-1} because in this range no peaks were detected.

The resemblance of the pure resin spectra (Figure 43 a)) indicates a similar molecular structure of the three primary components of each resin. The main difference is shown at 753 cm^{-1}, where the resin $E1$ stand out as the highest.

The spectra of the mix-resins showed noticeable differences, especially for *E3* (Figure 43 b)), where all peaks are lower than *E2* and *E1*, with more pronounced differences in the bands of 1508, 1182, 828 and 753 cm^{-1}, suggesting that the type of catalyst for *E3* has more differences in the molecular bonds concentration, as claimed by Tripathi and Srivastava (164).

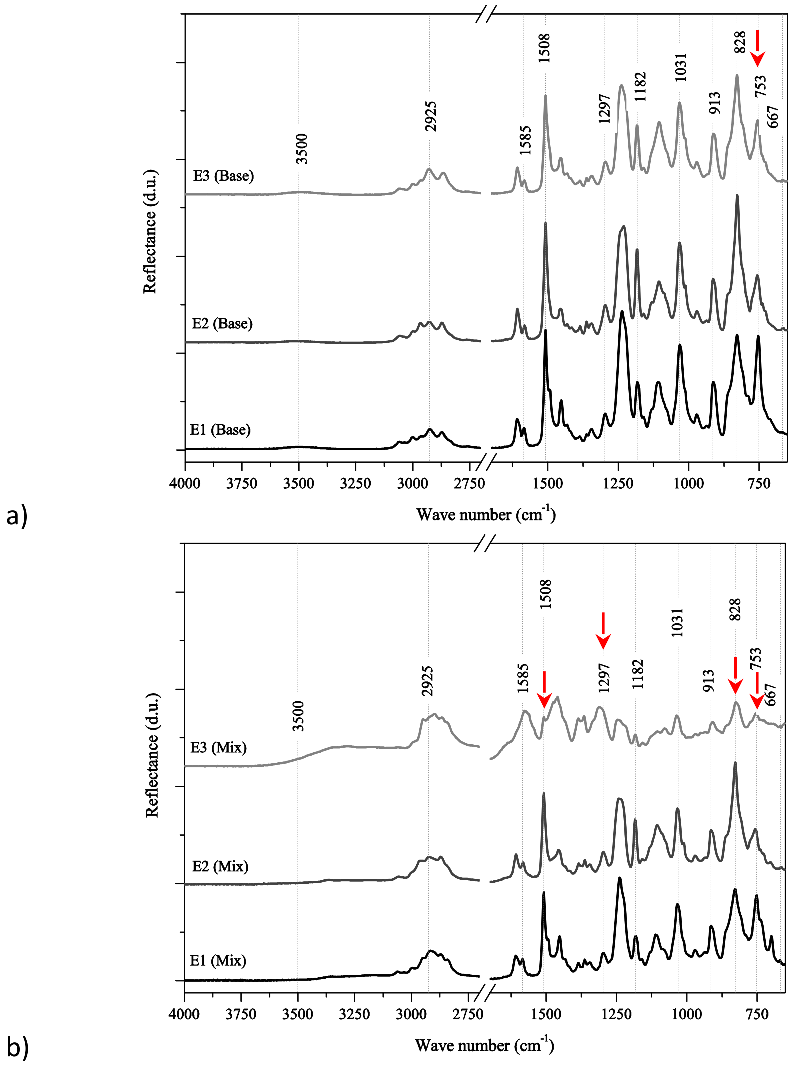

Figure 43. FTIR spectra of uncured epoxy resins *E1, E2*, and *E3*, for; a) base, and b) mix-resins

The reflectance band in Figure 43 b) at 3500 cm^{-1}, denotes the presence of ν OH on uncured epoxy-amine system of diglycidyl ether of bisphenol-A (DGEBA) (165, 166), while the peak at 2925 cm^{-1} is attributed to the –CH$_2$– stretching. The reflectance peaks for the aromatic C–H were also detected at 1585, 1508, 753 and 667 cm^{-1}. The more intense peak at 667 cm^{-1} for resin *E2*, can be related with its great pot life (167). The peaks shown at 1297 cm^{-1} are related with the P=N bound (167). The inflection at 1182 cm^{-1} is linked to the C–O stretching of aromatic ring (128) of the epoxy resin, and at 913 and 828cm^{-1} indicate the presence of epoxy groups on uncured epoxy system of DGEBA (128, 164-166, 168).

The results of resins viscosity, flexural strength, and flexural modulus are summarized in Table 25, showing their averages, standard deviations, and coefficients of variation, as well as the ratios of resins *E2* and *E3* to *E1*.

The viscosity at RT as a function of time of the uncured mix-resins is presented in Figure 44, where a strip of the first fifteen minutes is highlighted (time required to infiltrate all batches of specimens). The average viscosities for this period are: 289.38, 238.04, and 980.74 mPa.s for *E1, E2* y *E3*, respectively. This result shows that resin *E2* is almost 18% less viscous and *E3* is 240% more viscous than the reference resin *E1* (see Table 25). These small values in standard deviations and coefficient of variations (CV) mean that resins have a stable viscosity for the required time (less than first 15 minutes). This would allow an adequate time for an infiltration process.

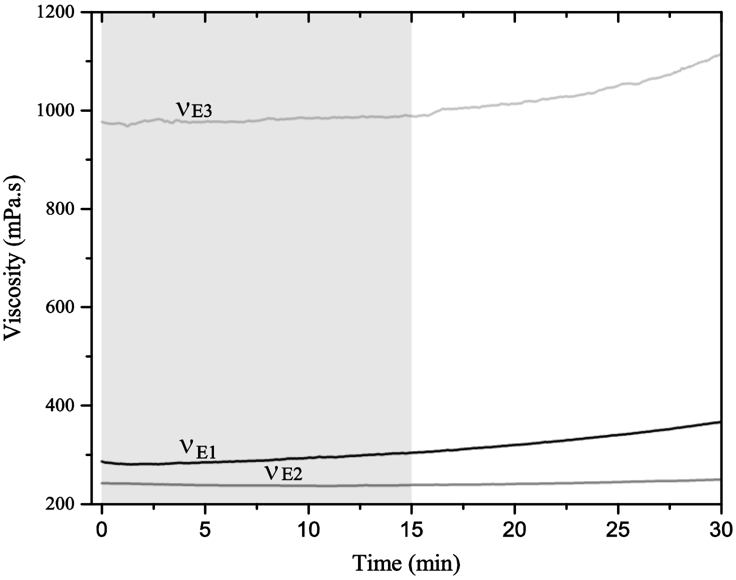

Figure 44. Viscosity "*ν*" at RT as a function of time of uncured mixed-resins *E1, E2* and *E3*

The highest flexural strength was obtained with *E1* resin (112.38 MPa), which is 6% higher than *E2* and 45% than *E3* (see Table 25 and Figure 50), while for flexural modulus, *E3* resin exhibits the largest modulus (see Table 25 and Figure 51).

Table 25. Viscosity, flexural strength and flexural modulus of epoxy resins, average with standard deviation and coefficient of variation (%)

Type of resins	**Resin Viscosity, "ν" (mPa.s) at RT.**			**Max. Flex. Strength, "σ_{fM}" (MPa)**			**E-Flex. Modulus, "E_B" (GPa)**		
E1	289.38	±7.26	3%	112.38	±2.34	2%	3.01	±0.09	3%
E2	238.04	±1.54	1%	105.40	±5.26	5%	3.11	±0.07	2%
E3	980.74	±5.00	1%	61.68	±18.01	29%	3.42	±0.12	4%
E2 / E1	0.82			0.94			1.03		
E3 / E1	3.39			0.55			1.14		

Comparing these results with the manufacturer data sheets (with other cure conditions) (149, 150), resins *E2* and *E3* reached 84% and 56% of their claimed flexural strength, while for modulus was 93% and 122%. These results highlight that resin *E3* was the most affected in its flexural strength by the selected processing conditions.

The decrease in the resistance of *E3* resin might be due to small air bubbles trapped inside the flexural samples, which were more difficult to eliminate due to its higher viscosity, while the increase in the modulus, among other factors, could be a consequence of the fast cooling rate occurred after post-cure. According to the glassy state theory, there is an exponential relaxation of the process of a specific volume with time (169, 170), therefore, the increase in modulus is directly related to the decrease in free volume available for segmental mobility (171).

5.9.2 Characterization of the infiltrated 3DP samples

The *RP*, flexural strength and flexural modulus results of the infiltrated 3DP samples are summarized in Table 26, which shows the averages and standard deviations for full 9 combinations of resin type vs. thickness of the samples.

According to the Eq. (1), if $m_a \rightarrow m_b$ (masses of the 3DP samples before and after the infiltration) there is no significant infiltration, i.e. no pore reduction occurs (i.e., *RP* = 1). *RP* is higher than 1 when m_a is greater than m_b. In this context, Table 26 and Figure 45 show a *RP* reduction for each combination type of resin—thickness of the sample. In general, a higher pore reduction rate (more infiltration) occurred in *C1*=2.5 mm infiltrated models, being the higher value (1.56) reached in *YE3-C1*.

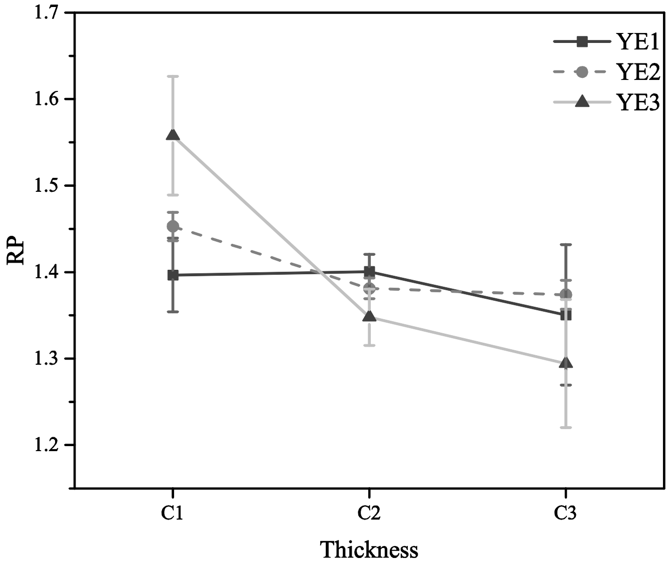

Figure 45. Pores reduction rate (*RP)* versus thickness of 3DP infiltrated samples

For the flexural strength, Figure 46 a), the highest and lowest strength was reached for 2.5 and 9.0 mm samples. Considering the same thickness, the maximum and minimum strength was achieved in samples infiltrated with resins *E2* and *E3*. This trend was kept for all thicknesses. Regarding the modulus Figure 46 b), the tendency is different for all thicknesses, with a higher dependency on the resin type instead of the thickness, where the parts infiltrated with resin *E2* have higher modulus, whereas the resin *E3* kept the lowest modulus.

Table 26. Experimental results of mass measurements, *RP*, σ_{fM}, and E_B of 3DP infiltrated samples (average and standard deviation for each condition)

Combination	**Code**	**m_b (g)**		**m_a (g)**		***RP***		**σ_{fM} (MPa)**		**E_B (GPa)**	
1	*YE1-C1*	1.85	±0.01	2.43	±0.04	1.40	±0.04	35.39	±0.68	6.63	±0.18
2	*YE2-C1*	1.85	±0.02	2.49	±0.02	1.45	±0.02	41.46	±1.00	7.15	±0.32
3	*YE3-C1*	1.88	±0.04	2.60	±0.08	1.56	±0.07	35.02	±1.74	5.58	±0.71
4	*YE1-C2*	6.51	±0.06	8.49	±0.03	1.40	±0.02	32.63	±4.67	5.62	±0.68
5	*YE2-C2*	6.59	±0.06	8.47	±0.05	1.38	±0.01	35.14	±1.96	6.82	±0.43
6	*YE3-C2*	6.63	±0.05	8.38	±0.10	1.35	±0.03	30.60	±1.61	5.91	±0.17
7	*YE1-C3*	23.11	±0.32	29.79	±1.22	1.35	±0.08	24.48	±2.51	7.24	±0.45
8	*YE2-C3*	22.78	±0.18	29.93	±0.17	1.37	±0.02	25.25	±0.85	7.85	±0.48
9	*YE3-C3*	22.90	±0.20	28.79	±1.21	1.29	±0.07	22.96	±1.95	6.03	±0.84

The factors, type of resin and thickness, as well as the obtained properties σ_{fM}, E_B, and RP, were all analysed through ANOVA, with a 95% confidence interval (95% ci), i.e. significance level of α = 0.05 (when P ≤ α, there are a significance effect on the response).

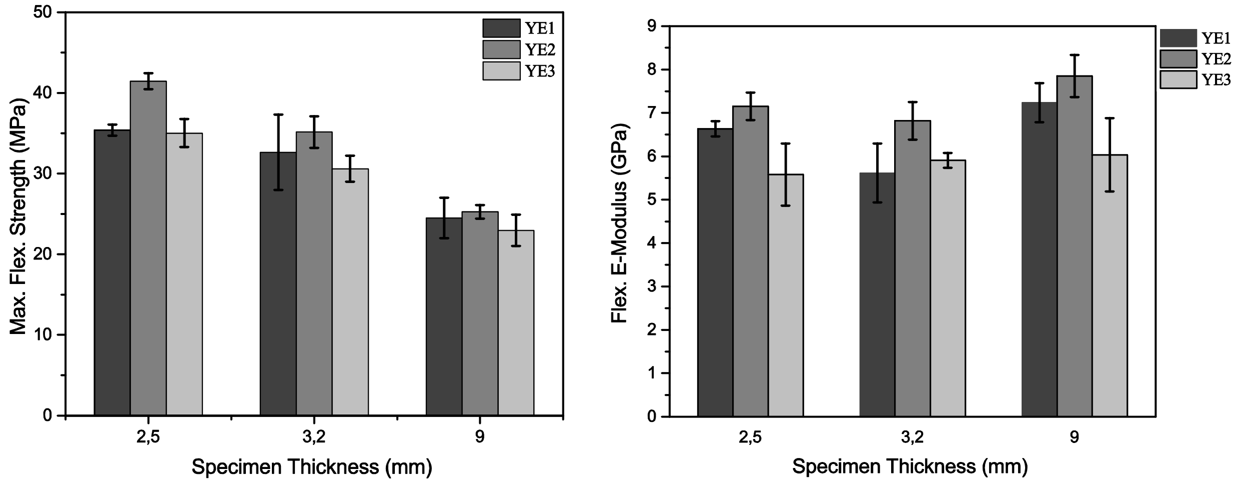

a) b)

Figure 46. Experimental results of; a) σ_{fM}, and b) E_B for 3DP infiltrated samples, (averages and standard deviations)

The analysis for *RP* (Table 27), shows the major contribution from "thickness of the sample" (43.46 %), followed by its interaction with the resin type (28.41%), both cases with p = 0.000. This result means that the thickness is a highly sensitive factor, while the resin type represents no significant contribution.

Table 27. ANOVA of porous reduction rate (*RP)* vs. resin and thickness of the sample (*ci* = 95%)

Source	**DF**	**Seq SS**	**Contribution**	**Adj SS**	**Adj MS**	**F-Value**	**P-Value**
Resin	2	0.00351	*1.14%	0.00	0.00	0.76	0.473
Thickness (mm)	2	0.13331	43.46%	0.13	0.07	28.99	0.000
Resin*thickness (mm)	4	0.08713	28.41%	0.09	0.02	9.47	0.000
Error	36	0.08278	26.99%	0.08	0.00		
Total	44	0.30673	100.00%				

*The contribution of the resin is not statistically significant, so its contribution should be added to the contribution of the error, the total will be 28.13%.

Analysing the main effect of the *RP* for resins (Figure 47 a)), it can be seen that there is no significant statistical differences among them. However, when the thickness of the samples is analysed, this figure shows the highest *RP* = 1.469 for 2.5 mm, making it significantly different relatively to 3.2 and 9.0 mm (with these last ones statistically equal to each other).

Focusing on the interaction plot, Figure 47 b) shows a superiority for *YE3-C1* with *RP* =1.56, followed by *YE2-C1* with *RP* =1.45, being *RP* lower in *C3* for all the infiltrants.

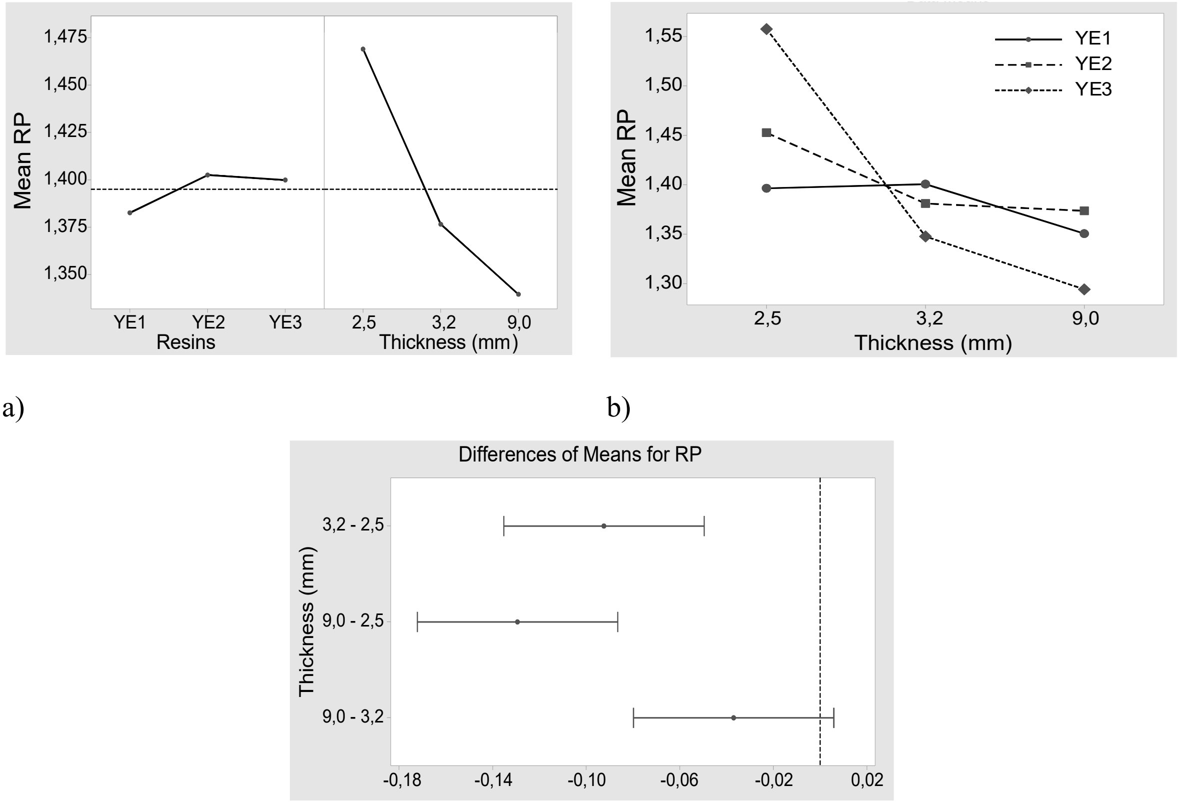

a) b)

c)

Figure 47. ANOVA analysis for *RP* by resin type and thickness of the samples; a) mean *RP* for resins and thickness, b) interaction of the two factors, and c) comparisons by Tukey pairwise, *ci=0.95*

Higher resistance was reached with upper *RP*, on one hand with the smaller thickness (2.5 mm), and on the other hand with the more viscous resin (*E3*). This viscosity effect is in opposition with Frascati (53) and Ipens (90, 106) results, at least for thinner thicknesses and a 980 mPa.s viscosity. This behaviour can be justified because in small thicknesses a high viscosity resin still penetrates the sample, but it is more difficult to spill after penetration, due to its greater surface tension, which allows retaining more resin inside the sample. Another factor that contributes to this phenomenon is the short pot life of the resin *E3*, giving less time to drain.

Concerning the flexural strength (σ_{fM}), Table 28 and Figure 48, the thickness factor is the one that shows a major contribution (78.08 %) and the resin shows a considerably minor influence (just 9.17%). In this case, these two factors are statistically significant (P= 0.000), again the thickness being the most influential factor.

Table 28. ANOVA of Flexural Strength "σ_{fM}" vs. resin and thickness of the sample (*ci = 95%*)

Source	DF	Seq SS	Contribution	Adj SS	Adj MS	F-Value	P-Value
Resin	2	155.07	9.17%	155.07	77.54	16.01	0.000
Thickness (mm)	2	1319.87	78.08%	1319.87	659.93	136.28	0.000
Resin*thickness (mm)	4	41.06	*2.43%	41.06	10.27	2.12	0.098
Error	36	174.33	10.31%	174.33	4.84		
Total	44	1690.34	100.00%				

*The contribution is not statistically significant, so its contribution should be added to the error, the total will be 12.74%.

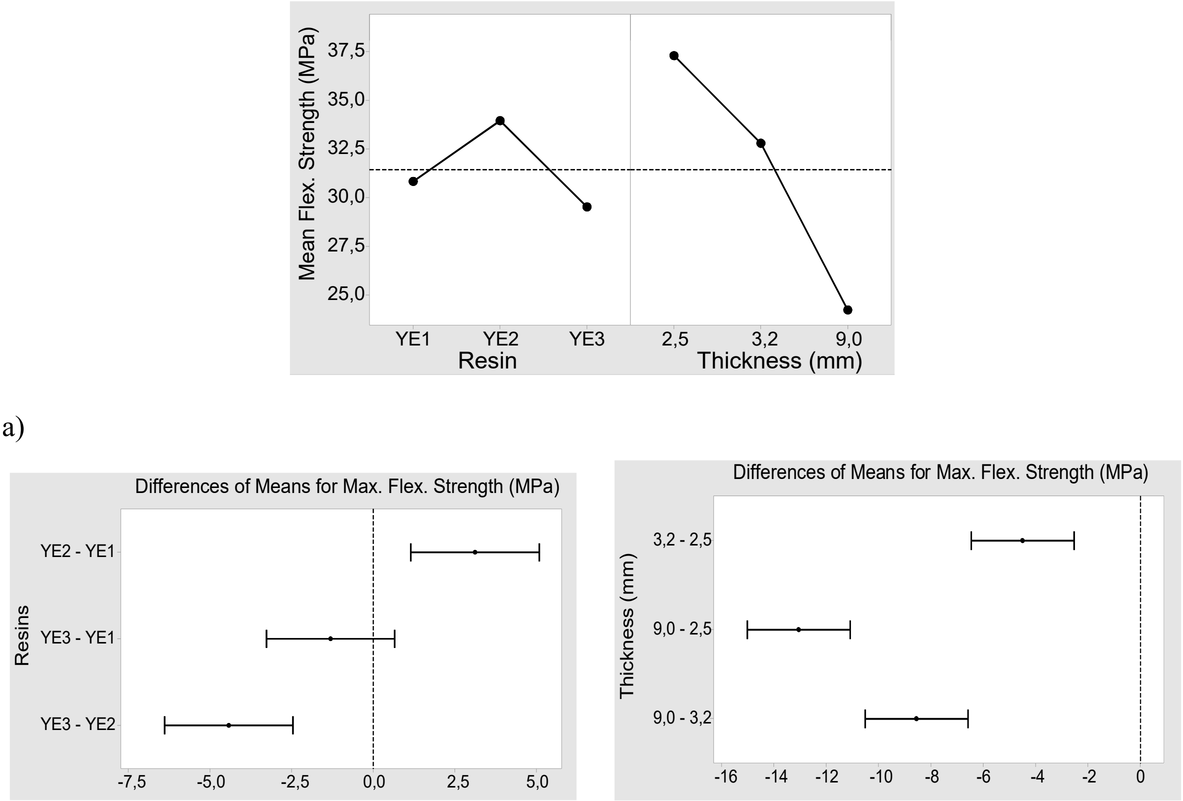

a)

b) c)

Figure 48. ANOVA analysis for σ_{fM} by resin type and thickness of the samples; a) means of main effects (MPa), b) and c) comparisons by Tukey pairwise, (*ci=0.95*)

The condition *YE2* with 33.95 MPa has the higher strength (Figure 48 a), however it is statistically different to *YE1* and *YE3*, with these ones being statistically equal to each other, as also confirmed in Figure 48 b).

YE2 is superior for all thicknesses, although *E2* resin itself does not have the greater resistance. This lower viscosity resin fills a large percentage of pores (see Figure 45), which is crucial for the thicker sample "*C3*" (see Table 26). This is consistent with the results published by Suwanprateeb et al. (87), indicating that the flexural strength and modulus increase with a decreasing percentage of soluble matter present in the infiltrant (lower viscosity resin).

Considering the analysis by thickness of the sample (Figure 48 a)), it can be seen that the highest strength was reached with 2.5 mm test samples, followed by 3.2 and 9.0 mm, respectively, verifying that all conditions are significantly different from each other (Figure 48 c)). This behaviour is similar to the one in Figure 47 a), so it can be considered that the flexural strength, as a function of the thickness, is proportional to the rate of pore reduction.

Finally, the ANOVA for the flexural modulus (Table 29), showed a larger contribution of the "resin type" (43.68%), followed by the thickness of the sample (18.66%). For both, P = 0.000 was obtained, and the interaction of the two factors is P = 0.026, which makes them statistically significant and with more balanced contributions than the above results.

Table 29. ANOVA of flexural Modulus "E_B" vs. resin and thickness of the sample (*ci = 95%*)

Source	**DF**	**Seq SS**	**Contribution**	**Adj SS**	**Adj MS**	**F-Value**	**P-Value**
Resin	2	15.446	43.68%	15.45	7.72	28.13	0.000
Thickness (mm)	2	6.598	18.66%	6.60	3.30	12.02	0.000
Resin*thickness (mm)	4	3.438	9.72%	3.44	0.86	3.13	0.026
Error	36	9.883	27.95%	9.88	0.27		
Total	44	35.365	100.00%				

The highest modulus, considering the type of infiltrant, was obtained in the 3DP samples *YE2* (7.27 GPa), as shown in Figure 49 a) and c), while for thickness, was 7.04 GPa, obtained with 9.0 mm (Figure 49 a) and d)). Figure 49 b) re-confirmed again that *YE2* specimens have the highest modulus for all the thicknesses, and within these specimens, the 9.0 mm ones reached the maximum value of 7.78 GPa.

Figure 49 shows a very interesting result; for thicknesses greater than 3.2mm (more porosity), the modulus increases (more brittle samples). This result is consistent with what was reported by Biswas (172) who claims that the flexural modulus of plaster materials exhibits a linear relationship with porosity.

This experimental work allowed to conclude that the thickness of the samples has a significant influence on the flexural strength (78.08%), while the resin has a higher impact on the modulus (43.68%) and, to a lesser extent, on the thickness of the sample (18.66%). Therefore, the following part will analyse this subject more deeply.

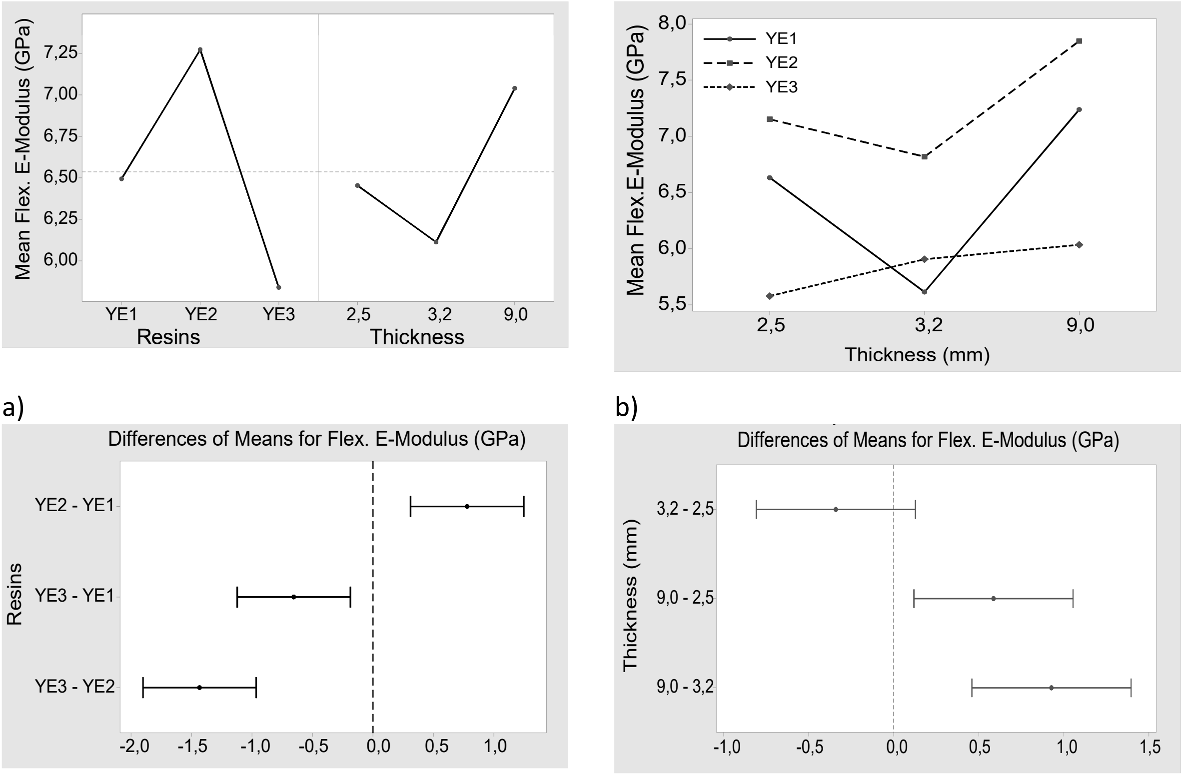

a) b)

c) d)

Figure 49. ANOVA analysis for E_B by resin type and thickness of the samples; a) means of main effects (GPa), b) their interaction, c) and d) comparisons by Tukey pairwise, (*ci* =0.95)

Figure 50 and Table 30 compares the strength of the infiltrated samples and the resins. *E3* resin, although less resistant (55% of *E1* – reference resin) and more viscous (240% of *E1*), is the one that generates a greater gain (ratio) in terms of transfer of its flexural strength to the post-infiltrated printed parts (from 0.37 to 0.57, according to last column in bold). The flexural strength of green 3DP plaster parts (no infiltrated) is so low, around to3 MPa (96), that their effect can be considered negligible in this analysis (116).

Considering the above results, it seems that to reach high flexural strengths in infiltrated 3DP models, it is advisable to use high strength infiltrants, however their effect can be attenuated due to the thickness and infiltration conditions.

For thicknesses greater than 3.2 mm, and in order to penetrate the inner pores, low viscosity resins are advisable, however, for smaller thicknesses, infiltrants with higher viscosity would be more convenient, to avoid the post-infiltration spillover from the infiltrated 3DP sample.

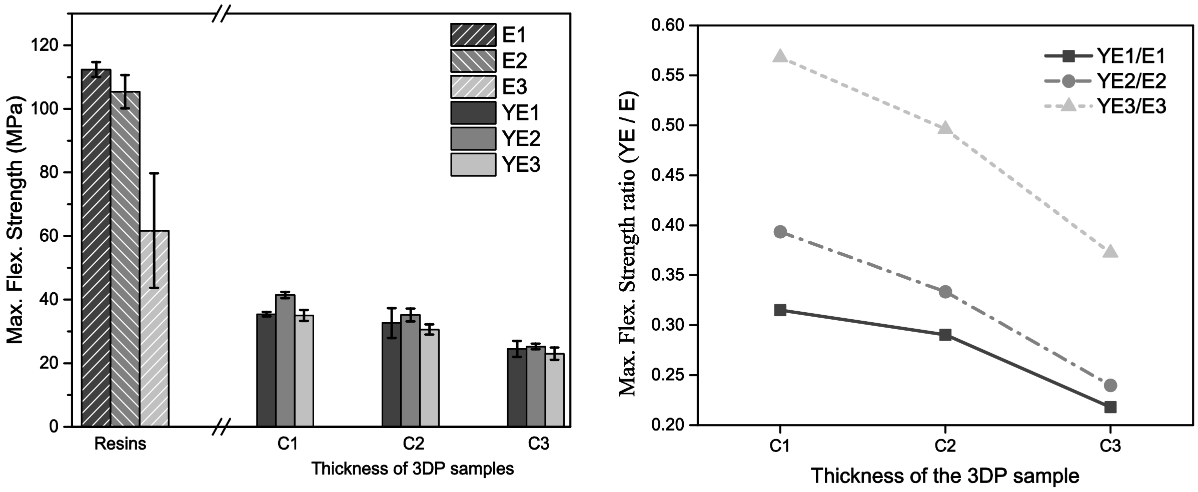

a) b)

Figure 50. a) Flexural Strength of infiltrated samples and resins, and b) their ratios

Figure 51 a) and Table 30 compare the flexural modulus of the resins and the infiltrated samples, with resin *E1* having the smallest value, slightly surpassed by *E2* and *E3*. In relation to the infiltrated samples, the same pattern is discernible for each thickness, having *YE3* the smallest modulus and *YE2* the highest.

Comparing the ratios (3DP samples / resins) of modulus (Figure 51 b) and Table 30), it is possible to understand that resin *E2* promotes the highest ratios from 2.30 to 2.53 (although is not the resin with best modulus). On the contrary, the *E3* resin, with the largest modulus has the lowest ratio, from 1.63 to 1.76.

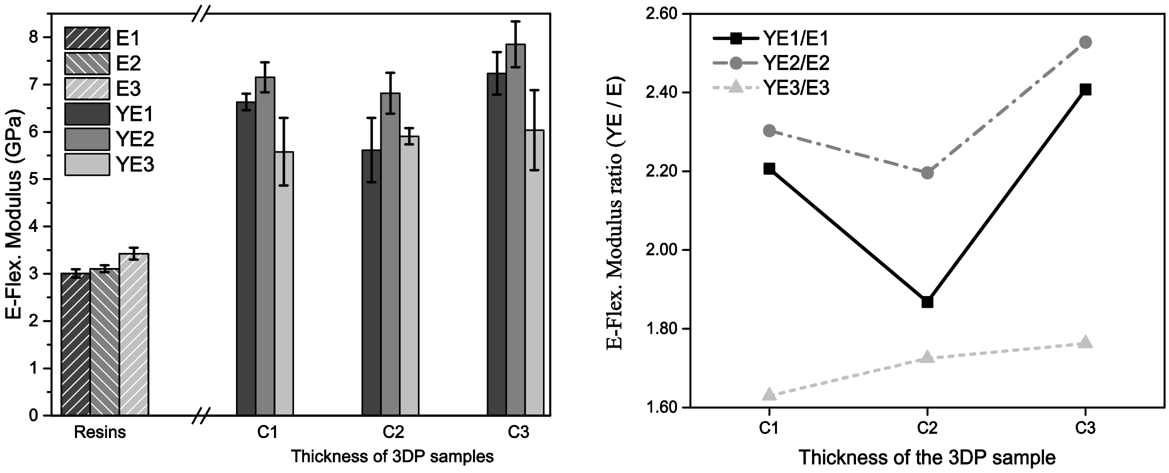

a) b)

Figure 51. a) Flexural modulus of infiltrated samples and resins, and b) their ratios

Table 30. Ratios (3DP models over resins) of flexural strength and flexural E-modulus

3DP Thickness (mm)	**Flexural strength ratios**			**Flex. E-modulus ratios**		
	YE1 / E1	*YE2 / E2*	*YE3 / E3*	*YE1 / E1*	*YE2 / E2*	*YE3 / E3*
2.5	0.32	0.39	**0.57**	2.21	**2.30**	1.63
3.2	0.29	0.33	**0.50**	1.87	**2.20**	1.73
9.0	0.21	0.24	**0.37**	2.41	**2.53**	1.76

5.10 Conclusions

Infiltration of 3DP models, obtained by binder jetting, is a requirement to manufacture prototypes able to be handled. These models can have different purposes, and for some of them, the mechanical resistance that they can withstand is very important.

At the first stage, the present chapter studied potential infiltrants characteristics. Later, different studies were reviewed where materials not devoted to infiltration of 3DP models were used, and finally four potential infiltrants were selected to characterize their thermo-mechanical properties, and compared with other potential infiltrants.

The mechanical characteristics and costs analysed in this stage suggests the selection of resins $E2$ and $E3$ to extend their behaviours as infiltrants of 3DP models, keeping the $E1$ resin as reference. The U-resin was discarded due to its low mechanical resistance, low T_g and high cost.

At the second stage, a case study was proposed to analyse the degree of influence of three types of epoxy resin (infiltrant) on the mechanical properties of 3DP models with three different thicknesses.

All 3DP models were infiltrated by simple full immersion with epoxy resins with similar molecular structure and slight differences in their catalysts. Resin *E1*, of low viscosity, was selected because it is the one indicated by 3DP suppliers. The other two resins are common ones for resin transfer moulding, have a lower price and show two different kinds of viscosities.

Resins *E1* and *E2* have the highest bending strength (112 and 105 MPa, respectively), while *E3* resin displaying higher viscosity, has the lowest flexural strength (62 MPa).

For the 3DP infiltrated models, the thickness has the most significant effect on the flexural strength. The higher resistance was reached with 2.5 and 3.2 mm, which is directly related to the amount of infiltrant absorbed (measured by the pore reduction rate, RP).

The type of resin had a greater effect than the thickness on the flexural modulus. The higher modulus was reached with the less viscous resin (*E2*), and within these, the 9.0 mm specimens were the ones with highest values, which made them the most brittle pieces.

In general, regarding the bending properties of the 3DP models, *E2* resin showed characteristics slightly higher than the *E1* resin (referential), while *E3* (least strength resin), revealed to be the most efficient resin in transferring its properties to the 3DP models. Therefore, these results suggest that it is feasible to use non devoted resins to successfully infiltrate 3DP parts.

In order to obtain the best mechanical properties, one must aim to increase the amount of resin retained in the part. For this, and for high thicknesses (greater than 3.2 mm), it is recommended to use low viscosity resins, while for thin thicknesses (less than or equal to 3.2 mm), resins of moderate viscosity are the most indicated.

For any models thicknesses, infiltrants with pot life close to the infiltration time are advisable to avoid post-drainage of the infiltrated resin, and to keep the resin into the model while it polymerizes.

Another option to increase the amount of infiltrant absorbed by the 3DP model, could be the improvement of the infiltration process, through its parameters, such as temperature or infiltration pressure, or optimizing the cure conditions, among others.

The resin $E3$, presented a good performance in the 3DP infiltrated parts, in addition to its excellent UV resistance. For such, this could be an attractive option to explore by improving its conditions of cure and viscosity with the use of simple resources such as a cure oven.

III. Improvement of the cure of the epoxy infiltrant (*E3*)

Epoxy systems are some of the thermosetting polymeric materials widely used as an infiltrants for plaster-based 3DP parts, woods or other material that need an increase in its strength and seal its porous structure (97). Nonetheless, in order to be attractive the infiltration process of 3DP models, it must be done in a short time without affecting its structural strength.

The commonly adopted practice, which involves the use of materials exclusively dedicated to the infiltration of 3DP plaster parts, an inadequate selection of another alternative infiltrant of infiltration process, is an expensive, time demanding and, therefore, unattractive process. For this reason, it is preferable to characterize the kinetics of the infiltrant reaction to enable model predictions and eventually optimize the process with the help of experimental tests or numerical simulation methods (98).

The post-cure process of epoxy resins involves the combination of at least three variables that can influence the final properties of the printed parts. These factors are:

- cure time;
- cure temperature and;
- heat and cooling rates.

Regarding the specimens of un-filled epoxy bisfenol-A- apiclorhidrina systems, it was possible to identify the influence of these factors in the final mechanical properties in decreasing order: cure temperature, cure time and finally the heating and cooling rates of cure (104). However, this can vary for other types of resins.

Additionally, the analysis of the factor “conditioning time before the corresponding test - *CT*” has been proposed. For thermosetting polymers, this factor consumes a considerable amount of time (161), which could be significant when reaching the final strength of a cured resin specimen.

Since the reaction mechanism (cure) can significantly vary between different resin systems it is necessary to know each cure process. Their properties are very sensitive to the conversion of the crosslinking reaction, i.e. the degree of curing. Thermo-mechanical and chemical properties vary strongly with the degree of curing (173). The isothermal curing reaction of an epoxy resin is complex, including gelation and vitrification, producing important changes in the macroscopic physical properties of the reacting system (174). This transformation takes place when the glass transition temperature (T_g) becomes equal to the curing temperature (T_c) (99) .

The DSC curve for an unreacted epoxy system shows an exothermic peak, which is related to the heat release due to the epoxy curing reaction. The area under this curve is related to the amount on unreacted reactants, and it is the total reaction heat or total enthalpy of reaction (Δh_{total}). As the curing progresses, the amplitude of the peak decreases and its area $A(t, T)$, changes. The ratio [1-$(\Delta h_{total}/A(t, T))$] is the degree of cure (α). When the degree of cure reaches a value of 1 (or 100%) it refers to a fully cured epoxy (173, 175, 176). The cure degree (α) is directly proportional to the released heat or enthalpy (97, 173, 177).

The time-temperature-transformation (TTT) isothermal diagram cure for epoxy systems is based on phenomenological changes that take place during cure, such as gelation and vitrification. This diagram, depicted in Figure 52, can be a very useful tool for analysing and designing the curing processes of epoxy systems (99).

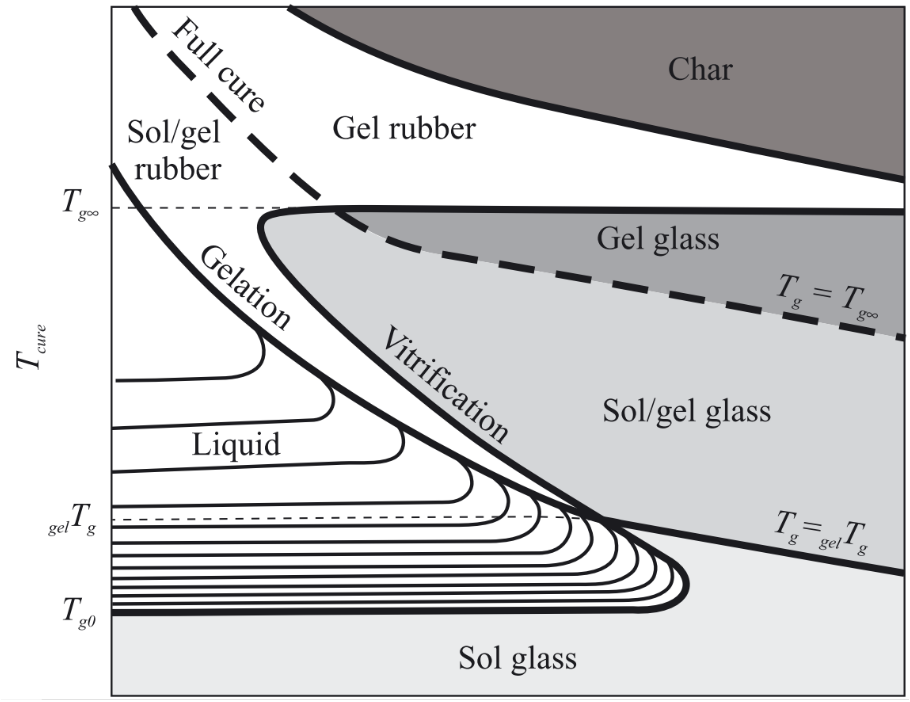

Figure 52. Generalized time-temperature-transformation (TTT) isothermal cure diagram, (adapted from (99))

TTT diagrams and suggestions from resin manufacturers (178), indicate that higher temperatures produce a more complete reaction with a greater degree of cross-linking than lower temperatures. Alternatively, increasing the length of time for a lower temperature cure does not always yield the same degree of crosslinking as curing at a higher temperature (178).

The final cure temperature should be reached slowly and gradually (heating and cooling rates of cure). This often provides a good balance between lower stress, as the cross-linked structure is locked in slower, and higher overall level of cross-linking as higher temperatures are ultimate achieved (178). Faster, high temperature cures enable chemical cross-links to form faster and more completely.

Regarding to the conditioning prior to mechanical testing for polymer materials, this has to be carried out for sufficient time for the material to reach equilibrium. The plastics standard requires not less than 4 hours for temperature alone and not less than 88 hours for temperature and humidity in atmospheric condition (161, 179). The ASTM D618 specifies only 40 hours for samples less than 7 mm thick. It also lists five other conditioning procedures including drying in an oven (180). However, a conditioning time from 40 to 88 h, could make the cure period a time-consuming process (161).

The question in practice is how important are temperature and humidity variations, and their effect will be dependent on both material and the room conditions. Test methods will specify the room conditions to be used, commonly 23 ± 2 °C and 50 ± 10 % relative humidity (RH) (161). For most materials, changes in room conditions over the range 20 to 25 °C are unlikely to be significant, the largest exception being if the material's glass transition (T_g) is around ambient.

This stage of the chapter proposes to increase the flexural strength, while maintaining the E-flexural modulus of the epoxy resin EC131LV-W342, considering the results obtained in part II, by optimizing its cure. The variables that will be analysed concerning the resin cure are the time and temperature of the cure, the rate of heating and cooling, and the conditioning time of the sample prior to the bending test.

5.11 Materials and Methods:

A two-component epoxy resin EC131LV / W342 (Elantas, Italy) was used for cure improvement (150), named as $E3$ for the purpose of this study. All the cure tests took place in a forced air convection oven SLW53 STD (PolEko, Poland).

Focusing on the most influential cure variables on the final mechanical properties of the epoxy resin (cure time-temperature) (104, 173, 178), while also intending to reduce the number of test, the heat and cooling rate variables, additionally the conditioning time before test variable were previously selected (as detailed in Appendix 6).The selected conditions for these variables offered the highest flexural strength (σ_{fM}), with a low E-flexural modulus (E_B), and shorter curing time, as presented in Table 31.

Table 31. Pre-selected variables for the analysis of curing time and temperature conditions

Cure variables	**Value**
heating rate (°C. h^{-1})	380
cooling rate (°C. h^{-1})	W_o
conditioning time (h)	24

The heating and cooling rates, called hereafter ramps, refer to the speed of heating and cooling, measured in °C. h^{-1}, allowing to reach and down to the isothermal platform of cure with respect to the room temperature. Some studies claim that the cure cycle temperature ramp can strongly influence the temperature and degree of cure gradients developed during the cure (181).

After the detailed analysis in Appendix 6, a heating cooling rate of 380 °C. h^{-1} was selected, and to allow the cured sample to cool down, it was decide not to use a cooling ramp, (naming it without ramp$-W_o$). W_o implies that, after its post-cure in the oven, the resin sample would be removed directly to cool down at room temperature. All ramps analysed in Appendix 6 allow to reach the isothermal level of cure in a shorter time than that suggested by the resin manufacturer (10 °C. h^{-1}) (150). These ramps becomes more influential as the thickness of the sample increases (160).

The selected conditioning time before bending test, (called hereafter, condition time$-CT$) was 24 hours. Additional details of these results are listed in Appendix 6 Heating and cooling rates (ramps) and conditioning time before bending test for resin cure improvement EC131LV-W342 (E3).

For the cure time and temperature, five levels were pre-established for each time-temperature combination (Table 32), based on the manufacturer's suggestion (150) of 60ºC for 15 hours , given it a level 5 ($N5$), this being the longest cure time considered. Maintaining an inverse relationship between these factors (104, 150), the time of cure was reduced, considering 80 ºC between these and being the glass transition temperature (T_g) suggested by the manufacturer for a cure period of 8 hours, assigning it as level 4 ($N4$). As a maximum temperature, a curing temperature of 140 ºC was selected for 1 hour, assigning it as level 1 ($N1$). This consideration was based on the onset point of the degradation found for the resin, which was considered at 140 ºC, as will be later shown (see Figure 53). These cure time-temperature levels are collected in Table 32.

Table 32. levels of cure time-temperatures proposed to study

Cure variable		**Level (N)**				
		1	**2**	**3**	**4**	**5**
Cure time	(h)	1	2	4	8	15
Cure temperature	(ºC)	140	120	100	80	60

A factorial or Taguchi design experimental (DoE) are not adequate for this purpose, but instead a pairwise analyses of these variables to maintain their pre-defined inverse relationship. Table 33 shows the five analysed time-temperature levels (N), which include the heating rate of 380 $℃.h^{-1}$ and cooling rate without ramp (W_o) according to the pre-selected ramps analysed in Appendix 6. The total time of the cure process is presented in the last column.

Table 33. Levels of the control variables in post-cure conditions

Level (N)	**Cure temperature** (ºC)	**Isothermal cure time**	**Heating time***	**Cooling time** (h)	**Total cure time**
1	140	1	0.3	0	1.3
2	120	2	0.25	0	2.3
3	100	4	0.20	0	4.2
4	80	8	0.15	0	8.2
5	60	15	0.10	0	15.1

*heating rate of 380 $℃.h^{-1}$, from RT (~23 ± 2 ºC) to level $\boldsymbol{N}$

5.11.1 Experimental Techniques

The thermogravimetric analysis (TGA) was performed in order to verify the maximum temperature at which it is pertinent to cure the resin, without affecting its properties, that is, without degrading it. The mass of uncured resin sample was evaluated as a function of temperature variation in a TA-SDT Q600 equipment (TA, USA). A heat ramp of 20 °C.min-^{1} up to 450 °C equilibrated from 30ºC was employed, with purge flow in the sample of 50 ml.min^{-1}, first with nitrogen, to simulate the real cure environment of the samples, and later with oxygen.

Samples of 16 to 24 mg of cured and uncured epoxy resin $E3$ were submitted to the non-isothermal differential scanning calorimetry analysis (DSC) to measure the reaction heat, the glass transition temperature (T_g), and the degree of cure. Samples were cured according to the time-temperature levels described in Table 32. Two heating and cooling runs were performed for each sample in a DSC Q20 equipment (TA instruments, USA) with a heating rate of 10°C.min $^{-1}$ from 30 ºC to 200 ºC, in an atmosphere of nitrogen, with a flow of 50 ml.min^{-1}.

Three-point bending tests were carried out at RT, according to ASTM D790, in a Multitest 2.5-dV testing machine with a 2.5 kN load cell (Mecmesin, UK). Five samples of 127.5 x 12 x 3.2 mm of each cure condition were tested. The samples were supported by two rods of 5 mm radius with a span of 50 mm, and loaded by an upper rod of 5 mm radius. The crosshead load speed was set at 2 mm.min^{-1}.

5.12 Results and discussions

5.12.1 Thermogravimetric analysis of resin $E3$

Thermogravimetric curves, resulting from analyses carried out both in atmosphere with nitrogen and with oxygen, are presented in Figure 53. It is possible to observe that, the loss of mass becomes significant from 353ºC on (about 5% of its original mass), when is tested in inert atmosphere, and when the end-of-test temperature (450ºC) is reached, it has lost almost 100% of its initial mass.

The result of a second test in oxidizing atmosphere with oxygen as the entraining gas presented itself similar to the previous one (Figure 53). The loss mass becomes significant from 344ºC on, a value slightly lower than the one in the previous case. Likewise, at the end of the test (450ºC) all its mass was consumed. This second test was taken because its simulates the post-cure process that is commonly carried out in air circulation ovens (oxidizing atmosphere).

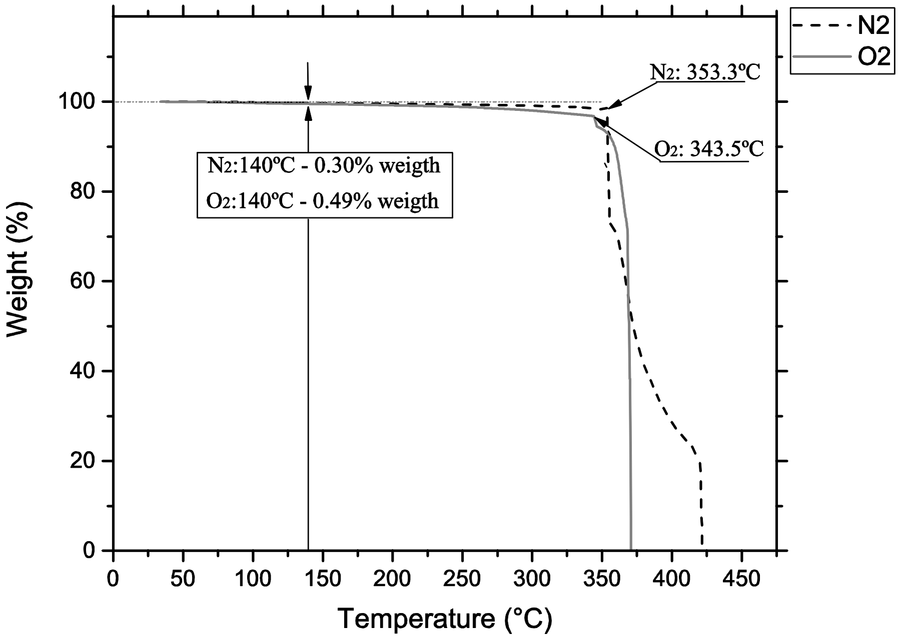

Figure 53. Thermogravimetry of uncured resin $E3$ under inert (N_2) and oxidizing (O_2) atmospheres

In the same Figure 53, it is visible that at 140ºC, the mass consumed at this temperature for both cases is 0.30% and 0.49% in nitrogen and oxygen atmosphere respectively. From these results, it is possible to admit that the post-cure process can be carried out at a temperature higher than 60ºC for 10 to 15 hours as the suppliers suggests (150). In this case, it is feasible to cure at 140ºC, hence classified as level 1 ($N1$).

5.12.2 Differential Scanning Calorimetry of resin $E3$

Tests were carried out in six samples to evaluate the different post-cure treatments, in accordance to Table 32. Typical DSC thermograms for the first scan are shown in Figure 54

and collected in Table 34, from non-isothermal experiments using different curing conditions ($N1, N2, .. N5$).

Common DSC tests involve measurements of the heat flow as a function of time, and the total enthalpy of reaction can be obtained by integration of the heat flow over the entire exothermic peak. In Figure 55, the area under the specific heat flow curve $q(t)$ corresponds to the specific reaction enthalpy $h(t)$:

$$h(t) = \int_{t_0}^{t} q(t).dt. \tag{8}$$

In equation (9), t_0 denotes the time at which reaction starts. Together with the specific total heat of reaction enthalpy Δh_{total}, the temporal evolution of the cure degree α(t), is given by:

$$\alpha(\mathrm{t}) = \frac{1}{\Delta h}.h(t) = \frac{1}{\Delta h}\int_{t_0}^{t} q(t).dt \tag{10}$$

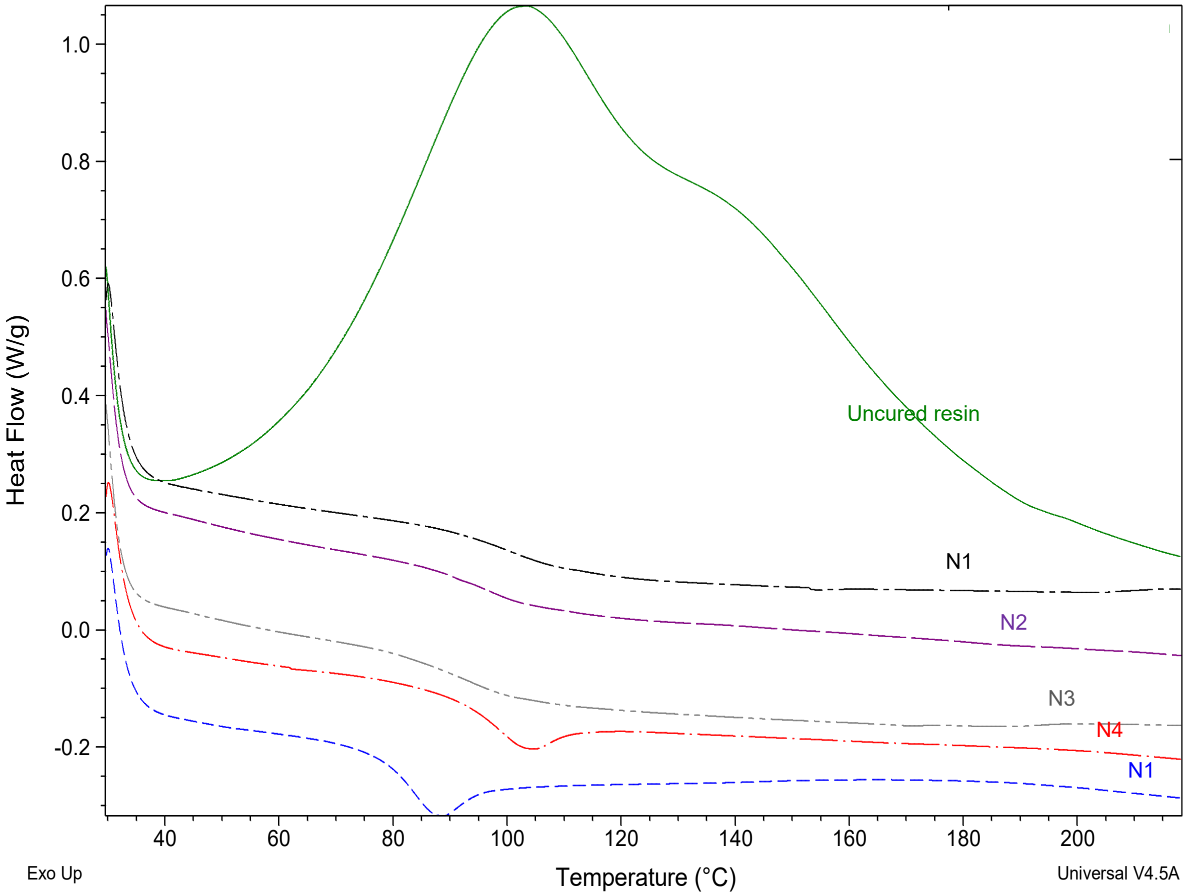

Figure 54. DSC curves (first scan) of $E3$ resin, uncured and submitted to different cure treatments

The total heat reaction does not depend on the level of cure, in this case for the uncured resin is Δh_{total} = 345.1 J/g with its onset point at 62.2ºC. The heat reaction associated to level $N2$ of 2.6 J/g was the lowest, with its onset point at 85.0ºC, representing a higher crosslink density and the higher cure degree (99.2%). While the heat reaction associated to level of cure $N4$ of 10.29 J/g was the highest, with its onset point at 84.8ºC, representing a lower crosslink density and cure degree (97.0%).

However, the $N3$ level with a relatively low cure-time condition of just 4 hours at 100ºC, reached one of the most highest degrees of cure (98.9%), making it an interesting option of almost complete cure.

Table 34. Exothermic peak temperatures and energy released by the samples during post-cure treatments.

	Uncured resin.	***N1***	***N2***	***N3***	***N4***	***N5***
Onset temperature (ºC)	62.2	87.3	85.0	78.6	84.8	74.3
Heat flow (J/g)	345.1	4.2	2.6	3.7	10.29	9.6
Cure degree (%)		98.8	99.2	98.9	97.0	97.2

The second scan results of the DSC tests are presented in Table 35 and Figure 55, where the values of T_g are collected for the different cure levels. It is possible to verify the existence of two groups: the first, formed by the levels $N3$, $N4$ y $N5$ shows little variation in the values of the T_g, staying around 101ºC. Regarding the group formed by levels $N2$ y $N1$ a marked variation of T_g of 103.8 and 108.1ºC respectively, is observed. This marked difference between the two groups of levels seems to indicate that the group of levels $N3$, $N4$ y $N5$, with a lower T_g (and in turn more stable) in the post-cure, would also provide a greater stability to the final properties of the cure resin.

Table 35. Glass transition temperatures obtained with post-cure treatments.

Condition	**N1**	**N2**	**N3**	**N4**	**N5**
T_g (ºC)	108.1	103.8	101.4	101.9	100.5

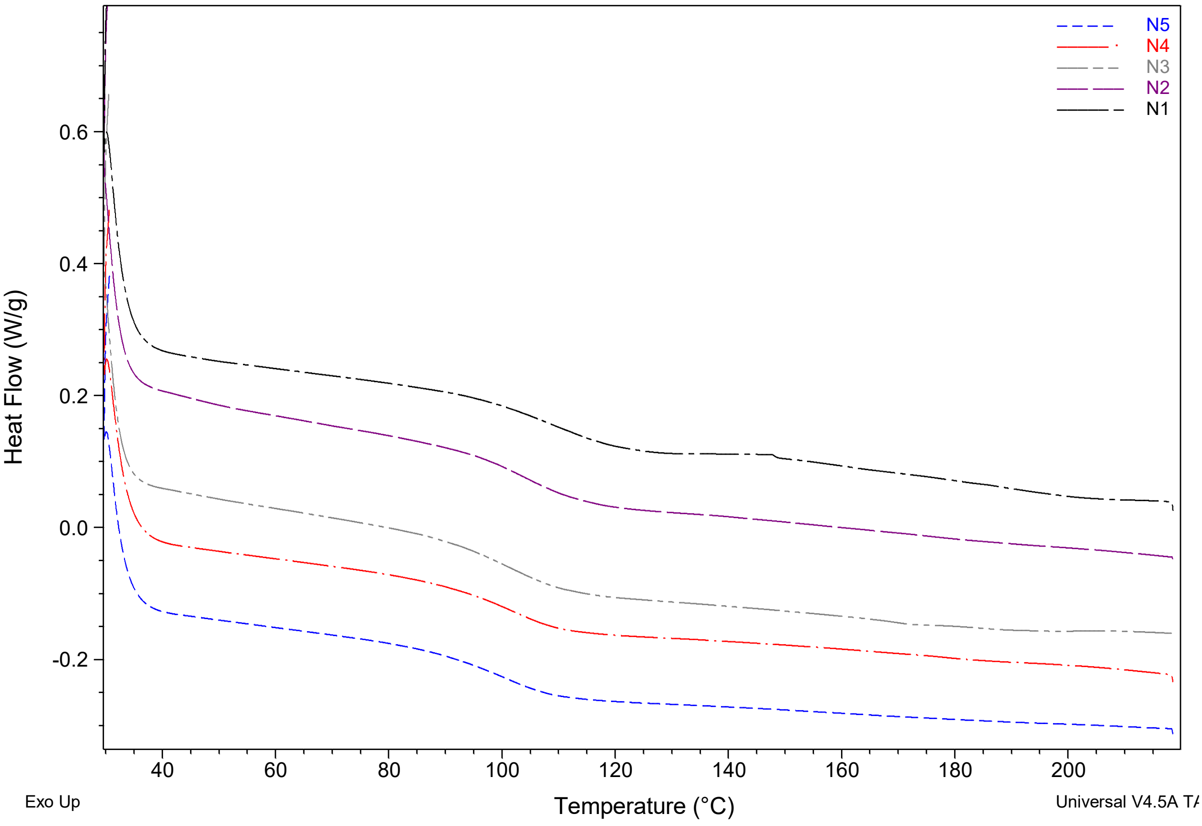

Figure 55. DSC curves (second scan) of $E3$ resin of uncured and subjected to different cure treatments

5.12.3 Post-cure treatment of $E3$ resin.

The average values and their standard deviations from flexural strength σ_{fM} and flexural E-modulus E_B with the corresponding curing process total times for each time-temperature level are shown in Table 36.

Table 36. Average and standard deviation of flexural strength (σ_{fM}) and flexural E-modulus (E_B) for different cure levels of resin $E3$

Level	**Cure temperature (ºC)**	**Isothermal cure time**	**Heat and cooling time***	**Total cure time**	**σ_{fM} (MPa)**		**E_B (GPa)**	
			(h)					
1	140	1	0:18	1.3	130.69	± 2.12	2.73	±0.23
2	120	2	0:15	2.3	141.45	± 0.77	2.89	±0.15
3	100	4	0:12	4.2	149.30	± 1.06	3.00	±0.05
4	80	8	0:09	8.2	151.98	± 3.12	2.99	±0.16
5	60	15	0:06	15.1	151.52	± 2.91	3.09	0.08

**heating rate of 380* $°C.h^{-1}$*, and cooling rate at room temperature after post-cure*

Concerning flexural strength (σ_{fM}), two groups with marked differences in their resistance values are also perceived, as in the previous case, as can be seen in Figure 56 a). The first group with levels $N3$, $N4$ and $N5$ show the highest resistance with little variation in their value (between 149.3 and 151.98 MPa). The group formed by levels $N1$y $N2$ show lower values of σ_{fM} (130.69 and 141.45 MPa). However, for all the levels analysed, their resistance is higher than 115 MPa, value indicated by the supplier, which would be achieved with a cure time of 24 hours plus a post-cure of 15 hours at 60 ºC (150).

Level $N3$ stands out as one with the highest resistance (σ_{fM}), a lower standard deviation 149.4 ±1.06 MPa (good stability) and a reasonable cure time of 4.2 hours. The $N4$ and $N5$ levels are cure options that require longer times (from 8.2 to 15.1 hours). Moreover, due to their higher standard deviations, they did not present significant differences in their resistance - σ_{fM} with respect to the $N3$ level.

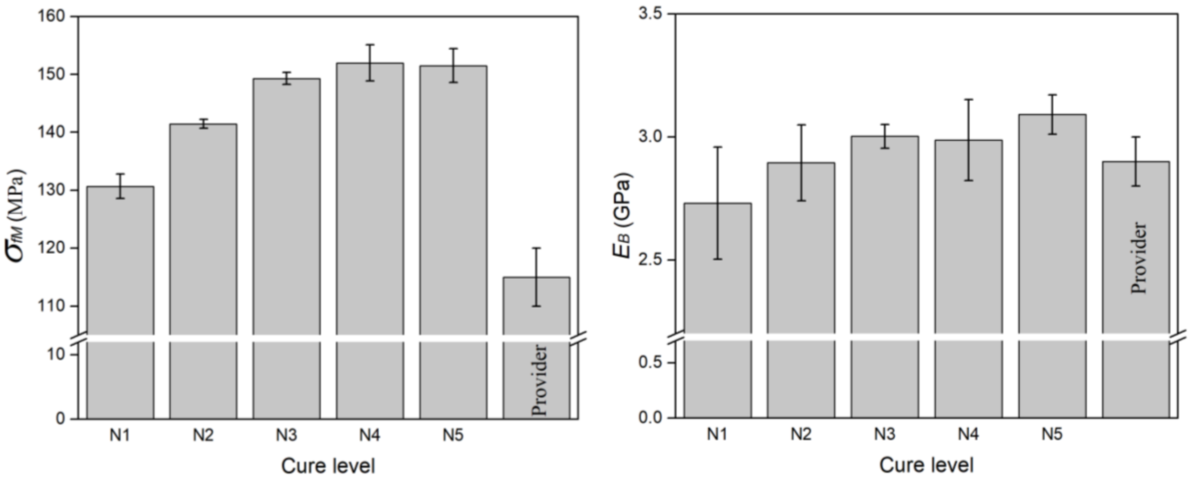

a) b)

Figure 56. a) flexural strength (σ_{fM}) and b) flexural E-modulus (E_B) for different cure levels of resin $E3$

Concerning flexural E-modulus (E_B), the values do not present significant differences in general. However, the $N1$ level is set apart by having the largest standard deviation, which could suggests a high cure temperature (140 ºC), resulting in an instability in the stiffness of the cured resin. Level $N3$ stands out for having the smallest standard deviation (3±0.05 GPa). This flexural E-modulus value is in accordance to what is recommended by the supplier (2.9±0.1 GPa) (150).

As aforementioned, level $N3$ stands out due to their high resistance (σ_{fM}), and acceptable flexural E-modulus (E_B), in both cases with the least standard deviations. Additionally, this level of cure requires a total time of 4.2 hours. This cure-time and mechanical properties achieved in bending make it an advisable cure option for the infiltration process of 3DP models.

Table 38 shows the bending properties obtained after improving the $E3$ resin cure process, compared to the referential resin that was considered for this study (Strength Max - $E1$). Additionally, their curing time and temperatures are also indicated.

Table 37. Viscosity and bending properties of $E3$ resin compared to reference resin $E1$

Type of resins	**Viscosity**	**Flex. strength**	**Flex. modulus**	**Cure temp. max.**	**Cure time**
	mPa.s at RT	(MPa)	(GP)	(ºC)	(h)
E1	289.38	112.38	3.01	70.0	26.5
E3	980.74	149.3	3.00	100.0	4.0
E3 / E1	3.39	1.33	1.00	1.43	0.15

It is observed that the $E3$ resin exceeded by 33% the flexural strength, maintaining almost the same flexural modulus regarding the resin $E1$. The cure time was only 15%, that is 4 hours instead of 26.5 hours, and a 43% increase in temperature is required for its cure. Regarding the viscosity, $E3$ is 339% more viscous at room temperature.

5.13 Final considerations

Considering that the resin $E3$ will be the infiltrant of 3DP models, and once its proposed mechanical properties have been improved compared to those obtained in the previous study II (and collected in Table 25), it remains to consider the problem of its high viscosity (980.74 mPa.s at RT), which hindered penetration especially for 3DP models of large thicknesses.

To overcome this low penetration, an infiltration process could be foreseen at a temperature slightly higher than the room temperature, without the need to having huge resources, or to modify the infiltrant properties or printed model. Based on the previous results about viscosity analyses (Appendix 7) and thermomechanical behaviour (Figure 35 and Table 18) carried out at the resin $E3$, an infiltration temperature of 40ºC is suggested (heating both the infiltrant and the 3DP models).

According to the results shown in Figure 35 and Table 18, the $E3$ resin maintains a storage modulus of 2048 MPa at 40ºC, slightly lower than the $E1$ resin (2324 MPa). This difference is practically the same as that maintained at RT. Additionally, $E3$'s useful operating range temperature is 79.9ºC, well above 40ºC, which confirms its properties at this temperature.

Making use of experimental results obtained with the resin $E3$, namely resistance to bending with the improvement of its cure and viscosity by varying the infiltration temperature, we aimed to predict mathematically a flexural strength showed by a 3DP model with these new characteristics of the resin.

To develop such a theoretical model, the viscosity was important factor at first, since experimentally it was observed that the viscosity of $E3$ resin at 40ºC (v = 270.65 mPa.s) is similar to the viscosity of $E1$ at RT (v = 289.38 mPa.s). This similarity allowed the percentage of resistance transfer of the resin to 3DP models infiltrated with $E1$ (31.5% for 2.5 mm thickness models and 21.8% for 9.0 mm thickness model obtained in part II), were referred to as comparison factor to show the possible resistances that would be obtained in printed models infiltrated with $E3$, as shown in Table 38. This means that similar behaviours would be expected in their penetration with both resin $E1$ and resin $E3$.

Table 38. Analogy of σ_{fM} of infiltrated 3DP parts when they are infiltrated with resins *E1* at RT, and *E3* at 40ºC.

Infiltrant and infiltration conditions	**Viscosity, ν** (mPa.s)	**Resin flexural strength, σ_{fM}** (MPa)	**% of σ_{fM} transferred to 3DP** 2.5mm	9.0mm	**σ_{fM} of infiltrated 3DP parts (MPa)** 2.5mm	9.0mm
$E1$ at RT	289.38	112.38	31.5%	21.8%	35.39	24.48
$E3$ at 40ºC	270.65	149.3	***31.5%***	***21.8%***	***51.99***	***35.96***

The values in bold were obtained theoretically

Table 38 shows that in a 2.5 mm thick 3DP model, the $E1$ resin transferred 31.5 % of its flexural strength, achieving in the infiltrated model 35.39 MPa. In this same scenario, with the new conditions, the $E3$ resin with σ_{fM} of 149.3 MPa and v of 270.65 mPa.s, would possibly transfer the same 31.5% of its strength, and a 3DP model with 51.99 MPa. Keeping the same analogy, when infiltrating a 3DP model of 9.0 mm thickness with $E1$, which transferred 21.8 % of its strength, achieving 24.48 MPa in the 3DP model, the $E3$ resin with the same percentage of transfer, would reach 35.96 MPa for flexural strength in the infiltrated model.

Despite the thickness, the σ_{fM} of models infiltrated with the $E3$ resin would surpass that was achieved with the $E1$ resin in the previous study in part II and Table 38 by 68%.

Regarding the flexural modulus (E_B), as previously mentioned, given the new cure conditions for resin $E3$, it remained with the same 3.0 GPa as the reference resin $E1$, which is convenient to maintain a similar stiffness in the infiltrated 3DP model.

Another important contribution of this study was the reduction of the curing process time to just 4 hours (15% of the 26.5 hours required with $E1$), making it a competitive time process.

Previously reviewed studies were summarized in Table 39, which show the type of infiltrant, its viscosity and the maximum flexural strengths achieved when infiltrating 3DP models. In any study and thicknesses for infiltrated plaster-based 3DP models, the maximum value achieved does not exceed 20 MPa (53). Contrasting these studies to be obtained when infiltrating with the $E3$ resin (51.99 and 35.96 MPa for flexural strength), these models have considerably exceeded the resistance achieved in studies collected in Table 39, even for models printed with PMMA based-materials that reached a maximum flexural strength value of 26.6 MPa (137).

Table 39. Maximum flexural strength achieved in plaster-based 3DP parts with infiltrants of different viscosities

Infiltrant system	**Viscosity, ν** (mPa.s)	**Max. flexural strength of infiltrated 3DP parts** (MPa)
HTR-212 and Ad-Tech Epoxy EEL-335, epoxy resins, (53)	800-1000	12.00
Three Clear Coat and Ad-Tech CER-112, epoxy systems (53)	600	20.00
LOCTITE® EA 9483, epoxy resin, (53)	1000	7.42 (for tensile)
Z-Max, epoxy resin, (81)	120	9.27
Poly(ε-caprolactone) (PCL), (135, 136)	-	10.00
EPO-Tek 301, medical grade epoxy resin, (137)	100-200	26.60 (PMMA 3DP part)
Acrylate infiltrant, (86)	-	18.00
Polyurethane glue, (90, 106)	-	11.00
Z-Max, epoxy resin, (90, 106)	120	17.99

5.14 Conclusions

In order to transfer better bending mechanical properties to 3DP models, when infiltrated with short time periods processes, we proposed an improvement in the cure process of the two-component epoxy systems EC131LV / W342 ($E3$ resin). Specifically, it was suggested a reduction of its cure time, with an increase of the flexural strength (σ_{fM}) and a decrease of the E-flexural modulus (E_B) with respect to the reference resin $E1$, by selecting the variables involved in the cure process. These variables are cure time and temperature, heating and cooling rate, and conditioning time of the sample prior to the bending test.

Based on the thermogravimetric analysis, it was established as a maximum cure temperature 140ºC, without degrading the resin. For this temperature (maximum isothermal level of cure), heating and cooling ramps (R) were studied in order to obtain the shortest times possible. Similarly, the short conditioning time (CT) was analysed. The heating ramp of 380 °C. h^{-1}, without the need to use a cooling ramp (W_o) and the CT of 24 hours were variables that contributed to the best results. These heating and cooling rates need considerably less time than the one suggested by the supplier (150), at least for samples of 3.2 mm thickness.

Five levels of cure time-temperature were analysed, between 1 to 15 hours, and 140 to 60 ºC, respectively, together with the previously selected ramps and CT. Of all the analysed levels, the best results were found for the level $N3$, with values of 149.3 MPa of flexural strength and 3.0 GPa of E-flexural modulus, achieved in 4 hours at an isothermal cure temperature of 100 ºC.

The differential scanning calorimetry analysis confirmed an almost complete degree of cure for the $N3$ level , reaching 98.9 %, and a T_g of 101.4 ºC, value slightly higher than 92 ºC suggested by the supplier (150).

In summary, a cure degree of 98.9 % in resin samples of EC131LV / W342 ($E3$) with 3.2 mm thickness will be reached, when curing them at 100º C during 4 hours (level $N3$), with a heating rate of 380 $℃.h^{-1}$ and no need for a cooling rate. For these conditions, a flexural strength of 149.3 MPa and a flexural modulus of 3.0 GPa were obtained, in a total cure period of just 4.2 hours.

Regarding the resin $E1$ (referential), $E3$ exceeded by 33 % its flexural strength, maintaining the same flexural modulus with a cure time of just 4 hours (15 % of that required for $E1$).

We suggest, as a future work research, to perform the infiltration process by simple immersion at a temperature of around 40 ºC (slightly higher than room temperature). This would decrease the viscosity of the $E3$ infiltrant from 981 to 240 mPa.s, to verify its improvement in penetration, and therefore increase the mechanical strengths especially of thick thickness models (10 to 20 mm), as theoretically predicted in 5.13 (Final considerations - Table 38). Regarding thicknesses greater than 20 mm, one could choose to use vacuum infiltration, although this turns the process more expensive due to the required infrastructure.

Chapter 6. Conclusions and suggestions for future works

6.1 Conclusions

This chapter summarizes the contributions, conclusions and future works presented and discussed throughout this study.

In the present work, we proposed to expand and disseminate the knowledge about materials and infiltration processes of three-dimensional printed (3DP) parts by Binder Jetting (BJ) technology with plaster-based materials. This knowledge, available to all type of user, allows selecting and applying both infiltrants and infiltration processes that simplify and reduce the post-processing costs, making it more competitive in terms of time, resources and final mechanical characteristics.

Criteria for the use of materials as well as simple and efficient infiltration processes require an understanding of both printing and infiltration processes. Besides, for a more meticulous analysis of the infiltration materials and processes, it was necessary to eliminate factors influencing from the printing process, so it was required to analyse the printing materials, green 3DP parts and their printing parameters, which were subsequently kept constant in the following studies. Additionally, the evaluation of infiltration materials and methods suggested by the BJ technology manufacturer was required, selecting those that provide better mechanical properties to the printed models.

Regarding the characterization of printing materials, this work contributes to the dissemination of BJ technology by providing users with cutting-edge technical knowledge about the properties of particle size distribution (PSD), and chemical composition of the used powder (VisiJetPXL core®). These analyses also allowed to contrast it with its predecessors (Zp150® and Zp131®), where it was verified that its main constituent is hemihydrate calcium sulphate of type α ($\alpha\text{-}CaSO_4.0.5H_2O$), certain improvements that prevent packaging by having a slightly larger grain size Dx90 = 77.3 μm were also detected. These can provide a new field of study about improvement of printing powder materials.

The green 3DP specimens presented a good repeatability with respect to the final mechanical properties (almost zero standard deviation), for a same solid geometry and printing conditions with the default parameters of the printer. Despite its mesostructure and porosity, they cannot be controlled, thus demonstrating a reliability associated with the 3D printer (Projet 660Pro). This was also achieved, as a result of the standardization of the post-processing additional to the infiltration process, such as: drying, handling and cleaning stages of the printed parts. All these actions strengthened a study more dedicated to infiltration materials and processes, leaving the materials and printing process (in these conditions) as noise factors of almost zero in the studied responses. In other words, by ensuring that the printed parts have similar properties, all the variations of responses observed during the infiltration would be affected in large part by the infiltrating materials and their application.

Nonetheless, to verify if actually exists an influence of the printing parameters on infiltration, this study showed that variations of some of these parameters, such as build orientation and binder saturation, are significant for the permeability (k) of a 3DP model constituted by more than 90 % of macropores (with diameters > 0.05 μm) of its total apparent porosity, which makes it a highly porous medium. The hydraulic conductivity (K) for the same 3DP model was also affected by varying its build orientation and the type of fluid that passes through it when simulating a infiltration process by immersion.

The permeability (k) and hydraulic conductivity (K) results about this type of 3DP models are state of the art and unpublished, since there is no information about it in the literature. For this, it was necessary to develop a custom made falling head permeameter, that allowed testing a unidirectional flow, with respect to a 3DP model previously saturated with fluids of different viscosities. Meanwhile, these conditions can be modified in a real situation of infiltration by immersion, where the flow enters three-dimensionally in an unsaturated porous medium.

The study performed on 3DP parts infiltrated with materials and methods suggested by the BJ technology manufacturer, allowed to conclude that the infiltration process by full immersion with epoxy resin provides a greater and more stable final mechanical resistance to the 3DP parts. This method, due to its simplicity and non-requirement of operator's skill, together with the used epoxy resin (Strength Max — $E1$), were the basis of comparison for subsequent studies. The results of mechanical resistance of the infiltrated models with this epoxy resin and the other suggested infiltrant (cyanoacrylate-based — ColorBond ™) are considerably lower than those indicated by the suppliers of these materials, as also mentioned by other studies cited in this work.

The characterization of the hydraulic conductivity made it possible to understand the considerable advantage of using a fluid of low viscosity, thus increasing the value of K and in turn the penetration of the model in an infiltration process (by immersion). This finding was confirmed with the case study where different epoxy infiltrants (Strength Max — $E1$, Biresin

CR83-6 — $E2$ and Elantas EC131LV/W342 — $E3$) were evaluated in printed models of different thickness (2.50 to 9.00 mm).

Infiltrants materials $E2$ and $E3$ are considered as an alternative due to their outline (conception) of manufacturing for other applications than not infiltration of 3DP models, which makes them more accessible to all types of users. These infiltrants, among others, were characterized and contrasted against a wide range of possible infiltrants. They demonstrated excellent thermal, mechanical and material cost characteristics, which allowed their selection for further studies.

In the case study presented in Chapter 5- part II, with infiltrants $E1$, $E2$ and $E3$, it was possible to suggest a simple alternative for users with minimal infrastructure available of an infiltration process that seeks to improve the mechanical resistance of 3DP models by two ways.

First, without the need to optimize the cure conditions, as suggested by the supplier of the epoxy infiltrant. This solution consists of using materials with characteristics inherent to the infiltrant itself, such as low viscosity (< 300 mPa.s at RT) and high mechanical strength (similar to resin $E2$). Additionally, if the infiltrant exhibits an adequate potlife (about 30 min.) and a fast cure time at room temperature it would be an attractive and competitive infiltrant. Unfortunately, combining all these material characteristics is not always accessible for any type of user or easy to find.

A second alternative to improve the mechanical strength of 3DP models consists on the use of resins capable of transferring greater percentages of their own resistance to the printed models, as observed in the $E3$ resin in part II of Chapter 5. $E3$ resin, like many alternatives available in the market, encompasses additional beneficial features for a 3DP model, such as good UV resistance, uncolourless, and a short potlife. Recurring to the optimization of the cure conditions, we were able to show (in part III, Chapter 5) that the $E3$ resin surpassed the reference resin $E1$ by 33 % in its flexural strength (149.3 MPa), maintaining a similar flexural modulus of 3.0 GPa, all this with a 85 % time cure reduction (just 4.0 hours), which makes it an attractive infiltration time.

Despite $E3$ being a high viscosity resin (980.74 mPa.s at RT), a common property of high mechanical and/or thermal resistance resins, when heated slightly above to 40 ºC, its viscosity decreased considerably to 270.65 mPa.s, a comparable viscosity to $E1$ at RT (289 mPa.s). Based on this premise, in addition to the cure optimization of the $E3$, a hypothetical analogy of improvement was suggested in the penetration of 3DP models of up to 9.0 mm thickness, in similar proportions as those observed with the $E1$ resin. This would therefore, improve its flexural strength up to 51.99 or 35.96 MPa for printed models with 2.5 and 9.0 mm thickness, respectively.

Therefore, this work demonstrated the feasibility of recurring to materials not dedicated to infiltration of plaster-based 3DP parts. Moreover, with an adequate selection and handling of the infiltrant and its infiltration parameters, it will be possible to obtain satisfactory final characteristics in the printed model. In addition, it provides wide range possibilities to all types of users, who seek to reduce costs, post-processing time and have limited infrastructure for this consuming stage, thus helping to be a competitive AM technology, not disregarding a wider dissemination of it.

6.2 Recommendations for future work

As recommendations for future work, the following is proposed:

- Apply the conditions of improvement in the cure and viscosity proposed for the infiltrant $E3$ in the infiltration of 3DP models of different thickness, and evaluate their mechanical resistant in bending and compression;
- Develop a simple infiltration device by immersion, with time, temperature and dosing control of the infiltrant quantity;
- Analyse the hydraulic conductivity of unsaturated 3DP models, with temperature variations of the fluid passing through it and control of its saturation;
- Analysis of the flow behaviour of the infiltrant during an immersion process in a 3DP model, through real time analysis of images (real-micro CT), generating concepts that together with those found in hydraulic conductivity would allow a simulation of the infiltration process;
- Explore the influence of the type of infiltrant on the colour changes, degradation of both mechanically and in coloration of infiltrated 3DP models;
- Other features of interest could be the surface finish and dimensional variations that would cause the models when infiltrated with different parameters;
- Based on the specific characteristics found for the alternative infiltrant, apply to functional 3DP printed prototypes.

References

1. Terry Wohlers I. C., Olaf Diegel, and Joseph Kowen. Wohlers Report 2018. Wohlers Associates I, editor. Fort Collins,CO.2018. 344 p.
2. Chua C. K., Wong C. H., Yeong W. Y. Standards, quality control, and measurement sciences in 3D printing and additive manufacturing. London Academic Press; 2017. 268 p.
3. Volpato Neri, et al. Manufatura Aditiva - Tecnologias e aplicações da impressão 3D. SP-Brasil Blucher; 2017. 400 p.
4. Islam M. N., Sacks S. An experimental investigation into the dimensional error of powder-binder three-dimensional printing. The International Journal of Advanced Manufacturing Technology. 2016; 82(5):1371-80.
5. ISO/TC 261, ASTM F42 Committees. ISO/ASTM 52900: Additive manufacturing - General principles -Terminology. Geneva, Switzerland. 2012 DOI: 10.1520/F2792-12A.2.
6. Gibson I., Rosen D., Stucker B. Binder Jetting. In: Additive Manufacturing Technologies: 3D Printing, Rapid Prototyping, and Direct Digital Manufacturing. Gibson I, Rosen D, Stucker B, editors. New York, USA.: Springer New York; 2015. p. 205 - 18.
7. Gibson I., Rosen D., Stucker B. Additive Manufacturing Technologies: 3D Printing, Rapid Prototyping, and Direct Digital Manufacturing. New York: Springer 2014. 498 p.
8. Brans K. 3D Printing, a Maturing Technology. IFAC Proceedings Volumes. 2013; 46(7):468-72.
9. Chua C. K., Leong K. F. 3D printing and Aditive Manufacturing - Principles and applicaitons. Singapore World Scientific Publishing Co.; 2016. 456 p.
10. Additively A. G. Binder Jetting Zürich 2016.Acceced: 13-03-2019]: Available from: https://www.additively.com/en/learn-about/binder-jetting.
11. Butscher A. Powder based three-dimensional printing of calcium phosphate structures for scaffold engineering. Zürich: ETH Zurich. Doctor of Sciences Degree; 2013.
12. Will J., et al. Porous ceramic bone scaffolds for vascularized bone tissue regeneration. Journal of Materials Science: materials in medicine. 2008; 19(8):2781-90.
13. Wohlers Report: Anual worldwide Progress Report. Fort Collins,CO; 2015.
14. Liu J., Rynerson M., inventors; Google Patents, assignee. Method for article fabrication using carbohydrate binder2003.
15. Utela B., et al. A review of process development steps for new material systems in three dimensional printing (3DP). Journal of Manufacturing Processes. 2008; 10(2):96-104.

16. Sachs E. M., et al., inventors; US Patent 005,340,656, assignee. Three dimensional printing techniques, United States Patent No1994.
17. Sachs E. M. Powder dispensing apparatus using vibration. Google Patents; 2000.
18. Sachs E. M., et al. Jetting layers of powder and the formation of fine powder beds thereby. Google Patents; 2003.
19. Liu J., Ryneson M. L. Blended powder solid-supersolidus liquid phase sintering. Google Patents; 2006.
20. Cima L. G., Cima M. J., inventorsPreparation of medical devices by solid free-form fabrication methods patent 0736-5845. 1996.
21. Kogel J. E., Society for Mining M., Exploration. Industrial Minerals & Rocks: Commodities, Markets, and Uses: Society for Mining, Metallurgy, and Exploration; 2006.
22. Davis J. R., ASM International. Handbook Committee.,. Casting. In: Metals handbook. 2nd. Desk Edition ed. Materials Park, Oh.: ASM International; 1998. p. xiv, 1521 p.
23. Blanco A. F. YESOS_Generalidades. Spain 2014.Acceced: 2015-09-16]: Available from: http://www6.uniovi.es/usr/fblanco/Tema6.YESOS.pdf.
24. Smith C. Plaster and Plaster board construction. New Zealand 2008.Acceced: 2016-08-12]: Available from: http://nzic.org.nz/ChemProcesses/inorganic/9D.pdf.
25. Utela B. R., et al. Development process for custom three-dimensional printing (3DP) material systems. Journal of Manufacturing Science and Engineering. 2010; 132(1):011008.
26. Greil P. Polymer derived engineering ceramics. Advanced engineering materials. 2000; 2(6):339-48.
27. 3DSystems I. ZPrinter® Consumables Catalogue. Austria2013.
28. Zañartu-Apara G., Ramos-Grez J. Characterization of the mechanical properties of samples fabricated by an experimental SGM device. Rapid Prototyping Journal. 2010; 16(5):356-64.
29. Apara G. J. Z. Caracterización de propiedades mecánicas de material particulado a traves de un sistema de prototipado rápido experimental. Santiago, Chile: Pontficia Universidad Católica de Chile. Magister en Ciencias de la Ingeniería Degree; 2009.
30. Asadi-Eydivand M., et al. Effect of technical parameters on porous structure and strength of 3D printed calcium sulfate prototypes. Robotics and Computer-Integrated Manufacturing. 2015; 37:57-67.
31. Marciniec A., et al. Application of ZP131 powder for manufacture of casting molds using ZCast technology for Al-alloys castings. Archives of Foundry Engineering. 2010:423-6.
32. Shirazi S. F. S., et al. A review on powder-based additive manufacturing for tissue engineering: selective laser sintering and inkjet 3D printing. Science and Technology of Advanced Materials. 2015; 16(3):033502-20.
33. Lowmunkong R., et al. Fabrication of freeform bone-filling calcium phosphate ceramics by gypsum 3D printing method. J Biomed Mater Res B Appl Biomater. 2009; 90(2):531-9.

34. Monkhouse D. C., et al. Rapid prototyping and manufacturing process. Google Patents; 2003.
35. Gharaie S. H., Morsi Y., Masood S. H. Tensile Properties of Processed 3D Printer ZP150 Powder Material2013: Trans Tech Publ.
36. Frascati J. Effects of position, orientation, and infiltrating material on three dimensional printing models. Orlando, Florida: University of Central Florida Orlando, Florida.2007.
37. Vaezi M., Chua C. K. Effects of layer thickness and binder saturation level parameters on 3D printing process. International Journal of Advanced Manufacturing Technology. 2011; 53(1):275-84.
38. Zañartu Apara G., Ramos Grez J. Characterization of the mechanical properties of samples fabricated by an experimental SGM device. Rapid Prototyping Journal. 2010; 16(5):356-64.
39. Asadi-Eydivand M., et al. Effect of technical parameters on porous structure and strength of 3D printed calcium sulfate prototypes. Robotics and Computer-Integrated Manufacturing. 2016; 37:57-67.
40. Feng P., et al. Mechanical properties of structures 3D printed with cementitious powders. Construction and Building Materials. 2015; 93:486-97.
41. Jiang C., et al. Investigation of Dynamic Crack Coalescence Using a Gypsum-Like 3D Printing Material. Rock Mechanics and Rock Engineering. 2016:1-16.
42. Lizardo B. F., et al. An assessment of thermosetting infiltrate in powder-based composites made by additive manufacturing. Journal of Composite Materials. 2018:1-10.
43. Farzadi A., et al. Effect of layer printing delay on mechanical properties and dimensional accuracy of 3D printed porous prototypes in bone tissue engineering. Ceramics International. 2015; 41(7):8320-30.
44. Levoguer C. Using laser diffraction to measure particle size and distribution. Metal Powder Report. 2013; 68(3):15-8.
45. Ma Z., et al. New developments in particle characterization by laser diffraction: size and shape. Powder Technology. 2000; 111(1):66-78.
46. Mohammadi M., Tulliani J.-M., Palmero P. Fabrication of dense and porous biphasic calcium phosphates: effect of dispersion on sinterability and microstructural development. International Journal of Applied Ceramic Technology. 2019; 0(ja).
47. Kuru M., Şaşmaz Kuru T., Bağcı S. The role of the calcium concentration effect on the structural and dielectric properties of mixed Ni–Zn ferrites. Journal of Materials Science: Materials in Electronics. 2019.
48. 3DSystems. VisiJet PXL Core - Powder CAS-No 10034-76-1 South Carolina USA.; Producer: Inc. D; 2013. [Acceced: 25-08-2018]: Available from: http://www.3dsystems.com/sites/www.3dsystems.com/files/22-83100-s12-00-bsds_ghsenglishvisijet_pxl_core.pdf.

49. 3DSystems I. VisiJet PXL-Binder Solution CAS Nº 616-45-5. South Carolina USA.; Producer: 3DSystems I; 2013. [Acceced: 16-08-2018]: Available from: http://www.3dsystems.com/files/22-83101-s12-01-asds_ghsenglish-australiavisijet_pxl_colors.pdf.

50. Albrecht L. H., et al. 2-Pyrrolidone. In: Ullmann's Encyclopedia of Industrial Chemistry. Wiley-VCH, editor. Weinheim 2011. p. 1-7.

51. 3DSystems I. ProJet x60 Series professional 3D printers. USA. : 3DSystems, Inc.; 2016.

52. 3DSystems I. 3DPrint™ 1.0 System Software - User guide. In: 3DSystems I, editor. South Carolina USA.: 3DSystems Inc.; 2013. p. 14.

53. Frascati J. Effects of position, orientation, and infiltrating material on three dimensional printing models. Orlando, Florida: B.S. Florida State University.2007.

54. Ocaña G. E., Alves J. L., Neto R. Study of the viability of manufacturing ceramic moulds by additive manufacturing for rapid casting. Ciência & Tecnologia dos Materiais. 2017; 29(1):e275-e80.

55. Spierings A. B., Herres N., Levy G. Influence of the particle size distribution on surface quality and mechanical properties in AM steel parts. Rapid Prototyping Journal. 2011; 17(3):195-202.

56. LeŠKeviČIenĖ V. α-Hemihydrate Gypsum from Flue Gas Desulphurization Gypsum. Materials Science/Medziagotyra. 2013; 19(2):197-202.

57. Bobby S. S. A preliminary Investigation of Gypsum bonded moulds by Three Dimensional Printing. International Journal of Research in Engineering and Technology. 2014; 3(06):501-7.

58. Gupta A. K., Paliwal D. K., Bajaj P. Melting behavior of acrylonitrile polymers. Journal of applied polymer science. 1998; 70(13):2703-9.

59. Viñas J. L. G. Nuevas aplicaciones de recursos yesíferos: desarrollo, caracterización y reciclado: Universidad Politécnica de Madrid.2005.

60. Dias M. R., et al. Permeability analysis of scaffolds for bone tissue engineering. Journal of Biomechanics. 2012; 45(6):938-44.

61. Yan M., et al. Hierarchically porous materials prepared by selective laser sintering. Materials & Design. 2017; 135:62-8.

62. Mitra S., Rodríguez de Castro A., El Mansori M. The effect of ageing process on three-point bending strength and permeability of 3D printed sand molds. The International Journal of Advanced Manufacturing Technology. 2018; 97(1):1241-51.

63. Latt K. M. M., Giao P. H. Prediction of permeability of cement-admixed soft clay using resistivity and time-domain IP measurements. Journal of Applied Geophysics. 2017; 137:92-103.

64. Rouquerol J., et al. Recommendations for the characterization of porous solids. Pure & Appl Cher. 1994; 66 (8):1739–58.

65. Bear J. Dynamics of fluids in porous media. New York: Courier Corporation; 2013.

66. Nijp J. J., et al. A modification of the constant-head permeameter to measure saturated hydraulic conductivity of highly permeable media. MethodsX. 2017; 4:134-42.

67. Sochi T. Non-Newtonian flow in porous media. Polymer. 2010; 51(22):5007-23.

68. Pal L., Joyce M. K., Fleming P. D. A simple method for calculation of the permeability coefficient of porous media. Tappi journal. 2006; 5(9):10.

69. Berger M. B. The importance and testing of density/porosity/permeability/pore size for refractories. Refractories 2010 Conference; 2010 2010.

70. Espinal L. Porosity and its measurement. Characterization of Materials. 2002:1-10.

71. Thommes M., et al. Textural characterization of native and n-alky-bonded silica monoliths by mercury intrusion/extrusion, inverse size exclusion chromatography and nitrogen adsorption. Journal of Chromatography A. 2008; 1191(1):57-66.

72. Gallé C. Effect of drying on cement-based materials pore structure as identified by mercury intrusion porosimetry: A comparative study between oven-, vacuum-, and freeze-drying. Cement and Concrete Research. 2001; 31(10):1467-77.

73. ASTM International. D 5856 – 2007 Standard test method for measurement of hydraulic conductivity of porous material using a rigid-wall, compaction-mold permeameter. ASTM International, West Conshohocken. PA. 2007

74. Darcy H. Les fontaines publiques de la ville de Dijon: exposition et application: Victor Dalmont; 1856.

75. Chen Q., et al. Variations of Permeability and Pore Size Distribution of Porous Media with Pressure. Journal of Environmental Quality. 2002; 31:500-5.

76. Xia M., Sanjayan J. Method of formulating geopolymer for 3D printing for construction applications. Materials & Design. 2016; 110:382-90.

77. Porcheron F., et al. Mercury Porosimetry in Mesoporous Glasses: A Comparison of Experiments with Results from a Molecular Model. Langmuir. 2007; 23(6):3372-80.

78. Feenstra F. K., inventor; TNO, assignee. Method for making a dental element. USA. patent US6955776B1. 2005 Oct. 18.

79. Bredt J. F., Anderson T. C., Russell D. B. Three dimensional printing material system and method. Google Patents; 2003.

80. Bredt J. F., Anderson T. C., Russell D. B., inventors; Z Corporation, assignee. Three dimensional printing material system and method. USA. patent US 6,610,429 B2. 2003 Aug. 26.

81. Galeta Tomislav K. I., Karakasic Mirko. Influence of processing factors on the tensile strength of 3d-printed models. Materiali in tehnologije. 2013; 47(6):781-8.

82. Skeist I. Handbook of Adhesives. Third ed: Springer US; 2012. 800 p.
83. Staff P. D. L. Adhesive and solvent bonding. In: Handbook of plastics joining: a practical guide. Press CU, editor. Norwich, USA: William Andrew; 2008. p. 141-2.
84. Warwick T., inventor; Patent US20160067925A1, assignee. Method and apparatus for infusing additive manufactured objects and the like. USA. patent US/20160067925 A1. 2016 march 10.
85. Stanić M. Structure, surface and permanence properties of three dimensional printing materials= Struktura i površinska svojstva te postojanost materijala za trodimenzijski tisak. Zagreb: University of Zagreb. Doctoral Thesis Degree; 2010.
86. Suwanprateeb J. Comparative study of 3DP material systems for moisture resistance applications. Rapid Prototyping Journal. 2007; 13(1):48-52.
87. Suwanprateeb J. Improvement in mechanical properties of three-dimensional printing parts made from natural polymers reinforced by acrylate resin for biomedical applications: a double infiltration approach. Polymer International. 2006; 55(1):57-62.
88. Maja S., Branka L., Diana Gregor S. Colorimetric properties and stability of 3D prints. Rapid Prototyping Journal. 2012; 18(2):120-8.
89. Gharaie S. H., Morsi Y., Masood S. H. Tensile Properties of Processed 3D Printer ZP150 Powder Material2013 2013: Trans Tech Publ.
90. Impens D., Urbanic R. J. A comprehensive assessment on the impact of post-processing variables on tensile, compressive and bending characteristics for 3D printed components. Rapid Prototyping Journal. 2016; 22(3):591-608.
91. Stanic M., Lozo B. Permanence and Color Stability in 3D Ink-jet Printing. NIP & Digital Fabrication Conference. 2010; 2010(2):541-4.
92. Lozo B., et al. Three-Dimensional Ink Jet Prints–Impact of Infiltrants. Journal of Imaging Science and Technology. 2008; 52(5):51004-1.
93. Impens D., Urbanic R. J. An Analysis of Variation Correlating Post Processing Infiltrate Types, Build Parameters and Mechanical Characteristics for Binder Jet Built Parts. ASME 2015 International Mechanical Engineering Congress and Exposition; 2015; Houston, Texas, USA. Volume 2A: Advanced Manufacturing.
94. Upcraft S., Fletcher R. The rapid prototyping technologies. Assembly Automation. 2003; 23(4):318-30.
95. Pilipović A., Raos P., Šercer M. Experimental analysis of properties of materials for rapid prototyping. The International Journal of Advanced Manufacturing Technology. 2009; 40(1-2):105-15.
96. Ocaña G. E., Alves J. L., Neto R. Influence of Infiltration Post-Processing in Binder Jetting Technology In: Advanced Structured Materials. Lucas F.M. da Silva, editor. 65. Porto, Portugal: Springer; 2016. p. 416.

97. Urbaniak M. A relationship between the glass transition temperature and the conversion degree in the curing reaction of the EPY® epoxy system. Polimery. 2011; 56(3):240-3.

98. Bernath A., Kärger L., Henning F. Accurate Cure Modeling for Isothermal Processing of Fast Curing Epoxy Resins. Polymers. 2016; 8(11):390.

99. Urbaniak M., Grudziński K. Time-temperature-transformation (TTT) cure diagram for EPY epoxy system. Polimery. 2007; 52(2).

100. Li Q., Li X., Yan M. Curing of DGEBA epoxy using a phenol-terminated hyperbranched curing agent: Cure kinetics, gelation, and the TTT cure diagram. Thermochimica Acta. 2012; 549:69-80.

101. Hu J., et al. Water resistance and curing kinetics of epoxy resins with a novel curing agent of biphenyl-containing amine synthesized by one-pot method. Thermochimica Acta. 2015; 606:58-65.

102. Hu J., et al. Isothermal curing kinetics of a flame retardant epoxy resin containing DOPO investigated by DSC and rheology. Thermochimica Acta. 2016; 632:56-63.

103. Penn L. S., Wang H. Handbook of composites1998.

104. Netto Sabino da Costa A. Desenvolvimento de compósito de resina epóxi e fibras curtas de aço para fabricação rápida de moldes para injeção de termoplásticos. Florianópolis: Universidade Federal de Santa Catarina. Doutor em engenharia mecânica Degree; 2008.

105. Impens D., Urbanic R. J. Assessing the Impact of Post-Processing Variables on Tensile and Compression Characteristics for 3D Printed Components. IFAC-PapersOnLine. 2015; 48(3):652-7.

106. Impens D. An experimental approach to assess the impact of post processing variables on the mechanical characteristics of 3D printed (powder binding process) parts. Ontario, Canada: University of Windsor. Master of Applied Science Degree; 2015.

107. Nietzsch-Gerätebau G. Gypsum and Quartz Sand - Phase Transitions. Germany 2016.Acceced: 2018-12-08]: Available from: https://www.netzsch-thermal-analysis.com/us/materials-applications/ceramics-glass/gypsum-and-quartz-sand-phase-transitions/.

108. 3D Systems I. StrengthMax and Z Max 90 Hardener, CAS-No 2855-13-2. South Carolina USA.; Producer: 3D Systems I; 2013. [Acceced: 29-12-1018]: Available from: http://www.3dsystems.com/company/datafiles/22-83106-S12-00-A-SDS-GHS-English-StrengthMax-and-Z-Max-90-Hardener.pdf.

109. 3DSystems I. Colorbond-Zbond 90 CAS-No 7085-85-0. South Carolina USA.; Producer: 3DSystems; 2013. [Acceced: 29-04-2018]: Available from: http://www.3dsystems.com/sites/www.3dsystems.com/files/22-83104-s12-02-a-sds-ghs-english-colorbond-and-zbond-90.pdf.

110. 3DSystems I. Magnesium Sulfate Heptahydrate (Epsom Salt), CAS Nº 10034-99-8. Houston USA Producer: 3DSystems I; 2010. [Acceced: 20-08-2015]: Available from: http://www.hillbrothers.com/msds/pdf/n/magnesium-sulfate.pdf.

111. ASTM International. ASTM D790 - 2010 Standard test methods for flexural properties of unreinforced and reinforced plastics and electrical insulating materials. ASTM International, West Conshohocken. PA. 2010; DOI: 10.1520/D0790-17.

112. ASTM International. ASTM D638 - 2010 Standard test method for tensile properties of plastics. ASTM International, West Conshohocken. PA. 2010; DOI: 10.1520/D0638-10.

113. 3D Systems I. ColorBond User Guide. Rock Hill, USA. 2013.Acceced: 19-02-2019]: Available from: http://infocenter.3dsystems.com/projetcjpx60/color-bond-user-guide.

114. 3D Systems I. StrengthMax User Guide. 2013.Acceced: 09-02-2019]: Available from: http://infocenter.3dsystems.com/projetcjpx60/post-processing-guide/post-processing-part/strength-max%E2%84%A2-user-guide.

115. Chaves A. A. S. Impressão 3D baixo custo versus impressão em equipamentos de elevado custo [Master]. Porto: University of Porto. Master Degree Degree; 2015.

116. Kuntze R. A. Gypsum: Connecting Science and Technology: ASTM International; 2009.

117. Margarido M. C. G. F. Materials for Construction and Civil Engineering: Science, Processing, and Design. Lisboa, Portugal: Springer International Publishing: Imprint: Springer; 2015.

118. Loos M. R., et al. The effect of acetone addition on the properties of epoxy. Polímeros. 2008; 18:76-80.

119. Han M. G., Kim S., Liu S. X. Synthesis and degradation behavior of poly(ethyl cyanoacrylate). Polymer Degradation and Stability. 2008; 93(7):1243-51.

120. Kim S., Peterson S. C. Development of degradable polymer composites from starch and poly(ethyl cyanoacrylate). Polymer Composites. 2012; 33(6):904-11.

121. Wang X., et al. Preparation, flame retardancy, and thermal degradation of epoxy thermosets modified with phosphorous/nitrogen-containing glycidyl derivative. Polymers for Advanced Technologies. 2010; 23(2):190-7.

122. Mansour M. B., et al. Thermal Characterization of a Tunisian Gypsum Plaster as Construction Material. Energy Procedia. 2013; 42:680-8.

123. Utela A. B. Development and application of new material systems for three dimensional printing (3DP). Washington, USA. : University of Washington PhD Degree; 2008.

124. Hackney P. M., Channappa L. C. Development of systems to increase the green part strength of the three-dimensional printed Z-Corps manufactured parts by infiltration processes to improve their range of application. Fifth National Conference on Rapid Design, Prototyping, and Manufacturing; 2004; United Kingdom2004.

125. Sachs E. M., et al., inventors; Patent US5340656A, assignee. Three dimensional printing techniques. USA. patent US;5340656;A. 1994.

126. Zhou J. G., et al. Low temperature polymer infiltration for rapid tooling. Materials & Design. 2004; 25(2):145-54.

127. Zhu J., et al. Water-based coatings for 3D printed parts. Journal of Coatings Technology and Research. 2015; 12(5):889-97.

128. Mirmohseni-Namin A., Nikafshar S., Mirmohseni F. Increasing toughness and tensile strength of an epoxy-diamine system using an inorganic ultra-accelerator. RSC Advances. 2015; 5(65):53025-35.

129. webshop L. Colorbond 3DS Infiltrant - 2kg. Houten, Netherlands. 2019.Acceced: 14-05-2019]: Available from: https://www.landre-webshop.nl/en/3d-systems-color-bond-large.html.

130. Ellis B., Smith R. Polymers: A Property Database. Second Edition ed. Group TF, editor. Florida: CRC Press; 2009. 1052 p.

131. Gardziella A., Pilato L. A., Knop A. Phenolic resins: chemistry, applications, standardization, safety and ecology: Springer Science & Business Media; 2013.

132. Hesse W. Phenolic Resins. In: in Ullmann's Encyclopedia of Industrial Chemistry. Wiley-VCH, editor. Weinheim: Ullmann's 2000.

133. Saad B., Suter U. W. Biodegradable Polymeric Materials. In: Encyclopedia of Materials: Science and Technology. Buschow KHJ, et al., editors. Oxford: Elsevier; 2001. p. 551-5.

134. CES EduPak Software. 2018 ed. Granta D., Limited. Limited GD, version: 18.1.1;2018.

135. Suwanprateeb J., Sanngam R., Panyathanmaporn T. Influence of raw powder preparation routes on properties of hydroxyapatite fabricated by 3D printing technique. Materials Science and Engineering: C. 2010; 30(4):610-7.

136. Thammarakcharoen Faungchat S. J. Preparation of 3DP Hydroxyapatite Composite by Single and Double Pass Poly(ε-caprolactone) Infiltration. Key Engineering Materials. 2013; 545:69-73.

137. Polzin Christian, Spath Sebastian, Seitz Hermann. Characterization and evaluation of a PMMA-based 3D printing process. Rapid Prototyping Journal. 2013; 19(1):37-43.

138. Min J. H., et al. Evaluation of penetration effect of resin infiltrant using optical coherence tomography. Journal of dentistry. 2015; 43(6):720-5.

139. Min J.-H., Inaba D., Kim B.-I. Evaluation of resin infiltration using quantitative light-induced fluorescence technology. Photodiagnosis and Photodynamic Therapy. 2016; 15:6-10.

140. Murugan R., Ramesh R., Padmanabhan K. Investigation on static and Dynamic Mechanical Properties of epoxy based woven fabric glass/carbon hybrid composite laminates. Procedia Engineering. 2014; 97:459-68.

141. Lorandi N. P., Cioffi M. O. H., Ornaghi Jr H. Análise Dinâmico-Mecânica de Materiais Compósitos Poliméricos. Scientia cum Industria. 2016; 4(1):48-60.
142. Nahm Steven, Fibercast Smith, Company Varco. Use of Dynamic Mechanical Analysis in thermoset resin development for composite applications. Composites 2001 Convention and Trade Show; 2001 2001; Tampa, FL USA.: CFA Resource Center.
143. ASTM International. ASTM D4092-Standard Terminology for Plastics: Dynamic Mechanical Properties. ASTM International, West Conshohocken. PA. 2013; DOI: 10.1520/D4092-07R13.
144. TA Instrument I. TS-15A_Characterization of resin curing using DMA, DEA, controlled stress rheology. In: TA Instrument I, editor. USA. 2016.
145. Bosze E. J., et al. High-temperature strength and storage modulus in unidirectional hybrid composites. Composites Science and Technology. 2006; 66(13):1963-9.
146. Stark W. Investigation of the curing behaviour of carbon fibre epoxy prepreg by Dynamic Mechanical Analysis DMA. Polymer testing. 2013; 32(2):231-9.
147. Deng S., Hou M., Ye L. Temperature-dependent elastic moduli of epoxies measured by DMA and their correlations to mechanical testing data. Polymer testing. 2007; 26(6):803-13.
148. Neto Salvador Claro. DMA – O que é preciso saber antes de sua utilização (parte II). Brazilian Journal of Thermal Analysis. 2013; 2(1):55-7E.
149. Sika. Biresin® CR83 Resin, MSDS Stuttgart; Producer: GmbH SD; 2014. [Acceced: 5-06-2018]: Available from: http://deu.sika.com/en/tooling-and-composites-redirect/tooling_composites/Dokumentendownload_Tooling/document_download/SDS-Biresin-CR.html.
150. Elantas E. I. EC 131LV/W 342 - Product Information. Germany; Producer: Elantas EI; 2014. [Acceced: 5-06-2017]: Available from: http://www.cristex.co.uk/uploads/Elan-tech_EC131LV_W342_ing.pdf.
151. Smooth-On Inc. Crystal Clear® 200. Chicago, USA; Producer: Inc. S-O; 2014. [Acceced: 25-01-2019]: Available from: https://www.smooth-on.com/msds/files/Clear_Flex_50_95.pdf.
152. ASTM International. E1356−Standard Test Method for Assignment of the Glass Transition Temperatures by Differential Scanning Calorimetry. ASTM International, West Conshohocken. PA. 2014; DOI: 10.1520/E1356.
153. Garay A. C. Propriedades mecânicas de compósitos estruturas sanduíche moldadas por RTM light e simulação numérica da infiltração. Lorena, São Paulo: Universidade Federal do Rio Grande do Sul.: Doutor em Engenharia de Minas, Metalúrgica e de Materiais Degree; 2016.
154. Michels J., et al. Thermo-mechanical properties of commercially available epoxy resins for structural applications. 2015.

155. Junk S., et al. Rapid tooling in metal forming processes using 3D-printed tools. 5th International Conference on Advanced Research in Virtual and Rapid Prototyping; 2011 Sept. 28 - Oct. 1; Leiria, Portugal: Taylor & Francis
156. Asadi-Eydivand M., et al. Optimal design of a 3D-printed scaffold using intelligent evolutionary algorithms. Applied Soft Computing Journal. 2016; 39:36-47.
157. Sachs E. M., inventor; Massachusetts Institute of Technology assignee. Powder dispensing apparatus using vibration. USA. patent US 6,036,777,A. 2000.
158. Miyanaji H., et al. Process development of porcelain ceramic material with binder jetting process for dental applications. JOM. 2016; 68(3):831-41.
159. Steele K. A. M., Herbert N., Pretet V. A study on the effects of resin infiltration techniques on parts produced using the three-dimensional printing process. Fifth National Conference on Rapid Design, Prototyping, and Manufacturing; 2004; Great Britain: John Wiley & Sons Inc.
160. Corcione E. C., Freuli F., Frigione M. Cold-Curing Structural Epoxy Resins: Analysis of the Curing Reaction as a Function of Curing Time and Thickness. Materials. 2014; 7(9).
161. Brown R. Handbook of Polymer Testing. Limited RT, editor. Shawbury, UK.2002.
162. Simons E. N. Testing of metals: Great Albion Books; 1972.
163. Viswanath D. S., et al. Viscometers. In: Viscosity of Liquids. Dordrecht: Springer; 2007. p. 82-3.
164. Tripathi G., Srivastava D. Effect of carboxyl-terminated poly(butadiene-co-acrylonitrile) (CTBN) concentration on thermal and mechanical properties of binary blends of diglycidyl ether of bisphenol-A (DGEBA) epoxy resin. Materials Science and Engineering: A. 2007; 443(1–2):262-9.
165. Romão B. M. V., et al. Characterization of the curing agents used in epoxy resins with TG/FT-IR technique. Polímeros. 2006; 16:94-8.
166. Kersting D., Wiebeck H., Esper F. J. Caracterização de resinas epóxi para compósitos curadas através de irradiação de micro–ondas. Revista Iberoamericana de Polímeros. 2015; 16(3):148-56.
167. Liu J., et al. Synthesis, characterization and curing properties of a novel cyclolinear phosphazene-based epoxy resin for halogen-free flame retardancy and high performance. RSC Advances. 2012; 2(13):5789-99.
168. Sun T., Chang X. L., Lai J. W. Experimental studies on epoxy-amine system using microwave and conventional curing approaches2012 2012: Trans Tech Publ.
169. Debenedetti P. G., Stillinger F. H. Supercooled liquids and the glass transition. Nature. 2001; 410(6825):259.
170. Kauzmann W. The Nature of the Glassy State and the Behavior of Liquids at Low Temperatures. Chemical Reviews. 1948; 43(2):219-56.

171. Garton A., et al. Additives for improving the strength, stiffness, and ductility of epoxy resins. Polymer Engineering & Science. 1987; 27(21):1620-6.

172. Biswas D. R. Influence of porosity on the mechanical properties of lead zirconate--titanate ceramics. California Univ., Berkeley (USA). Lawrence Berkeley Lab.; 1976.

173. Granado L., et al. Kinetic regimes in the curing process of epoxy-phenol composites. Thermochimica Acta. 2018; 667:185-92.

174. Prime R. B. Thermosets. In: Thermal characterization of polymeric materials. Turi E, A.,, editor. 2. London: Academic Press; 1997. p. 1377—766.

175. Lapique F., Redford K. Curing effects on viscosity and mechanical properties of a commercial epoxy resin adhesive. International Journal of Adhesion and Adhesives. 2002; 22(4):337-46.

176. Hardis R., et al. Cure kinetics characterization and monitoring of an epoxy resin using DSC, Raman spectroscopy, and DEA. Composites Part A: Applied Science and Manufacturing. 2013; 49:100-8.

177. Javdanitehran M., et al. An iterative approach for isothermal curing kinetics modelling of an epoxy resin system. Thermochimica Acta. 2016; 623:72-9.

178. Epoxy Technology I. Cure Matters Determining the Proper Cure Schedule. MA, USA; Producer: ©Epoxy Technology I; 2012. [Acceced: 2018-02-15]: Available from: http://www.epotek.com/site/files/brochures/pdfs/Cure_Matters_Final.pdf.

179. Standardization I. O. f. DIN ISO 291 - 2008 Plastics -Standard atmospheres for conditioning and testing. 2008

180. ASTM International. ASTM 618 - 2000 Standard Practice for Conditioning Plastics for Testing. ASTM International, West Conshohocken. PA. 2000; DOI: 10.1520/D0618-00.

181. Zhang J., Xu Y. C., Huang P. Effect of cure cycle on curing process and hardness for epoxy resin. Express Polymer Letters. 2009; 3(9):534-41.

Appendices

Appendix 1 Study of the viability of manufacturing ceramic moulds by additive manufacturing for rapid casting

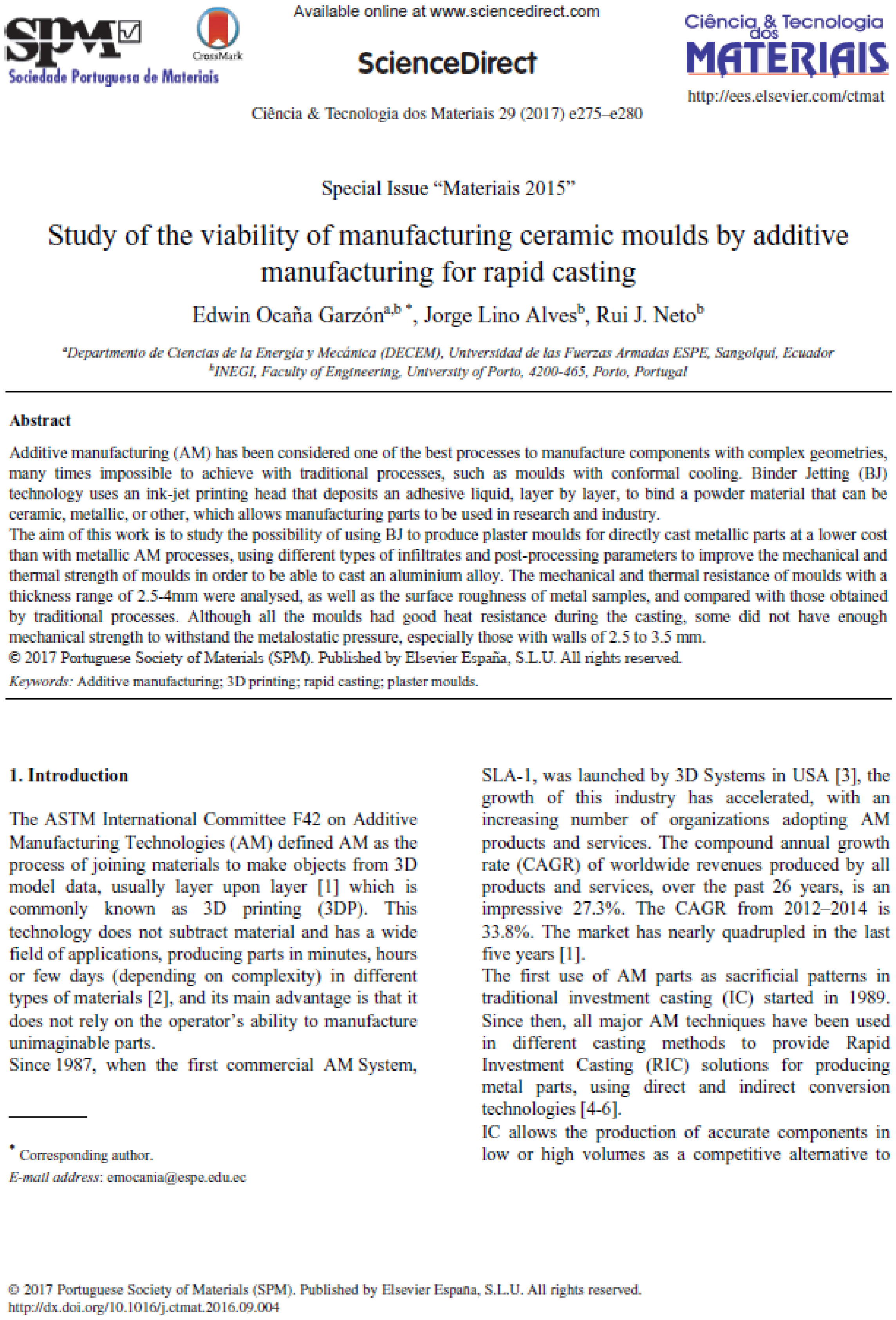

Available online at www.sciencedirect.com

Ciência & Tecnologia dos Materiais 29 (2017) e275–e280

http://ees.elsevier.com/ctmat

Special Issue "Materiais 2015"

Study of the viability of manufacturing ceramic moulds by additive manufacturing for rapid casting

Edwin Ocaña Garzón[a,b] *, Jorge Lino Alves[b], Rui J. Neto[b]

[a] *Departmento de Ciencias de la Energía y Mecánica (DECEM), Universidad de las Fuerzas Armadas ESPE, Sangolquí, Ecuador*
[b] *INEGI, Faculty of Engineering, University of Porto, 4200-465, Porto, Portugal*

Abstract

Additive manufacturing (AM) has been considered one of the best processes to manufacture components with complex geometries, many times impossible to achieve with traditional processes, such as moulds with conformal cooling. Binder Jetting (BJ) technology uses an ink-jet printing head that deposits an adhesive liquid, layer by layer, to bind a powder material that can be ceramic, metallic, or other, which allows manufacturing parts to be used in research and industry.
The aim of this work is to study the possibility of using BJ to produce plaster moulds for directly cast metallic parts at a lower cost than with metallic AM processes, using different types of infiltrates and post-processing parameters to improve the mechanical and thermal strength of moulds in order to be able to cast an aluminium alloy. The mechanical and thermal resistance of moulds with a thickness range of 2.5-4mm were analysed, as well as the surface roughness of metal samples, and compared with those obtained by traditional processes. Although all the moulds had good heat resistance during the casting, some did not have enough mechanical strength to withstand the metalostatic pressure, especially those with walls of 2.5 to 3.5 mm.

Keywords: Additive manufacturing; 3D printing; rapid casting; plaster moulds.

1. Introduction

The ASTM International Committee F42 on Additive Manufacturing Technologies (AM) defined AM as the process of joining materials to make objects from 3D model data, usually layer upon layer [1] which is commonly known as 3D printing (3DP). This technology does not subtract material and has a wide field of applications, producing parts in minutes, hours or few days (depending on complexity) in different types of materials [2], and its main advantage is that it does not rely on the operator's ability to manufacture unimaginable parts.
Since 1987, when the first commercial AM System, SLA-1, was launched by 3D Systems in USA [3], the growth of this industry has accelerated, with an increasing number of organizations adopting AM products and services. The compound annual growth rate (CAGR) of worldwide revenues produced by all products and services, over the past 26 years, is an impressive 27.3%. The CAGR from 2012–2014 is 33.8%. The market has nearly quadrupled in the last five years [1].
The first use of AM parts as sacrificial patterns in traditional investment casting (IC) started in 1989. Since then, all major AM techniques have been used in different casting methods to provide Rapid Investment Casting (RIC) solutions for producing metal parts, using direct and indirect conversion technologies [4-6].
IC allows the production of accurate components in low or high volumes as a competitive alternative to

---

* Corresponding author.
E-mail address: emocania@espe.edu.ec

http://dx.doi.org/10.1016/j.ctmat.2016.09.004

forging or metal turning since the waste material is kept to a minimum [7].

The economic benefits derived from AM patterns are limited to small quantity production due to high AM material costs [8]. The choice of the AM technique to be used will depend on many factors such as shape, dimensional tolerances, the cost assigned to the model, among others [9].

The Projet 660 Pro machine uses a ColorJet Printing (CJP) technology that consolidates a plaster-ceramic powder by selective jetting of a water based binder. Complex cores and cavities can be produced directly from the CAD model, completed with the gating system and air vents, avoiding the construction of patterns and core boxes [10]. Post-processing is a critical important aspect of 3D printing, but it is often overlooked or underemphasized in product literature and by the media. 3D printing requires specific knowledge and techniques to produce a "finished" part [1]. Typically, post-processing is needed to remove support material from parts by water jet, air jet, dissolution, or other mechanical process. In the Projet 660 Pro (Fig. 1) the loose powder is removed with a brush and by air jet, and the part is posteriorly infiltrated with hardeners as cyanoacrylate, polymeric resins, or other material to increase the strength and brighten colours to get a functional component.

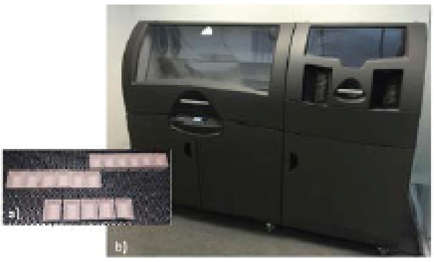

Fig. 1. a) Printed specimens; b) FEUP's ProJet 660 PRO Series machine.

This research has the following objectives:

- Feasibility of making moulds for casting aluminium by 3D printing, using the Projet 660 Pro;
- The raw material is the one recommended by the manufacturer: calcium sulphate hemihydrate 80-90% (3D Systems USA) by selective jetting of water-based binder [11]. It is known that the binder does not support high temperatures, so the research will focus on finding adequate infiltrates, in the post-processing, to provide satisfactory results for a mould with enough strength to withstand the casting of the selected aluminium alloy;
- Determine the tolerance and surface roughness of the castings.

2. Experimental work

2.1. CAD design

The experimental process began by defining a simple shape mould, as shown in Fig. 2. This geometry was initially adopted because the goal was to test different infiltrates to harden the mould. This geometry was modelled in 3D CAD software, and the internal dimensions were maintained, according to Fig. 2. Four different wall thicknesses were selected; 2.5, 3.0, 3.5 and 4.0 mm to evaluate mould resistance.

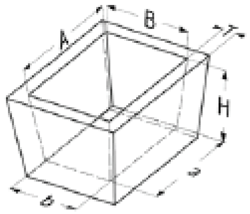

Fig. 2. Specimen shape used as mould.

2.2. AM of moulds

The CAD file was saved in a STL extension and later used along with the 3D Edit Pro 2.0 printer software; all the specimens were located in optimum position for printing. The samples were printed in different batches, and Table 1 specifies the main characteristics of the job, in terms of printing time and amount of powder and binder. It should be noted that although this printer has the possibility to print in colour, in this work, this feature was not necessary; thus, all the samples were printed in the monochrome mode, so the amount of binder basically reflects clear binder.

Table 1. Specimen printing characteristics: time, volume of powder and binder.

Wall thickness (mm)	Build time; 12 samples (min)	Volume binder/part (mL)	Volume powder/part (cm^3)
2.50	77.94	8.30	8.20
3.00	82.78	6.07	10.29
3.50	82.78	7.08	12.01
4.00	87.00	8.13	14.31

Prior to impregnation, the internal dimensions were controlled with a Vernier (for each dimension, 3 measurements were made; extremities and middle, and the average value presented in Table 2), in 4 specimens of each thickness, randomly chosen. Table 2 also indicates the average deviation (relative to the expected CAD value), allowing to verify internal dimensional accuracy in printing, and compare it with other equipment of similar characteristics [12].

Table 2. Internal dimensions of green samples and difference relative to the CAD dimensions (mm).

	CAD dimension	Average size by wall thickness				Average	Average deviation
		2.5	3.0	3.5	4.0		
A	35.00	34.94	34.99	34.99	35.00	34.98	0.02
B	25.00	24.97	24.98	25.03	24.96	24.99	0.02
a	30.00	30.15	30.14	30.07	30.12	30.12	0.02
b	20.00	20.22	20.10	20.03	20.09	20.11	0.05
H	20.00	20.48	20.32	20.26	20.25	20.33	0.08

2.3. *Impregnation*

Moulds were impregnated during different times, by full immersion with six different infiltrates: ethyl silicate (Wacker, Germany), Levasil (AkzoNovel N.V., Sweden), Ludox SK (Grace Davison, USA), Aerodisp (Evonik Industries, Germany), Ticoat-N (Rement, USA) and Zirconium acetate (Nyacol Nanotech Inc., USA), which are typically used in ceramic block moulding and investment casting [13-15].

Table 3 does not present equal number of moulds infiltrated for each thickness since some of them were destroyed during the exploratory tests with different infiltrating times, due to the lower wall thickness.

Moulds were allowed to dry at room temperature with forced air for 2h. Table 3 indicates the conditions used for all samples. Specimens without infiltrate were also used to observe the behaviour of only the printer's binder. Three different cycles (first column) were employed to check the effect of heating temperature on moulds' behaviour. The identification of the specimens "iTxx" means that "i" is the No. of specimen (Table 3), and "Txx" corresponds to the wall thicknesses.

2.4. *Mould heating and casting*

The moulds were heat treated according to a recommended heating cycle for plaster moulds used in investment casting [16,17]. Three different cycles were adopted as shown in Fig. 3; Ticoat-N and Zirconium Acetate infiltrates require sintering temperatures of 1100ºC [18], and so are only considered in cycle 3.

Table 3. Specimen's specifications.

Heat cycle nº	Spec. nº "i"	Wall thickness spec. (mm) "T"	Immersion time (s)	Type of infiltrate
1	1P	2.5	-	Without infiltrate
2	1	3.0 ; 3.5	120	Ethyl silicate*
	2	3	5	Ethyl silicate
	3	2.5 ; 3.0	120	Ethyl silicate
	4	2.5 ; 3.5	5	Levasil
	5	2.5 ; 3.5	5	Ludox SK
	6	2.5 ; 3.5	5	Aerodisp**
	7	2.5 ; 3.5	5	Aerodisp
	8	3.5	-	-
3	9	4.0	10 ; 20	Ludox SK
	10	4.0	10 ; 20	Levasil
	11	4.0	10 ; 20	Aerodisp
	12	4.0	10 ; 20	Ticoat - N
	13	4.0	10 ; 20	-
	14	4.0	10 ; 20	Zirconium acetate

* Hydrolyzed (50% ethyl silicate + 50% isopropyl alcohol silicate)
** 50% H_2O

After each thermal cycle, the furnace was turned off and the samples allowed to cool to 450ºC. The moulds were then removed and the aluminium alloy AlSi9Cu3 casted on them at 700ºC [19]. This alloy was selected because was available in INEGI and is frequently used in foundry.

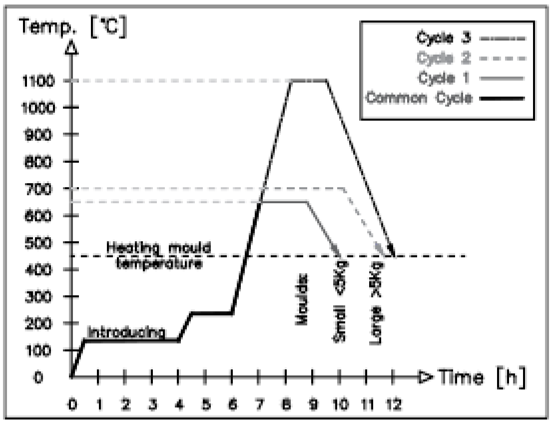

Fig. 3. Heating cycles of plaster moulds.

It should be referred that in cycles 2 and 3, at least two specimens were heated with each type of infiltrate. For each sample, one mould was kept unfilled to analyse the friability (see Fig. 4 and Table 5).

2.5. Roughness test

The roughness measurement was only performed in aluminium parts submitted to cycle 3 because this cycle produced higher moulds resistance, which is a result of using thicker walls and the best infiltrates of cycle 2. Fig. 4 shows the surface quality of casted samples. The roughness was measured 3 times, in the directions indicated with arrows, in different regions of each face indicated on Fig. 4 (X–base, Y–long side, and Z–small side).

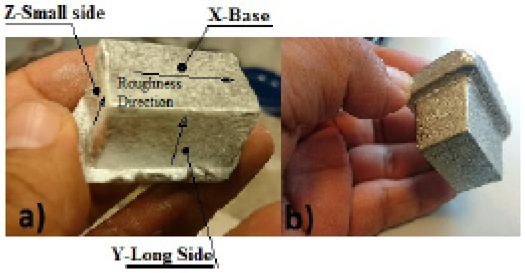

Fig. 4. Aluminium parts obtained from moulds: a) with infiltrate Ludox SK, and b) without infiltrating.

The values obtained are depicted on Table 6. The measurements on faces Y and Z were done perpendicular to the printing direction of the mould. In these directions, the roughness will be higher due to the printed layers orientation. The test was conducted in a length of 4.8 mm with a roughness meter "Hommel Werke".

3. Results and Discussion

3.1. AM of moulds and impregnation

It should be noted that moulds were printed in different positions but all of them with the same orientation, so there will be no significant differences in their mechanical resistance, as demonstrated by J. Frascati [20].

It was observed that longer immersion times, maximum 120s (depending on type of infiltrate, since not all the infiltrates allowed to work with these times), gets greater penetration into the mould, but when this time is too long, it produces a surface softening, with the consequent complication in handling.

After casting and infiltrating tests, it was possible to evaluate the thickness stability. The 4 mm wall thickness specimens kept their integrity during the casting independently of the immersion time.

Table 4 indicates the dimension control after impregnation. It presents the results of moulds that kept their integrity to cast aluminium. Fig. 5 shows the average size of the specimens indicated in Table 4, before and after impregnation. These results are relative to the second heat cycle, where most of the infiltrates were used.

It is evident, in terms of dimensional stability, that sample 1T30 in general is the best one. For example, specimen 7T3.5 (specimen nº 7 and wall thickness 3.5 mm, immersed in AERODISP®) experienced mould shrinkage, and specimen 3T2.5 immersed in pure silicate (120s in ethyl silicate) exhibited some growth.

Table 4. Internal dimensions of the moulds after impregnation (mm).

Mould dimension	Identification of specimens					
	1T3.0	3T2.5	4T2.5	5T2.5	5T3.5	7T3.5
A	34.99	35.02	34.96	35.21	35.10	34.99
B	25.02	25.07	25.05	25.07	24.91	24.90
A	30.10	30.17	30.05	30.01	29.86	30.05
B	20.20	20.18	19.93	20.03	19.97	20.04
H	20.27	20.26	20.37	20.35	20.26	20.27

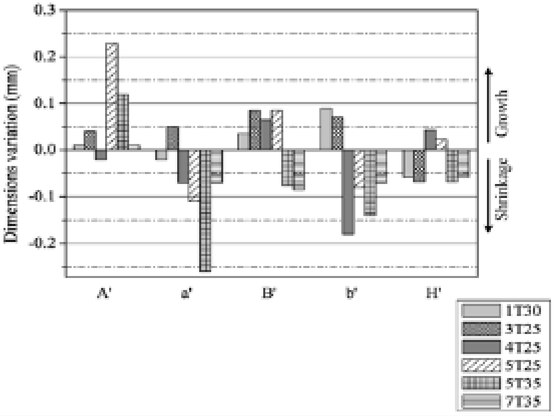

Fig. 5. Variation of the internal dimensions in specimens after impregnation (heating cycle 2).

3.2. Mould heating and casting

During casting, some problems occurred with the samples submitted to cycle 2: the height of the crucible relatively to the small moulds originated high metal impact that contributed to moulds fracture (Fig. 6). Considering this problem, for cycle 3, the moulds were enclosed with ceramic plates, the size of the crucible was reduced as well as the same height was set at 150 mm, and the mould wall thickness was increased to 4 mm; this contributed to achieve better results as shown in Fig. 6.

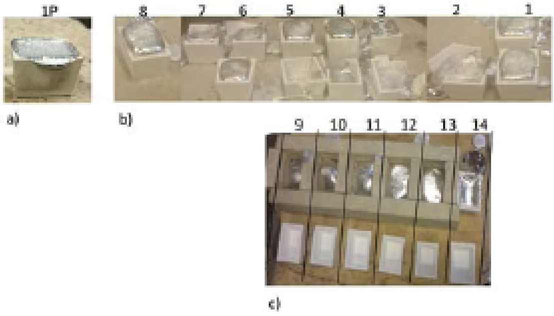

Fig. 6. Moulds submitted to heat treating: a) cycle 1, b) cycle 2 and c) cycle 3, after casting.

Table 5 indicates a friability property that uses an arbitrary scale, with values from 1 to 8, where 1 was assigned to the specimen with better consistency and 8 to the worst.

Table 5. Post-processing moulds condition.

Heat cycle n°	Spec. n°	Type of infiltrate	Infiltrate penetration after treatment	Friability
1	1P	Without infiltrate	-	4
2	1	Ethyl silicate*	poor	6
	2	Ethyl silicate	poor	7
	3	Ethyl silicate	poor	8
	4	Levasil	fair	2
	5	Ludox SK	good	1
	6	Aerodisp**	poor	3
	7	Aerodisp	poor	4
	8	Without infiltrate	-	6
3	9	Ludox SK	fair	5
	10	Levasil	fair	6
	11	Aerodisp	poor	3
	12	Ticoat - N	good	1
	13	Without infiltrate	-	7
	14	Zirconium acetate	poor	8

* Hydrolyzed (50% ethyl silicate + 50% isopropyl alcohol silicate)
** 50% H_2O

3.3. Roughness

Table 6 and Fig. 7 show the average roughness "Ra" obtained on faces X, Y and Z of aluminium specimens, with their respective standard deviations. These values are also compared with the average roughness of some other casting processes, namely investment casting CLA (counter-gravity low-pressure casting of air-melted alloys) or CLV (counter-gravity low-pressure casting of vacuum-melted alloys) with Ra=2.4 mm [21,22], and shell moulding casting with Ra=2.9 mm [22].

Table 6. Average roughness "Ra" of the specimens (µm).

Sample n°		9	10	11	12	13	14
		Ludox SK	Levasil	Aerodisp	Ticoat-N	Without infiltrating	Zirconium acetate
Side	X	10.17 ±2.02	7.99 ±0.53	11.10 ±1.06	10.33 ±2.85	12.34 ±0.75	9.88 ±9.88
	Y	9.73 ±0.76	7.88 ±1.35	7.84 ±1.23	9.64 ±1.48	7.26 ±2.15	3.24 ±0.71
	Z	6.94 ±0.40	5.96 ±0.81	7.47 ±1.19	7.05 ±1.04	6.28 ±0.61	5.10 ±1.26

In analysing the roughness of each side, Fig. 7 shows that Z-small side has less roughness, while the side offering greater roughness is X-base, and the Y-long side shows an intermediate roughness against other sides. So, for each side, the standard deviations of the roughness of different infiltrates intersect among them, which indicates, first hand, that there is no significant statistical influence of the type of infiltrate on the response of surface roughness. However, on the Y-long side, Zirconium Acetate is statistically significant.

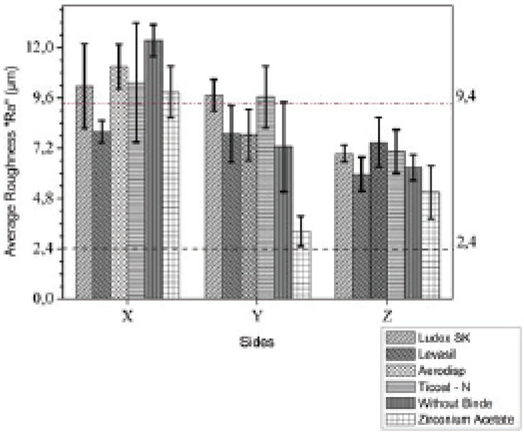

Fig. 4. Average roughness and their standard deviations of the aluminium specimens - Ra (µm).

4. Conclusions

All infiltrated moulds, reached a suitable thermal resistance to withstand the casting since none of them presented the visual sign of inflammation or burn.

The mechanical resistance of the moulds was not enough to withstand the pressure of molten metal,

especially in the wall of thickness from 2.5 to 3.5 mm. However, best results are achieved with Ludox SK, Ticoat-N, Levasil and Aerodisp, infiltrating with friability scale with designation of 1, 1, 2 and 3, respectively.

The roughness Ra is not statistically significant according to the infiltrating, with the exception being the Zirconium acetate, on the Y-Long side; X-Base is found to have the worst roughness when compared with the other faces, whereas, the Z-Small side shows the best surface roughness. This analysis also revealed that aluminium parts in almost all the cases found to be within the range of roughness, which are obtained with the traditional processes of foundry, *viz.* investment casting CLA/CLV and shell mould casting. Behaviour of infiltrated moulds, when they are heated during cycle 3, did not improve the strength of mould, as the plaster above 1000ºC changes to insoluble anhydrite at temperature in the range 380-1180ºC [23]; so, it has no significance on the sinter of the infiltrating that was intended to give in this heat cycle. Future work can be routed to search new infiltrating types that can support high temperature and also can be subjected to thermal cycles with lower temperatures.

Acknowledgements

Authors gratefully acknowledge funding of Project to Universidad de las Fuerzas Armadas ESPE, and SAESCTN-PII&DT/1/2011 co-financed by Programa Operacional Regional do Norte (ON.2 – O Novo Norte), under Quadro de Referência Estratégico Nacional (QREN), through Fundo Europeu de Desenvolvimento Regional (FEDER).

References

[1] Wohlers Associates, Wohlers Report 2015, 3D Printing and AM State of the Industry, Annual Worldwide Progress Report, 20th ed., Wohlers Associates Inc., Colorado, USA, 2015.

[2] D.P.C. Velazco, E.F. Sancet, F. Urbaneja, M. Piccico, M.F. Serra, M.F. Acebedo, N.M. Rendtorff, Ceramica 60 (2014) 465.

[3] S.C.K. Chua, K.F. Leong (Ed.), 3D Printing and Additive Manufacturing, 4th. ed., World Scientific Publishing. Co. Pte. Ltd., Singapore, 2015.

[4] M. Chhabra, R Singh, Rapid Prototyping J. 328 (2011) 350.

[5] V. Csaky, R.J. Neto, T.P. Duarte, J.L. Alves, A framework for custom design and fabrication of cranio-maxillofacial prostheses using investment casting, in Engineering Optimization IV, Rodrigues *et al.* (Ed.), Taylor & Francis Group, London, UK, 2015, pp. 941-945.

[6] F. Lino, P. Ala, R. Neto, B. Paiva, R. Paiva, R. Sousa, Proceedings of VRAP2003 - 1st International Conference on Advanced Search in Virtual and Rapid Prototyping, Leiria, Portugal, October 1-4, 2003, pp. 517-524.

[7] C. Yuan, S. Jones, J. Eur. Ceram. Soc. 23, (2003) 399.

[8] C.M. Cheah, C.K. Chua, C.W. Lee, C. Feng, K. Totong, Int. J. Adv. Des. Manuf. Technol. 25 (2004) 308.

[9] T.M. Duarte, Fabrico rápido de ferramentas por fundicão de precisão, Repositorio FEUP/DEMEGI, 2002.

[10] E. Bassoli, A. Gatto, L. Iuliano, MG. Violante, Rapid Prototyping J. 13 (2007) 3.

[11] I. Gibson, D. Rosen, B. Stucker, Binder Jetting, in Additive Manufacturing Technologies 3D Printing, Rapid Prototyping, and Direct Digital Manufacturing, Springer, New York, 2015, pp. 205-218.

[12] M. Asadi-Eydivand *et al.*, Rob. Comput. Integr. Manuf. 37 (2015) 57.

[13] S. Pattnaik, D.B. Karunakar, P.K. Jha, J. Mater. Process. Technol. 212 (2012) 2332.

[14] B. Previtali, D. Pocci, C. Taccardo, Composites, Part A 39 (2008) 10.

[15] N. Yadav *et al.*, International Journal of Emerging Technology and Advanced Engineering 3 (2013), 543.

[16] J. Nunes, MSc thesis, Faculdade de Engenharia da Universidade do Porto, Porto, Portugal, 1999.

[17] J.P. Costes, M. Bigerelle, A. Iost, Sci. Arts Métiers (2007).

[18] Yuan, C., X. Cheng, and P.A. Withey, Mater. Chem. Phys. 155 (2015) 205.

[19] V.D. Tsoukalas, Mater. Des. 29 (2008) 10.

[20] J. Frascati, MSc thesis, Department of Mechanical Materials and Aerospace Engineering, University of Central Florida, Florida, USA, 2007.

[21] I. Gibson, D. Rosen, B. Stucker (Ed.), Additive Manufacturing Technologies: 3D Printing, Rapid Prototyping, and Direct Digital Manufacturing, Springer New York, USA, 2014.

[22] M.F. Ashby, Materials Selection in Mechanical Design, 4th ed., E. Butterworth-Heinemann-Elsevier Science, Oxford, UK, 2011.

[23] R.A. Kuntze (Ed.), Gypsum: Connecting Science and Technology, ASTM International, USA, 2009.

Appendix 2 Technical data sheet of the resin Strength Max (*E1*)

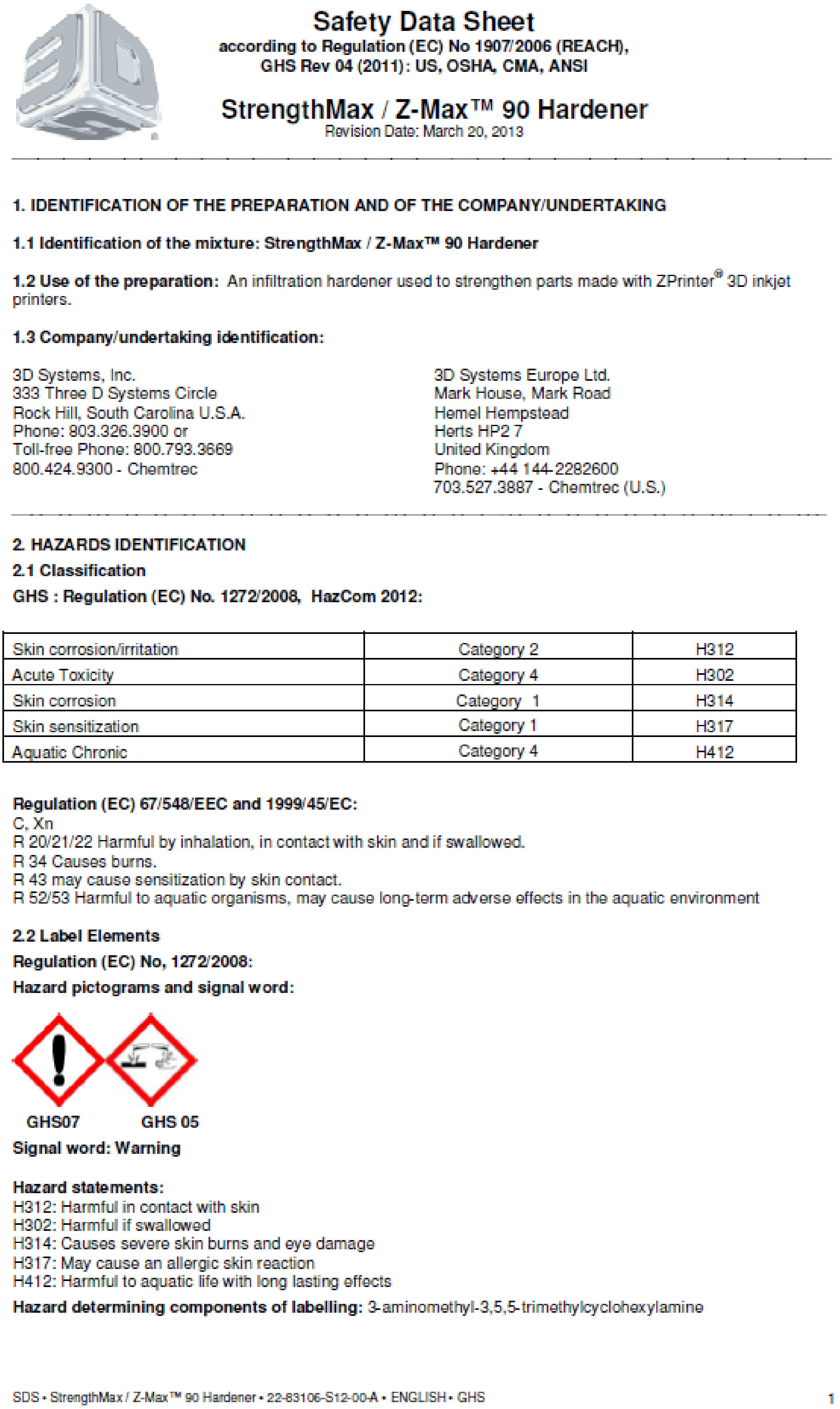

Safety Data Sheet

according to Regulation (EC) No 1907/2006 (REACH),
GHS Rev 04 (2011): US, OSHA, CMA, ANSI

StrengthMax / Z-Max™ 90 Hardener

Revision Date: March 20, 2013

1. IDENTIFICATION OF THE PREPARATION AND OF THE COMPANY/UNDERTAKING

1.1 Identification of the mixture: StrengthMax / Z-Max™ 90 Hardener

1.2 Use of the preparation: An infiltration hardener used to strengthen parts made with ZPrinter® 3D inkjet printers.

1.3 Company/undertaking identification:

3D Systems, Inc.
333 Three D Systems Circle
Rock Hill, South Carolina U.S.A.
Phone: 803.326.3900 or
Toll-free Phone: 800.793.3669
800.424.9300 - Chemtrec

3D Systems Europe Ltd.
Mark House, Mark Road
Hemel Hempstead
Herts HP2 7
United Kingdom
Phone: +44 144-2282600
703.527.3887 - Chemtrec (U.S.)

2. HAZARDS IDENTIFICATION

2.1 Classification

GHS : Regulation (EC) No. 1272/2008, HazCom 2012:

Skin corrosion/irritation	Category 2	H312
Acute Toxicity	Category 4	H302
Skin corrosion	Category 1	H314
Skin sensitization	Category 1	H317
Aquatic Chronic	Category 4	H412

Regulation (EC) 67/548/EEC and 1999/45/EC:
C, Xn
R 20/21/22 Harmful by inhalation, in contact with skin and if swallowed.
R 34 Causes burns.
R 43 may cause sensitization by skin contact.
R 52/53 Harmful to aquatic organisms, may cause long-term adverse effects in the aquatic environment

2.2 Label Elements

Regulation (EC) No, 1272/2008:

Hazard pictograms and signal word:

GHS07 **GHS 05**

Signal word: Warning

Hazard statements:
H312: Harmful in contact with skin
H302: Harmful if swallowed
H314: Causes severe skin burns and eye damage
H317: May cause an allergic skin reaction
H412: Harmful to aquatic life with long lasting effects

Hazard determining components of labelling: 3-aminomethyl-3,5,5-trimethylcyclohexylamine

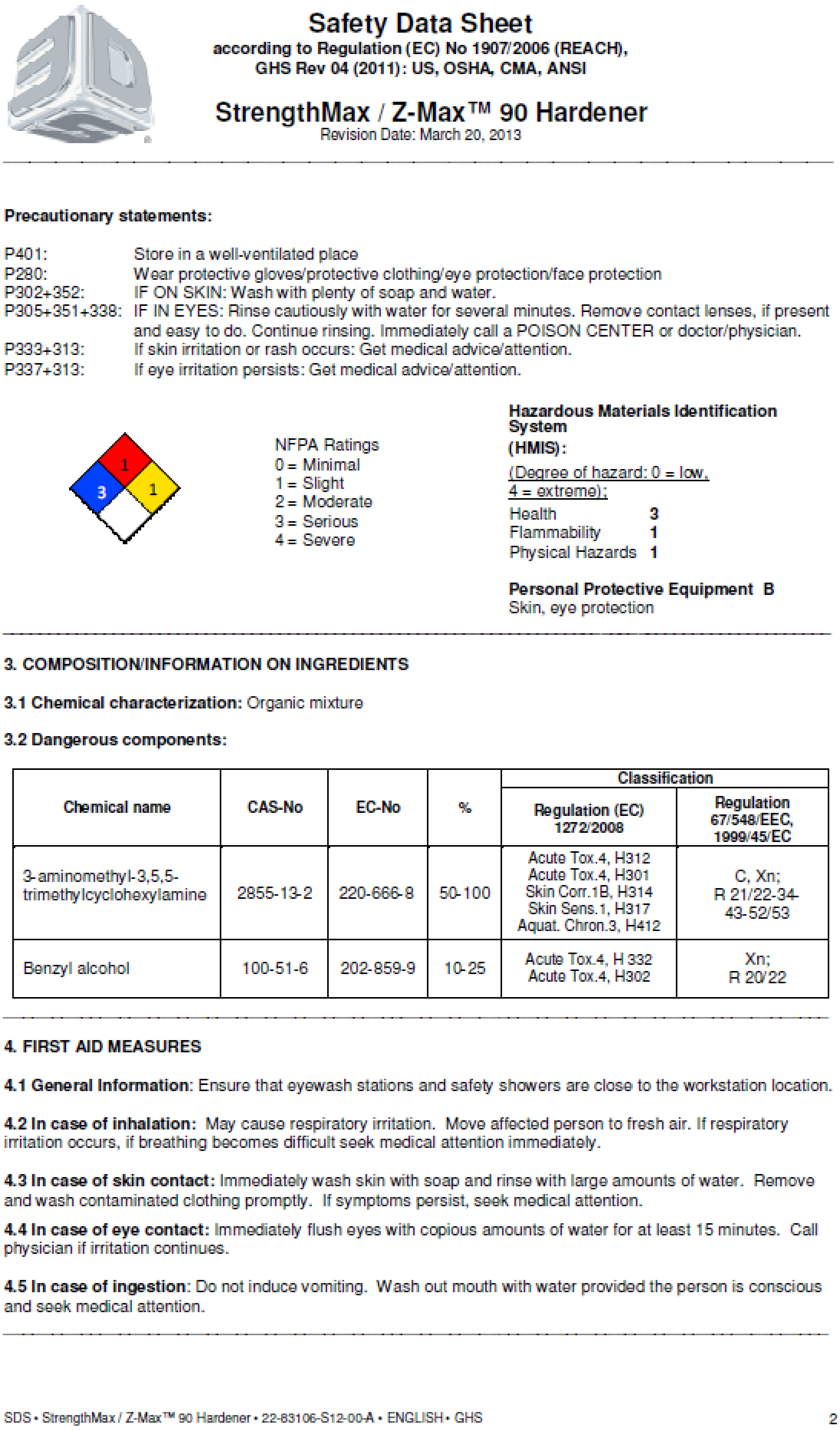

Safety Data Sheet

according to Regulation (EC) No 1907/2006 (REACH),
GHS Rev 04 (2011): US, OSHA, CMA, ANSI

StrengthMax / Z-Max™ 90 Hardener

Revision Date: March 20, 2013

Precautionary statements:

P401:	Store in a well-ventilated place
P280:	Wear protective gloves/protective clothing/eye protection/face protection
P302+352:	IF ON SKIN: Wash with plenty of soap and water.
P305+351+338:	IF IN EYES: Rinse cautiously with water for several minutes. Remove contact lenses, if present and easy to do. Continue rinsing. Immediately call a POISON CENTER or doctor/physician.
P333+313:	If skin irritation or rash occurs: Get medical advice/attention.
P337+313:	If eye irritation persists: Get medical advice/attention.

NFPA Ratings
0 = Minimal
1 = Slight
2 = Moderate
3 = Serious
4 = Severe

Hazardous Materials Identification System (HMIS):

(Degree of hazard: 0 = low, 4 = extreme);

Health	**3**
Flammability	**1**
Physical Hazards	**1**

Personal Protective Equipment B
Skin, eye protection

3. COMPOSITION/INFORMATION ON INGREDIENTS

3.1 Chemical characterization: Organic mixture

3.2 Dangerous components:

Chemical name	CAS-No	EC-No	%	Classification	
				Regulation (EC) 1272/2008	Regulation 67/548/EEC, 1999/45/EC
3-aminomethyl-3,5,5-trimethylcyclohexylamine	2855-13-2	220-666-8	50-100	Acute Tox.4, H312 Acute Tox.4, H301 Skin Corr.1B, H314 Skin Sens.1, H317 Aquat. Chron.3, H412	C, Xn; R 21/22-34-43-52/53
Benzyl alcohol	100-51-6	202-859-9	10-25	Acute Tox.4, H 332 Acute Tox.4, H302	Xn; R 20/22

4. FIRST AID MEASURES

4.1 General Information: Ensure that eyewash stations and safety showers are close to the workstation location.

4.2 In cause of inhalation: May cause respiratory irritation. Move affected person to fresh air. If respiratory irritation occurs, if breathing becomes difficult seek medical attention immediately.

4.3 In case of skin contact: Immediately wash skin with soap and rinse with large amounts of water. Remove and wash contaminated clothing promptly. If symptoms persist, seek medical attention.

4.4 In case of eye contact: Immediately flush eyes with copious amounts of water for at least 15 minutes. Call physician if irritation continues.

4.5 In case of ingestion: Do not induce vomiting. Wash out mouth with water provided the person is conscious and seek medical attention.

Safety Data Sheet

according to Regulation (EC) No 1907/2006 (REACH),
GHS Rev 04 (2011): US, OSHA, CMA, ANSI

StrengthMax / Z-Max™ 90 Hardener

Revision Date: March 20, 2013

5. FIRE-FIGHTING MEASURES

5.1 Suitable extinguishing media: Water mist, dry chemical, carbon dioxide, or appropriate foam.

5.2 Extinguishing media which must not be used for safety reasons: High volume water jet.

5.3 Special exposure hazards arising from the substance or preparation itself, combustion products, resulting gases: Thermal decomposition products can include CO_2, CO, NO_x and smoke.

5.4 Special protective equipment for fire-fighters: Wear full protective clothing, including helmet, self-contained positive-pressure or pressure demand breathing apparatus, protective clothing and facemask.

6. ACCIDENTAL RELEASE MEASURES

6.1. Personal precautions: Keep unnecessary personnel away. Wear appropriate protective equipment and clothing. Consult expert immediately.

6.2 Environmental precautions: Do not allow product to enter sewage systems, surface water or ground water.

6.3 Methods for cleaning up: Absorb product with liquid-binding material such as diatomite, sand, acid binders, universal binders, sawdust. Do not flush down drains. Place in closed containers. Ventilate area and wash spill site after material pickup is complete.

6.4. Waste Disposal Method: Follow safe solid waste disposal guidelines in accordance with federal, state and local regulations. National or regional provisions may also be in force. It is the responsibility of the generator to determine whether the material meets the criteria of a hazardous waste.

7. HANDLING AND STORAGE

7.1 Handling: Provide adequate ventilation. Use suitable protective equipment. Avoid contact with skin and eyes. Do not breathe vapors or mist. Avoid ignition sources. Do not allow to enter drains or watercourses.

7.2 Storage: Store sealed in the original container at room temperature. Keep this material indoors in a cool, dry, well ventilated place.

8. EXPOSURE CONTROLS / PERSONAL PROTECTION

8.1 Exposure limit values:

Component	Component Manufacturer IEL (Internal Exposure Limit)
3-aminomethyl-3,5,5-trimethylcyclohexylamine	NA
Benzyl alcohol	NA

8.2 Exposure controls

Technical measures to prevent exposure: Use explosion-proof local exhaust ventilation.
Instructual measures to prevent exposure: When using, do not eat, drink or smoke. Wash hands after handling and before eating, smoking and using the lavatory and at the end of the day.
Personal protection equipment:
Respiratory protection: If ventilation cannot effectively keep vapor concentrations below established limits, appropriate certified respiratory protection must be provided (respirator FFP3).
Hand protection: Use impervious Neoprene gloves.
Eye protection: Wear safety glasses or chemical goggles.
Body protection: Use apron and closed shoes.

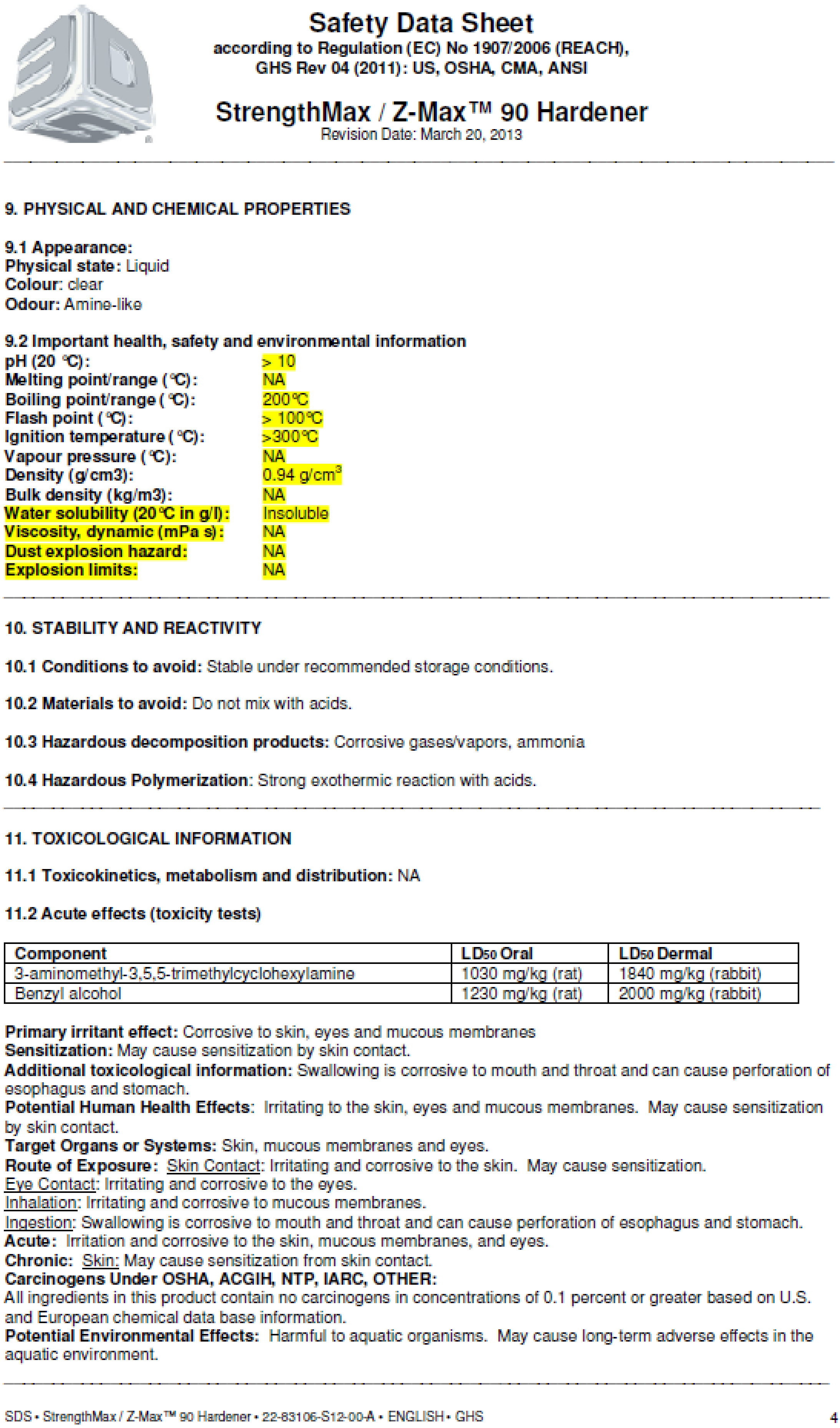

Safety Data Sheet

according to Regulation (EC) No 1907/2006 (REACH),
GHS Rev 04 (2011): US, OSHA, CMA, ANSI

StrengthMax / Z-Max™ 90 Hardener

Revision Date: March 20, 2013

9. PHYSICAL AND CHEMICAL PROPERTIES

9.1 Appearance:
Physical state: Liquid
Colour: clear
Odour: Amine-like

9.2 Important health, safety and environmental information

pH (20 °C):	> 10
Melting point/range (°C):	NA
Boiling point/range (°C):	200°C
Flash point (°C):	> 100°C
Ignition temperature (°C):	>300°C
Vapour pressure (°C):	NA
Density (g/cm3):	0.94 g/cm^3
Bulk density (kg/m3):	NA
Water solubility (20°C in g/l):	Insoluble
Viscosity, dynamic (mPa s):	NA
Dust explosion hazard:	NA
Explosion limits:	NA

10. STABILITY AND REACTIVITY

10.1 Conditions to avoid: Stable under recommended storage conditions.

10.2 Materials to avoid: Do not mix with acids.

10.3 Hazardous decomposition products: Corrosive gases/vapors, ammonia

10.4 Hazardous Polymerization: Strong exothermic reaction with acids.

11. TOXICOLOGICAL INFORMATION

11.1 Toxicokinetics, metabolism and distribution: NA

11.2 Acute effects (toxicity tests)

Component	LD50 Oral	LD50 Dermal
3-aminomethyl-3,5,5-trimethylcyclohexylamine	1030 mg/kg (rat)	1840 mg/kg (rabbit)
Benzyl alcohol	1230 mg/kg (rat)	2000 mg/kg (rabbit)

Primary irritant effect: Corrosive to skin, eyes and mucous membranes
Sensitization: May cause sensitization by skin contact.
Additional toxicological information: Swallowing is corrosive to mouth and throat and can cause perforation of esophagus and stomach.
Potential Human Health Effects: Irritating to the skin, eyes and mucous membranes. May cause sensitization by skin contact.
Target Organs or Systems: Skin, mucous membranes and eyes.
Route of Exposure: Skin Contact: Irritating and corrosive to the skin. May cause sensitization.
Eye Contact: Irritating and corrosive to the eyes.
Inhalation: Irritating and corrosive to mucous membranes.
Ingestion: Swallowing is corrosive to mouth and throat and can cause perforation of esophagus and stomach.
Acute: Irritation and corrosive to the skin, mucous membranes, and eyes.
Chronic: Skin: May cause sensitization from skin contact.
Carcinogens Under OSHA, ACGIH, NTP, IARC, OTHER:
All ingredients in this product contain no carcinogens in concentrations of 0.1 percent or greater based on U.S. and European chemical data base information.
Potential Environmental Effects: Harmful to aquatic organisms. May cause long-term adverse effects in the aquatic environment.

Appendix 3 Technical data sheet of the resin Biresin CR83-6 (*E2*)

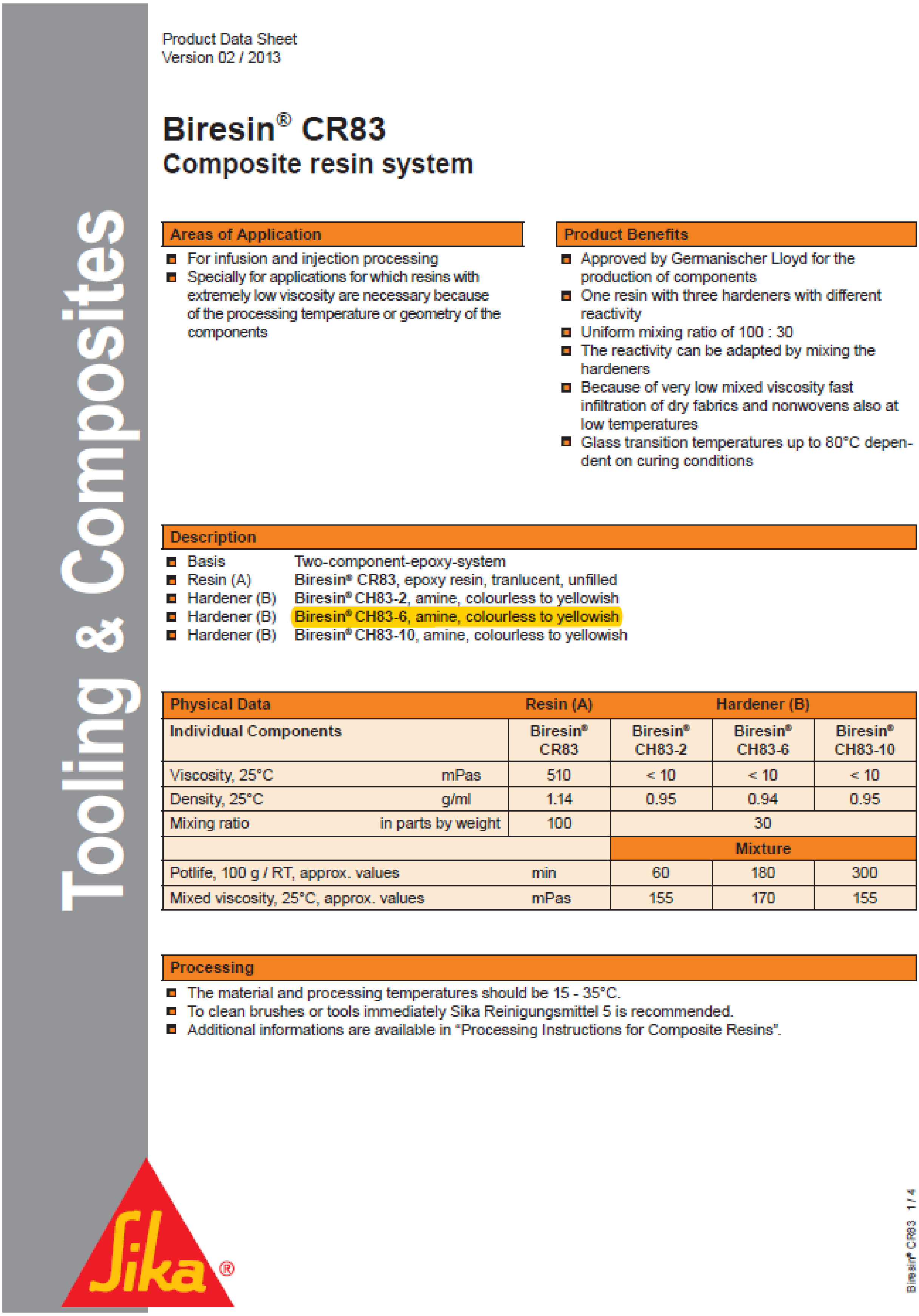

Tooling & Composites

Product Data Sheet
Version 02 / 2013

Biresin® CR83
Composite resin system

Areas of Application

- For infusion and injection processing
- Specially for applications for which resins with extremely low viscosity are necessary because of the processing temperature or geometry of the components

Product Benefits

- Approved by Germanischer Lloyd for the production of components
- One resin with three hardeners with different reactivity
- Uniform mixing ratio of 100 : 30
- The reactivity can be adapted by mixing the hardeners
- Because of very low mixed viscosity fast infiltration of dry fabrics and nonwovens also at low temperatures
- Glass transition temperatures up to 80°C dependent on curing conditions

Description

Basis	Two-component-epoxy-system
Resin (A)	Biresin® CR83, epoxy resin, tranlucent, unfilled
Hardener (B)	Biresin® CH83-2, amine, colourless to yellowish
Hardener (B)	Biresin® CH83-6, amine, colourless to yellowish
Hardener (B)	Biresin® CH83-10, amine, colourless to yellowish

Physical Data		Resin (A)	Hardener (B)		
Individual Components		Biresin® CR83	Biresin® CH83-2	Biresin® CH83-6	Biresin® CH83-10
Viscosity, 25°C	mPas	510	< 10	< 10	< 10
Density, 25°C	g/ml	1.14	0.95	0.94	0.95
Mixing ratio	in parts by weight	100	30		
			Mixture		
Potlife, 100 g / RT, approx. values	min		60	180	300
Mixed viscosity, 25°C, approx. values	mPas		155	170	155

Processing

- The material and processing temperatures should be 15 - 35°C.
- To clean brushes or tools immediately Sika Reinigungsmittel 5 is recommended.
- Additional informations are available in “Processing Instructions for Composite Resins”.

Biresin® CR83 1 / 4

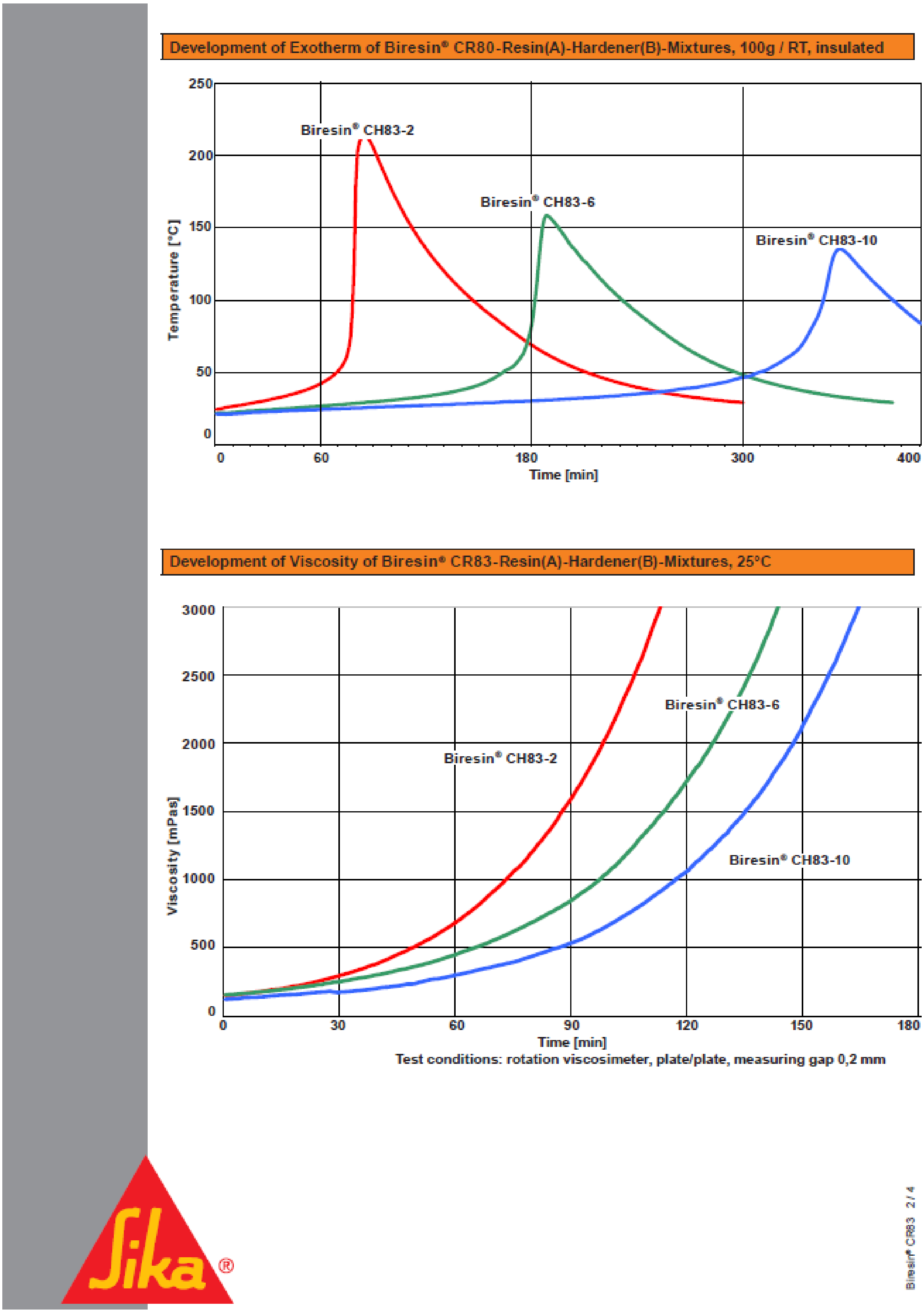

Development of Exotherm of Biresin® CR80-Resin(A)-Hardener(B)-Mixtures, 100g / RT, insulated

Development of Viscosity of Biresin® CR83-Resin(A)-Hardener(B)-Mixtures, 25°C

Test conditions: rotation viscosimeter, plate/plate, measuring gap 0,2 mm

Mechanical Data, neat resin specimen at different post curing conditions

Part 1: approx. values after 12 h / 55°C (source: Sika internal)

Biresin® CR83 resin (A)	with hardener (B) Biresin®		CH83-2	CH83-6	CH83-10
Density	ISO 1183	g/cm^3	1.15	1.15	1.15
Flexural-E-Modul	ISO 178	MPa	3,150	3,250	3,200
Tensile-E-Modul	ISO 527-2	MPa	3,300	3,300	3,350
Flexural strength	ISO 178	MPa	122	126	123
Tensile strength	ISO 527-2	MPa	88	93	91
Elongation at break	ISO 527-2	%	6,7	6,7	6,5
Water absorption after 7 d	ISO 175	%	0.50	0.44	0.42

Part 2: approx. values after 8 h / 70°C (source: Sika internal)

Biresin® CR83 resin (A)	with hardener (B) Biresin®		CH83-2	CH83-6	CH83-10
Shore-hardness	ISO 868		D 85	D 85	D 85
Density	ISO 1183	g/cm^3	1.15	1.15	1.15
Flexural E-Modulus	ISO 178	MPa	3,125	3,360	3,340
Tensile E-Modulus	ISO 527	MPa	2,960	3,200	3,100
Flexural strength	ISO 178	MPa	129	134	131
Elongation at break	ISO 527	%	4.7	8.4	7.9
Tensile strength	ISO 527	MPa	84	91	86
Impact resistance	ISO 179	kJ/m^2	93	84	83
Compressive strength	ISO 604	N/mm^2	107	111	109

Thermal data of neat resin specimen at different post curing conditions

Biresin® CR83 resin (A)	with hardener (B) Biresin®			CH83-2	CH83-6	CH83-10
	Post curing conditions					
Heat distortion temperature	12 h/55°C	ISO 75A	°C	74	72	73
	8 h/70°C	ISO 75A	°C	79	79	78
	8 h/70°C	ISO 75B	°C	83	83	83
Glass transition temperature		ISO 11357	°C	84	80	81

Packaging

Individual components	**Biresin® CR83 resin (A)**	200 kg; 10 kg net
	Biresin® CH83-2, CH83-6, CH83-10 hardener (B)	20 kg; 3.0 kg net

Storage

- Minimum shelf life of Biresin® CR83 resin (A) is 24 month and of Biresin® CH83-2, CH83-6 and CH83-10 hardener (B) is 12 month under room conditions (18 - 25°C), when stored in original unopened containers.
- The tendence of cristallisation with this system is very low. However, if cristallisation of the resin component appears, it can be easily removed by warming up the resin for a sufficient time to 50-60°C.
- Containers must be closed tightly immediately after use. The residual material needs to be used up as soon as possible.

Appendix 4 Technical data sheet of the resin Elantas EC131LV / W342 (*E3*)

ELANTAS

EN **Product Information**

Elan-tech ®
EC 131LV/W 342
100:25 by weight

2. IDENTIFICACION DE LOS PELIGROS.

El producto en contacto con los ojos provoca irritaciones que pueden perdurar màs de 24 horas y, en contacto con la piel, provoca inflamaciòn si no se quita ràpidamente.
El producto en contacto con la piel puede provocar sensibilizaciòn cutànea.
El producto es peligroso para el medio ambiente, siendo toxico para los organismos aquàticos en caso de exposicion intensa.
El producto puede provocar a largo plazo efectos negativos para el medio ambiente acuático, siendo dificilmente biodegradable.

3. COMPOSICION/INFORMACION SOBRE LOS INGREDIENTES

Contiene sustancias peligrosas según la directiva 67/548/CEE o por las cuales existen limites de exposición comunitarios:
75% - 100% producto de reacción: bisfenol-A-epiclorhidrina
N.67/548/EEC: 603-074-00-8 CAS: 25068-38-6 EC: 500-033-5
Xi,N; R36/38-43-51-53
10% - 20% Polipropilenglicole
CAS: 25322-69-4
Xn; R22
5% - 10% 1-(2,3-epoxipropoxi)-2,2-bis[(2,3-epoxipropoxi)metil]butano
CAS: 3454-29-3 EC: 222-384-0
Xi,N; R36/38-43-51-53
5% - 10% 1,4-bis(2,3-epoxipropoxi)butano
N.67/548/EEC: 603-072-00-7 CAS: 2425-79-8 EC: 219-371-7
Xn,Xi; R20/21-36/38-43

4. MEDIDAS DE PRIMEROS AUXILIOS

Sales office South Europe:
ELANTAS Italia S.r.l.
Strada Antolini n° 1 loc. Lemignano
43044 Collecchio (PR)
Italy
Tel +39 0521 304711
Fax +39 0521 804410
EEMEurope.ELANTAS@altana.com
www.elantas.com

Sales office North Europe:
ELANTAS Beck GmbH
Grossmannstr. 105
20539 Hamburg
Germany
Tel +49 40 78946 0
Fax +49 40 78946 349
info.elantas.beck@altana.com
www.elantas.com

A member of ALTANA

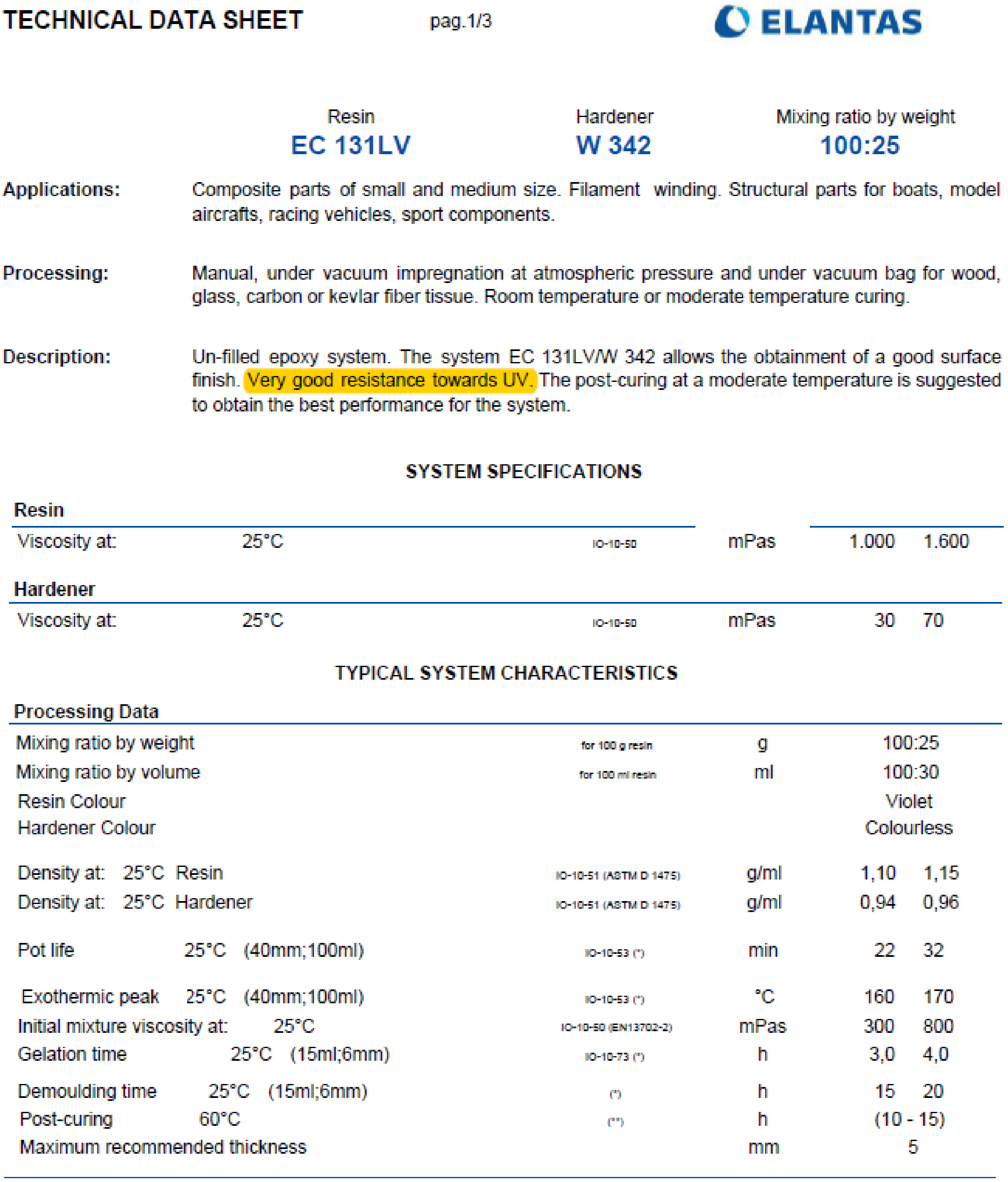

TECHNICAL DATA SHEET pag.1/3 ELANTAS

Resin	Hardener	Mixing ratio by weight
EC 131LV	**W 342**	**100:25**

Applications: Composite parts of small and medium size. Filament winding. Structural parts for boats, model aircrafts, racing vehicles, sport components.

Processing: Manual, under vacuum impregnation at atmospheric pressure and under vacuum bag for wood, glass, carbon or kevlar fiber tissue. Room temperature or moderate temperature curing.

Description: Un-filled epoxy system. The system EC 131LV/W 342 allows the obtainment of a good surface finish. Very good resistance towards UV. The post-curing at a moderate temperature is suggested to obtain the best performance for the system.

SYSTEM SPECIFICATIONS

Resin					
Viscosity at:	25°C	IO-10-50	mPas	1.000	1.600
Hardener					
Viscosity at:	25°C	IO-10-50	mPas	30	70

TYPICAL SYSTEM CHARACTERISTICS

Processing Data					
Mixing ratio by weight		for 100 g resin	g	100:25	
Mixing ratio by volume		for 100 ml resin	ml	100:30	
Resin Colour				Violet	
Hardener Colour				Colourless	
Density at:	25°C Resin	IO-10-51 (ASTM D 1475)	g/ml	1,10	1,15
Density at:	25°C Hardener	IO-10-51 (ASTM D 1475)	g/ml	0,94	0,96
Pot life	25°C (40mm;100ml)	IO-10-53 (*)	min	22	32
Exothermic peak	25°C (40mm;100ml)	IO-10-53 (*)	°C	160	170
Initial mixture viscosity at:	25°C	IO-10-50 (EN13702-2)	mPas	300	800
Gelation time	25°C (15ml;6mm)	IO-10-73 (*)	h	3,0	4,0
Demoulding time	25°C (15ml;6mm)	(*)	h	15	20
Post-curing	60°C	(**)	h	(10 - 15)	
Maximum recommended thickness			mm	5	

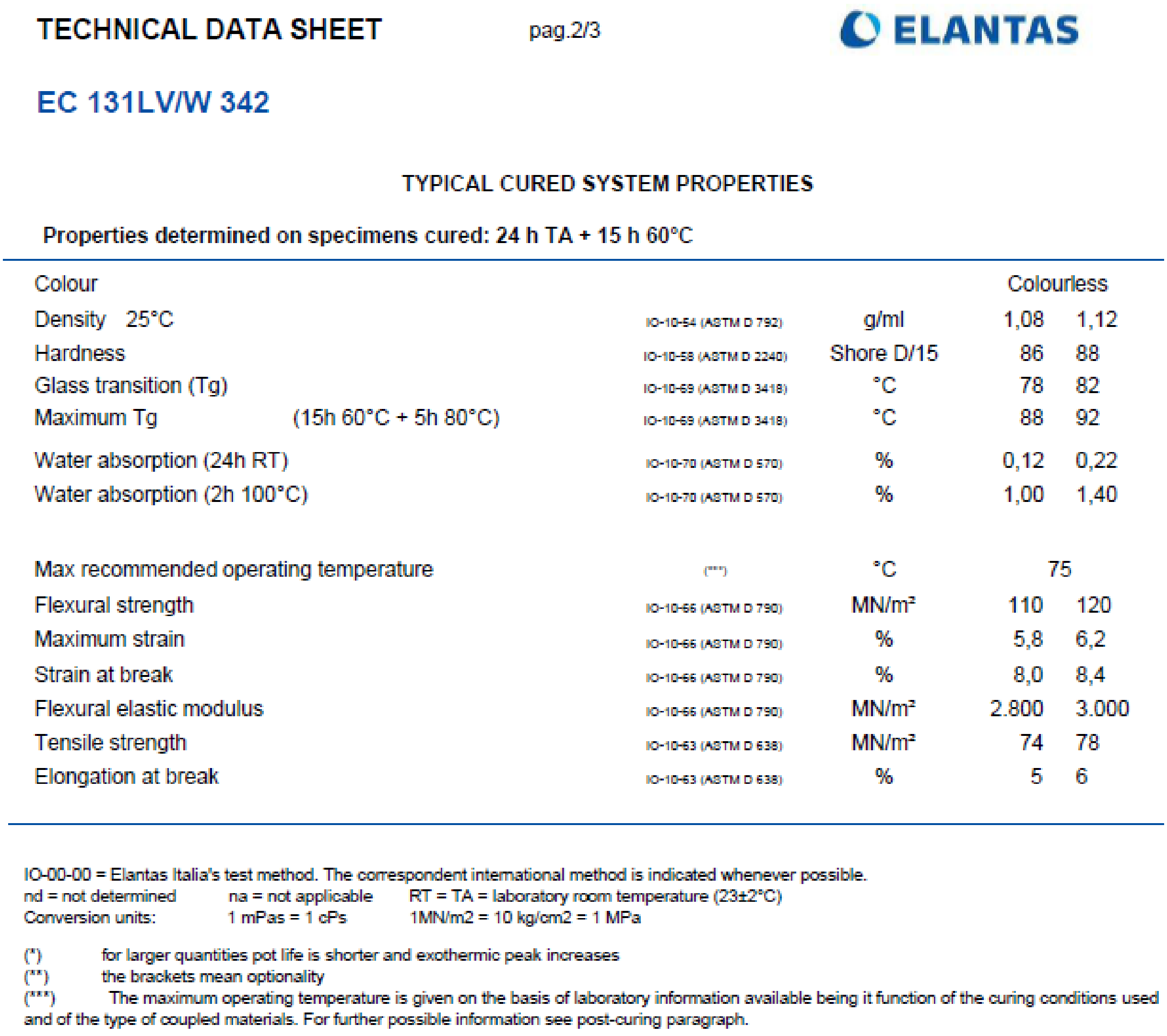

TECHNICAL DATA SHEET pag.2/3 ELANTAS

EC 131LV/W 342

TYPICAL CURED SYSTEM PROPERTIES

Properties determined on specimens cured: 24 h TA + 15 h 60°C

Colour				Colourless	
Density 25°C		IO-10-54 (ASTM D 792)	g/ml	1,08	1,12
Hardness		IO-10-58 (ASTM D 2240)	Shore D/15	86	88
Glass transition (Tg)		IO-10-69 (ASTM D 3418)	°C	78	82
Maximum Tg	(15h 60°C + 5h 80°C)	IO-10-69 (ASTM D 3418)	°C	88	92
Water absorption (24h RT)		IO-10-70 (ASTM D 570)	%	0,12	0,22
Water absorption (2h 100°C)		IO-10-70 (ASTM D 570)	%	1,00	1,40
Max recommended operating temperature		(***)	°C	75	
Flexural strength		IO-10-66 (ASTM D 790)	MN/m²	110	120
Maximum strain		IO-10-66 (ASTM D 790)	%	5,8	6,2
Strain at break		IO-10-66 (ASTM D 790)	%	8,0	8,4
Flexural elastic modulus		IO-10-66 (ASTM D 790)	MN/m²	2.800	3.000
Tensile strength		IO-10-63 (ASTM D 638)	MN/m²	74	78
Elongation at break		IO-10-63 (ASTM D 638)	%	5	6

IO-00-00 = Elantas Italia's test method. The correspondent international method is indicated whenever possible.
nd = not determined na = not applicable RT = TA = laboratory room temperature (23±2°C)
Conversion units: 1 mPas = 1 cPs 1MN/m2 = 10 kg/cm2 = 1 MPa

(*) for larger quantities pot life is shorter and exothermic peak increases
(**) the brackets mean optionality
(***) The maximum operating temperature is given on the basis of laboratory information available being it function of the curing conditions used and of the type of coupled materials. For further possible information see post-curing paragraph.

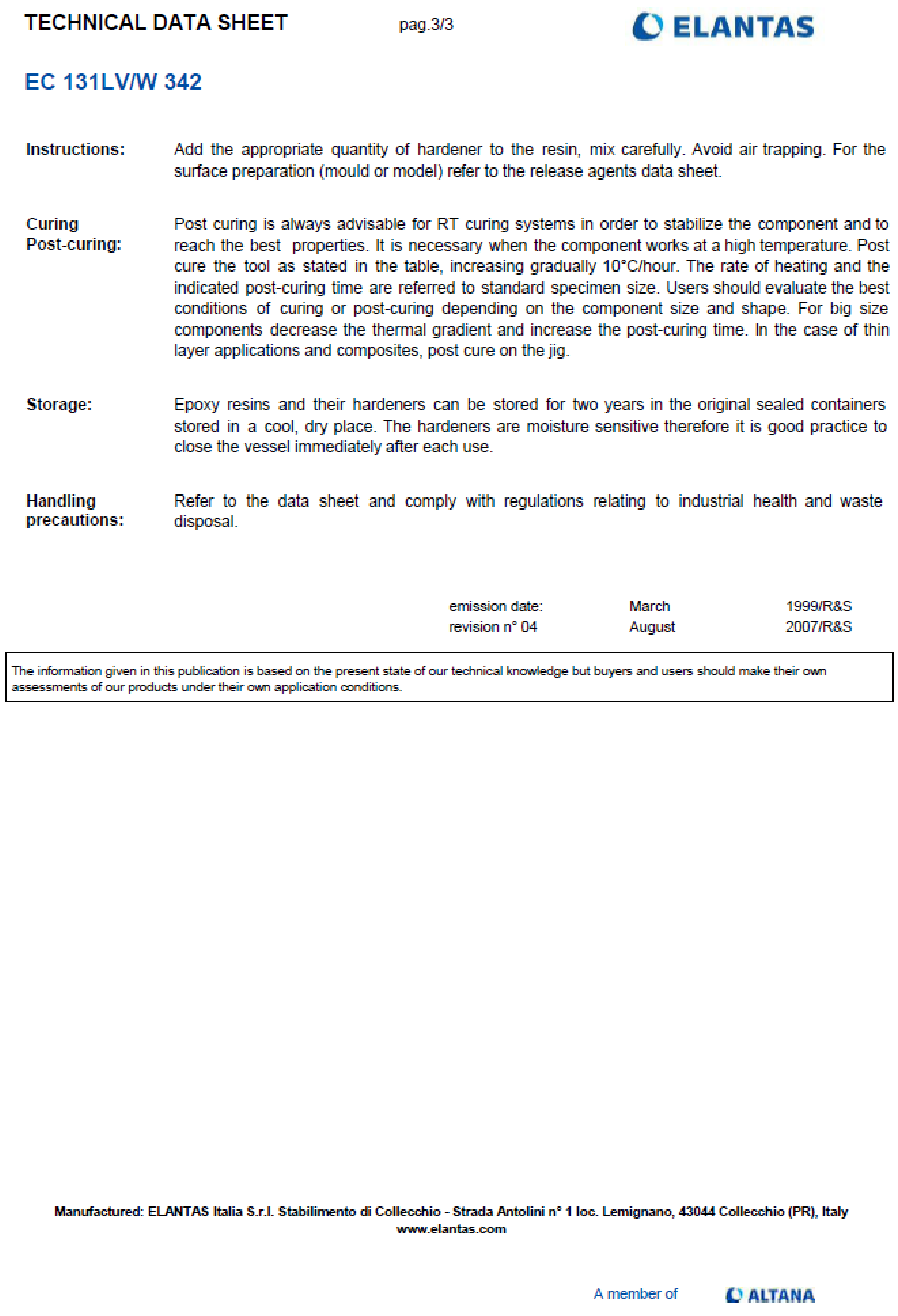

TECHNICAL DATA SHEET pag.3/3 ELANTAS

EC 131LV/W 342

Instructions:	Add the appropriate quantity of hardener to the resin, mix carefully. Avoid air trapping. For the surface preparation (mould or model) refer to the release agents data sheet.
Curing Post-curing:	Post curing is always advisable for RT curing systems in order to stabilize the component and to reach the best properties. It is necessary when the component works at a high temperature. Post cure the tool as stated in the table, increasing gradually 10°C/hour. The rate of heating and the indicated post-curing time are referred to standard specimen size. Users should evaluate the best conditions of curing or post-curing depending on the component size and shape. For big size components decrease the thermal gradient and increase the post-curing time. In the case of thin layer applications and composites, post cure on the jig.
Storage:	Epoxy resins and their hardeners can be stored for two years in the original sealed containers stored in a cool, dry place. The hardeners are moisture sensitive therefore it is good practice to close the vessel immediately after each use.
Handling precautions:	Refer to the data sheet and comply with regulations relating to industrial health and waste disposal.

emission date:	March	1999/R&S
revision n° 04	August	2007/R&S

Manufactured: ELANTAS Italia S.r.l. Stabilimento di Collecchio - Strada Antolini n° 1 loc. Lemignano, 43044 Collecchio (PR), Italy
www.elantas.com

A member of ALTANA

Appendix 5 Technical data sheet of the resin Crystal Clear 200 (*U*)

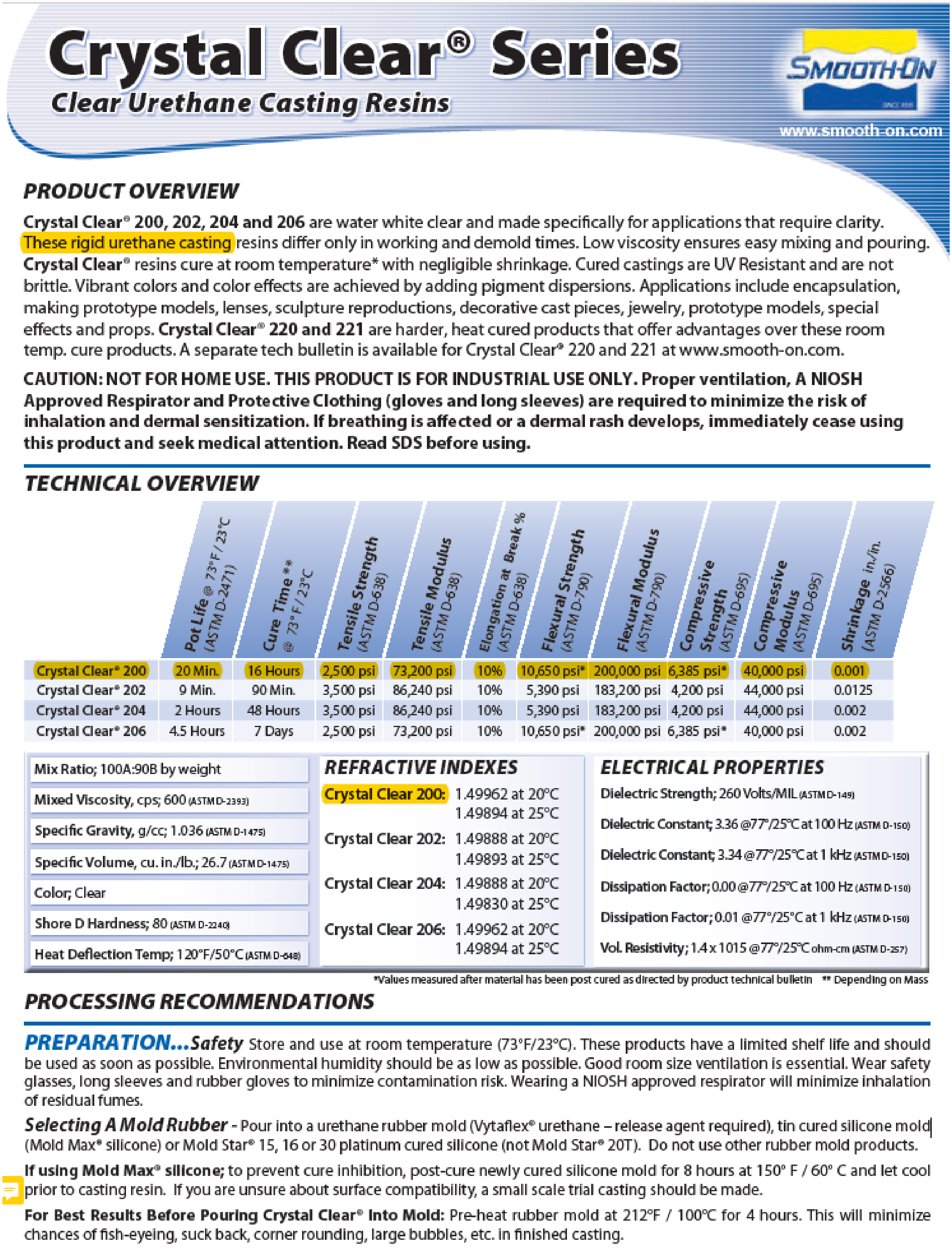

Crystal Clear® Series

Clear Urethane Casting Resins

www.smooth-on.com

PRODUCT OVERVIEW

Crystal Clear® 200, 202, 204 and 206 are water white clear and made specifically for applications that require clarity. These rigid urethane casting resins differ only in working and demold times. Low viscosity ensures easy mixing and pouring. **Crystal Clear®** resins cure at room temperature* with negligible shrinkage. Cured castings are UV Resistant and are not brittle. Vibrant colors and color effects are achieved by adding pigment dispersions. Applications include encapsulation, making prototype models, lenses, sculpture reproductions, decorative cast pieces, jewelry, prototype models, special effects and props. **Crystal Clear® 220 and 221** are harder, heat cured products that offer advantages over these room temp. cure products. A separate tech bulletin is available for Crystal Clear® 220 and 221 at www.smooth-on.com.

CAUTION: NOT FOR HOME USE. THIS PRODUCT IS FOR INDUSTRIAL USE ONLY. Proper ventilation, A NIOSH Approved Respirator and Protective Clothing (gloves and long sleeves) are required to minimize the risk of inhalation and dermal sensitization. If breathing is affected or a dermal rash develops, immediately cease using this product and seek medical attention. Read SDS before using.

TECHNICAL OVERVIEW

	Pot Life @ 73°F / 23°C (ASTM D-2471)	Cure Time ** @ 73°F / 23°C	Tensile Strength (ASTM D-638)	Tensile Modulus (ASTM D-638)	Elongation at Break % (ASTM D-638)	Flexural Strength (ASTM D-790)	Flexural Modulus (ASTM D-790)	Compressive Strength (ASTM D-695)	Compressive Modulus (ASTM D-695)	Shrinkage in./in. (ASTM D-2566)
Crystal Clear® 200	20 Min.	16 Hours	2,500 psi	73,200 psi	10%	10,650 psi*	200,000 psi	6,385 psi*	40,000 psi	0.001
Crystal Clear® 202	9 Min.	90 Min.	3,500 psi	86,240 psi	10%	5,390 psi	183,200 psi	4,200 psi	44,000 psi	0.0125
Crystal Clear® 204	2 Hours	48 Hours	3,500 psi	86,240 psi	10%	5,390 psi	183,200 psi	4,200 psi	44,000 psi	0.002
Crystal Clear® 206	4.5 Hours	7 Days	2,500 psi	73,200 psi	10%	10,650 psi*	200,000 psi	6,385 psi*	40,000 psi	0.002

Mix Ratio; 100A:90B by weight

Mixed Viscosity, cps; 600 (ASTM D-2393)

Specific Gravity, g/cc; 1.036 (ASTM D-1475)

Specific Volume, cu. in./lb.; 26.7 (ASTM D-1475)

Color; Clear

Shore D Hardness; 80 (ASTM D-2240)

Heat Deflection Temp; 120°F/50°C (ASTM D-648)

REFRACTIVE INDEXES

Crystal Clear 200:	1.49962 at 20°C 1.49894 at 25°C
Crystal Clear 202:	1.49888 at 20°C 1.49893 at 25°C
Crystal Clear 204:	1.49888 at 20°C 1.49830 at 25°C
Crystal Clear 206:	1.49962 at 20°C 1.49894 at 25°C

ELECTRICAL PROPERTIES

Dielectric Strength; 260 Volts/MIL (ASTM D-149)

Dielectric Constant; 3.36 @77°/25°C at 100 Hz (ASTM D-150)

Dielectric Constant; 3.34 @77°/25°C at 1 kHz (ASTM D-150)

Dissipation Factor; 0.00 @77°/25°C at 100 Hz (ASTM D-150)

Dissipation Factor; 0.01 @77°/25°C at 1 kHz (ASTM D-150)

Vol. Resistivity; 1.4 x 1015 @77°/25°C ohm-cm (ASTM D-257)

*Values measured after material has been post cured as directed by product technical bulletin ** Depending on Mass

PROCESSING RECOMMENDATIONS

PREPARATION...Safety Store and use at room temperature (73°F/23°C). These products have a limited shelf life and should be used as soon as possible. Environmental humidity should be as low as possible. Good room size ventilation is essential. Wear safety glasses, long sleeves and rubber gloves to minimize contamination risk. Wearing a NIOSH approved respirator will minimize inhalation of residual fumes.

Selecting A Mold Rubber - Pour into a urethane rubber mold (Vytaflex® urethane – release agent required), tin cured silicone mold (Mold Max® silicone) or Mold Star® 15, 16 or 30 platinum cured silicone (not Mold Star® 20T). Do not use other rubber mold products.

If using Mold Max® silicone; to prevent cure inhibition, post-cure newly cured silicone mold for 8 hours at 150° F / 60° C and let cool prior to casting resin. If you are unsure about surface compatibility, a small scale trial casting should be made.

For Best Results Before Pouring Crystal Clear® Into Mold: Pre-heat rubber mold at 212°F / 100°C for 4 hours. This will minimize chances of fish-eyeing, suck back, corner rounding, large bubbles, etc. in finished casting.

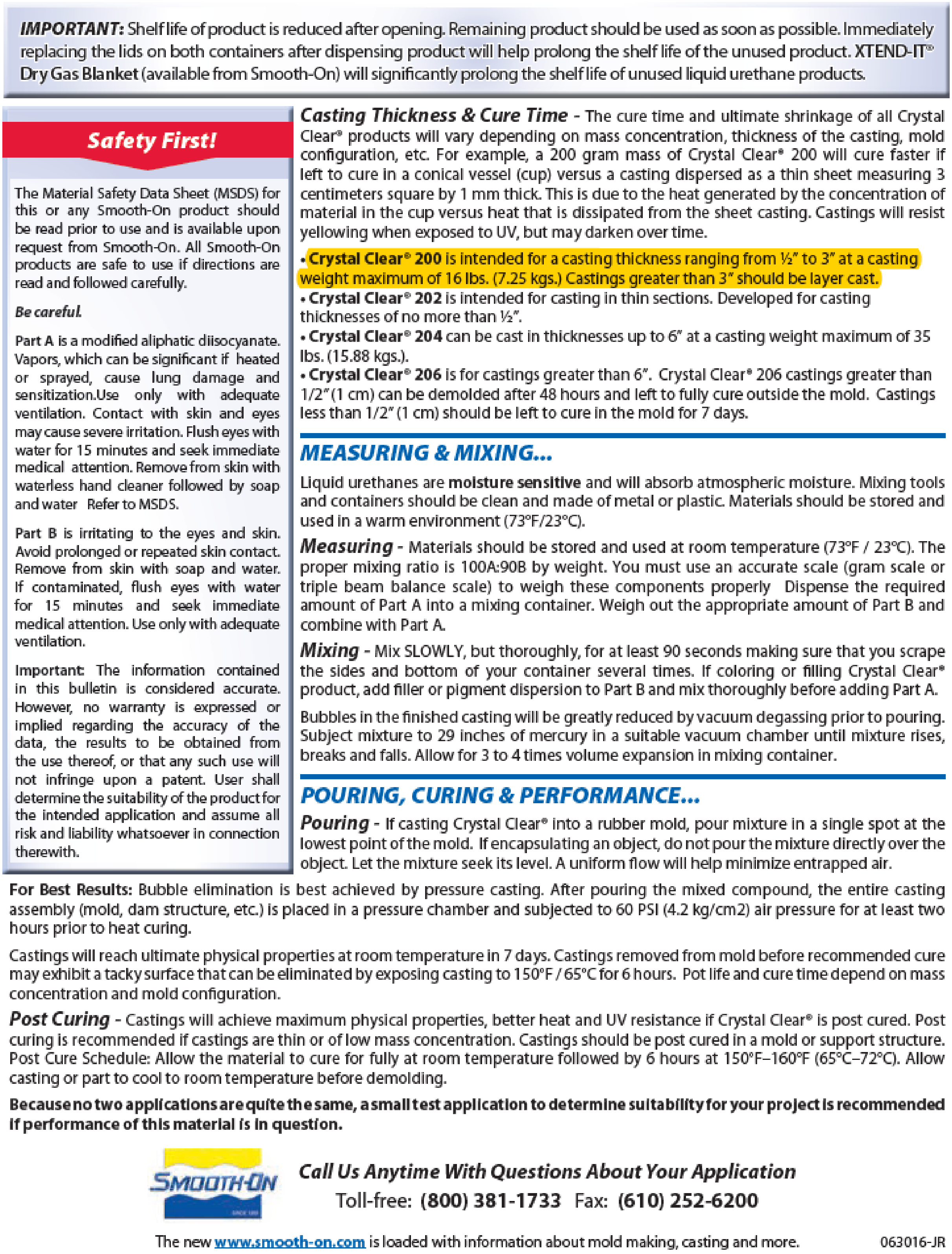

IMPORTANT: Shelf life of product is reduced after opening. Remaining product should be used as soon as possible. Immediately replacing the lids on both containers after dispensing product will help prolong the shelf life of the unused product. **XTEND-IT® Dry Gas Blanket** (available from Smooth-On) will significantly prolong the shelf life of unused liquid urethane products.

Safety First!

The Material Safety Data Sheet (MSDS) for this or any Smooth-On product should be read prior to use and is available upon request from Smooth-On. All Smooth-On products are safe to use if directions are read and followed carefully.

Be careful.

Part A is a modified aliphatic diisocyanate. Vapors, which can be significant if heated or sprayed, cause lung damage and sensitization.Use only with adequate ventilation. Contact with skin and eyes may cause severe irritation. Flush eyes with water for 15 minutes and seek immediate medical attention. Remove from skin with waterless hand cleaner followed by soap and water Refer to MSDS.

Part B is irritating to the eyes and skin. Avoid prolonged or repeated skin contact. Remove from skin with soap and water. If contaminated, flush eyes with water for 15 minutes and seek immediate medical attention. Use only with adequate ventilation.

Important: The information contained in this bulletin is considered accurate. However, no warranty is expressed or implied regarding the accuracy of the data, the results to be obtained from the use thereof, or that any such use will not infringe upon a patent. User shall determine the suitability of the product for the intended application and assume all risk and liability whatsoever in connection therewith.

Casting Thickness & Cure Time - The cure time and ultimate shrinkage of all Crystal Clear® products will vary depending on mass concentration, thickness of the casting, mold configuration, etc. For example, a 200 gram mass of Crystal Clear® 200 will cure faster if left to cure in a conical vessel (cup) versus a casting dispersed as a thin sheet measuring 3 centimeters square by 1 mm thick. This is due to the heat generated by the concentration of material in the cup versus heat that is dissipated from the sheet casting. Castings will resist yellowing when exposed to UV, but may darken over time.

• **Crystal Clear® 200** is intended for a casting thickness ranging from ½″ to 3″ at a casting weight maximum of 16 lbs. (7.25 kgs.) Castings greater than 3″ should be layer cast.
• **Crystal Clear® 202** is intended for casting in thin sections. Developed for casting thicknesses of no more than ½″.
• **Crystal Clear® 204** can be cast in thicknesses up to 6″ at a casting weight maximum of 35 lbs. (15.88 kgs.).
• **Crystal Clear® 206** is for castings greater than 6″. Crystal Clear® 206 castings greater than 1/2″ (1 cm) can be demolded after 48 hours and left to fully cure outside the mold. Castings less than 1/2″ (1 cm) should be left to cure in the mold for 7 days.

MEASURING & MIXING...

Liquid urethanes are **moisture sensitive** and will absorb atmospheric moisture. Mixing tools and containers should be clean and made of metal or plastic. Materials should be stored and used in a warm environment (73°F/23°C).

Measuring - Materials should be stored and used at room temperature (73°F / 23°C). The proper mixing ratio is 100A:90B by weight. You must use an accurate scale (gram scale or triple beam balance scale) to weigh these components properly Dispense the required amount of Part A into a mixing container. Weigh out the appropriate amount of Part B and combine with Part A.

Mixing - Mix SLOWLY, but thoroughly, for at least 90 seconds making sure that you scrape the sides and bottom of your container several times. If coloring or filling Crystal Clear® product, add filler or pigment dispersion to Part B and mix thoroughly before adding Part A.

Bubbles in the finished casting will be greatly reduced by vacuum degassing prior to pouring. Subject mixture to 29 inches of mercury in a suitable vacuum chamber until mixture rises, breaks and falls. Allow for 3 to 4 times volume expansion in mixing container.

POURING, CURING & PERFORMANCE...

Pouring - If casting Crystal Clear® into a rubber mold, pour mixture in a single spot at the lowest point of the mold. If encapsulating an object, do not pour the mixture directly over the object. Let the mixture seek its level. A uniform flow will help minimize entrapped air.

For Best Results: Bubble elimination is best achieved by pressure casting. After pouring the mixed compound, the entire casting assembly (mold, dam structure, etc.) is placed in a pressure chamber and subjected to 60 PSI (4.2 kg/cm2) air pressure for at least two hours prior to heat curing.

Castings will reach ultimate physical properties at room temperature in 7 days. Castings removed from mold before recommended cure may exhibit a tacky surface that can be eliminated by exposing casting to 150°F / 65°C for 6 hours. Pot life and cure time depend on mass concentration and mold configuration.

Post Curing - Castings will achieve maximum physical properties, better heat and UV resistance if Crystal Clear® is post cured. Post curing is recommended if castings are thin or of low mass concentration. Castings should be post cured in a mold or support structure. Post Cure Schedule: Allow the material to cure for fully at room temperature followed by 6 hours at 150°F–160°F (65°C–72°C). Allow casting or part to cool to room temperature before demolding.

Because no two applications are quite the same, a small test application to determine suitability for your project is recommended if performance of this material is in question.

SMOOTH-ON

Call Us Anytime With Questions About Your Application
Toll-free: **(800) 381-1733** Fax: **(610) 252-6200**

The new www.smooth-on.com is loaded with information about mold making, casting and more. 063016-JR

Appendix 6 Heating and cooling rates (ramps) and conditioning time before bending test for resin cure improvement EC131LV-W342 (*E3*)

Materials and methods:

In order to find the best bending mechanical properties of the EC131LV/W342 (Elantas, Italy) epoxy bi-component system, called $E3$, a selection of the factors that provide the shortest possible time during the healing process was proposed. All the curing trials of the resin were carried out in forced air convection oven SLW53 STD (PolEko, Poland).

Because $E3$ resin is the infiltrant of 3DP models, it must transfer the highest possible bending strength, and a low E-flexural modulus, in such a way that it transmits an adequate rigidity to the 3DP model, which in green presents a high fragility. Two of these factors analysed in this appendix are:

- Heating and cooling rates (ramps), called hereafter "Ramps $-R$" and;
- Conditioning time before bending test, called hereafter "condition time $-CT$".

Bending specimens were built with the open mould method. As far as their cure is concerned, the most extreme level of the time-temperature factors pre-established in Chapter 5 (part number III) was selected. The selected level $N1$ has a curing time of 1 hour at 140 ºC. This level corresponds to the shortest cure time and maximum cure temperature.

Initially it was proposed to analyse the influence on the flexural strength σ_{fM} and E-modulus E_B of two factors: Ramps $-R$ and condition time$-CT$ each one in two levels, according to Table A 1.

Table A 1. Initial ramps and conditioning time before bending test

Factors	**Levels**	
	A	**B**
Moderate ramp –R_m, (ºC.h^{-1})	Wo	Rm
Conditioning time - CT, (h)	24	96

Level A uses the shortest possible times, so it was considered not to use heating or cooling ramp – W_o" (without ramp), and the condition time of 24 hours. For level B, a moderate ramp – R_m was proposed of 55 ºC.h^{-1} for heating, and R_m of 50 ºC.h^{-1} for cooling. W_o implies that the resin specimens, once the polymerization has started, its post-cure would start directly in the furnace at the established temperature level (isothermal). After the cure, these would be directly removed from the oven to room temperature (see Figure A 2 a)).

These results will be analysed through an analysis of variance (ANOVA) to verify the statistical significance of the factors involved in this stage, and with this validation consider the proposal for the second stage.

Results:

A full factorial DoE was performed, providing a total of four combinations of the moderate ramp$-R_m$ factors versus the condition time $-\ CT$ ($R_m - CT$). For each combination, three tests were repeated, which gave a total of twelve samples to be tested. Their averages and standard deviations of the flexural strength (σ_{fM}) and the E-modulus (E_B) are presented in Table A 2 and Figure A 3.

Table A 2. Flexural strength σ_{fM} and the E-modulus E_B for the combination of R_m- CT factors

Run	**Combination** $\boldsymbol{R_m - CT}$	$\boldsymbol{\sigma_{fM}}$ *(MPa)*		$\boldsymbol{E_B}$ *(GPa)*	
1	Wo-24	138.88	±3.96	3.10	±0.09
2	Rm-24	132.63	±3.70	3.29	±0.19
3	Wo-96	128.31	±5.00	3.16	±0.15
4	Rm-96	128.37	±4.33	3.27	±0.09

With the obtained results in Table A 2, the analysis of variance (ANOVA) was performed for a confidence interval of 95% ($P \leq 0.05$). For the flexural strength σ_{fM} only the condition time $-CT$ factor was statistical significant, with a value $P = 0.017$, and an average value of flexural strength σ_{fM} = 135.75 MPa for a condition time $-CT$ = 24 horas (see Table A 3 and Figure A 1 a)). Meanwhile, for the E-modulus (E_B), there was no statistical significance of any factor or their interaction, obtaining the lowest E_B for the condition “without ramp $-W_o$”, with a value of E_B = 3.13 GPa (see

Table A 4 and Figure A 1 b)).

Table A 3. Analysis of variance for flexural strength σ_{fM} versus R_m and CT

Source	**DF**	**Seq SS**	**Contribution**	**Adj SS**	**Adj MS**	**F-Value**	**P-Value**
Ramp - R_m	1	28,71	7,76%	28,71	28,71	1,57	0,246
condition time-CT	1	165,07	44,63%	165,07	165,07	9,03	0,017
R_m* CT	1	29,76	8,05%	29,76	29,76	1,63	0,238
Error	8	146,30	39,56%	146,30	18,29		
Total	11	369,84	100,00%				

Table A 4. Analysis of variance for E-modulus E_B versus R_m and CT

Source	**DF**	**Seq SS**	**Contribution**	**Adj SS**	**Adj MS**	**F-Value**	**P-Value**
Ramp - R_m	1	0,0674	30,30%	0,0674	0,0674	3,59	0,095
condition time-CT	1	0,0007	0,32%	0,0007	0,0007	0,04	0,851
R_m* CT	1	0,0041	1,85%	0,0041	0,0041	0,22	0,652
Error	8	0,1503	67,53%	0,1503	0,0187		
Total	11	0,2226	100,00%				

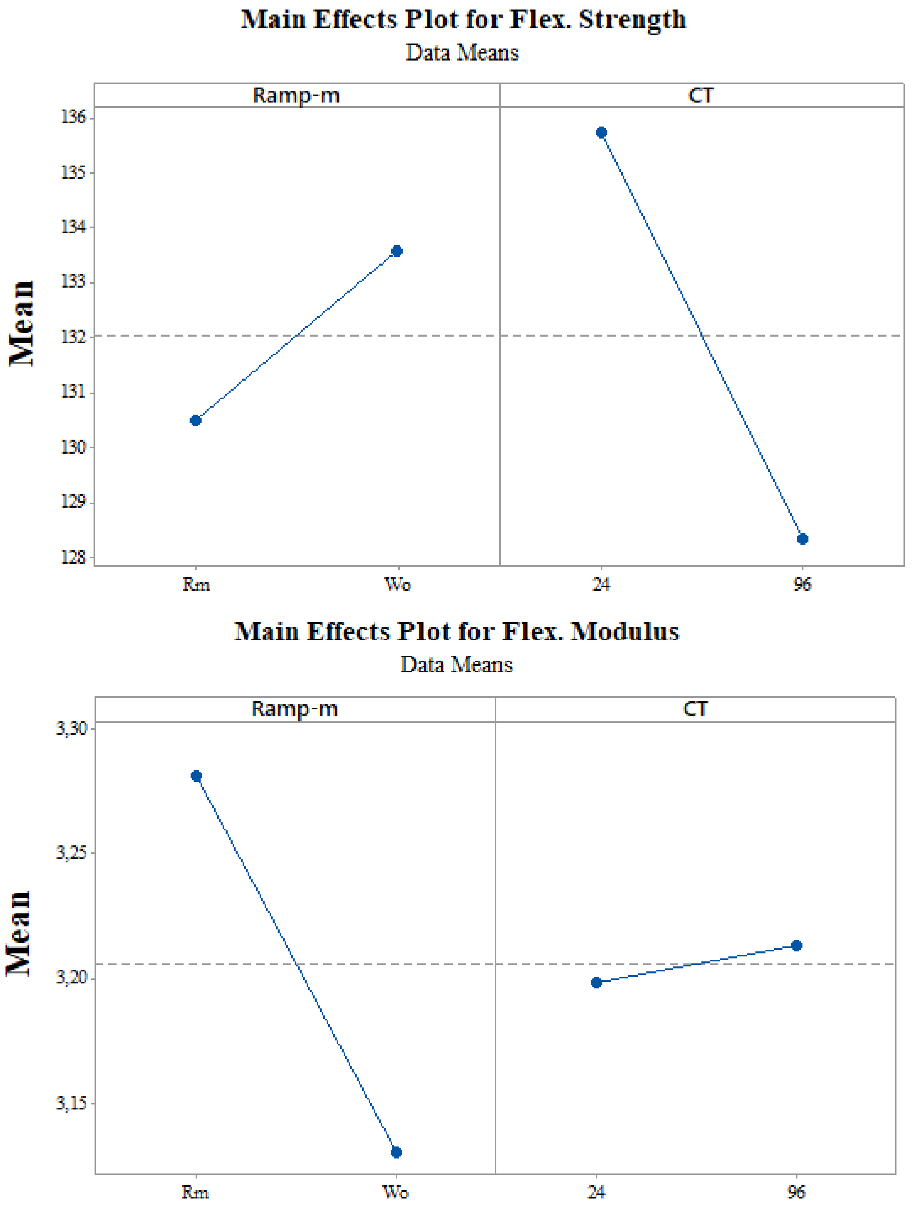

a) ***b)***

Figure A 1. Mean effects by factors R_m- CT for a) flexural strength σ_{fM}, and b) the E-modulus E_B

Based on the results obtained, the significant factor and level were set (which result showed a higher flexural strength σ_{fM} and lower E-modulus E_B for the condition time $-CT$ = 24 hours). A new intermediate ramp was proposed between the option of not using ramp and using the moderate ramp, as initially studied. This ramp was called fast ramp $-R_f$ with heating rate of 380 °C. h^{-1}, and for cooling it will be considered not to use ramp (W_o). These data were acquired in oven SLW53 STD and shown in Figure A 2.

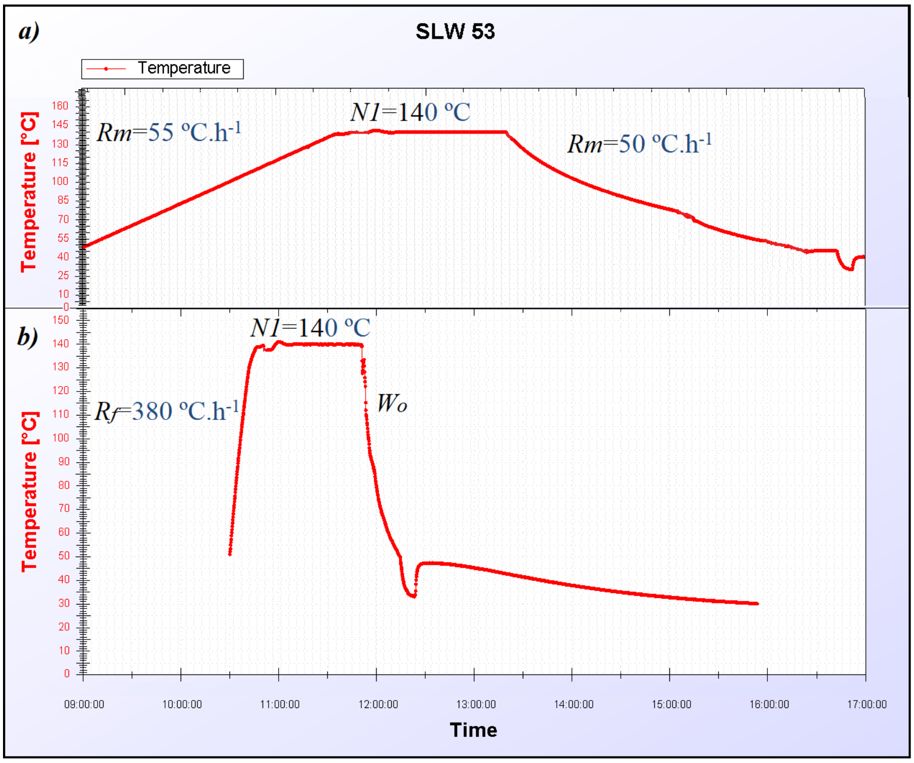

Figure A 2. Time-temperature data in the curing oven for isothermal cure level $N1$ = 140 °C, with heating and cooling ramps for a) R_m, and b) R_f

Three point bending test was carried out for the combination fast ramp versus condition time of 24 h ($R_f - CT = 24h$). Three samples were tested for such condition, whose averages and standard deviations of the flexural strength σ_{fM} and the E-modulus E_B are shown in Table A 5.

Table A 5. Flexural strength σ_{fM} and the E-modulus E_B for the combination of R_f- CT factors

Combination $\boldsymbol{R_f - CT}$	$\boldsymbol{\sigma_{fM}}$ *(MPa)*		$\boldsymbol{E_B}$ *(GPa)*	
Rf-24	130.69	±2.12	2.73	±0.23

The obtained results of flexural strength σ_{fM} and the E-modulus E_B are collected in Table A 2, Table A 5 and depicted in Figure A 3, were all these results can be compared.

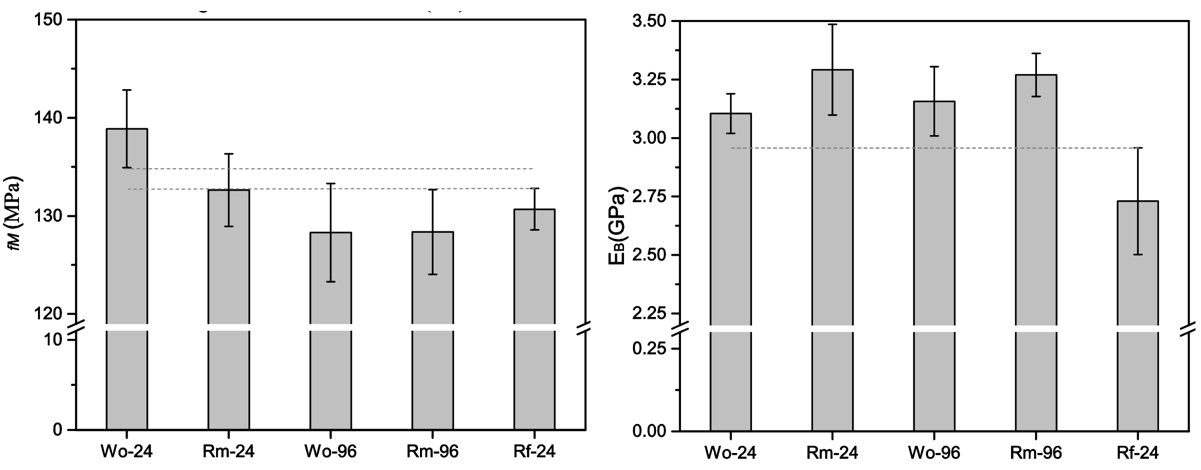

a) ***b)***

Figure A 3. Flexural strength σ_{fM} and the E-modulus E_B for the combination of R_m, R_f and CT factors

Final considerations

According to Figure A 3, it is possible to see that the combination $W_o - 24$ shows a highest value in terms of flexural strength (σ_{fM}= 138.88 ±3.96 MPa). All other combinations were found to have a statistically equal flexural strength with values ranging from 128 to 132 MPa, with the combination $R_f - 24$ showing the second best flexural strength (σ_{fM}= 130.69 ± 2.12 MPa).

Regarding the E-modulus, the ANOVA analysis showed that all the moderate ramp combinations $-R_m$ versus condition time $-CT$ ($R_m - CT$) were statistically equal with values of 3.1 and 3.29 GPa. However, analysing Figure A 3 and Table A 5, a considerable lower value of E-modulus is observed (E_B= 3.1 ±0.09 GPa) for the combination, fast ramp $-R_f$ versus condition time – CT 24 hours, (i.e. $R_f - 24$). This last result is convenient for an infiltrant to be used with fragile 3DP models.

Considering the explained in the previous paragraphs, for the analysis of the time-temperature curing factors, the ramps of Figure A 2 b) will be used, that is:

- heating ramp: $R_f = 380\ °\text{C}.h^{-1}$;
- cooling ramp: without ramp W_o, and
- conditioning time before bending test: $CT = 24\ hours$.

Appendix 7 Experimental measurement of viscosity vs. temperature of the mixed components of epoxy resin EC131LV-W342 (*E3*)

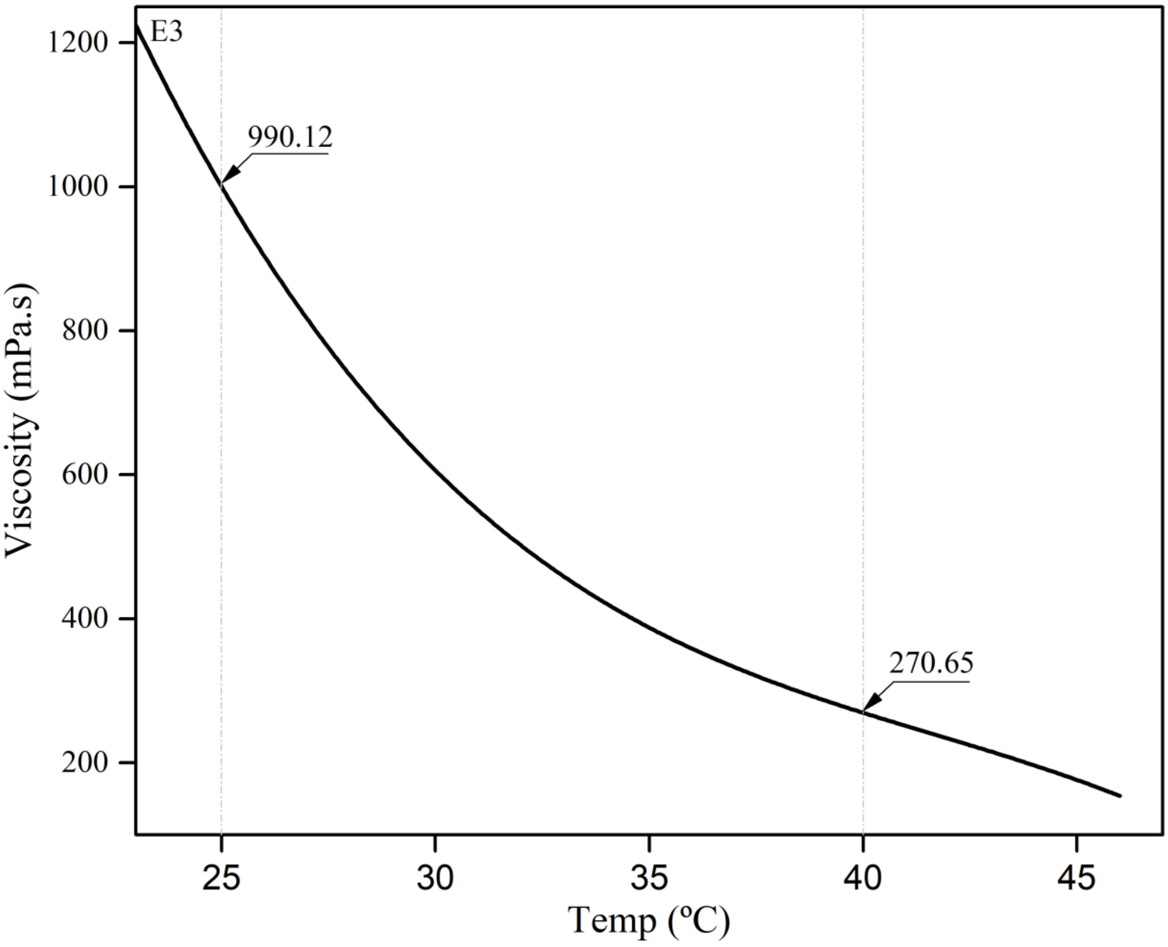

Figure A 4. Temperature of the mixed components of epoxy resin EC131LV-W342 ($E3$)

Appendix 8 Curriculum Vitae

Edwin Marcelo Ocaña Garzón

Born 24th May 1977 in Quito, Ecuador

Married to Margoth Vinocuña

Education:

2019	PhD thesis, under the supervision of Professor Jorge Lino Alves, PhD, Associate Professor FEUP, Portugal,
2014	MBA - mention in Strategic Direction, UIDE, Ecuador,
2002	Mechanical Engineer, EPN, Ecuador,
1995	Bachelor in physical and-mathematical sciences, High School Experimetal Montúfar, Ecuador.

Professional experience:

- 2008, until now: Full time professor in the Department of Energy Sciences and Mechanics (DECEM) of the Universidad de las Fuerzas Armadas-ESPE, in the area of Manufacturing and Design, Quito- Ecuador,
- 2004-2010: Independent contractor, of Siemec Cia. Ltda, and Andes Construcciones & Montajes, Quito-Ecuador,
- 2003-2004: Head plant engineer of construction firm Proyectos Myrco S.A., Quito-Ecuador,
- 2002-2003: Head plant engineer of construction firm Beecons S.A., Quito Ecuador,
- 2001-2002: General Services Director and Supervisor in remodelling of the shopping centre Plaza de las Américas, Quito-Ecuador

"All that man ignores, does not exist for him. Therefore, the universe of each, is summed up to the size of his knowledge."

Albert Einstein